The extrusion limits, parameters and microstructures of aluminium 2014 solid and powder.

Thesis

The Extrusion Limits, Parameters and Microstructures of Aluminium 2014 Solid and Powder

Heying Shi

A Thesis submitted for the

Degree of Doctor of Philosophy

Materials Discipline

May 1990

Contents

List of Tables

List of Figures

List of Plates

25. Inner core microstrucutres of solid extrusions with different temperatures
26. Higher magnification of Plate 25
27. Higher magnification of Plate 26
28. TEM microstructures of extrusions at 250, 400 and 450°C
29. Dislocation and precipitate structures of extrusion at 250, 400 and 450°C
30. Optical microstructures of extrusion with different extrusion ratios
31. Inner core microstructures of extrusions with different extrusion ratios
32. Higher magnification of Plate 31
33. Higher magnification of Plate 32
34. Subgrain and dislocation structures with different extrusion ratios
35. Fine powder extrusions with different temperatures
36. Higher magnification of Plate 35
37. Coarse powder extrusions with different temperatures
38. Higher magnification of Plate 37
39. TEM microstructures for powder extrusions
40. Surface finish of solid and powder extrusions
41. Precipitates in different deformation processes

Terminology

A	cross section area of billet or container
A_{1-3}	constants in hot working theory
B	platen breadth in compression test
b	width of strip in compression test
c_p	specific heat of a medium
D	diameter of billet or container
D_e	diameter of extrusion
d	subgrain diameter
g	thermal conductivity of a medium
H	total heat
h	height of deformation zone, thickness of strip
J	mechanical equivalent of heat
k,τ	shear stress
L	load
l	length of billet
M	twist moment
m	variable in upper-bound solution
P	extrusion pressure
Pmax	maximum extrusion pressure where extrusion starts
Pmin	minimum extrusion pressure where steady-state extrusion starts
Q	amount of heat dissipated per unit time per unit length
R	extrusion ratio or gas constant
r	radius of container
r_0	radius of billet
s	length of line in upper-bound solution
T	transient temperature (°C)
Ti	initial billet temperature (°C)

Tc	container temperature (°C)
T_0	temperature difference between billet and container (°C)
Te	temperature at start of extrusion (°C)
Tx	temperature at start of steady-state condition (°C)
ΔT	temperature rise due to deformation energy (°C)
t	time
v	velocity
V	ram speed
V_c	ram speed of compression press
V_D	volume of deformation
W	mechanical work
X	ram travel distance during compaction
x	ram travel distance when pressure falls from Pmax to Pmin
Y	yield tensile stress
Z	Zener-Hollomon parameter
α, β, n, n'	constants in hot working theory
α'	thermal diffusivity of medium
γ	shear strain
$\dot{\gamma}$	shear strain rate
ΔH	activation energy
ΔP	difference between Pmax and Pmin
$\epsilon, \bar{\epsilon}$	strain and mean equivalent strain
$\dot{\epsilon}, \dot{\bar{\epsilon}}$	strain rate and mean equivalent strain rate
ϵ_c	compression strain
θ	amount of twist
μ	friction coefficient
ρ	density
σ	mean equivalent stress
σ_c	compression stress
ω	assumed deformation zone angle ω=45°

Acknowledgements

The Author would like to thank:

Dr. A.Greasley	His great supervision and encouragement
Dr. L.Edwards	His supervision
Harwell Laboratory	This project, financial support, materials and technical help
Staffs in the Dept.	Their help and encouragement

Abstract

Solid and powdered Al-2014 alloy extrusions, heat transfer during compaction, temperature changes during extrusion, microstructures of extrusion products, hot torsion and plane strain compression tested specimens have been extensively investigated.

Estimation of maximum and minimum pressure allows the prediction of the possibility of an extrusion and the amount of heat transferred from mechanical work to be obtained.

Temperature changes during extrusion have a major effect on the extrusion pressure, microstructure and quality of the products. Temperature changes are mainly in two stages: compaction and steady-state and a numerical model of these stages has been developed.

Hot torsion and plane strain compression data has been analysed and this data is used to predict the shear stress at any temperature and strain rate by using hot working theory. The minimized extrusion pressure may then be obtained by upper-bound solution.

Microstructures of hot torsion, plane strain compression and extrusion have been extensively examined. ATLASES of microstructures at hot working condition for both solid and powdered material have been created.

The thermal model has been shown to be essential for the fundamental prediction of hot shortness limits and for the comparison of microstructures between extrusion and metal working tests.

Chapter 1

AIMS AND PROBLEMS

1.1 Problems

Although extrusion is considered a relatively young metal-working process [1,2], it has grown rapidly since the very first extrusion press was developed by Joseph Bramah in 1797 [1] to become one of the major fabrication methods. The advantage of extrusion is that there is no or little machining needed for the extruded products and complex sections can be produced in one operation. Aluminium is widely used in extruded sections because of the high demand for aluminium products in industry and daily life due to its excellent properties; high strength–to–weight ratio, good electrical and heat conductivity. In addition, aluminium is very ductile compared to many other strong materials. Hence large reductions, a wide variety of shapes, good surface finishes and high production rates can be produced. Extrusion ratios are limited about 40:1 for hot extrusion of steel but may be as high as 400:1 for aluminium [3,89].

However, extrusion is a complicated process. There are many parameters influencing the quality of extruded product. These parameters include properties intrinsic to the material and those related to the operation of the extrusion process. Additionally, the press capacity determines whether a given extrusion is possible. It must exceed the resistance of the material to flow which is determined by the shear yield stress of the material, the extrusion ratio of the process (the strain), strain rate (including ram speed), the die shape, the initial billet temper-

ature and the frictional conditions prevailing. In order to produce a good quality product in many advanced alloys it is very important to know the exact working temperature at which the material is deformed. This allows the microstructure of the product to be controlled and helps to prevent the occurrence of hot shortness. Die conditions (shape and surface quality) and lubricant conditions also affect the surface quality of the product.

1.2 Aims of this work

Aluminium 2014 alloy is a strong heat treatable alloy and can be used in structural components. The powdered version is a popular matrix material for metal matrix composites. The properties of the material are dominated by the microstructure which is partially determined by the temperature and strain rate at which the material is deformed.

The main aim of this work is to be able to predict the microstructure of solid and powdered aluminium 2014 alloy from the feedstock condition and the extrusion parameters planned.

As will be shown in later chapters, for a particular alloy at a specific strain, the billet temperature at the end of compaction stage (see Section 4.2) primarily determines the maximum extrusion pressure at the strain rate employed. This temperature also influences the temperature at the start of steady–state conditions and it is this latter temperature that primarily influences the microstructure and properties of the extruded product. So it is very important to obtain an accurate estimate of temperature at the end of the compaction stage.

A complementary aim is to be able to use the microstructures of extruded products as independent checks on the accuracy of the analytical models.

In order to be able to do this it is necessary to generate standard microstructures produced at controllable temperatures and strain rates. Hot working tests, (torsion and plane strain compression) performed at controlled temperatures and strain rates can be used to produce such an atlas of microstructures for the alloys

involved.

These tests not only provide microstructural samples but also provide independent flow stress data which can be used to provide an independent analytical check on extrusion pressure models. This then allows flow stresses to be derived from a range of extrusion data which covers a wider range of temperature and strain rate than the original metal working temperatures.

Chapter 2

LITERATURE SURVEY

2.1 Extrusion

2.1.1 The stages of extrusion

Direct extrusion involves forcing a billet to pass through a static shaped die corresponding to the section required using the pressure delivered by an advancing ram to obtain desired product dimensions.

Fig. 2.1 shows a typical load–displacement curve for direct extrusion of solid material. It is usually divided into three stages [1]. Stage I is the upset, when the billet is compacted to fill the container. During this stage the pressure rises rapidly until its maximum and the ram travels a limited distance. A small amount of material called the "pre–extrusion" is forced through die mouth.

In stage II, there is an initial rapid decrease in pressure followed by a steady pressure change until the end of extrusion, hence this is known as the steady–state stage.

Stage III is the end of extrusion when only a thin disc of the billet is left in the container and the ram interferes with the deformation zone. There is usually a significant increase in load here. This region is often not observed because a thick discard is left in the container and then ejected. Just before stage III the rear surface of the billet may begin to be extruded. This often causes a defect. Hence the discard is often left even thicker to avoid this.

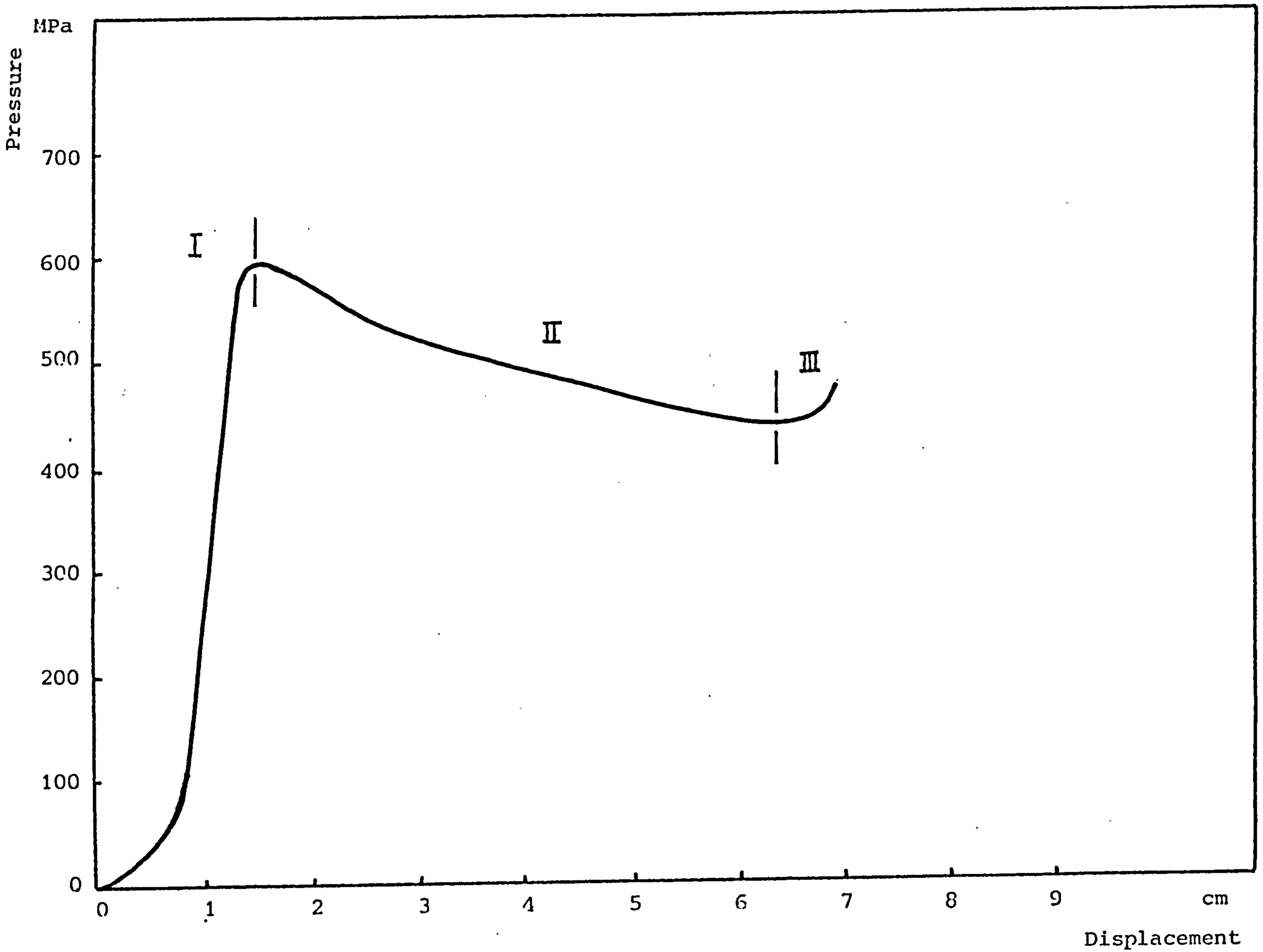

Fig. 2.1 Typical solid extrusion trace

2.1.2 Extrusion limits and predictions

It is well known that when extrusion temperatures and ram speeds are high, circumferential cracks, known as hot shortness will occur at the surface of extruded product. Usually process conditions are optimized to produce defect-free products with controlled dimensions, microstructure and mechanical properties [4].

Hirst and Ursell [5] presented the first limit diagram to describe the possibility of extrusion, based upon the extrusion ratio, billet temperature and ram speed (shown in Fig.2.2 (a)). The pressure required for the extrusion is obtained from a modified Johnson's equation.

$$P = Y(0.47 + 1.2\ln R)$$

This limit diagram indicates a satisfactory extrusion within the capacity of a press and an unsatisfactory extrusion due to incipient melting. It consists of a plot of the extrusion ratio against the billet temperature. The limit line on the left side represents the capacity of press, whilst the boundary on the right side is the onset of incipient melting which in the worst case is represented by adiabatic conditions.

Ashcroft and Lawson [6] presented a limit diagram for Al–Zn–Mg–Cu alloy extrusion (see Fig.2.2 (b)) including a specific ram speed which gave the extrusion ratio for hot shortness failure at different initial billet temperatures. Meadows and Cutler [7] produced an extrusion diagram for Al–Mg–Si alloy which included the temperature rise from the heat generated by the deformation work.

Sheppard with Raybould [8] and Castle [9,10] improved limit diagrams including strain rate, temperature rise and structural property changes for aluminium alloy.

Stenger [11] produced a ram speed versus temperature limit diagram for some aluminium alloys. The boundaries were considered to be the observation of the commencement of cracking during hot extrusion. Paterson [12] produced a limit diagram from his research work for aluminium 2014 alloy in direct and indirect extrusion (see Fig. 2.3). For both direct and indirect extrusions, the limit diagrams were constructed with ln R versus initial billet temperature at two constant ram

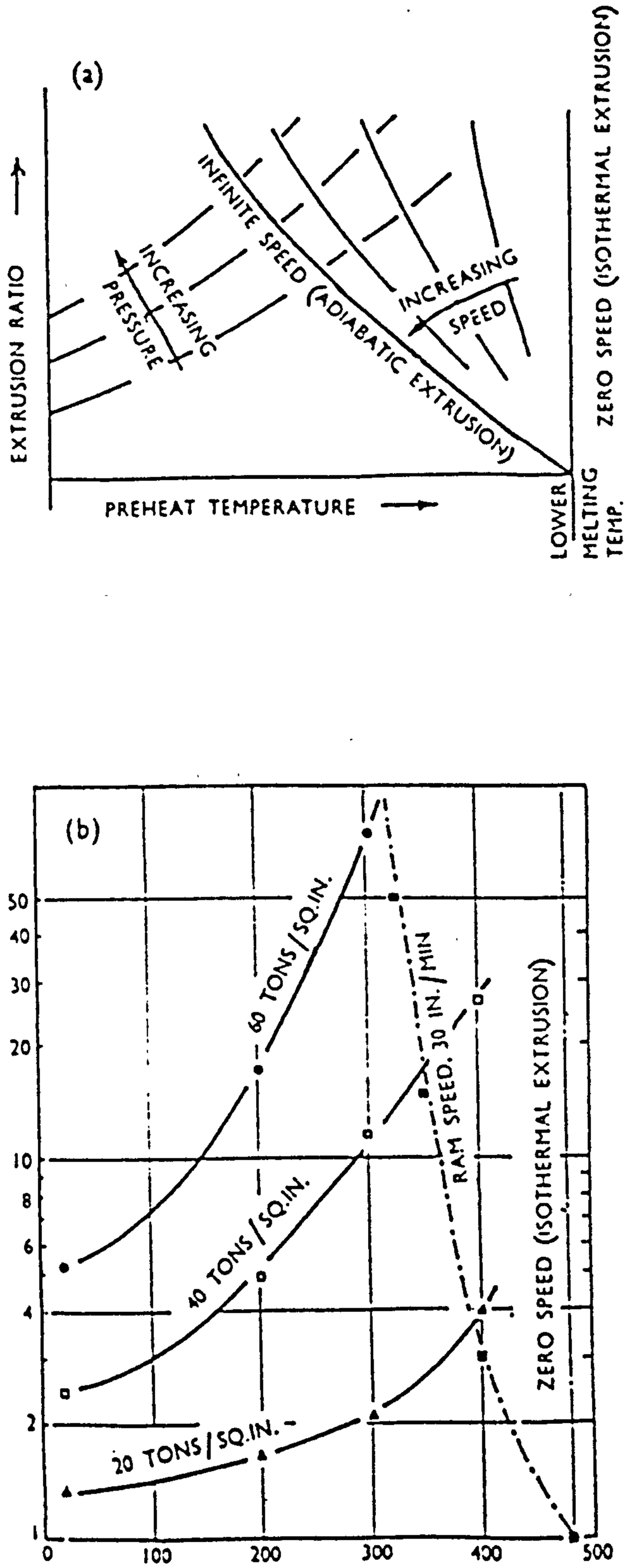

Fig. 2.2 (a) *Limiting factors in extrusion.* (*Hirst and Ursell*).
(b) *Limiting curves for the extrusion of Al–Zn–Mg–Cu alloy at a ram speed of 30 in./min, and at various pressures.* [6]

■ Failure due to hot shortness.

speeds. These diagrams demonstrated that the lower pressure required for indirect extrusion resulted in an increase in extrusion limit.

Hence limit diagrams provide a useful way of presenting considerable amounts of data.

2.1.3 Temperature models

Among the extrusion parameters, temperature is one of the most important factors [13] to be considered in the extrusion of metals as it not only helps determine the pressure required for the process, but also affects the surface finish, structure and properties of the products. Repeated attempts have been made at controlling the temperature changes during extrusion. There are many variables that can affect the billet temperature change; press mechanics, extrusion conditions, material properties and deformation characteristics. Temperature changes arise from the temperature difference between billet and surroundings (tools), and the deformation energy which is mainly converted to heat.

Hughes and Sellars [14] considered the heat transfer to various elements: billet withdrawal from the furnace, heat loss of billet during upset and upon entering deformation zone, heat loss to the tool and lubricant, and also to heat gained from deformation energy.

During deformation the applied mechanical work is largely converted to heat energy. Only a small proportion of the mechanical energy is expended in the deformation. This work appears as an increase in crystal defects such as dislocations and grain boundaries and microstructural change [15]. The major portion of the mechanical work heats the billet and raises the billet temperature. The deformation energy can be found as the product of stress and strain. It has been reported that 92—93% of the mechanical work is transformed to heat for polycrystalline aluminium, 95—95.5% for aluminium single crystal, 86.5% for steel and 90.5—92% for copper [16,3,17]. In extrusion, the logarithm of the extrusion ratio represents the strain. The higher the extrusion ratio, the greater will be the heat generated and the higher the temperature rise. Typical temperature rises of 74°C for alu-

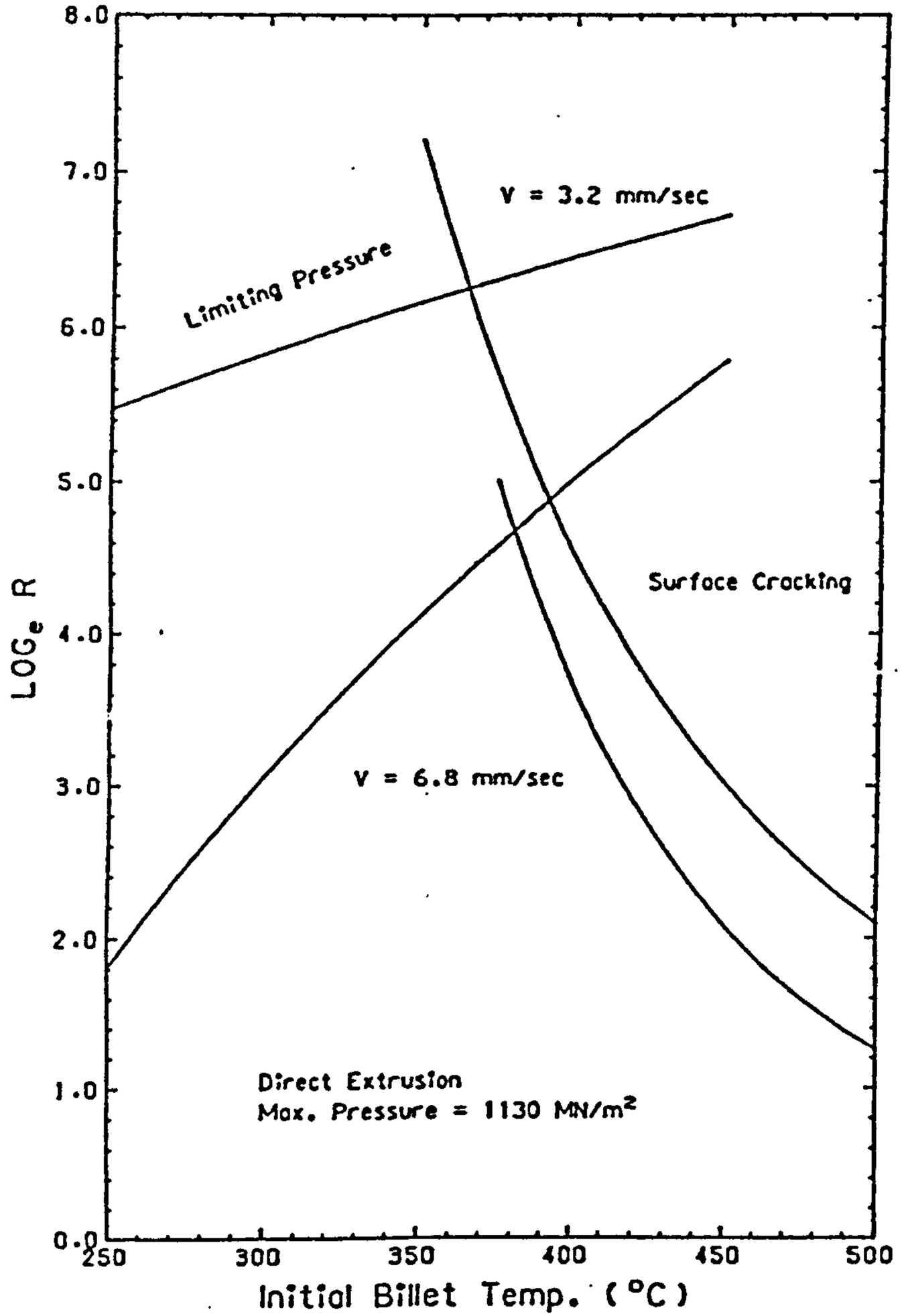

a. Direct extrusion

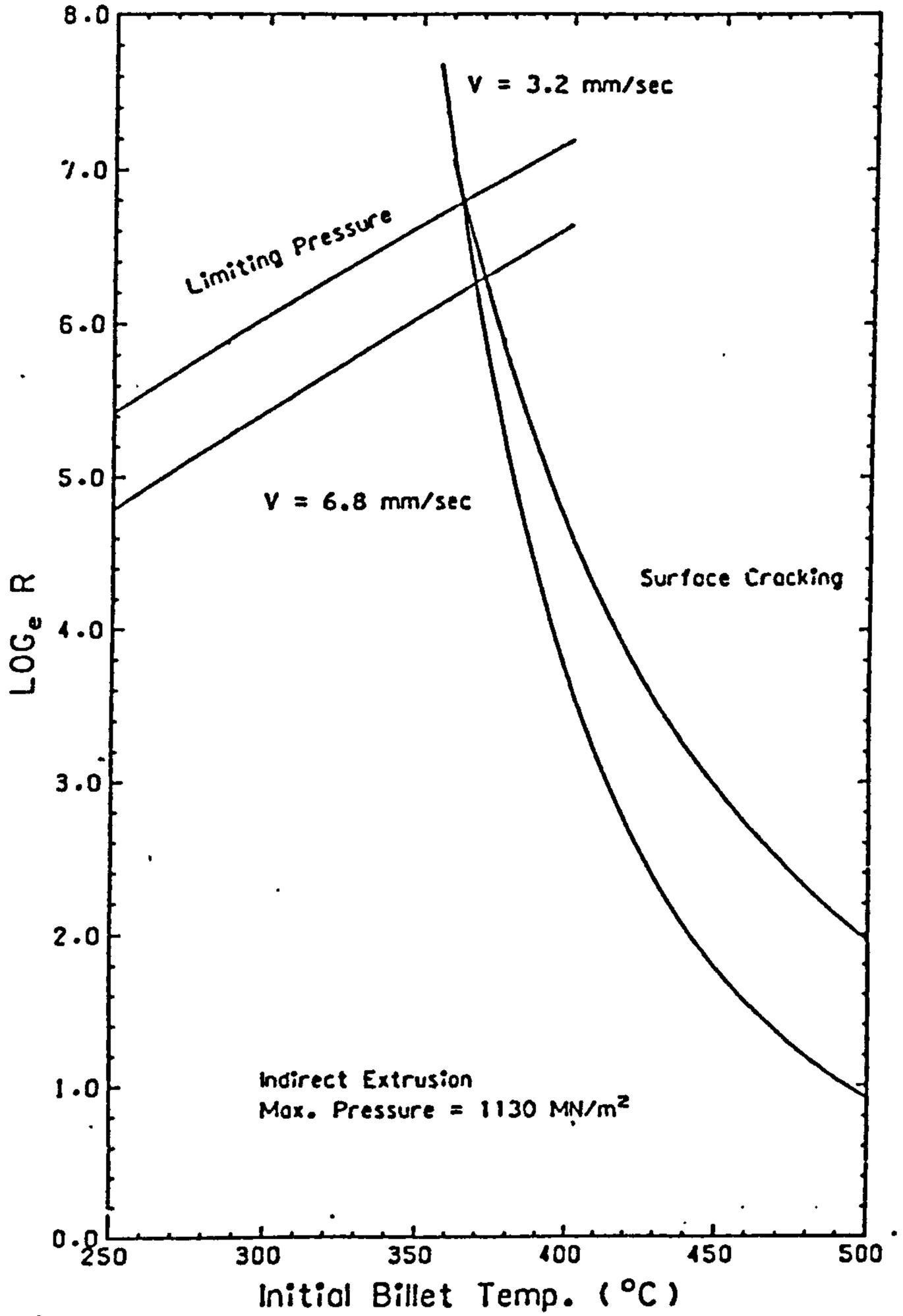

b. Indirect extrusion

Fig. 2.3 Limit diagrams for Al–2014 Alloy [12]

minium [3], and 60°C in aluminium alloys have been reported [1]. Singer [13] has stated that for aluminium alloys the theoretical temperature rise might be as high as 300°C in industrial extrusion. Singer and Coakham [18] have confirmed this by extruding aluminium at room temperature at a speed of 12.5 mm/sec. and recording a temperature rise of 260°C measured by a thermocouple inserted into the die region.

Bishop [16] has contributed a fundamental basis for determining heat distribution in plane-strain extrusion at the steady-state condition. He assumes a fraction of the distortion energy is converted into heat and this heat is a function of time and velocity components in the two direction of the plane. This heat is generated in rapid jerks followed by conduction period in a stationary medium and is reported [16] to be an overestimate by 10%.

Akeret's [19] numerical analysis divided the billet into transverse discs with a heat source due to the plastic deformation in the foremost disc. Heat conduction to the container was analysed with annular cells of the same thickness as the disc. A constant coefficient of heat transfer was assumed between billet and cooler tools. He found that only 20 mm depth of the container wall was influenced by the billet temperature. All these models refer to steady–state conditions.

If adiabatic conditions cannot be assumed then the temperature rise also varies with ram speed. The higher the ram speed, the higher the temperature rise. Singer and Samarrai [20] found a linear relationship between the temperature rise and the logarithm of ram speed and extrusion ratio. Their model assumes heat is generated in the plane of the die and partly conducted back to the billet. There is no radial heat loss to the container.

Sharman [21] has developed a model for radial temperature profile during steady-state extrusion. Tanner and Johnson [15] have predicted the temperature distribution in the deformation zone and exit plane, calculated from the temperature rise caused by mechanical work.

The maximum temperature rise ΔT is stated by Meadows and Cutler [7] as:

$$\Delta T = \frac{3.7Y(0.47 + 1.2\ln R)(1 + \frac{2\mu l}{D})}{\rho c_p} \tag{2.1}$$

Castle and Sheppard give an expression for temperature rise including temperature difference between billet and container [22] as:

$$T = \frac{0.9V\ L\ t\ J^{-1} - T_D\ C_2}{C_1} \tag{2.2}$$

where

C_1, C_2—time dependent constant in temperature analysis

T_D —temperature differential between product and tools

Altan et al [23] have an approximate calculation of velocity and temperature distribution for steady-state in extrusion. The heat generated from deformation and friction heats the billet in deformation zone and is conducted back to the tooling.

These models too, are confined to the steady-state condition of extrusion and calculate temperature change once the extrusion is well under way.

When a preheated billet is placed into a container which has a different temperature to the billet, transfer of heat occurs. This heat flow can significantly change the original billet temperature if the temperature difference between the billet and container is large. This heat transfer influences the extrusion temperature, the extrusion pressure and the temperature at the start of steady–state deformation. Due to the complexity of the heat transfer, experimental monitoring of the temperature changes during extrusion has been attempted. Thermocouples have been inserted into the billet [14] and extruded to investigate the temperature change. Product temperature has also been monitored immediately it emerges from the die [13,18]. It is well known that the extrusion temperature must be kept below the temperature where incipient melting occurs [14,8,7,5,6]. With the complication of heat transfer between billet and tooling some workers [24,25,26,27,29,28,30,31] have controlled the container temperature to 50°K below the billet temperature to counter the heat generated by friction and deformation energy during extrusion.

Under these conditions, the initial heat transfer may be ignored until steady-state extrusion begins. Other workers [32,33,12,9] have used predetermined cooling curves to monitor heat losses to the container.

Carslaw and Jaeger [35] produced a mathematical integration for heat transfer by conduction for this type of situation in 1938. It contains an infinite integral of a certain combination of Bessel functions. This equation describes the characteristics of transient heat flow caused by conduction into an infinite medium from a cylindrical heat source that is kept at a certain temperature different from the surroundings. Gemant [36] used this equation to solve the heat flow from a heated pipe which was suddenly introduced into surroundings which had a temperature difference with the pipe. However, in 1946, this integration was not suitable for numerical calculation. It was therefore expanded into a series and integrated by terms to produce a series of curves to represent the heat flow. These curves permit the determination of temperature for any combination of the variables: time and distance from the heat source and are now well established for non-steady heat flow. One of the curves is shown in Fig. 2.4 which illustrates the rate of heat loss per unit time and per unit length.

The situation in extrusion is quite similar to Gemant's solution. When a preheated billet is suddenly brought into a container, conduction of heat occurs. The container can be considered radially infinite. The temperature of the billet can be considered constant and uniform. So this theory can be directly used in extrusion to describe the conduction of heat between the billet and the tooling. Many researchers [20,19] have found that their results are in agreement with Gemant's curve. Greasley [37] produced a model using this integration to predict the billet temperature during upset stage. He calculated the heat loss or gained from the container by the conduction of heat and combined it with the heat converted from mechanical work during the upset stage. This enabled the billet temperature at the start of extrusion to be predicted. Practically he observed a 'jerk' period occurring when the pressure fell from the maximum to minimum and during this 'jerk' period the ram travels a certain distance producing a certain amount of

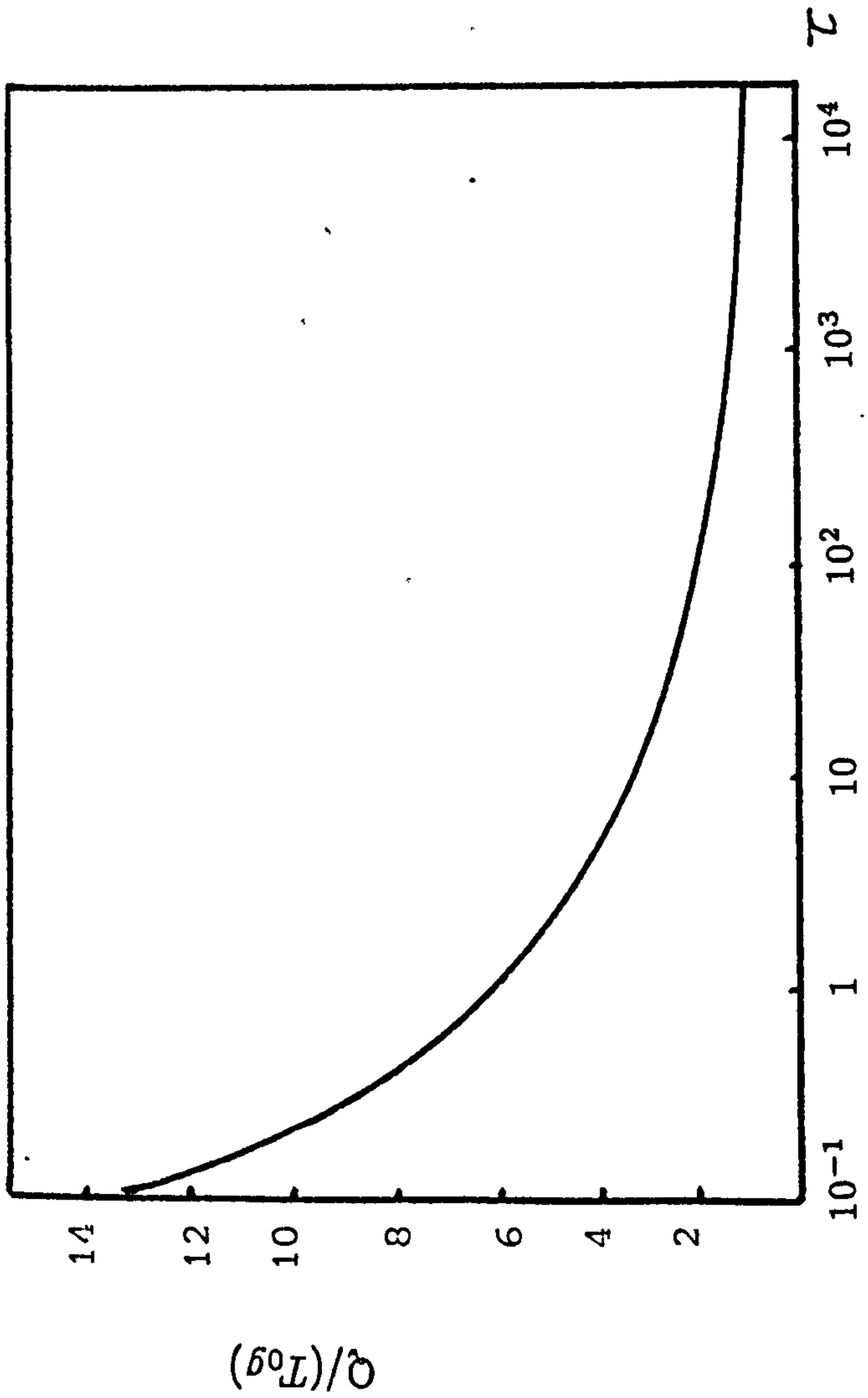

Fig. 2.4 Heat dissipated per unit time and per unit length of pipe as function of time [36]

mechanical work. The work done during this jerk period was considered to adiabatically heat the deformation zone. The temperature at the start of steady–state extrusion was estimated to be the temperature after the upset period plus the temperature rise during the 'jerk' period. Once obtained, the temperature at the start of steady–state condition and the strain rate, given by the extrusion conditions, allow the flow stress to be obtained. This first estimate can be used in conjunction with analytical and empirical models to predict the maximum and steady–state extrusion pressure. Iteration can follow to improve the accuracy of these interdependent parameters. Improved estimates of the temperature at which the steady state extrusion begins also allows more accurate prediction of hot shortness limits.

2.1.4 Extrusion load models

Before start of an extrusion, the first consideration of an operator is to decide whether the maximum extrusion pressure required for the particular extrusion conditions (billet temperature, extrusion ratio and ram speed) is within the capacity of the press, to make sure a sticker (a billet that 'sticks' in the container without going through the die because the required pressure exceeds the capacity of the press) will not occur.

A great deal of effort has gone into understanding how temperatures, ram speed and extrusion ratios affect extrusion pressures. Early work [1] produced empirical relationships derived from experimental data, which have been proved useful and established the basis of analysing the extrusion process.

Johnson and Kudo [38] and Bishop [39] suggested that the peak pressure may be caused by a friction effect. Wilson [41], Duffill and Mellor [42] explain it as a temporary breakdown of lubrication. Wilcox and Whitton [43] and Avitzur [44] associate these phenomena with the formation of a dead metal zone within the billet.

Sheppard [45,46,32] explained the pressure as the energy required for establishing the quasi–static deformation zone and the accumulation of friction effects.

The drop in pressure after the maximum has been explained by improved

lubrication [42] or due to billet temperature increase [47].

Others have paid attention to predicting the maximum pressure using slip–line field techniques for idealized non–work hardening rigid plastic material in the condition of plane–strain deformation [2,38] and upper–bound solutions [38] which consider velocity fields in an incompressible material and require a maximum amount of work to produce the required strain. The latter analysis gives an excess of work compared with that predicted by slip–line field and minimization is required to obtain a load nearer to that given by the slip–line field. Upper–bound solutions can also be used for axisymmetric deformation. Johnson and Kudo [38] gave cylindrical coordinates to express the axisymmetric deformation. Usually the axis of symmetry is the extrusion axis. The velocity component in the radial direction causes a circumferential strain in axisymmetric extrusion. The billet is divided into cylindrical regions then again divided by triangular velocity fields to give the load [2,38,44,48].

Halling and Mitchell [49] use a single and double triangle arrangement of velocity discontinuities to describe the axisymmetric extrusion through conical dies to produce circumferential straining. It is found [6] that a linear relationship between the maximum extrusion pressure and the logarithm of extrusion ratio R exists when $R > 4$. When extrusion ratio is lower than 3 extrusion pressure is proportional to R [43].

For axisymmetric extrusion, assuming homogeneous deformation is obtained, Bishop [39] shows an upper–bound solution of the form:

$$W = \int_{l_i}^{l_f} \frac{YV\delta l}{l} \tag{2.3}$$

where

W is the total work done.

From which the pressure can be evaluated as:

$$P = Y \ln R \tag{2.4}$$

Chamber	Die	Range of reduction,%	a	b
Smooth	Smooth	67 — 97	0.63	0.95
Rough	Smooth	79 — 94	1.19	0.83
Smooth	Rough	89 — 97	0.37	1.24
Rough	Rough	93 — 97	0.63	1.28
Hom. defor. theory			0.00	1.00

Table 2.1 Empirical formulae for extrusion pressure

Further, he supplies the following empirical formula for the extrusion pressure [50].

$$\frac{P}{2k} = a + b\ln R + \mu l \tag{2.5}$$

where

a — redundant work

b — efficiency factor

μl — friction

k — the shear yield stress

The relation between k and the uniaxial tensile yield stress Y is $Y = \sqrt{3}k$ or 2k depending on whether Von Mises' or Tresca's yield criterion is adopted. Bishop presented a table for the constants a and b (see Table 2.1) [39].

Dodeja and Johnson [51] found that for pure lead, (which is used to simulate a non-hardening material as it is self-annealing at room temperature), extrusion through square dies at a speed about 0.04 mm/sec. produces an expression for pressure:

$$\frac{P}{Y} = 0.8 + 1.5\ln R \tag{2.6}$$

for lubricated condition.

and

$$\frac{P}{Y} = 0.6 + 1.8\ln R \tag{2.7}$$

for unlubricated condition.

It is reported that the former equation fits well for aluminium [2].

Johnson [52] also gives his empirical results which are in agreement with the value of a and b in Table 2.1.

Kudo [48] derived the following relationships between P/Y from upper-bound solution for axisymmetric extrusion:

$$\frac{P}{Y} = 0.88 + 1.30 \ln R \tag{2.8}$$

for smooth die.

$$\frac{P}{Y} = 1.06 + 1.55 \ln R \tag{2.9}$$

for rough die.

Farag and Sellars [53] report the extrusion pressure at deformation zone to be:

$$\frac{P}{\sigma} = 1.0 + 1.4 \ln R \tag{2.10}$$

Jonas et al [54,55] suggest that the extrusion pressure (P_t) in direct extrusion is the sum of the pressure for homogeneous deformation pressure (P_h), overcoming friction (P_f) and pressure expended for redundant deformation (P_r).

$$P_t = P_h + P_f + P_r \tag{2.11}$$

and thus for an extrusion ratio of 40:1 is:

$$\begin{aligned} P_h &= \bar{\sigma} \ln R = 3.7\bar{\sigma} \\ P_f &= \bar{\sigma}[exp(\frac{4\mu l}{D_o}) - 1] = 1.2\bar{\sigma} \\ P_r &= 2.0\bar{\sigma} \end{aligned}$$

Finally

$$\frac{P_t}{\bar{\sigma}} = 6.9 \tag{2.12}$$

where

$\bar{\sigma}$ — mean equivalent flow stress

Method of calculation	P_h	P_r	P_f
Pearson	3.7 $\overline{\sigma}$		
Siebel			0.5 $\overline{\sigma}$
Sachs & Eisbein	3.7 $\overline{\sigma}$	2.0 $\overline{\sigma}$	1.2$\overline{\sigma}$
Thomsen et al	3.7 $\overline{\sigma}$	1.9$\overline{\sigma}$	1.2$\overline{\sigma}$
Rowe			1.7 $\overline{\sigma}$

Table 2.2 Value of P_h, P_f, P_r

Calculated values of P_h, P_f, P_r using different methods are listed in Table 2.2 for a 40:1 extrusion.

Pearson [1] finds the extrusion pressure is :

$$P = 1.45Y \ln R \tag{2.13}$$

for plane strain and axisymmetric extrusion.

Hirst and Ursell [5] and Crane [50] report that for frictionless conditions between billet and container wall from Johnson's equation:

$$\frac{P}{Y} = 0.47 + 1.2 \ln R \tag{2.14}$$

for frictional effect [5]:

$$\frac{P}{Y} = (0.47 + 1.2 \ln R)\, exp(\frac{4\mu l}{(D - D_e)}) \tag{2.15}$$

Avitzur [56] produces a more generalized expression based on a spherical velocity field for direct extrusion:

$$\frac{P}{Y} = -2\left\{ f(\alpha) \ln R + \frac{1}{\sqrt{3}}[\frac{\alpha}{\sin^2 \alpha} - \cot \alpha + (cot\alpha) \ln R + \frac{l}{r_0} - (1 - R) \cot \alpha] \right\} \tag{2.16}$$

where

$f(\alpha)$ — complex function of dead zone angle

$$f(\alpha) = \frac{1}{\sin^2 \alpha} \left\{ 1 - \cos \alpha \sqrt{1 - \frac{11}{12} \sin^2 \alpha} + \frac{1}{\sqrt{11.12}} \ln \frac{1 + \sqrt{\frac{11}{12}}}{\sqrt{\frac{11}{12}} \cos \alpha + \sqrt{1 - \frac{11}{12} \sin^2 \alpha}} \right\}$$

Depierre [3] gives an expression:

α	a	b
30	0.419	1.006
45	0.659	1.016
60	0.945	1.034

Table 2.3 Values of α , a and b

$$\frac{P}{Y} = (a + b\ln R) + mk\ cot\alpha\ \ln R \tag{2.17}$$

where

$$m = \tau_i/k$$

τ_i is uniform interface shear stress between billet and container liner and a and b are in Table 2.3.

Castle and Sheppard [32] suggest a semi–empirical equation for extrusion load:

$$L = \frac{\pi}{4}\sigma D^2\ (a + b\ln R)\ exp(\frac{4\mu l}{D}) \tag{2.18}$$

Sheppard and Raybould [8] give the load expression by using minimized upper-bound solution:

$$Load = A\ \sigma(0.52 + 1.32\ln R) \qquad 1 < R < 100 \tag{2.19}$$

$$Load = A\ \sigma(-13 + 4.78\ln R) \qquad 100 < R < 1000 \tag{2.20}$$

Extrusion pressure is also reported to increase with ram speed V and the following expressions have been used:

$$P = a + bV \qquad [47] \tag{2.21}$$

$$P = A_3\ V^m \qquad [57] \tag{2.22}$$

with

$$m = 0.1 - 0.3$$

Extrusion pressure is always related to the flow stress of a particular material and the flow stress depends on the strain rate and temperature of deformation. Meadows and Cutler [7] obtain a relationship from iteration and regression:

$$Y = 6.987 + 0.13\dot{\epsilon} - 0.0028\dot{\epsilon}^2 + 0.11 \ln R - 0.008T - 0.71 \times 10^{-8} T^3 \quad (2.23)$$

These expressions have provided a good guide for predicting extrusion pressure. However, there are some limitations in directly employing these models into practice. The general expressions of the relationship between extrusion pressure and yield strength of the material are based on empirical tests and are of the form.

$$\frac{P}{Y} = A + B \ln R$$

These do not include local friction condition, die shape, which also contributes to redundant work and do not specify strain rate and temperature.

Later expressions have made some improvement which include friction conditions and die angles but not relate directly to deformation temperature. It is difficult to express all the parameters which influence extrusion pressure in one formula. The work carried out in this investigation is to find out the actual temperature at which the material is deformed and to relate the conditions to the flow stresses measured from metalworking tests. The upper–bound solution has provided a fundamental method of predicting the extrusion pressure. Using this method and the actual deformation temperature, strain rate and flow stress of the material it is possible to predict the extrusion pressure without the use of purely empirical results.

2.1.5 Structural aspects

Hot extrusion is usually carried out at temperatures above $0.5T_m$ in the hot working range. Hence microstructural changes can be extensive considering both the

thermal and mechanical effects.

During hot working a metal is usually above its recrystallization temperature. Softening usually occurs and a recrystallized structure is often found in the cooled specimen. Dynamic recrystallization is thought to be the major softening mechanism. However, aluminium alloys have been observed where dynamic recovery was the sole restoration mechanism during deformation since a fully recovered subgrain structure was found [58,59,60,52]. Commercial purity α iron and ferritic alloys also develop subgrains when specimen are cooled rapidly after small and large amounts of deformation. Copper and its alloys, nickel and its alloys and austenitic steel, show recovered substructures within distorted original grains after low hot strains. When steady-state conditions were established, fully recrystallized structures were formed [60,61,62]. Dynamic recovery and recrystallization are related to the stacking–fault energy of a particular material [63]. Activation energies are also different in materials which show dynamic recovery or recrystallization. The activation energy for dynamic recrystallization is about 20% higher than that for dynamic recovery [3,59].

In the materials having high stacking-fault energy dynamic recovery is the sole softening mechanism [55,64,65,66,62,67,68,52,45,69,70,61]. Dynamic recovery may commence in the strain hardening regime [71]. The shear component of the applied stress changes the shape of deforming material, increases dislocation density, promotes cross–slip at low temperature and cross–slip and climb at higher temperature [73]. With high stacking–fault energy metals screw and edge dislocations cross-slip and climb easily to surmount barriers and meet each other. Those dislocations having opposite sign annihilate and the remaining dislocations rearrange themselves in a polygonization process forming subgrains. Hence dislocation density is lowered and a lower energy configuration is obtained. Subgrain boundaries are walls of dislocations. Misorientation between subgrains is low and subgrain boundaries cannot migrate like recrystallized grain boundaries. As strain and dislocation density increase, the rate of annihilation rises to match that of dislocation generation. This process finally leads to an equilibrium between dis-

location generation and annihilation so a steady–state condition is obtained after the strain hardening regime, where dislocation density, subgrain size, flow stress and temperature are constant. Dislocation networks and subgrain formations are a significant recovery mechanism in such materials. Dislocations are generated within subgrains and annihilated at the subgrain boundaries in a climb controlled process [60]. Aluminium 2014 alloy in particular is reported to be softened by dynamic recovery during extrusion [46,30].

For low stacking–fault energy material dislocations are more extended, cross–slip and climb are inherently more difficult, and dynamic recovery is impeded. At low strain, dynamic recovery processes may initially occur and form subgrains within the distorted original grains. However, when large strains are produced quickly they cause dense tangles of dislocations which increase misorientation. Eventually high–angle boundaries are formed of sufficient energy to nucleate recrystallized grains [59,46]. Recrystallization is initiated at a critical strain that is a little less than the strain to the peak flow stress. Hence the formation of a nucleus is the result of a congregation of dislocations into a high angle boundary which is capable of rapid migration [70,68]. The recrystallized subgrains are usually equiaxed and smaller with dislocation cell walls that are more densely tangled compared with equivalent recovered material [59,3,75]. In dynamic recovery, single dislocations annihilate individually [75] while for recrystallization, dislocations are annihilated in large numbers through the migration of high angle boundaries.

However, several researchers [76,65,59,77] claim that dynamic recrystallization does occur in some aluminium alloys. Magnesium containing alloys are reported where the operative mechanism at high temperature is dynamic recrystallization with very fine recrystallized grains [25,28]. It is explained that solute atoms may lower the stacking–fault energy [59,78] and pin dislocations, thereby hindering dislocation motion and raising the work hardening rate. This effect increases with increasing alloy concentration and produces an increased dislocation density at the same strain. This produces an increased driving force for recrystallization without significantly decreasing the boundary mobility and dynamic recrystallization

occurs at dislocation clusters. Another possibility leading to recrystallization is the dispersion of precipitates, which pin the dislocations and raise the dislocation density until a sufficient dislocation density is generated and the boundary thus formed migrates into a particle free region.

After hot deformation has ceased, if the product is not immediately quenched it will undergo static recovery and recrystallization. The driving force for static recovery and recrystallization is the stored plastic strain energy. In dynamically recovered materials the subgrain boundaries are dislocation boundaries and they store a certain amount of plastic strain energy. This energy leaves the product in a higher energy configuration and thermodynamically unstable. During cooling if the temperature is high enough for long enough times, the product will try to release the energy and return to a low energy configuration. Thus static recovery and recrystallization may occur. Static recovery refers to dislocation annihilation and rearrangement forming subgrains and hence reducing dislocation density and subgrain growth. 50% or more of the total stored energy can be released during recovery in f.c.c materials [74]. Further, with growing subgrains or subgrain coalescence recrystallization nuclei may form. So following the static recovery, if the temperature is still high enough, static recrystallization may occur if sufficient plastic strain energy remains. The coalescence of subgrains results in increasing misorientation between subgrains and leads to the formation of large angle boundaries. Recrystallization nuclei are formed at preferred sites; original grain boundaries, boundaries between deformation bands within a grain, large particles or by grain boundary bulging. Subsequently new grains can grow rapidly because of the high mobility of the high angle boundary. Static recovery and recrystallization can overlap and they compete with each other for the available stored energy. The newly formed strain–free grains can grow at the expense of the polygonized matrix by the migration of high–angle boundaries.

When the polygonized matrix is completely replaced by new strain–free grains, grain growth may occur. The driving force for grain growth is the reduction in grain boundary energy. When grains grow, large numbers of grains are replaced

and the total grain boundary area decreases. The energy of the material is therefore lowered. However, if the material contains a fine dispersion of second phase particles exerting a pinning force on grain boundary motion, inhibiting grain growth, the material may show abnormal grain growth. Some grains can overcome the inhibiting force by chance and grow out of proportion to the rest.

The most important features of hot worked substructures are the mean subgrain size, misorientation and dislocation density. Substructures relate to flow stress [33] and changes in substructure alter the properties of the material [79]. Misorientation does not play an important role in determining the flow stress and the role of dislocation density has not yet been completely established [80]. Hence, mean subgrain size is taken as an important factor in relation to the flow stress [81,60] and is found to be inversely proportional to the flow stress at certain temperatures:

$$\sigma = \sigma_0 + kd^{-N} \tag{2.24}$$

where

σ_0 ,k, N — constants.

σ_0 has a minor effect and k increases with alloy content. A value of 11 for k is obtained with $N = 1.25$ for aluminium alloy [71]. Some other values for N are 1.4, 1.5, 1.56, or 1 [60,78,63].

For recrystallized grains, σ_0 is negligible and N is in the range 0.5–1 [62].

Some other relations between σ and d are: [82,83,84]

$$\sigma = 3 + 9.2 \times 10^5 d^{-1} \tag{2.25}$$

$$d^{-1} = a + b\log[\sinh(\alpha\sigma)] \tag{2.26}$$

$$d^{-1} = p[\sinh(\alpha\sigma)]^q \tag{2.27}$$

where

a, b, p, q — constants.

d can also be related to the temperature compensated strain rate Z [71,60,69,63,166].

$$d^{-1} = a' + b' \log Z \tag{2.28}$$

$$d^{-1} = p'(Z)^{q'} \tag{2.29}$$

where

$$Z = \dot{\epsilon}\, exp(\frac{\Delta H}{RT})$$

The subgrain size increases significantly with increasing temperature and decreasing strain rate [73].

Better fit with experimental data is obtained using [85].

$$d^{-1} = -0.6 + 0.08 \ln Z \tag{2.30}$$

$$d^{-1} = -0.364 + 0.056 \ln Z \tag{2.31}$$

$$d^{-1} = 0.23 + 0.227 \ln[\sinh(\alpha\sigma)] \tag{2.32}$$

Raybould and Sheppard give [86]:

$$d^{-1} = -0.125 + 0.375 \log[\sinh(\alpha\sigma)] \tag{2.33}$$

for air cooled specimens, and

$$d^{-1} = -0.17 + 0.55 \log[\sinh(\alpha\sigma)] \tag{2.34}$$

for water quenched specimens.

2.1.6 Powder extrusion

Aluminium powder metallurgy is being paid more and more attention because it allows more flexibility in alloy design. For example it is used to achieve exceptionally high volume fractions of thermally stable, fine, uniformly dispersed phases distributed in the matrix [31,87,88,89,90,27,95,96]. These can provide dispersion hardening and elevated temperature microstructural stability. The rapid solidification that occurs when powders are atomized also provides alloy design flexibility.

It allows solute contents and amounts of phases to be varied. The properties of the final product therefore depend upon many powder characteristics. Powder is usually consolidated to produce engineering materials. Extrusion is used as a consolidation process and hot extrusion is capable of achieving 100% density [98,99]. In addition, powder extrusion can be used to produce wrought bar in alloys which are normally too brittle to be conventionally worked. [95,97].

Extrusion is a highly compressive process and the large shear deformations can disrupt metal powder particle surfaces and expose clean metal. Hence full densification and maximum particle bonding can be obtained [98,100,31]. This is particularly useful in disrupting the oxide film on aluminium alloy powder.The massive shear causes extensive grain refinement and a level of dispersion of second phase [37] which are a function of extrusion ratio. Up to a threshold value the higher the extrusion ratio, the higher the final density and the stronger the product unless the increased temperature interferes.

Hot powder extrusion can be performed in three methods [7]; extrusion of loose powder, extrusion with a can and extrusion of a compacted billet.

For compacted billets, loose powder is firstly cold compacted to a billet of 75 – 90 % of theoretical density [101,88,27,31] in order to facilitate handling then preheated in a furnace to reach required temperature for extrusion and extruded in the conventional way.

Chare [37] reports that a 99% product density is obtained when the extrusion ratio exceeds 6:1 and at 0.67 homologous temperature for aluminium alloys. Other reports by Chare and Sheppard [103,104,106,108,107] state that coherent 100% dense material can be produced by extrusion with a threshold extrusion ratio $R = 10 : 1$ and below it coherent material cannot be obtained [101]. However, it is dependent on extrusion temperature, the higher the temperature, the lower the critical extrusion ratio. It is found that the use of a 10 – 13 mm thick pad of solid metal (aluminium) placed in the container ahead of the billet can provide additional lubrication and prevent a 'fir–tree' type defect resulting from excessive die pick–up [106,37,100,101,102]. Usually lubricants are a graphite based mixture.

The following considerations need to be taken into account when powder extrusion is analysed.

(1) Densification of the porous body takes place during extrusion and the relative density is not uniform so there is a volume change during extrusion [109].

(2) Compressibility of the porous body may change the deformation zone characteristics.

(3) At every shear boundary the value of yield shear stress is different, dependent on the actual value of density.

(4) The change in material properties and deformation geometry will affect the extrusion load, temperature range and product.

With these considerations, an upper bound solution applied to powder extrusion will lead a very low accuracy on pressure [101]. Duszczyk et al [102] produced a mathematical model from upper bound theory for powder extrusion in an attempt to improve this situation.

As before the work done during powder extrusion can be expressed:

$$W = a + Y \ln R + \mu l \tag{2.35}$$

where

W takes into account redundant, homogeneous and frictional work.

For aluminium powder extrusion, a relationship between pressure P and logarithmic extrusion ratio R is obtained [107,108]:

$$P = 160 + 70.6 \ln R \tag{2.36}$$

$$P = 375 + 175 \ln R \tag{2.37}$$

2.1.7 Effect of powder on extrusion limits

In ingot extrusion at the initial stage of load–displacement curve there is normally a linear upset zone before peak load is reached. Powder extrusion shows a non–linear compaction zone which corresponds to the billet density increasing from 75 – 90% to 100%. At this stage the powder billet is "brittle" and has low resistance to shear [170,106,108]. The extrusion pressure required for powder extrusion is much lower than that for a conventional ingot extrusion [96,98,48,103,104,106,88,110,111,113,108].

The reduction in pressure requirement reduces the total work done on the billet so that the heat converted from this mechanical work is reduced hence the temperature rise during extrusion decreases and the extrusion limits are widened [31]. It is claimed [106] that the redundant work is 27% of the total energy for powder and 10% for ingot at an extrusion ratio of 40. In solid extrusion the minimization of redundant work is often attempted since it does not help to change the shape or improve the properties of the product. However in powder extrusion a higher proportion of redundant work is essential [114] because it breaks up the oxide layer to expose the metal and welds the powder particles together. It was reported that the activation energy is lower for powder material than that for ingot [88]. ($\Delta H = 30.83$ kcal/mole for powder and $\Delta H = 37.28 kcal/mole$ for ingot for Al–7090 and 7091 alloys)

2.1.8 Effect of powder on extruded microstructure

The gas atomised powders used in this work and elsewhere have a cast structure containing very fine dendritic or cellular structure. Precipitates and possible dispersoids are all in the submicron size range [106]. The way that dynamic recovery and recrystallization and static recovery and recrystallization affect the extruded structure will be reported later and has been considered by other workers [106,31,110]. The work on PM Al–2024 [4] is of particular relevance.

The oxide film around powder particles makes a big difference in aluminium

Material	Cu	Mg	Si	Mn	Fe	Al
Solid	3.92	0.62	0.64	0.56	0.38	bal.
Powder(fine)	4.96	0.84	0.78	0.91	<0.03	bal.
Powder(coarse)	5.05	0.83	0.83	1.01	0.06	bal.

Table 2.4 Compositions of Al–2014 alloy

powder extrusion from ingot extrusion. The tenacious film of aluminium oxide is fragmented during extrusion and these fragments remain in the extruded product, preventing recrystallization and grain growth [110]. In addition hydrogen and other gases (eg. nitrogen and air) trapped in the material during manufacture, packing, storage and extrusion [111] remain in the extruded products causing blisters or fissures [108,110,111]. These blisters or fissures are not usually evident in the extruded product until after heat treatment. It has been found that higher extrusion temperatures result in many small blisters and lower extrusion temperatures give fewer large blisters [110]. This is in agreement with the findings in this work.

2.2 Al – Cu – Mg – Si – Mn alloys

2.2.1 Alloying elements

Al–Cu–Mg was practically the first heat–treatable aluminium alloy to be discovered [112] and has been widely used since. Al–2014 alloy is a high strength development with additional silicon and manganese which increase the response to artificial age hardening [115]. It has relatively good formability, high hardness [116] and has been used for aircraft construction since the First World War [117] when its high strength to weight ratios was first required. It is also used in bridges, truck frames, rivets and structural fittings.

The composition of Al–2014 alloys used are shown in Table 2.4. More detail follows in Chapter 3.

The presence of alloying elements significantly increases yield strength of the alloy and steady state flow stress at elevated temperature but decreases ductility

[71,118].

Copper plays an important role in strengthening Al–2014 alloy because of its appreciable solubility. The strengthening increases with increasing copper content up to a maximum of approximately 6%.

Magnesium can remain in solid solution and produce an increase in strength, excellent corrosion resistance and weldability [119]. Magnesium lowers the stacking–fault energy so that it decreases the degree of recovery and favors recrystallization [71]. Magnesium can also combine with copper to accelerate and increase the precipitation hardening reaction at room temperature. The degree of precipitation hardening depends on the ratio of copper to magnesium. At high ratios, it is achieved by the sequence of G.P. zones through a coherent phase (θ') to $CuAl_2(\theta)$. At low ratios, it is achieved in the sequence of G.P. zones through a coherent phase to $CuMgAl_2$ [119].

Manganese forms a fine dispersion of intermetallic compound particles less than 1 μm in diameter during homogenization and gives a modest increase in strength and toughness [120] but decreases ductility [119]. These fine stable dispersion particles do not dissolve during hot working or annealing [119] and can be used to pin grain or subgrain boundaries and improve strength, toughness and resistance to stress corrosion cracking. When these dispersoids lie on grain boundaries, they may impede boundary migration and hence inhibit recrystallization and grain growth [121,122,123]. In solution manganese solute also increases recrystallization temperature [123,8] and slows down recovery.

The addition of silicon into this alloy can improve artificial ageing by forming precipitate particles [24,124,115] which have some strengthening effect and therefore improves mechanical properties [121]. It firstly forms Mg_2Si. at 595°C then combines with copper and magnesium to form other compounds such as: $Cu_2Mg_8Si_6Al_5$ and $(FeMn)_3SiAl_{12}$.

The precipitates formed depend not only on the amount of solute present but also on their ratios, for instance: [124,125,126].

Cu:Mg>2 and Mg:Si>1.7 $CuMgAl_2$ is formed.

Cu:Mg>2	and Mg:Si≃1.7	Mg_2Si and $CuAl_2$ are in equilibrium
Cu:Mg>2	and Mg:Si≤1	$Cu_2Mg_8Si_6Al_5$ is formed usually together with $CuAl_2$

Isothermal sections such as that shown in Fig. 2.5 are used to display this type of data.

Iron has a beneficial strengthening effect, especially at high temperature to form $(CuFe)Al_6 + Cu_2FeAl_7$ which appear as long needles. However these can produce an embrittling effect. Iron has another major role in Al–Cu–Mg–Si alloys in forming coarse constituent particles with Mn, Cu and Si. These form directly from the melt and once formed it is difficult to get the elements involved back into solution.

Aluminium forms eutectics with high proportions of copper, silicon and magnesium. Hence in rapidly cooled cast material unexpected eutectic phases can be produced by non-equilibrium cooling effects. This may include primary silicon under certain circumstances.

The main phases expected in Al–2014 are [116]:

CuAl_2, $Cu_2Mg_8Si_6Al_5$, $(FeMn)_3SiAl_{12}$ with the additional possibility of primary silicon in cast ingot and powder alloys.

2.2.2 Phase reactions and properties

Changes in properties may be induced by heat treatment which produces phase reactions to produce metastable equilibrium [127]. The strengthening produced is derived through finite precipitates [128].

When the material is heated just above the solvus but below the eutectic temperature and held at this temperature for a certain time, second phases dissolve into the solid solution that is the aluminium rich matrix. If the time is sufficiently long, a maximum amount of the hardening solutes such as Cu, Mg, Si dissolve into matrix. Then if the material is subjected to quenching with cold water, a

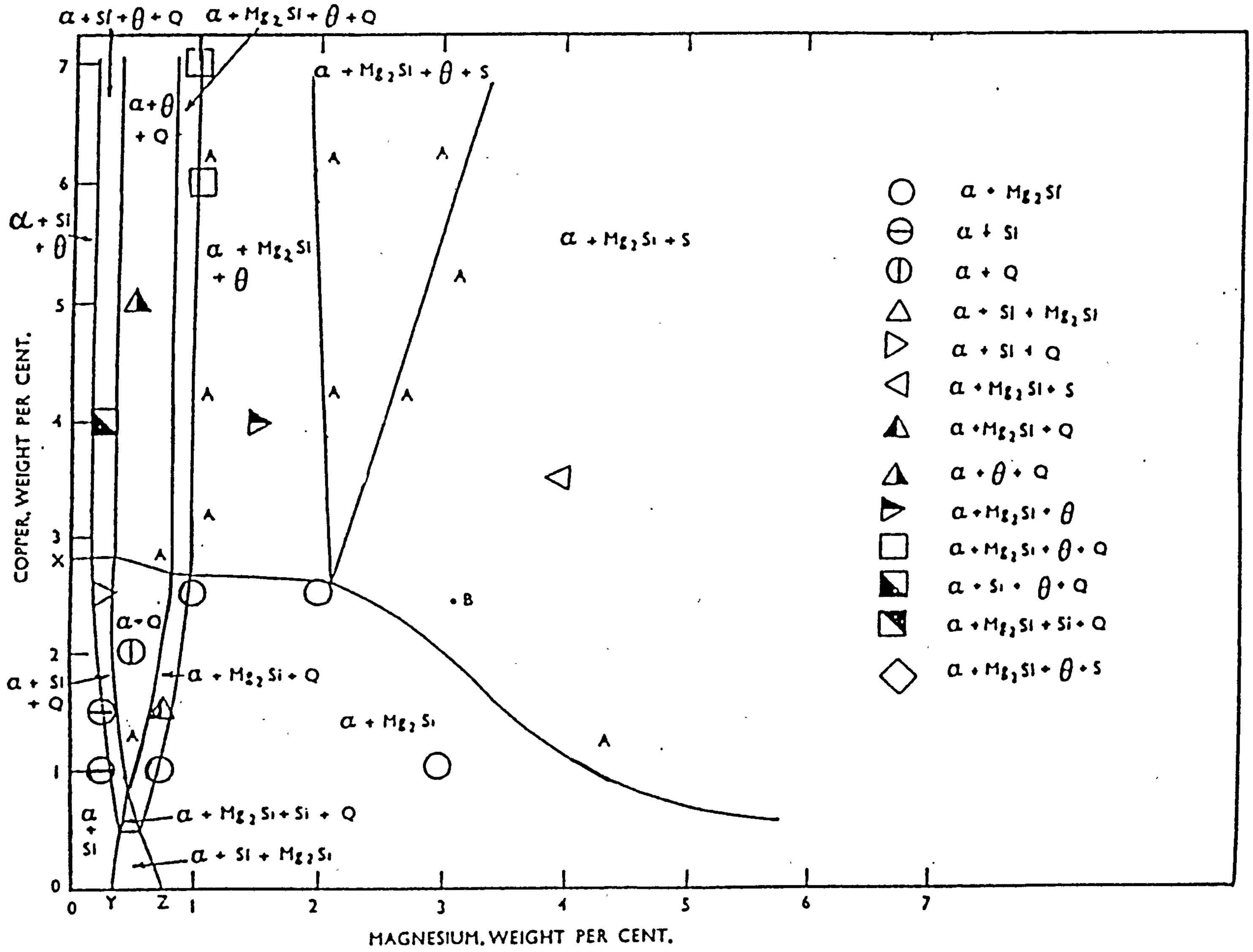

Fig. 2.5 The 460° C. Isothermal for Aluminium-Rich Alloys Containing Magnesium, Copper, and Silicon. [126]

supersaturated solid solution is obtained. Quenching also increases the vacancy concentration above the equilibrium level which assists in promoting the low temperature diffusion required for zone formation [119]. During quenching dislocations and precipitates can develop. Dislocations are generated at constituent or dispersoid particles appearing as helices, loops or tangles as a result of quenching strains and the condensation of excess vacancies.

If the cooling is not rapid, precipitate particles nucleate at heterogeneous sites such as grain boundaries because of their misorientation, dislocation tangles or dispersoid particles.

The supersaturated solid solution obtained from rapid quenching is unstable and decomposes to form equilibrium phases. This decomposition starts at a temperature of about 0.3 – 0.4 Tm (Tm is the melting temperature of the matrix phase) [127] by forming Guinier–Preston zones rich in solute elements [47]. The shape of the G.P. zone precipitate is dependent on the atom diameter of the solute and solvent. If both of the diameters are almost the same, the zone is spherically shaped. In Al – Cu alloys ageing normally starts with the segregation of Cu atoms into very fine clusters. As the copper atoms are smaller than aluminium atoms [127], platelet G.P.1 zones form in matrix oriented parallel to { 100 } planes. They are 4–6 $\mathring{A}$ thick (one atom of Cu) and 30 – 50 $\mathring{A}$ in diameter [119] consisting of single planes of Cu atoms. They still remain part of the parent lattice [129]. Because of the difference in atomic size, coherency strains develop [130,127,131] both within the zones and extending for several atom layers into the matrix. When dislocations move and cut the G.P.1 zones, higher stresses are required to move the dislocations through the region distorted by the coherency stresses so that the flow stress of the alloy will increase. The number or density of G.P.1 zones increases with time and the strength of the alloy correspondingly increases. In the subsequent stage, the zones are either converted into θ'' (G.P.2 zones) by Cu atoms diffusing to the G.P.1 zones, or replaced by the formation of transition θ'' which is 8 $\mathring{A}$ thick and 150 $\mathring{A}$ in diameter but still coherent [131,125] lying parallel to the {100} planes by means of the adaptation of the matrix through

local elastic strain [119] . The lattice strain and precipitate particles still impede dislocation motion. When dislocations meet these particles the dislocation have to cut through them and hence more energy is required.

Further precipitate reaction produces growth of the θ'' particles resulting in the partially coherent phase θ' . These particles are about 200 $\mathring{A}$ thick [125], platelike and lie parallel to the {100}, in an ordered pattern. This produces the maximum hardness.

Overageing means that coherency disappears with a change in the structure of precipitate from transition phase to form equilibrium θ $(CuAl_2)$ which nucleates on the θ' . It is reported [132] that although θ nucleates on θ' , few θ' particles act as nuclei. Most of the θ phase is formed by diffusional growth. The θ phase appears as thicker plates which are randomly distributed. As the coherency strain is lost, when dislocations meet the precipitates, less stress is required to loop around the precipitates rather than to cut them. The strengthening effect decreases with growth of equilibrium phase particles and an increase in interparticle spacing [119]

The structural sequence is:

SSS $\longrightarrow$ G.P.1 $\longrightarrow$ G.P.2 (θ'') $\longrightarrow$ θ' $\longrightarrow$ θ [119]

θ'', θ', θ all have a tetragonal structure [125].

In Aluminium 2014 alloy it is observed that θ' phase is the main strengthening phase [133,119]. $Cu_2Mg_8Si_6Al_5$ (Q) phase also produces some hardening with natural ageing [124]. For artificial ageing in Al-2014 alloy, it is recommended that to obtain T6 temper(solution treated, quenched and artificially aged) [135] it should be heated at 170–190°C for 8–12 hours [134,119].

Artificial ageing is used to control and accelerate the decomposition process in order to form finely dispersed precipitates. For Al–2014 alloy this means reheating the solution treated and water quenched material at temperature of 170—190°C for a long enough time to develop high strength properties. Sufficient time is needed to produce and grow GP zones to obtain the maximum strength and hardness.

Since the properties of a product depends on the microstructure the ther-

momechanical history plays an important rule of influencing the microstructure especially in products that are to be used as extruded. Even for those that are heat treated after extrusion it is necessary to be able to control the starting microstructure in order to be able to optimise the heat treatment.

In extrusion the extrusion load, extrusion temperature and microstructure are all interrelated. Hence it is necessary to produce an ATLAS of microstructure from controlled tests, eg. hot torsion and compression tests. These give independent checks of microstructures produced from extrusion and other thermomechanical processes.

Chapter 3

EXPERIMENTAL TECHNIQUE AND MATERIALS

3.1 Extrusion

3.1.1 Materials and billet preparation

Aluminium 2014 alloy has been investigated both in ingot and powdered form. The ingot was supplied in rod of 76 mm in diameter in the condition of TB, BS1474.

The powder was supplied as gas atomized stock in two average sizes of 11 μm for fine powder and 45 μm for coarse powder.

Ingot billets were sawn from the raw material to 75 mm length, heated in furnaces for 2 – 3 hours to the required temperature (250 – 550°C) and stabilized. They were then quickly transferred to the press. Powder billets were prepared by cold compacting the loose powder to a billet 76 mm in diameter and 79 mm in length at 80 % density. They were preheated in several furnaces to the required temperature, quickly transferred to the press and extruded in the conventional way. No solid pad was used in front of the billet.

The microstructures of the materials before extrusion are considered in Section 8.1.1 and 8.2.1.

3.1.2 Extrusion details

Extrusions were performed on a Fielding 500 Tons vertical downstroking hydraulic laboratory press (see Plate 1) specially designed for development of extrusion, forging and deep drawing. A Fielding 45.4 litre nitrogen/oil piston type accumulator used in conjunction with a 500 litre nitrogen bottle accompanies the press. The circuit is designed for hand control and can be accumulator powered or direct pumped so that a high or low ram speed can be obtained. Ram speeds were in the range 2 mm/sec. to 79 mm/sec. and the ram moves at a pre-set speed during extrusion.

The container having a nominal bore of 80 mm diameter is preheated with a container heating coil placed around the container, a heating lid and a bore heater. A thermocouple inserted into the container 20 mm away from the bore gives the container temperature for each extrusion.

A pressure transducer on the hydraulic circuit is linked with a pressure transducer amplifier to give pressure data. A linear vertical displacement transducer gives the ram displacement data.

The dies used were "shear" dies, of square, rectangular or round shaped and of different sizes to give extrusion ratios of 10, 20, 30, 50, and 53. All dies and rear pressure pads are heated in a furnace close to the press at 400°C then rapidly transferred to the press before extrusion.

A 10 mm disc of the billet is discarded in the container and removed after each extrusion.

3.2 Examination of extruded products

3.2.1 Surface examination

Examination of the surface finish is the first step in assessing the quality of the extruded product. Surface quality can range from:

— A good surface finish along whole length;

— Fine cracks along part or whole length (indicating the boundary of acceptable and unacceptable extrusion); or

— Cracks and hot shortness along the entire or part of the length.

3.2.2 Post extrusion heat treatment

Specimens were cut from the extruded product at fixed points 17.5%, 35% and 88% of the overall length from the front. Specimens were then solution treated at 505°C for half an hour quenched to room temperature, and allowed to age naturally. The responses were followed by hardness and microhardness tests carried out before solution treatment, after quenching and during ageing. The macrohardness test was performed on a Wolpert hardness test machine with 5 kg weight. Microhardness was measured on a Leitz Miniload tester with a weight of 50 grams.

3.2.3 Optical microscopy

Both longitudinal and transverse specimens were taken at the same positions as the previous samples. These sections were cold mounted in a resin then ground on 240, 400, 600 and 1200 grade silicon carbide papers and subsequently polished on 3 μm, 1μm and 1/4 μm diamond paste. Some of these specimens were polished finally on alumina.

Specimens were etched with modified Kellar's etchant for 15 – 20 seconds. Modified Kellar's etchant has a composition of:

2 ml HF, 3 ml HCl, 20 ml HNO_3, 175 ml H_2O.

After etching, specimens were washed in warm water then blow dried and examined on a Reichert MEF3 optical microscope.

3.2.4 Electron microscopy

Specimens for Scanning Electron Microscopy were mounted with conductive bakelite, ground and polished then etched as for optical microscopy, then examined on

a Jeol JSM 820K Scanning Electron Microscope.

Transverse and longitudinal sections were cut at 30% from the front of the extrusions for Transmission Electron Microscopy. These sections were turned to 3 mm in diameter then sliced on a diamond saw to the thickness of 0.4 – 0.5 mm discs. These discs were ground on 400, 600 and 1200 silicon carbide paper to 0.2 – 0.25 mm, then electropolished in a Struers Tenupol jet thinning apparatus.

For ingot extrusion, a solution of 30% nitric acid plus methanol was used with a voltage of 14 volts at temperature of –20°C to –10°C.

For powder products, a solution of 20% perchloric acid plus 80% methanol, was employed with a voltage of 21 volts at temperature of –30°C. The perforated discs were examined on a Jeol 2000FX Transmission Electron Microscope.

3.3 Hot torsion testing[1]

Hot torsion testing is a useful method of simulating metal working because it can be performed at a known temperature and deformation rate. The torque vs. twist diagram obtained during testing can be used to calculate the shear yield strength. Hot torsion tests are carried out at testing temperatures above 0.6 Tm and give flow stresses at constant true strain rates in the range of 10^{-3} to $10^{3} sec^{-1}$ up to a strain of 20 without plastic instability.

Specimens for solid material were machined directly from the raw ingot in order to keep the same condition as for extrusion. The dimension and shape of the specimens is shown in Fig. 3.1. For powder material, specimens were machined from partially extruded billet.

Tests were carried out on a torsion test machine at shear strain rates of 0.86/sec. to 13.8/sec. at temperatures in the range 250°C $\sim$ 550°C.

A Chromel–Alumel thermocouple was inserted in one end of the specimen and connected with a temperature control unit. Strain and strain rate data was measured with a lightsource and a wheel containing 20 holes evenly spaced around

[1]Courtesy of Sheffield University.

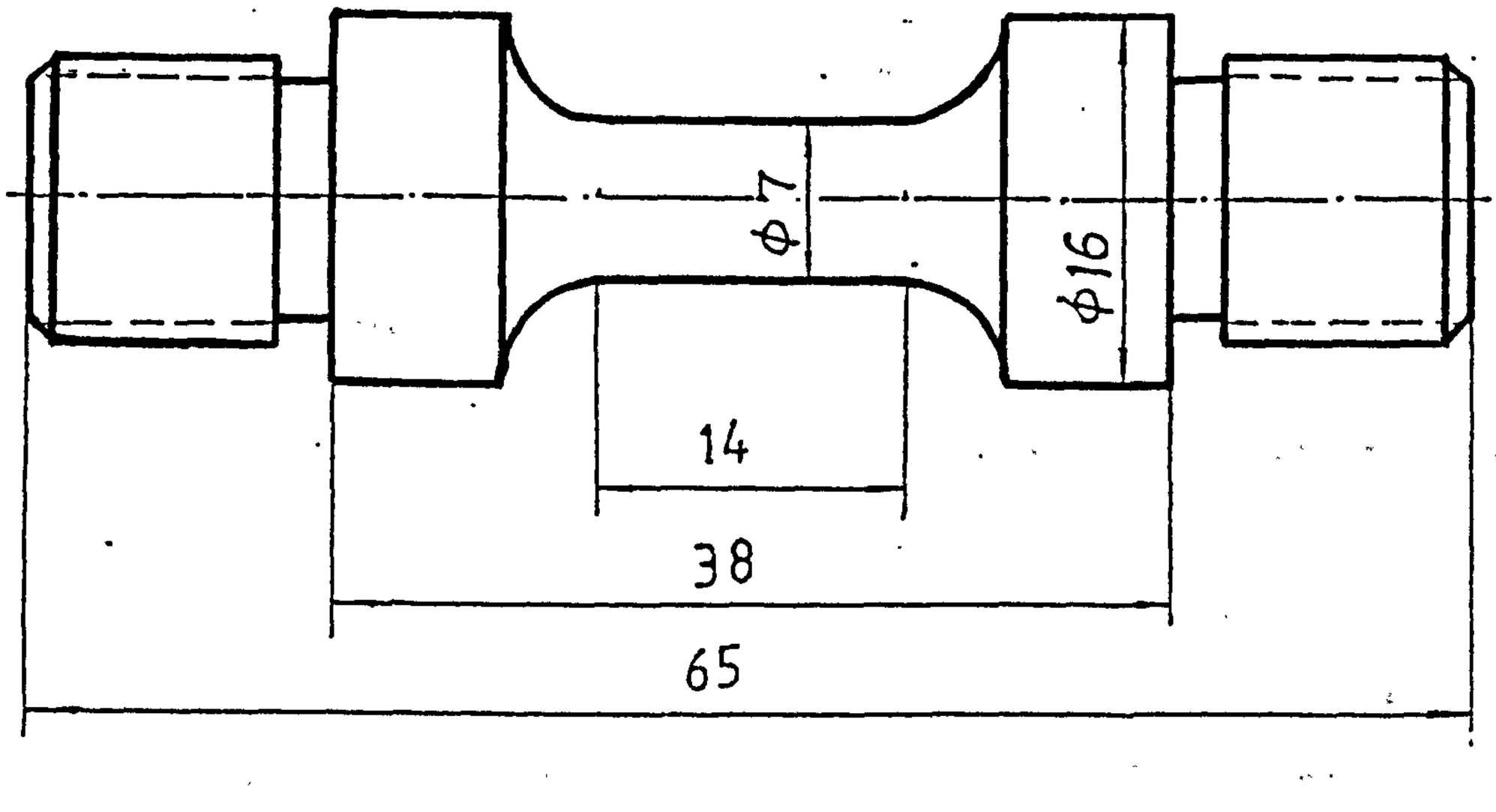

Fig. 3.1 Torsion specimen

its circumference. The torque was monitored by a load cell which was calibrated before each test. Torque and twist data were recorded on a high speed Ultraviolet recorder.

After testing specimens were rapidly quenched with cold water in about one second in order to retain the hot deformed microstructure.

Unfortunately none of the powder samples possessed sufficient ductility for torsion testing. For solid specimens the torsion results are presented in Figs. 3.2 – 3.11. Figs. 3.2 – 3.7 show torque-twist curves at constant temperature but different strain rate and Figs. 3.8 – 3.11 show torque-twist curves at constant strain rate but different temperature. Fig. 3.14 is the measurement of the strain to failure of solid material obtained in torsion tests.

3.4 Hot compression testing[2]

As powder specimens failed in torsion testing, plane strain compression testing was used in order to obtain flow stresses. Tests were carried out on a computer – controlled Servotest hydraulic press that gives a constant strain rate.

Specimens for powder material were cut from a partially extruded billet. Control specimens were also cut from the received solid ingot. The dimensions of the specimens are illustrated in Fig. 3.15.

All specimens were coated with a graphite lubricant over the area to be contacted with the plane strain platens. The test temperatures were in the range of 250°C $\sim$ 550°C. The specimens were heated in a furnace to the required temperature for half an hour then transferred to the test machine, and heated for another 5 minutes to equalize the temperature before testing. A Chromel – Alumel thermocouple inserted into the midplane of the specimen was used to measure the change in temperature during the test. Specimens were tested to a final true strain of 0.8, 1.6 and 2.4 with true strain rates of 0.8, 3.4 and 6.9/sec. respectively. Immediately after testing specimens were rapidly quenched inside the machine. Compression

[2]Courtesy of Sheffield University.

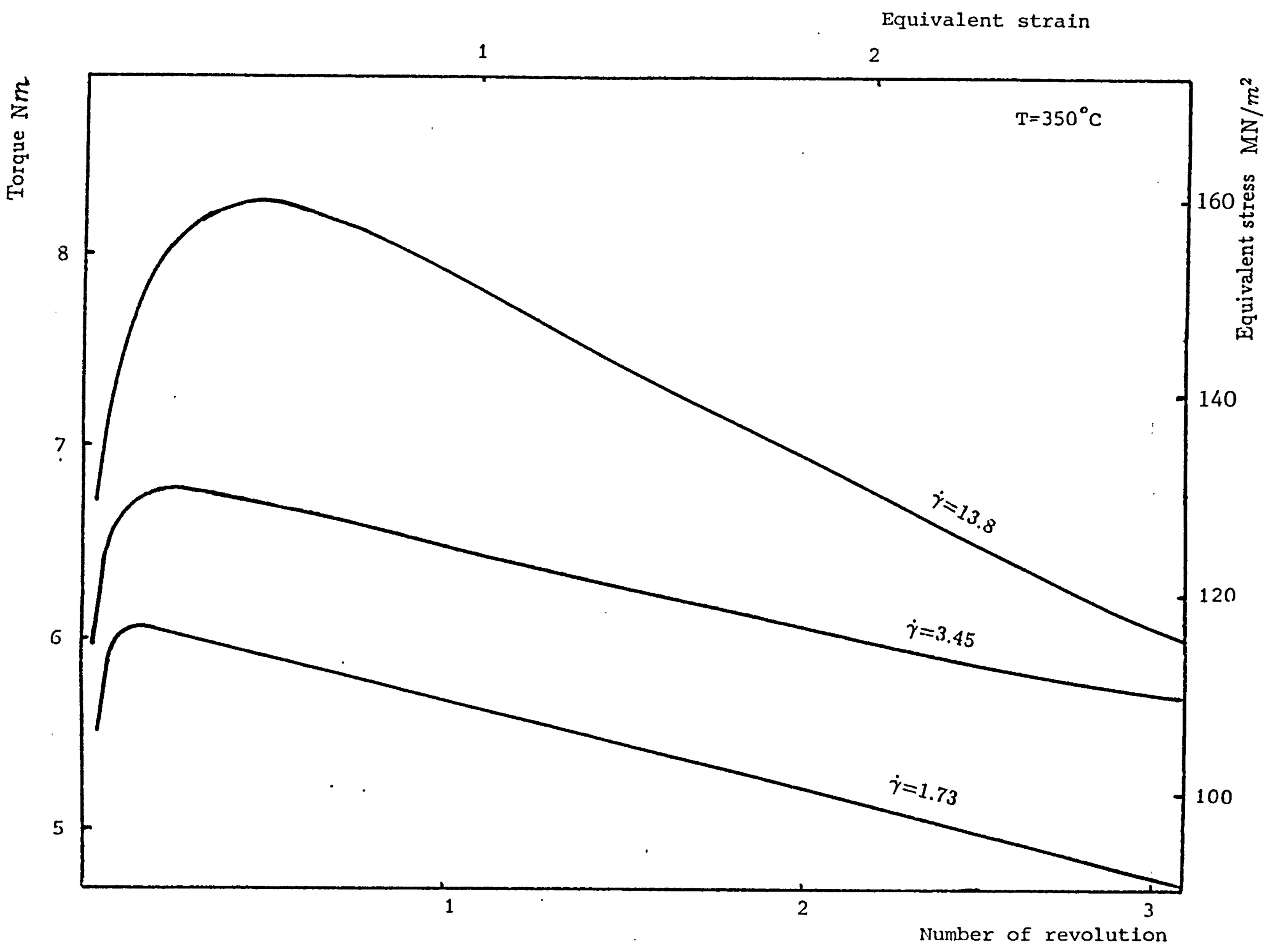

Fig. 3.2 Specimens twisted at 350°C with different strain rate

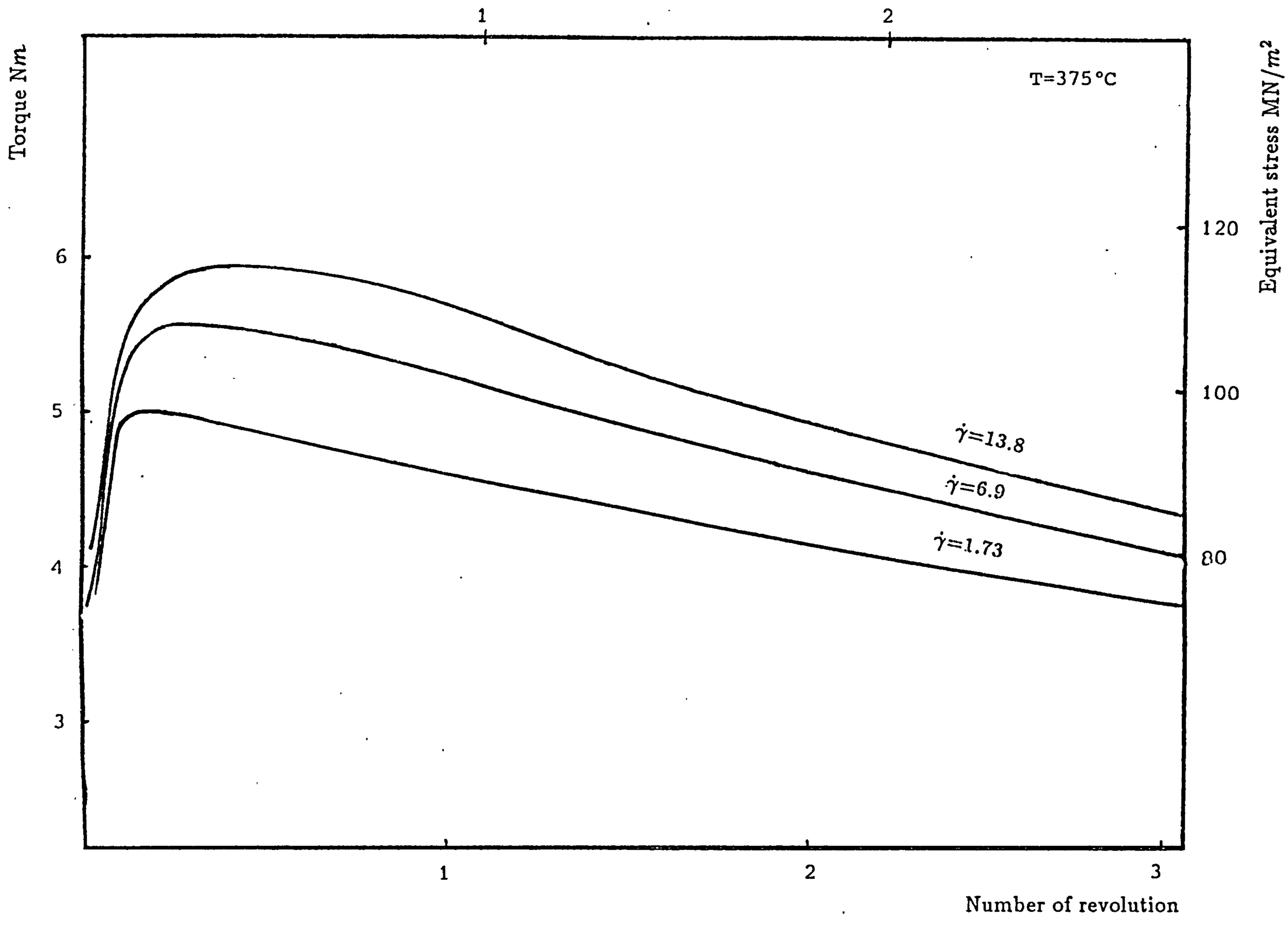

Fig. 3.3 Specimens twisted at 375°C with different strain rate

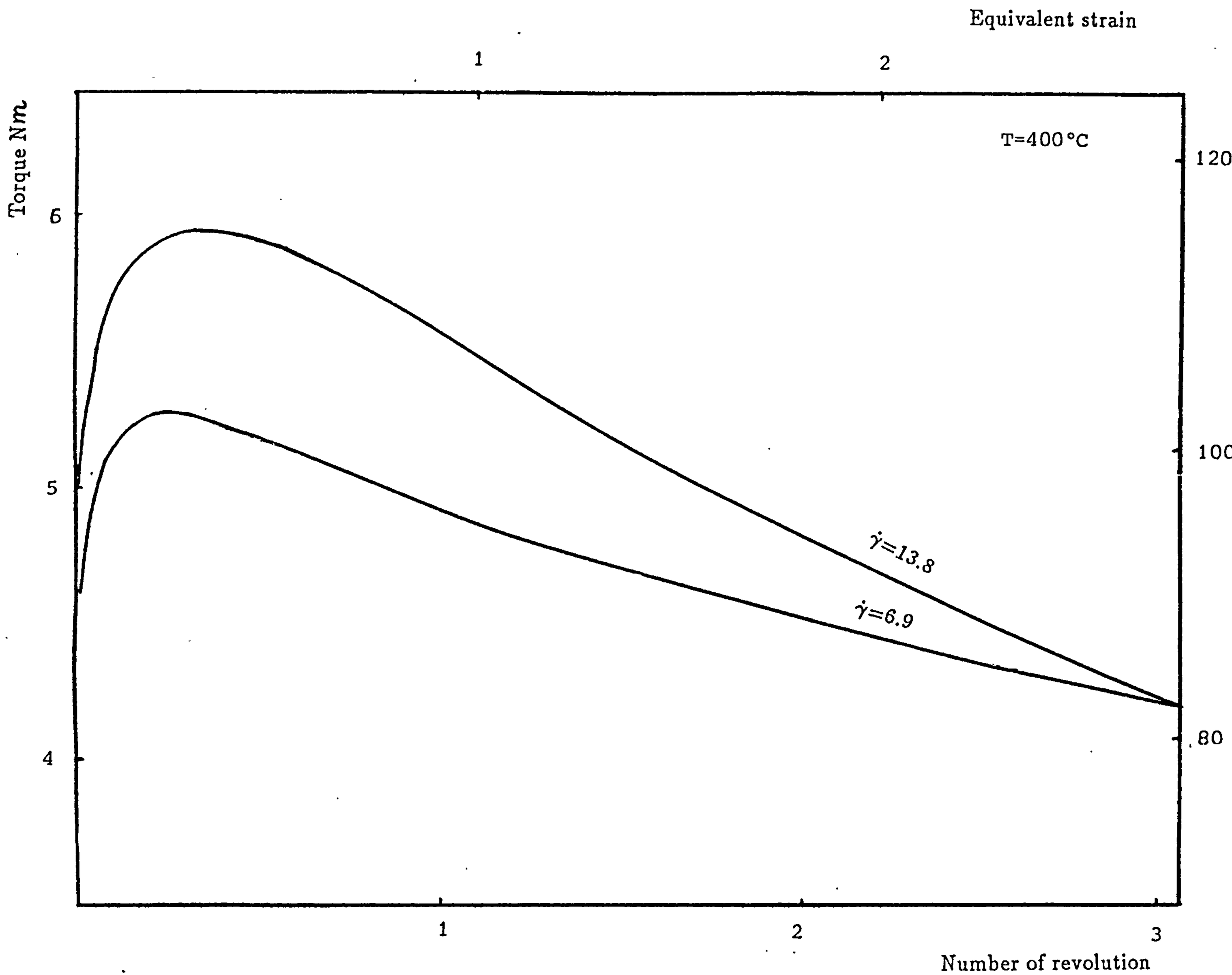

Fig. 3.4 Specimens twisted at 400°C with different strain rate

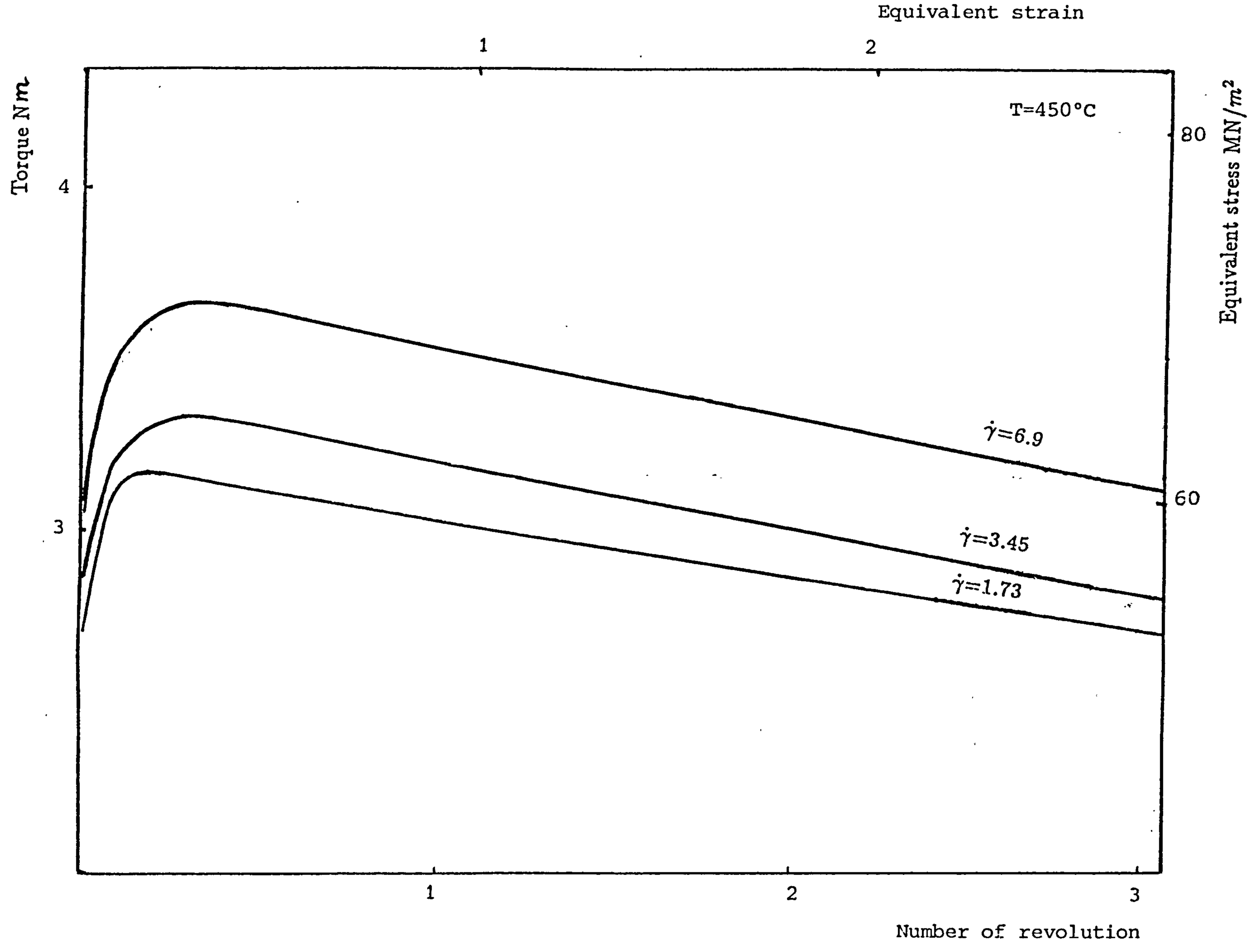

Fig. 3.5 Specimens twisted at 450°C with different strain rate

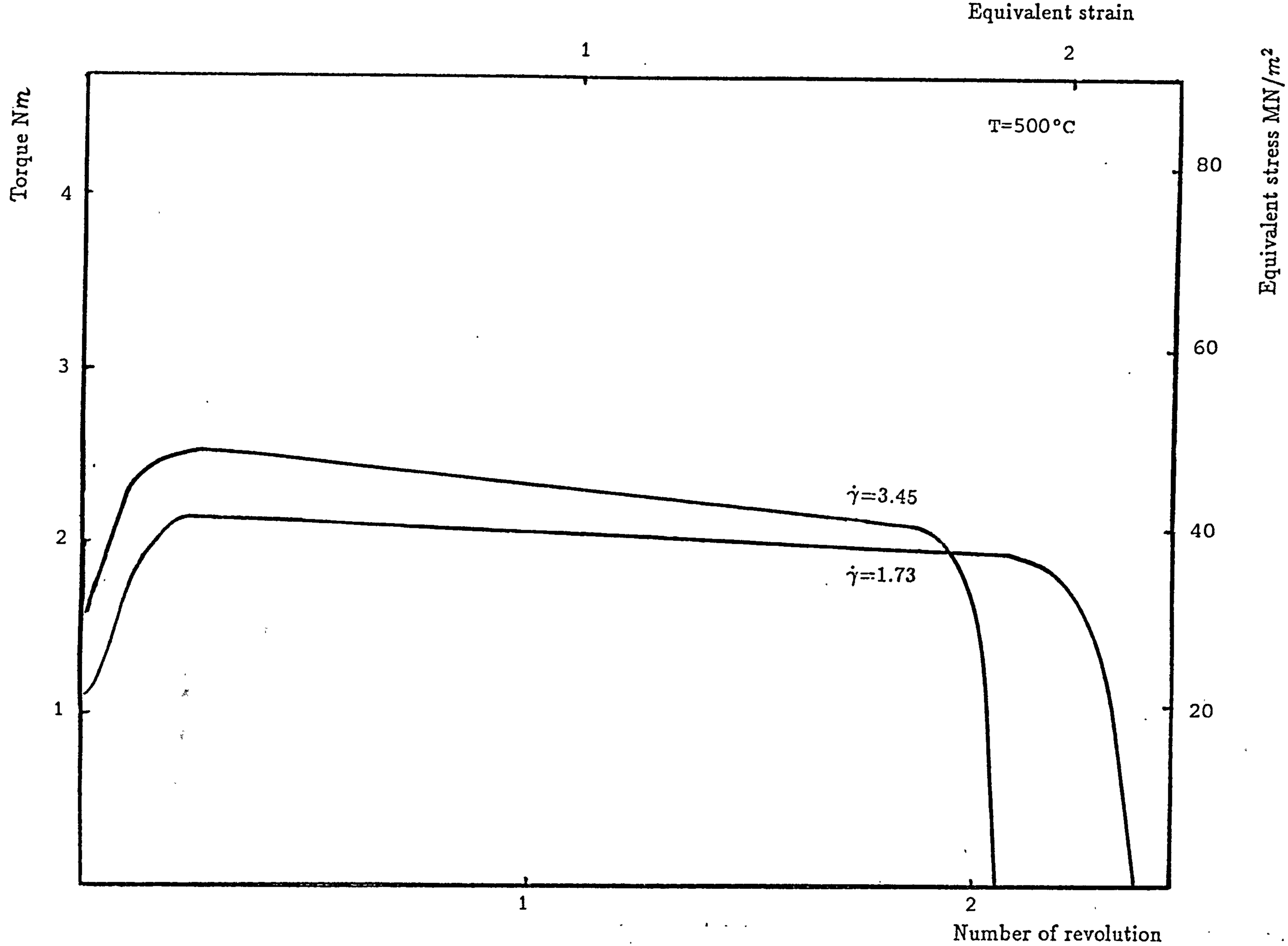

Fig. 3.6 Specimens twisted at 500°C with different strain rate

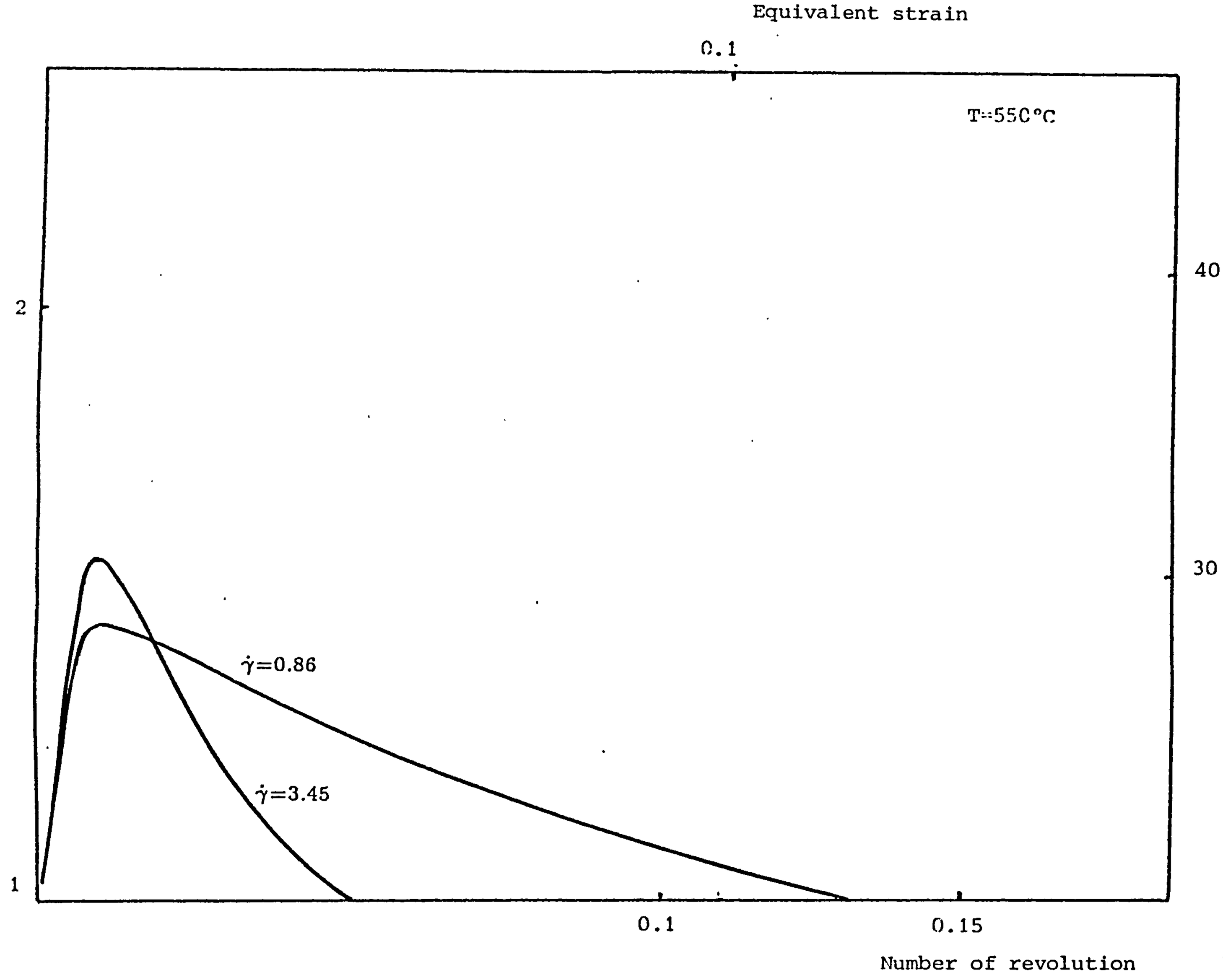

Fig. 3.7 Specimens twisted at 550°C with different strain rate

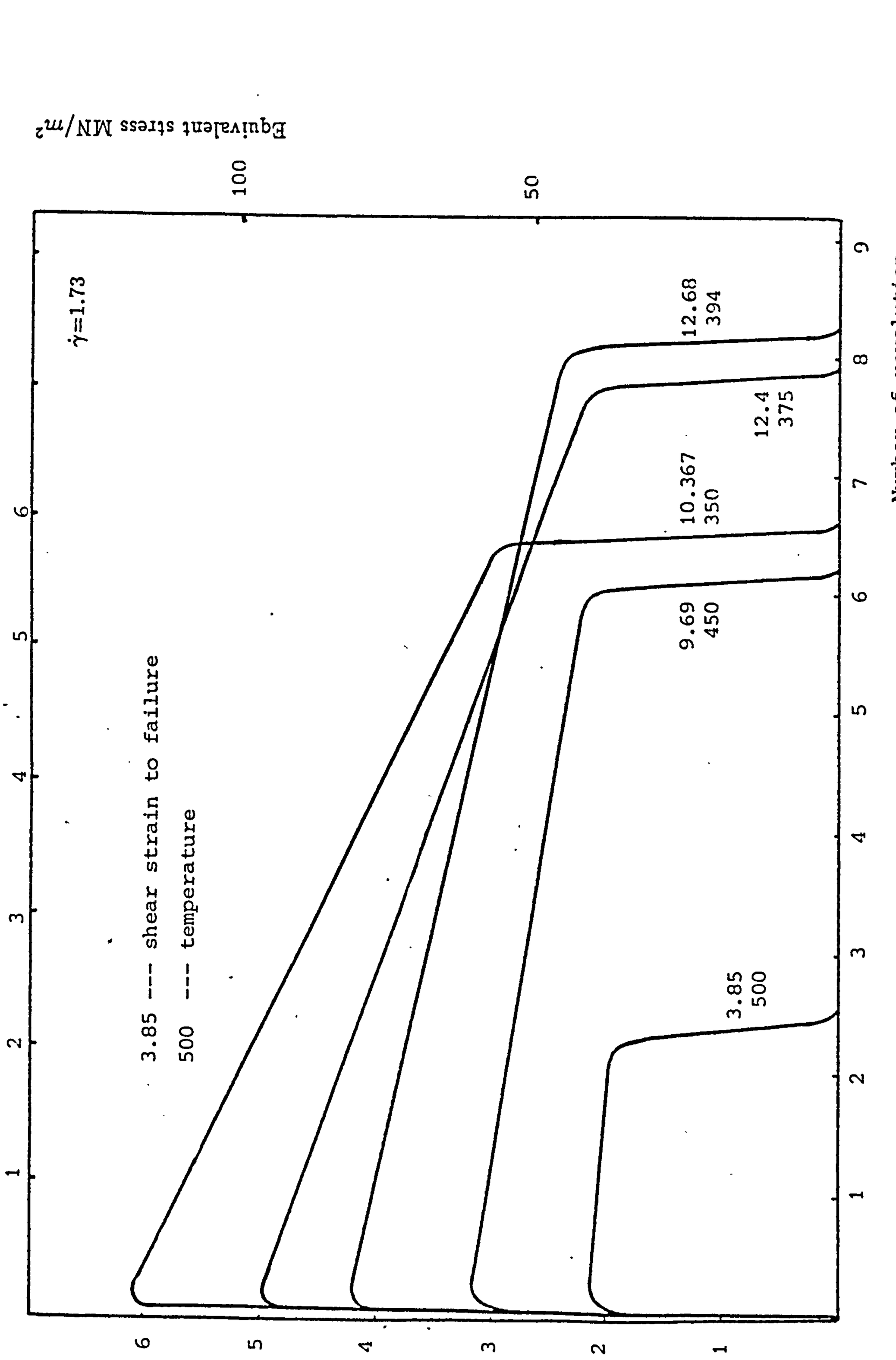

Fig. 3.8 Specimens twisted at strain rate 1.73 with different temperature

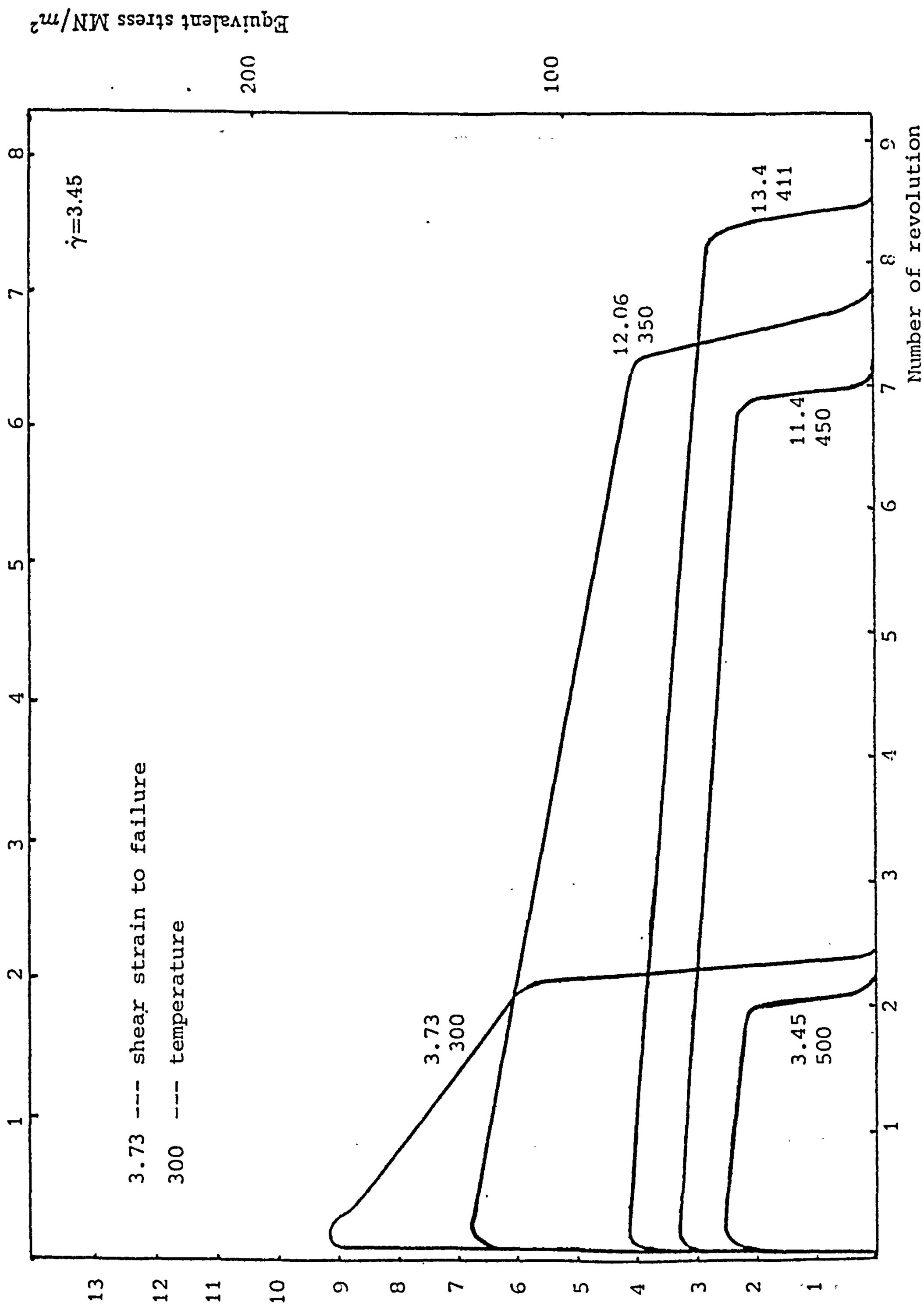

Fig. 3.9 Specimens twisted at strain rate 3.45 with different temperature

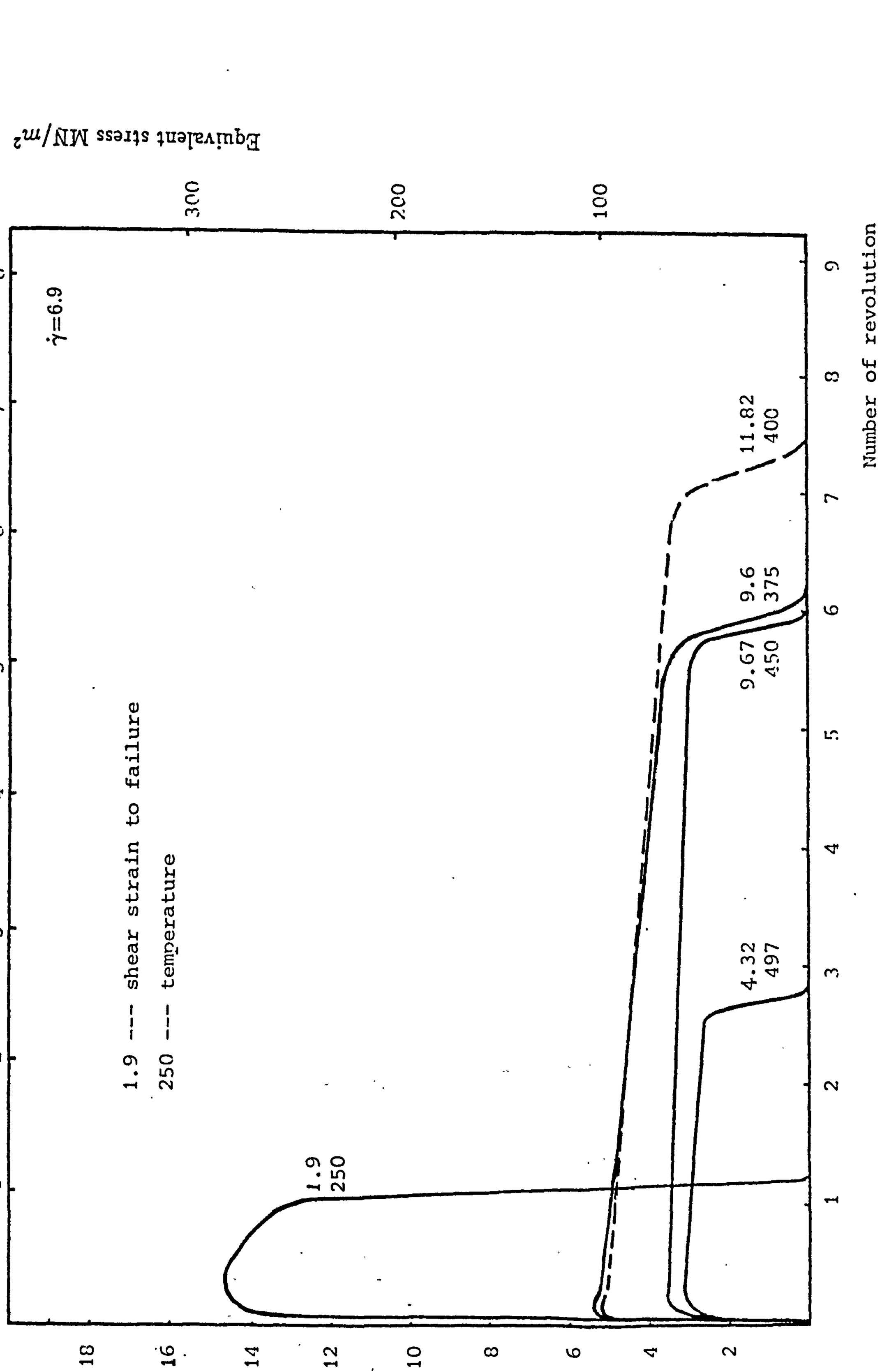

Fig. 3.10 Specimens twisted at strain rate 6.9 with different temperature

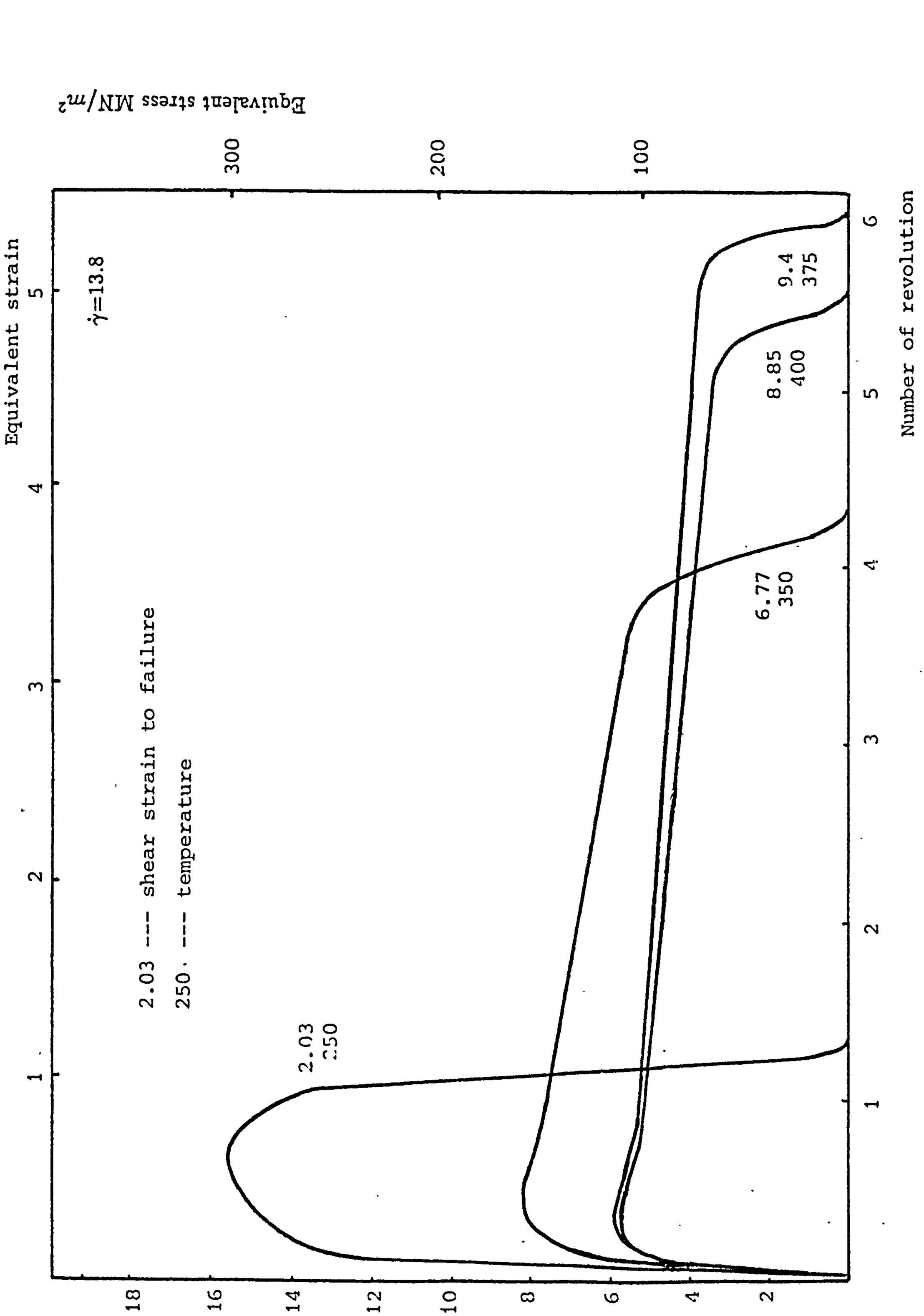

Fig. 3.11 Specimens twisted at strain rate 13.8 with different temperature

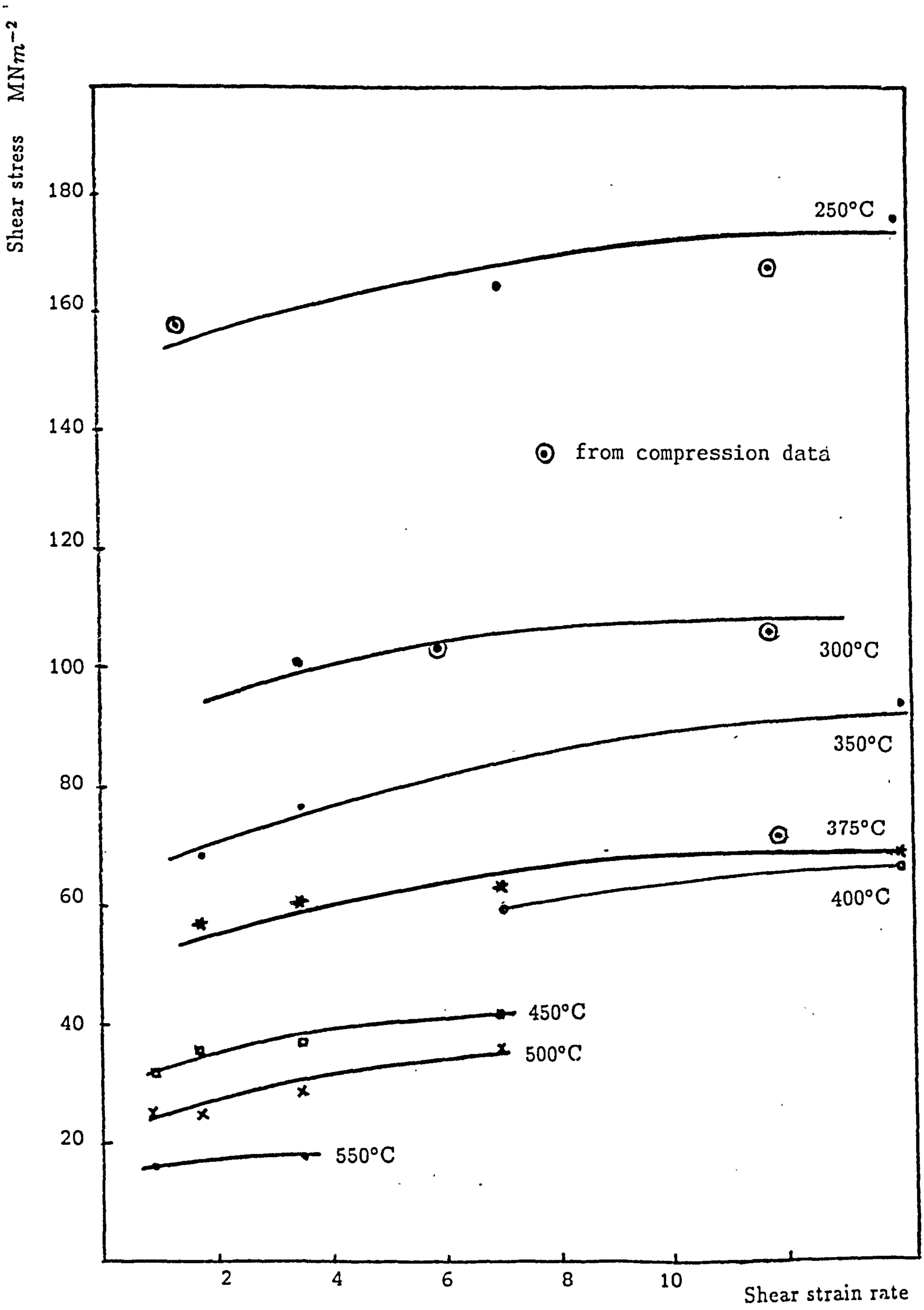

Fig. 3.12 Hot torsion and plane strain compression result for solid 2014 alloy

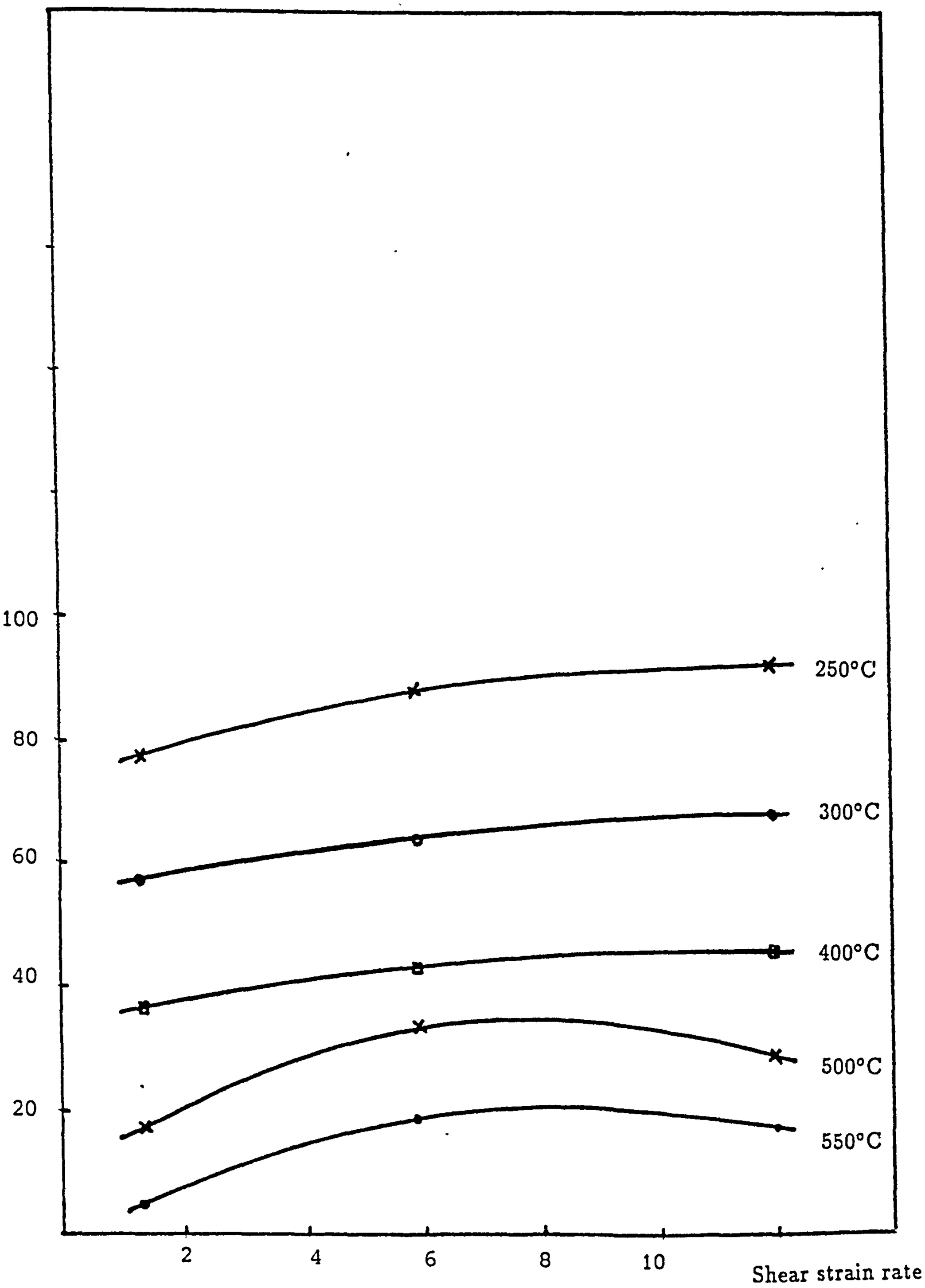

Fig. 3.13 Hot plane strain compression for powder 2014 alloy

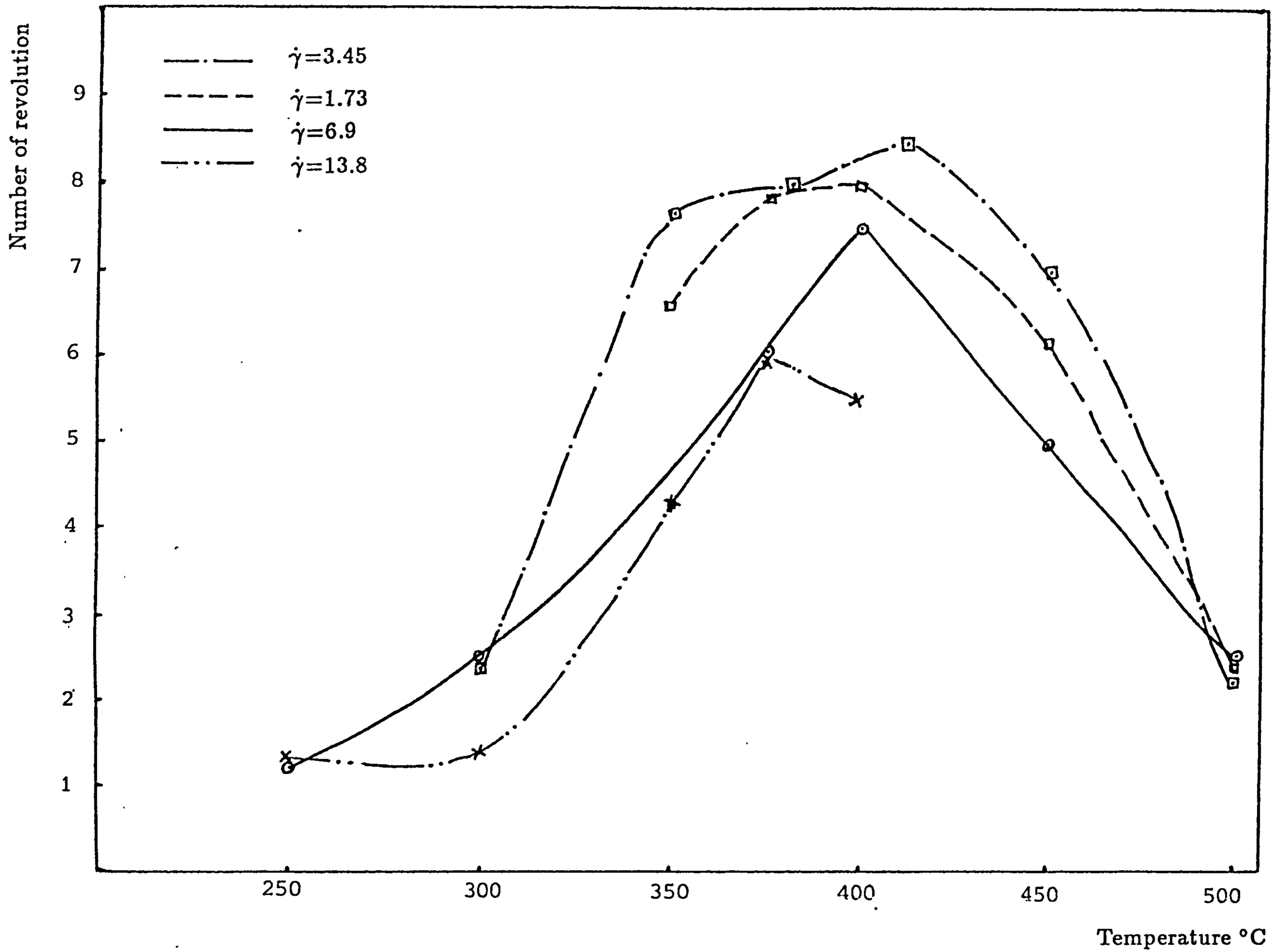

Fig. 3.14 Ductility of material in torsion test

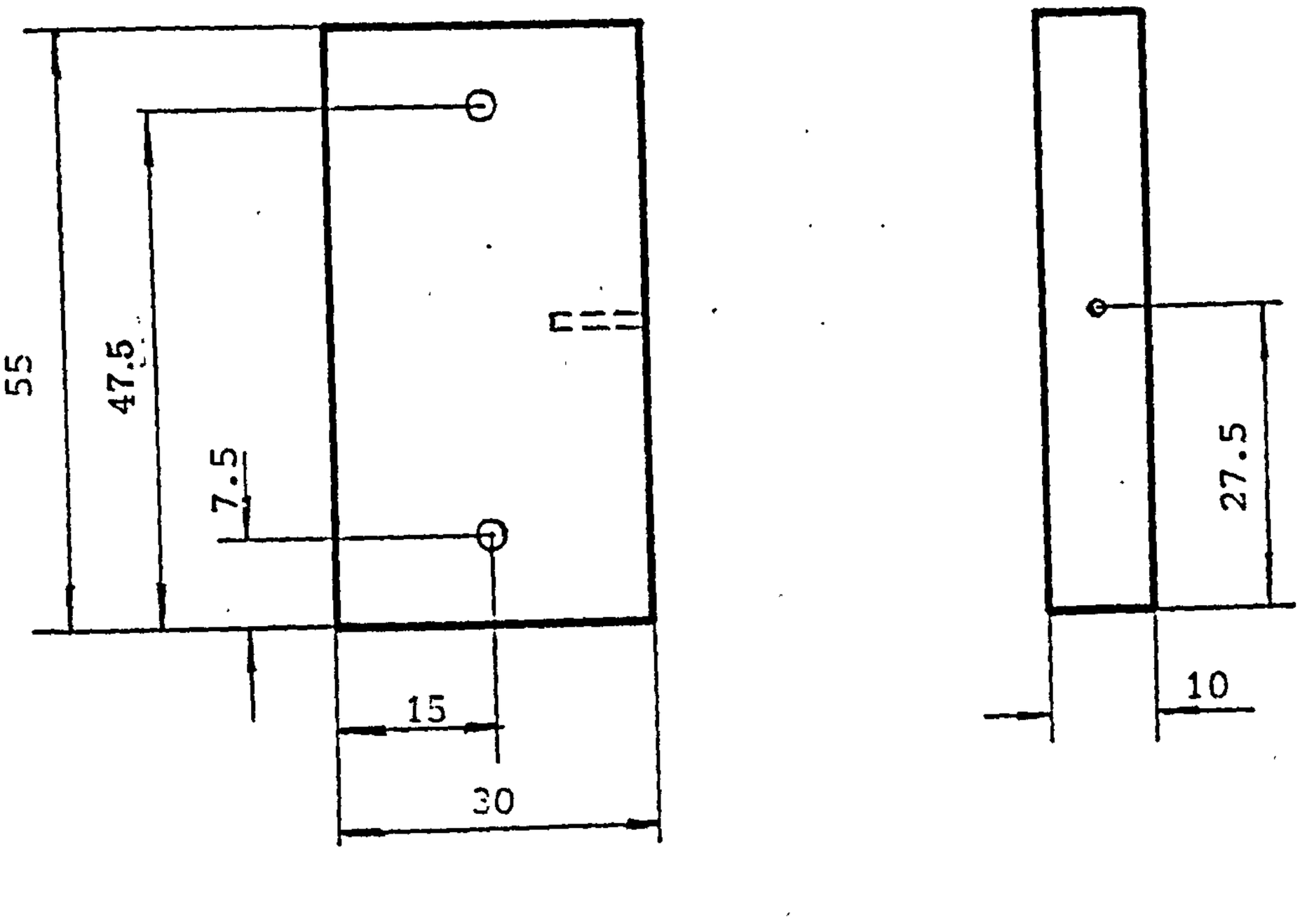

Fig. 3.15 Compression specimen

stress, strain and strain rate were recorded automatically and stress versus strain curves were obtained. The effects of friction and lateral spreading were corrected automatically by the software. Fig. 3.12 has been plotted to show the agreement between compression and torsion testing for the solid control samples. Fig. 3.13 shows shear stress versus strain rate at different temperatures. Figs. 3.16 – 3.20 are the compression stress versus strain with different strain rates at the various test temperatures. Figs. 3.21 – 3.23 are the compression stress versus strain with different temperatures at different strain rates.

3.5 Macro-analysis

The application of the visioplasticity technique to extrusion enables the flow pattern of the material during extrusion to be obtained [160]. The flow pattern formed by flow lines represents the direction and extent of material movement during deformation. In the present work, preheated billets were partially extruded. The process was carried out in the usual way but stopped as soon as the extrusion pressure reached its maximum. The billet was then removed from the press, cut into two halves along the axis, ground and etched with Kellar's etchant. A flow pattern and the shape of deformation zone were obtained. This technique was employed both for ingot and powder partial extrusion.

Observations have shown that the plastic region is limited in a well defined deformation zone bounded by a frustum of a right circular cone with severe shear on the boundary [137,139,39]. The deformation zone for the solid material is presented in Plate 2. However for powdered material it was difficult to see the deformation zone so it was worked out by metallographic examination. The flow pattern is different from the solid one and also shown in Plate 2.

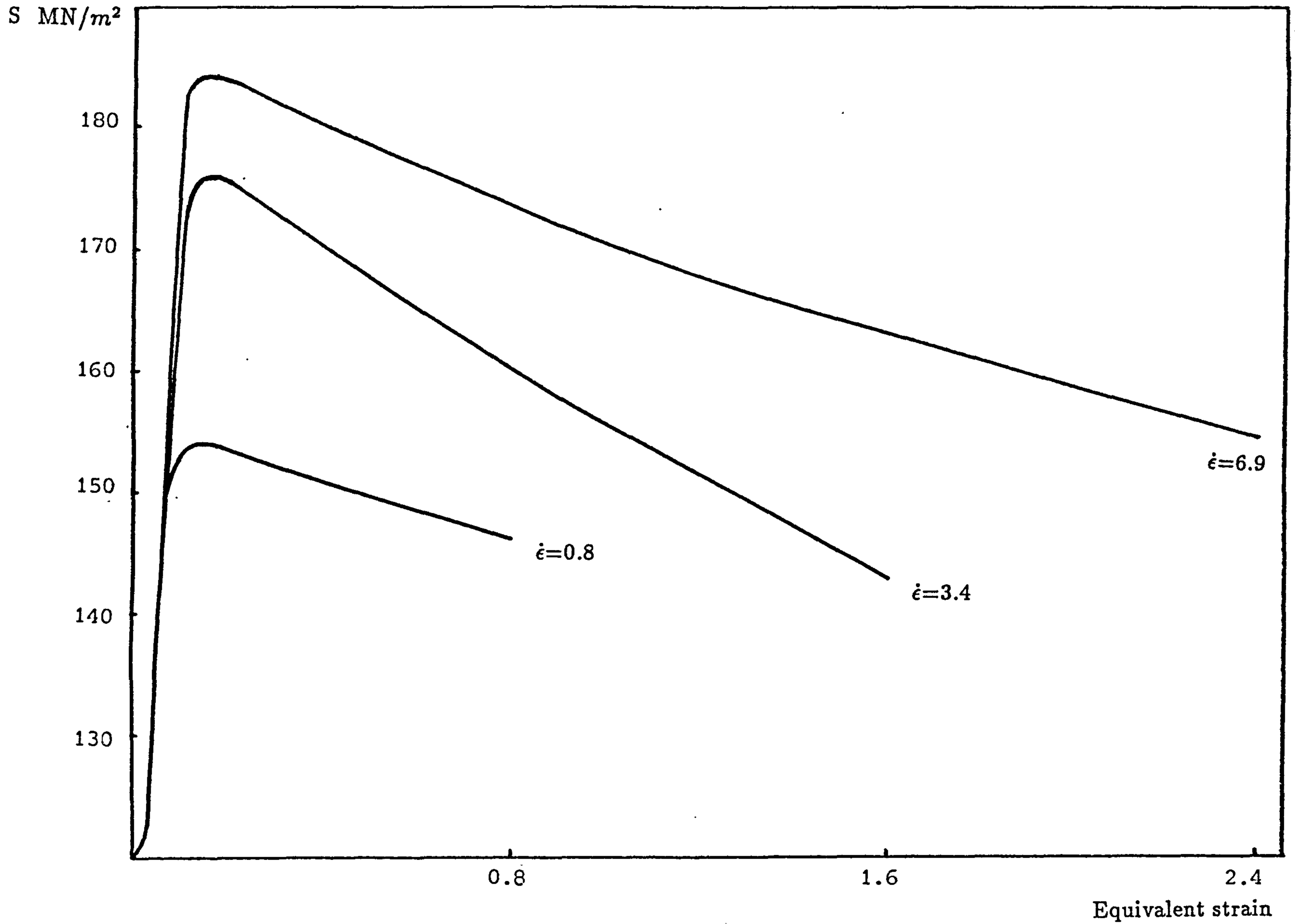

Fig. 3.16 Compression tested at 250°C with different strain rate

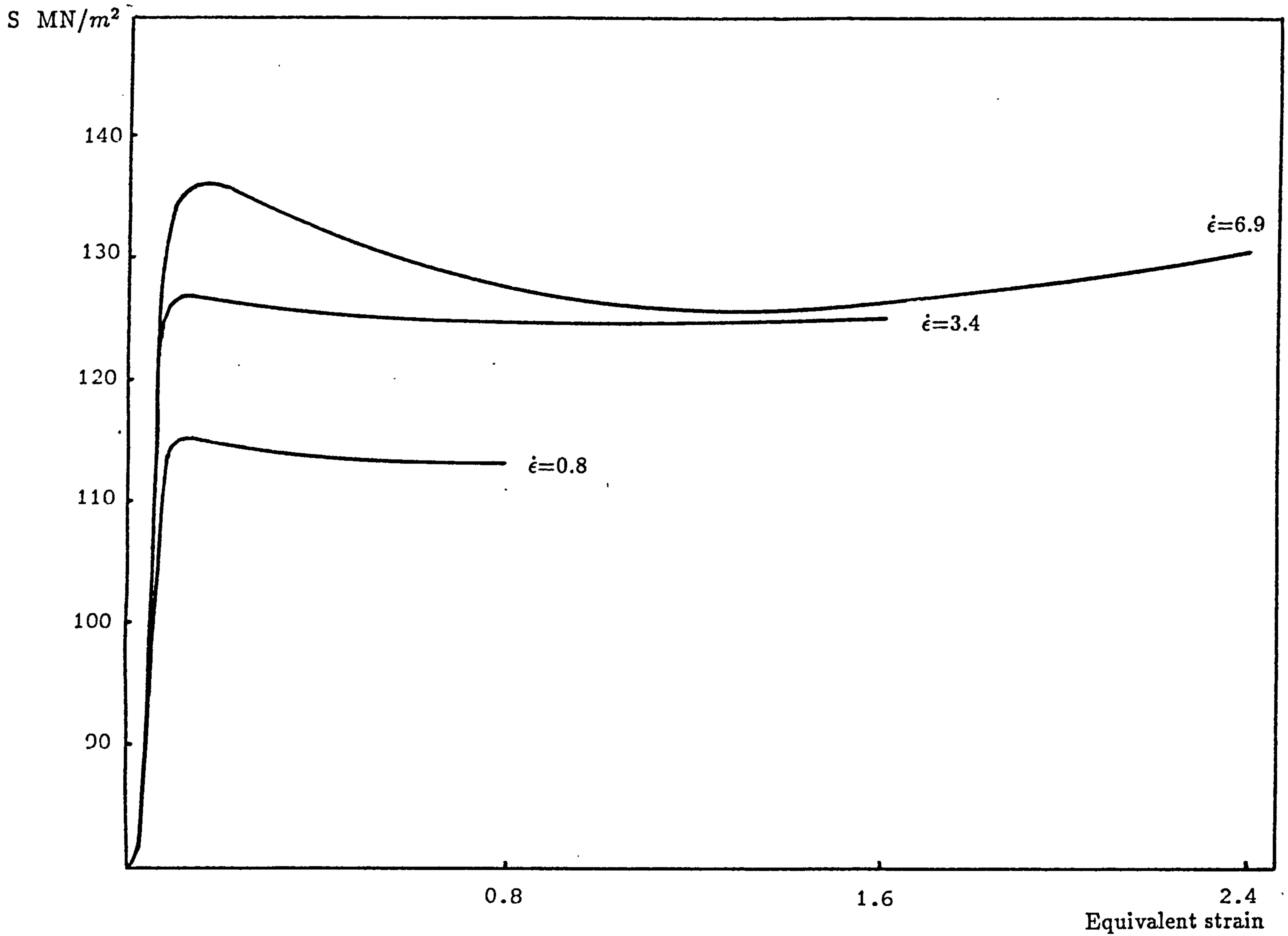

Fig.3.17 Compression tested at 300°C with different strain rate

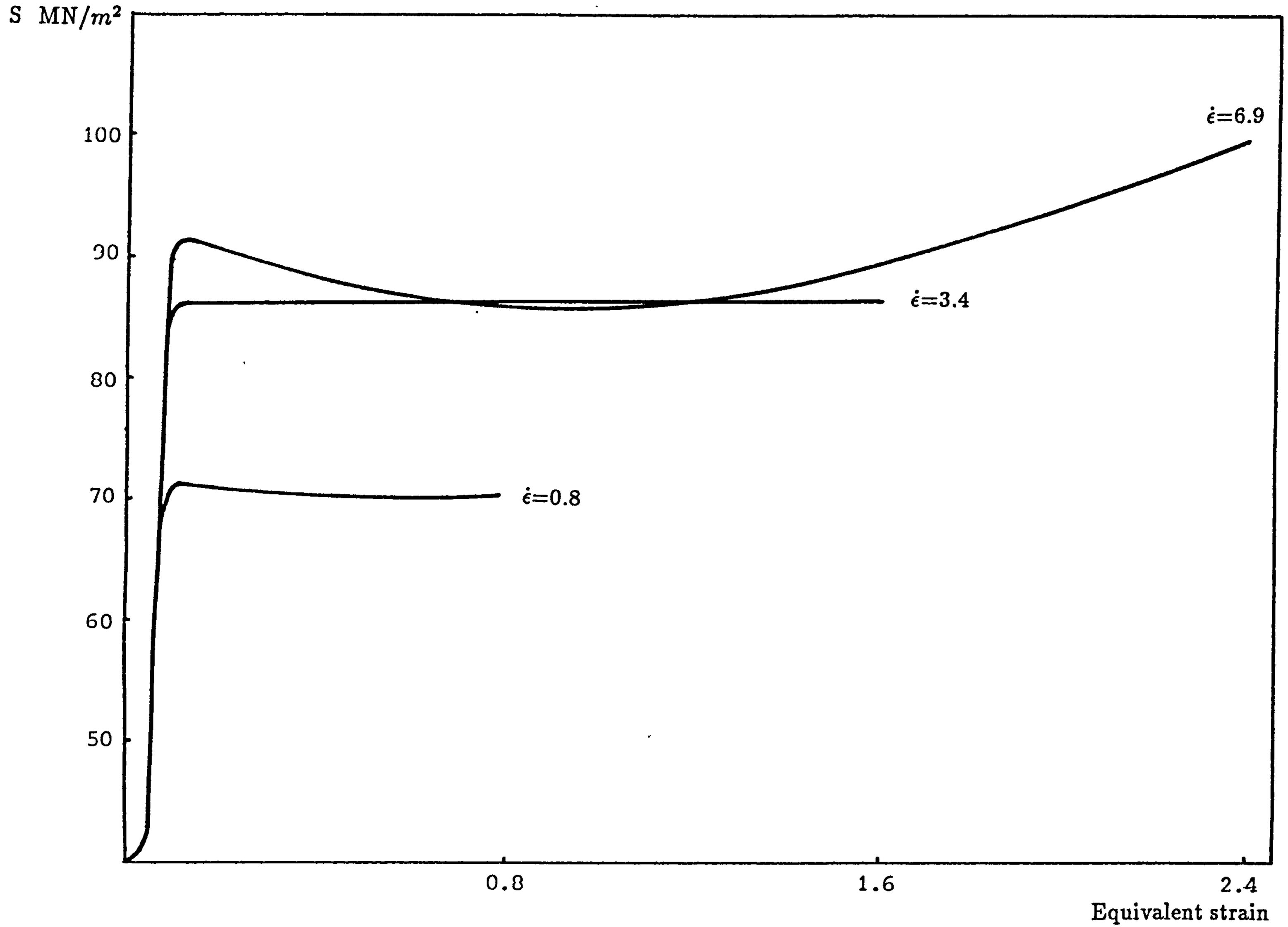

Fig.3.18 Compression tested at 400°C with different strain rate

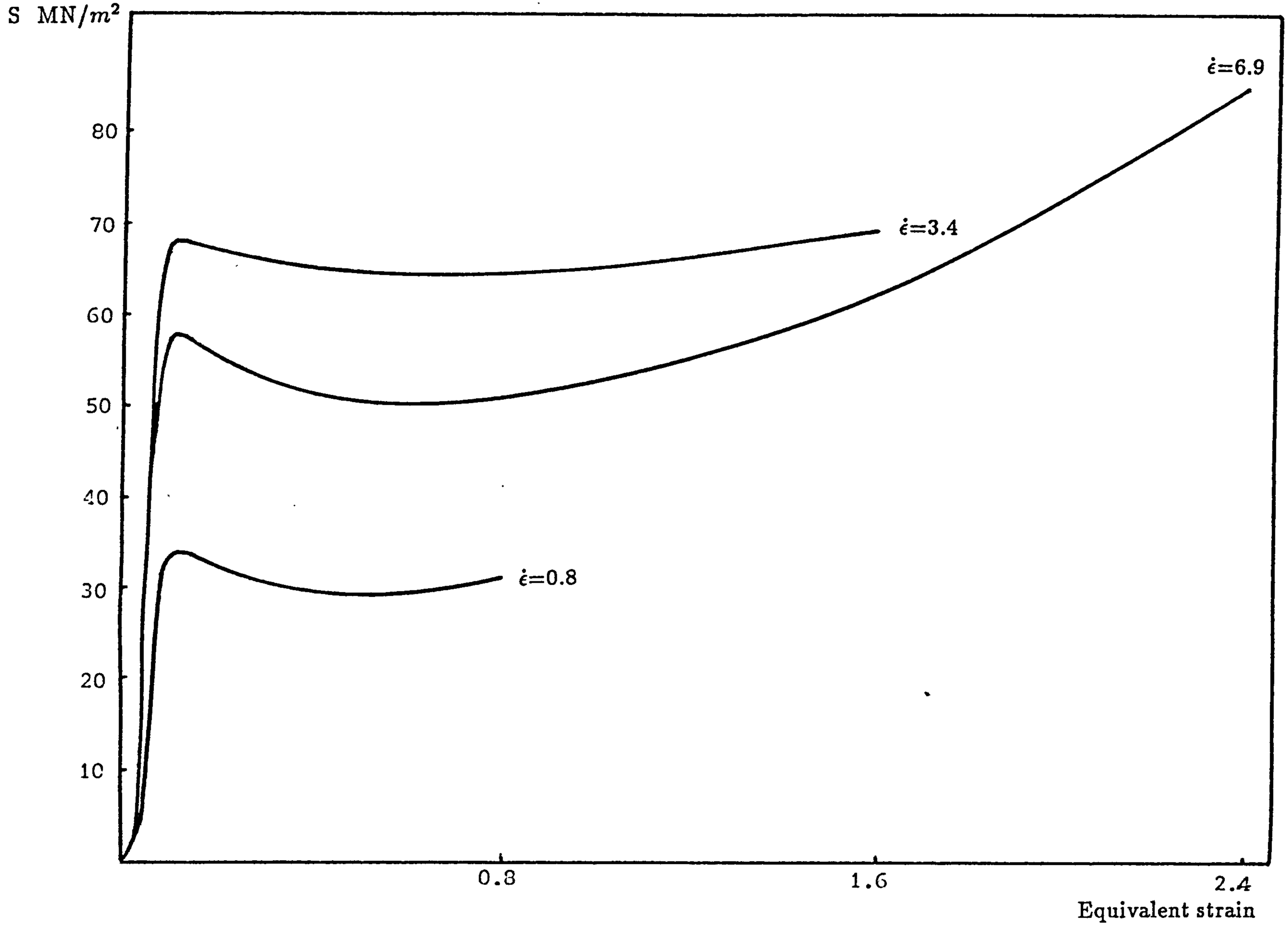

Fig.3.19 Compression tested at 500°C with different strain rate

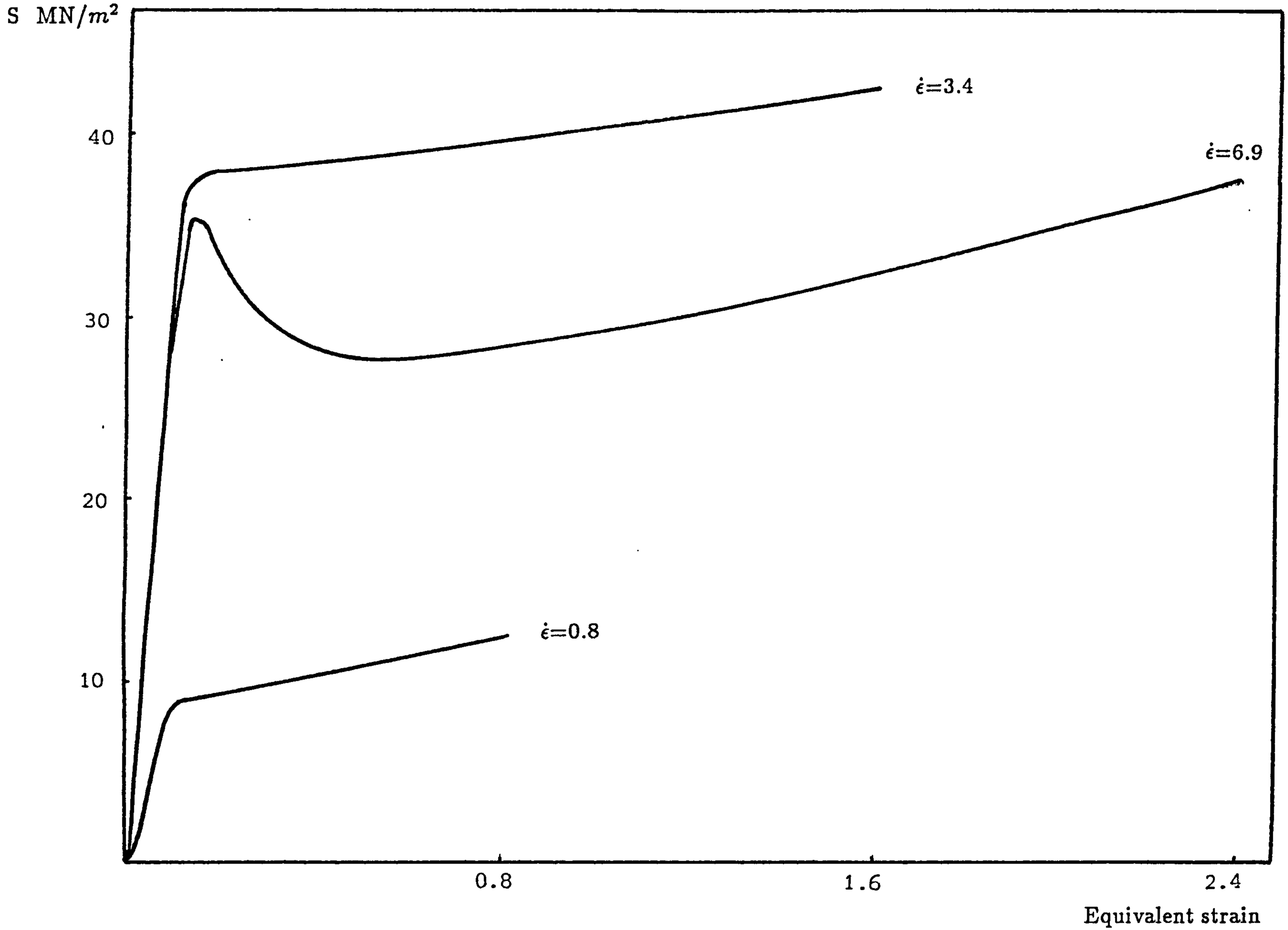

Fig.3.20 Compression tested at 550°C with different strain rate

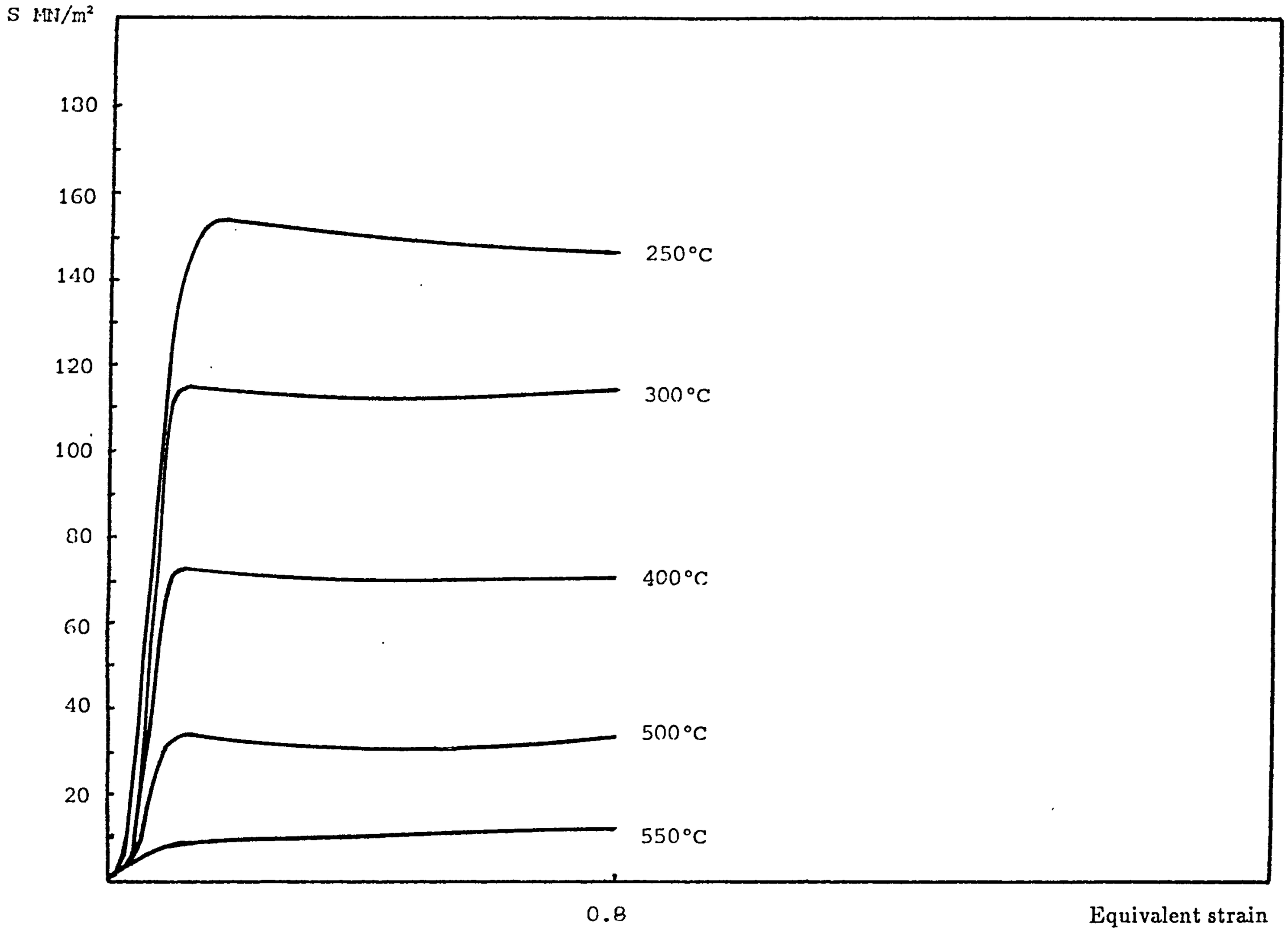

Fig.3.21 Compression tested at strain rate 0.8 with different temperatures

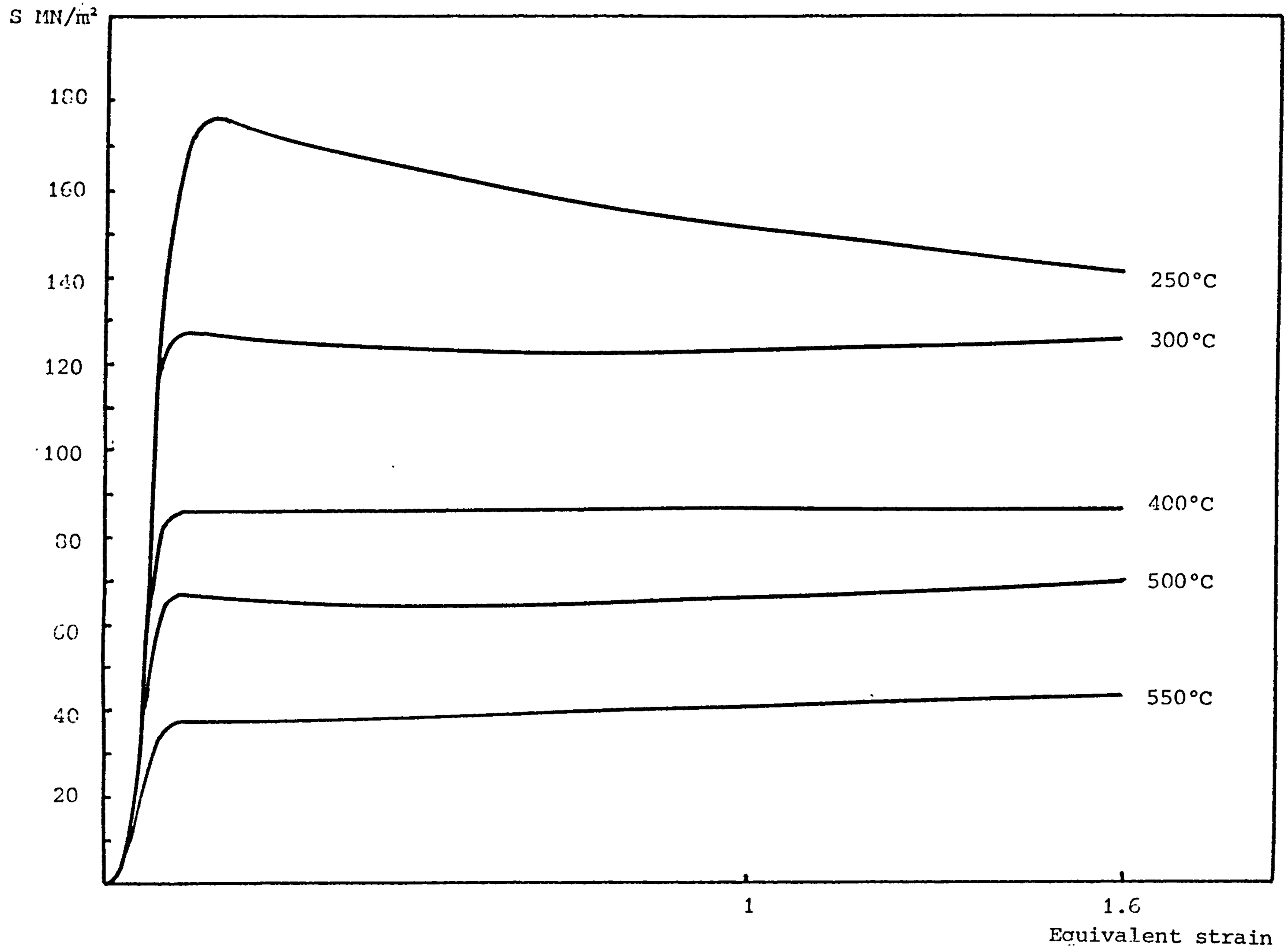

Fig.3.22 Compression tested at strain rate 3.4 with different temperatures

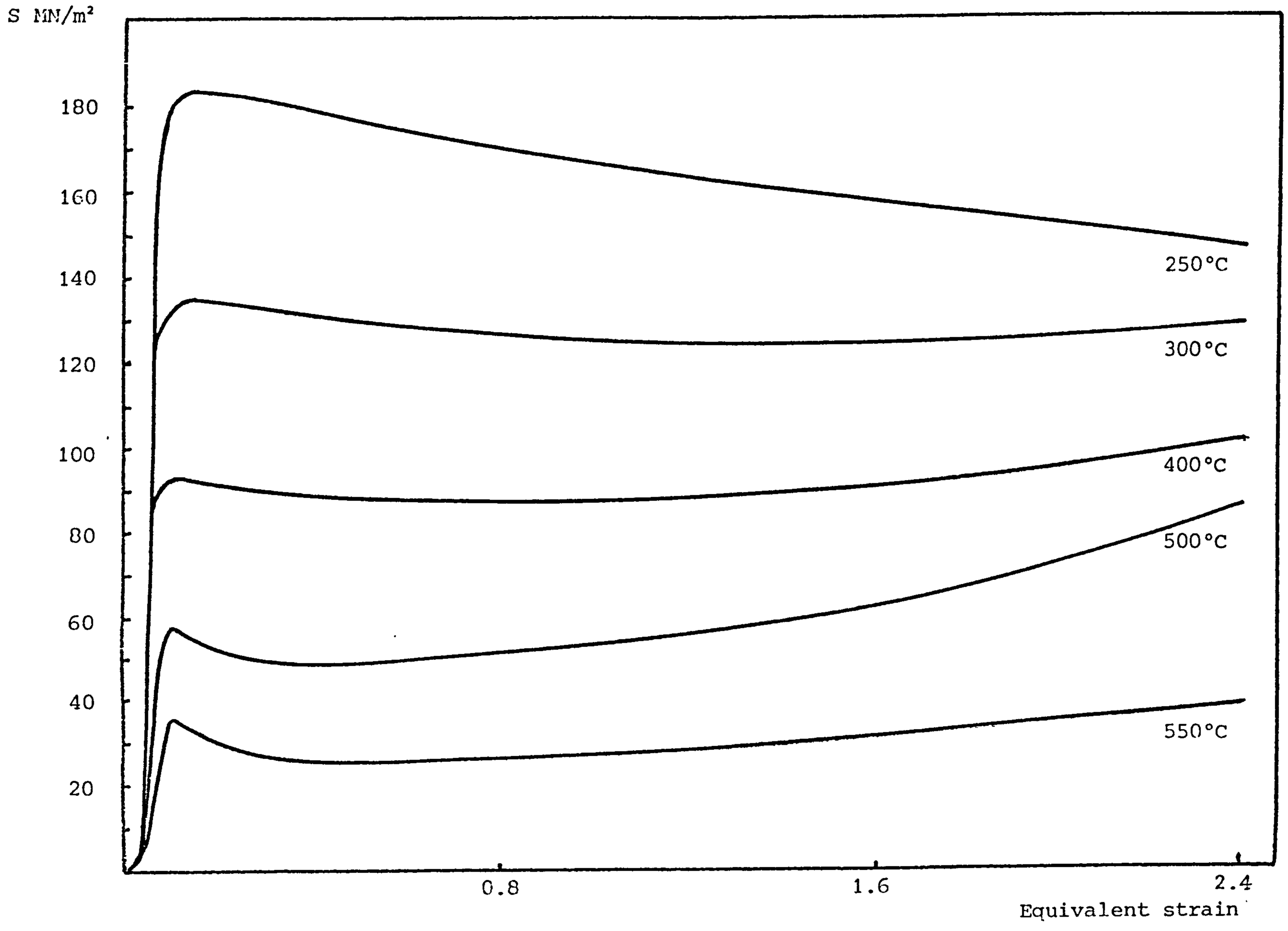

Fig.3.23 Compression tested at strain rate 6.9 with different temperatures

Chapter 4

PREDICTIVE MODELS

4.1 Introduction

As described in Section 2.1.3 and 2.1.4 it is of paramount importance to predict the extrusion pressure and temperature. This work uses experimental data and analytical models to predict extrusion pressure and temperatures. A computer program has been written to predict useful output data from basic extrusion parameters. The absence of analytical models to predict maximum extrusion pressure and the relationship between extrusion pressure and ram displacement has made it necessary to resort to multiple regression analysis and polynomial curve fitting techniques for certain parts of the computational model.

The approach has been to predict the temperature change during the upset stage of the billet which is caused by conduction of heat to or from it and the conversion of the mechanical work into billet heat. This allows an estimate of the uniform billet temperature at the point of maximum extrusion pressure to be made. This temperature is difficult to monitor experimentally for process control purposes but is essential to understand extrusion and the microstructures that are produced.

This temperature can then be used to predict the temperature of the deformation zone when steady-state extrusion occurs and hence the pressure at key stages. Iteration can be used within the program since pressure and temperatures developed are obviously interdependent.

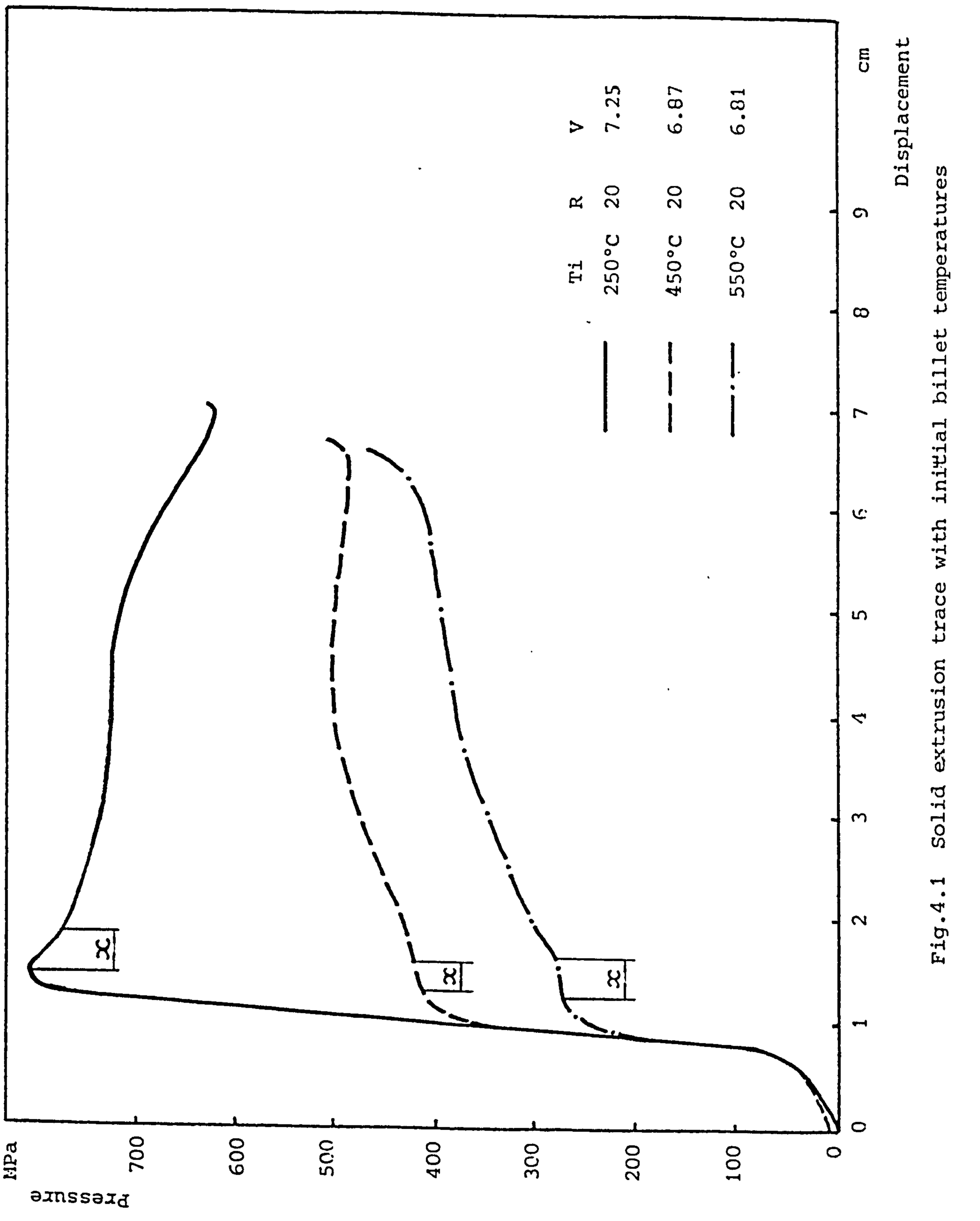

Fig.4.1 Solid extrusion trace with initial billet temperatures

The pressure versus ram displacement curves obtained for the solid billets in this investigation demonstrate the typical characteristics of aluminium extrusion covered in Section 2.1.1. Fig.4.1 illustrates the main features of the pressure change with different billet temperatures at similar ram speeds and constant extrusion ratio. The pressures at all billet temperatures increase rapidly during the upset stage until their maxima. The formation of a maximum pressure has been explained in Section 2.1.4 in terms of establishing a quasi-static deformation zone. The maximum pressure obviously increases markedly with decreasing billet temperature. However, at lower billet temperature the maximum pressures occur after large strains have built up. This phenomenon also occurs in other hot working process [69,60,168,40,156,170]. The higher flow stress requires larger strain to reach the peak and the required strain increases with decreasing temperature at a given strain rate and with increasing strain rate at a constant temperature. This indicates that an equilibrium is needed between the strain hardening and the thermal-softening process. Similarly the relative magnitude of the fall in pressure after the maximum differs for different temperatures. The relative fall in pressure at lower temperature is larger than that at higher temperature where the effects may be swamped by the general temperature fall which masks the peak.

The pressure during steady-state conditions also presents different features. At lower temperatures, the pressure decreases progressively as ram travel increases. The reason for this is that the friction between billet and container wall decreases with decreasing billet length and billet heating reduces the shear yield stress of the material.

At higher temperature, the pressure often increases with ram travel. Here the effect of billet cooling and the subsequent rise in shear yield stress can outweigh the reducing frictional drag.

The three extrusion stages also appear in powder extrusion. However, the pressure rise during the upset stage is different from solid extrusion as shown in Fig. 4.2. The pressure rises more rapidly in solid extrusion than in powder extrusion. This is because the cold compacted powder billet is only 80% dense and

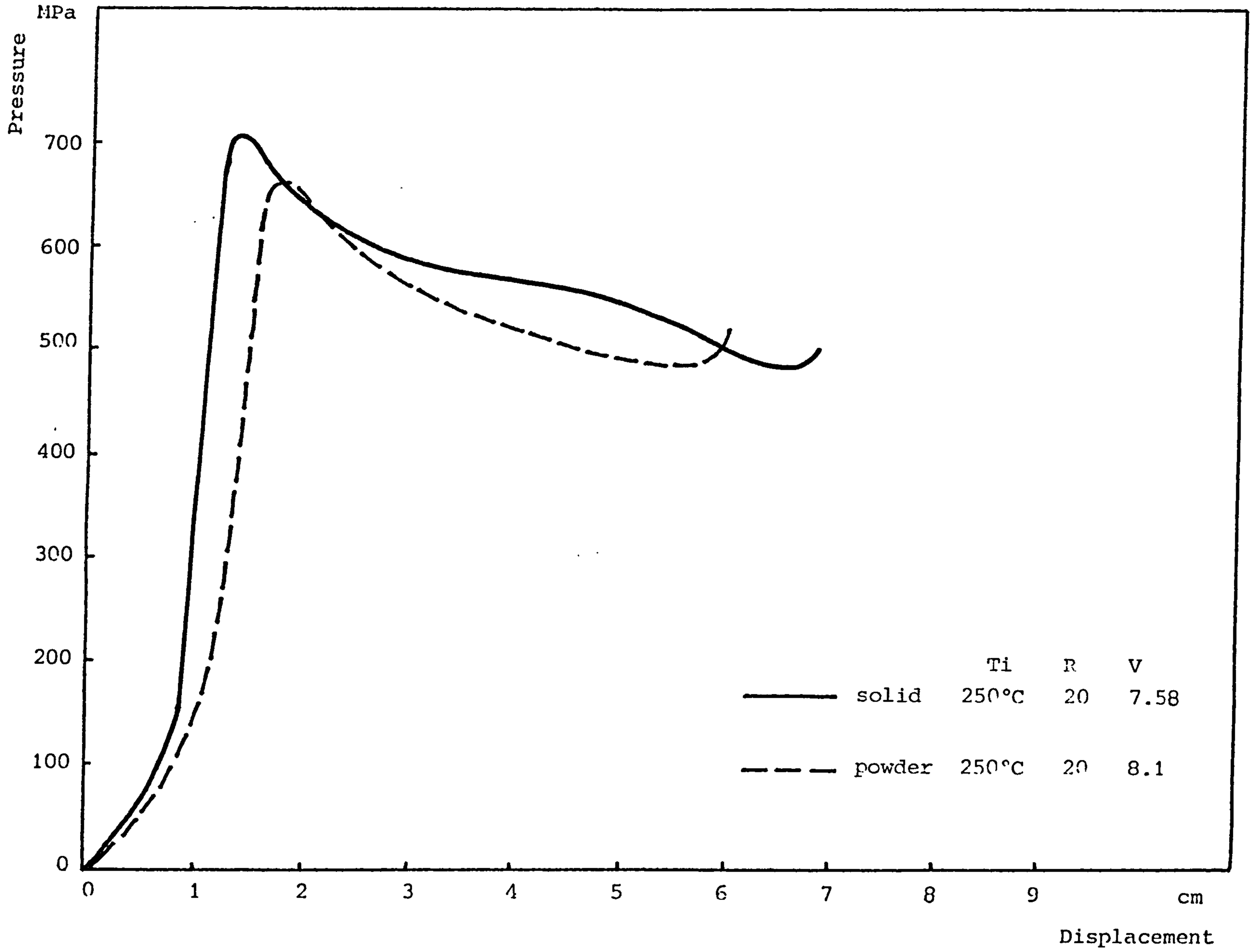

Fig.4.2 Comparison between solid and powder extrusions

when it is upset densification occurs. Fig. 4.2 also illustrates the different pressures required for solid and powder extrusion under identical extrusion conditions and as many workers have reported, the powder needs lower pressure than the equivalent solid extrusion [96,98,101,103,111,31,108,113].

Fig.4.3 and 4.4 illustrate the pressure change with different billet temperatures and different extrusion ratios in powder extrusions. As with solid extrusion, they demonstrate that the pressures increase with decreasing temperature and increasing extrusion ratio. As in the solid extrusion, the magnitude of the drop in pressure is larger at lower temperature than at high temperature and the maximum pressures occur at higher ram displacement (strain) at lower temperatures and higher strain rates.

4.2 Models for the upset stage

4.2.1 Models for prediction of pressure during solid upset

As described in Section 4.1, the pressure increases rapidly during the upset stage until it reaches its maximum. This maximum pressure must be within the capacity of the press and it primarily depends on extrusion ratio, initial billet temperature and ram speed.

Based on experimental data, multiple regression has been used to predict the maximum extrusion pressure. After analysed again and again, the maximum extrusion pressure was found to related with logarithm of extrusion ratio, initial billet temperature and ram speed. For a round die this was found to be:

$$Pmax = 4213 + 80.3\, ln\, R - 657\, ln\, Ti - 11.4\, ln\, V \qquad (4.1)$$

with correlation coefficient $r = 86.1\%$

The increase in redundant work when shaped dies are employed results in higher pressures given by the relationship:

$$Pmax = 2542 + 89.3\, ln\, R - 368\, ln\, Ti - 33.6\, ln\, V \qquad (4.2)$$

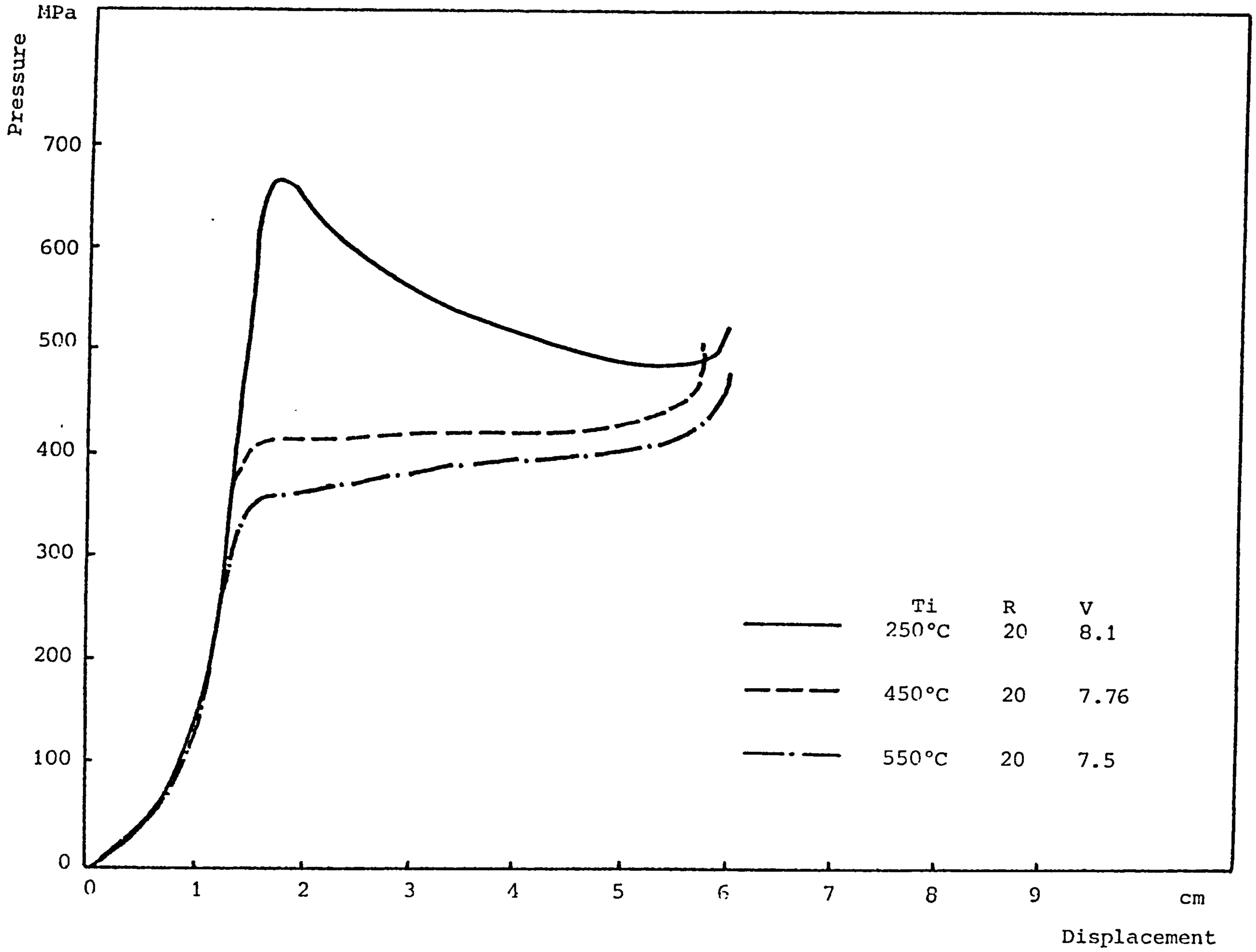

Fig.4.3 Powder extrusion trace with initial billet temperature

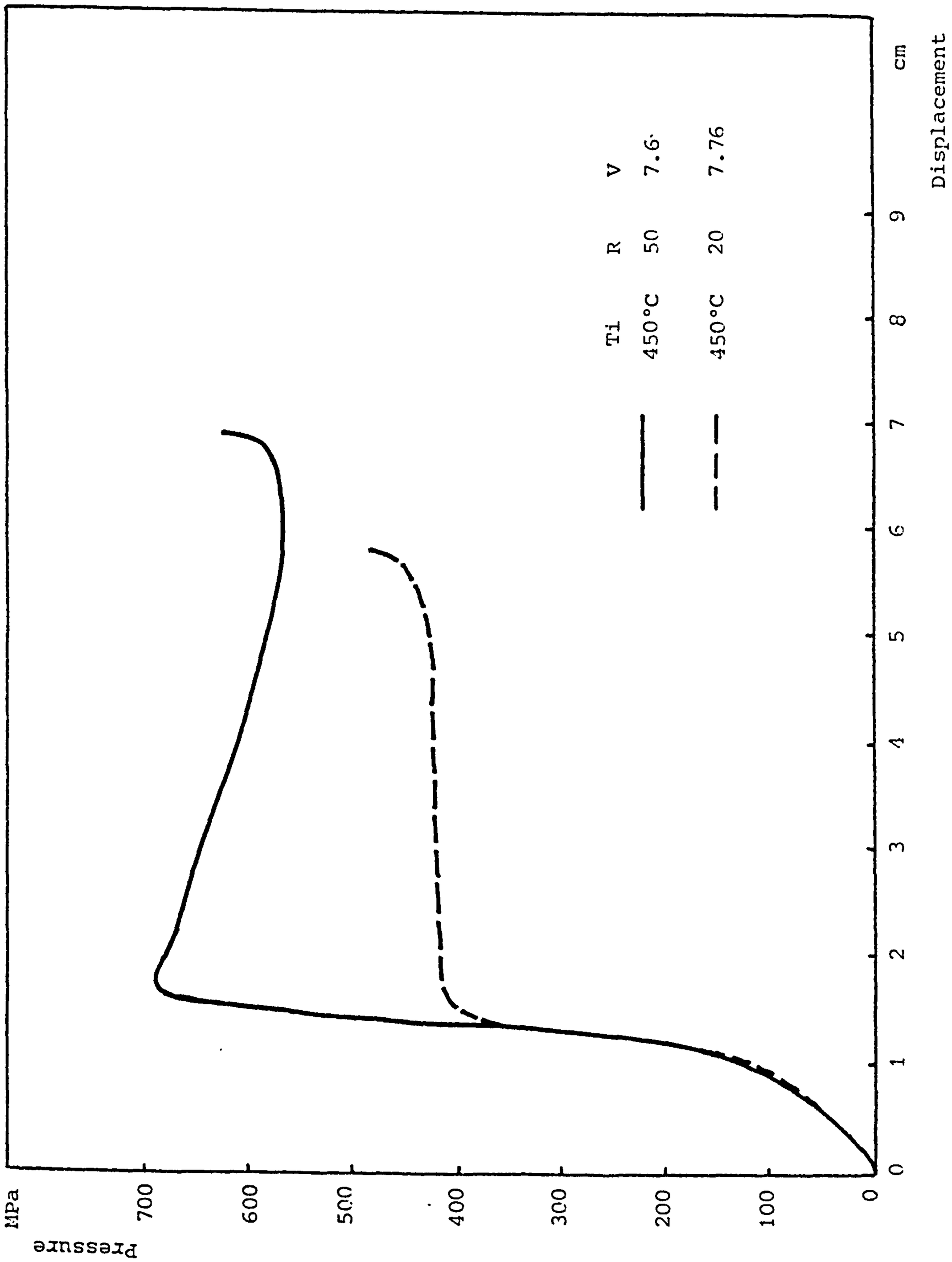

Fig.4.4 Powder extrusion trace with extrusion ratios

with correlation coefficient $r = 86.5\%$

When the ram moves a certain distance under pressure, an amount of mechanical work is done and this mechanical work is converted to heat and raises the billet temperature. So the rate of increase in pressure is important in that it determines the heat input rate into the billet. The relationship between the pressure and ram displacement has been modeled by polynomial curve fitting and a best curve is picked to present the relationship between the pressure and ram displacement as follows (see Fig. 4.5).

$$P = 0.58 * 10^{06} + 0.28 * 10^{11} X - 0.66 * 10^{13} X^2 + 0.57 * 10^{15} X^3 \quad (4.3)$$

4.2.2 Models for prediction of pressure during powder upset

The reduced maximum pressure for powder extrusion considered in Section 2.1.6 [103,104,88,96] has also been found to be related to the logarithm of extrusion ratio, initial billet temperature and ram speed. Multiple regression analysis again gives a relationship between the maximum extrusion pressure and extrusion parameters for powder extrusion through round dies as follows.

$$Pmax = 1050 + 285\, ln\, R - 240\, ln\, Ti - ln\, V \quad (4.4)$$

with a correlation coefficient $r = 80.7\%$

and for shaped dies the increased pressure is given by:

$$Pmax = 3486 + 135\, ln\, R - 567\, ln\, Ti + 6.8\, ln\, V \quad (4.5)$$

with a correlation coefficient $r = 91\%$

The relationship between pressure and the ram travel distance during compaction in powder extrusion has also been approximated by the following polynomial expression (Fig.4.6):

$$P = 0.23 * 10^{06} + 0.15 * 10^{11} X - 0.29 * 10^{13} X^2 + 0.24 * 10^{15} X^3 \quad (4.6)$$

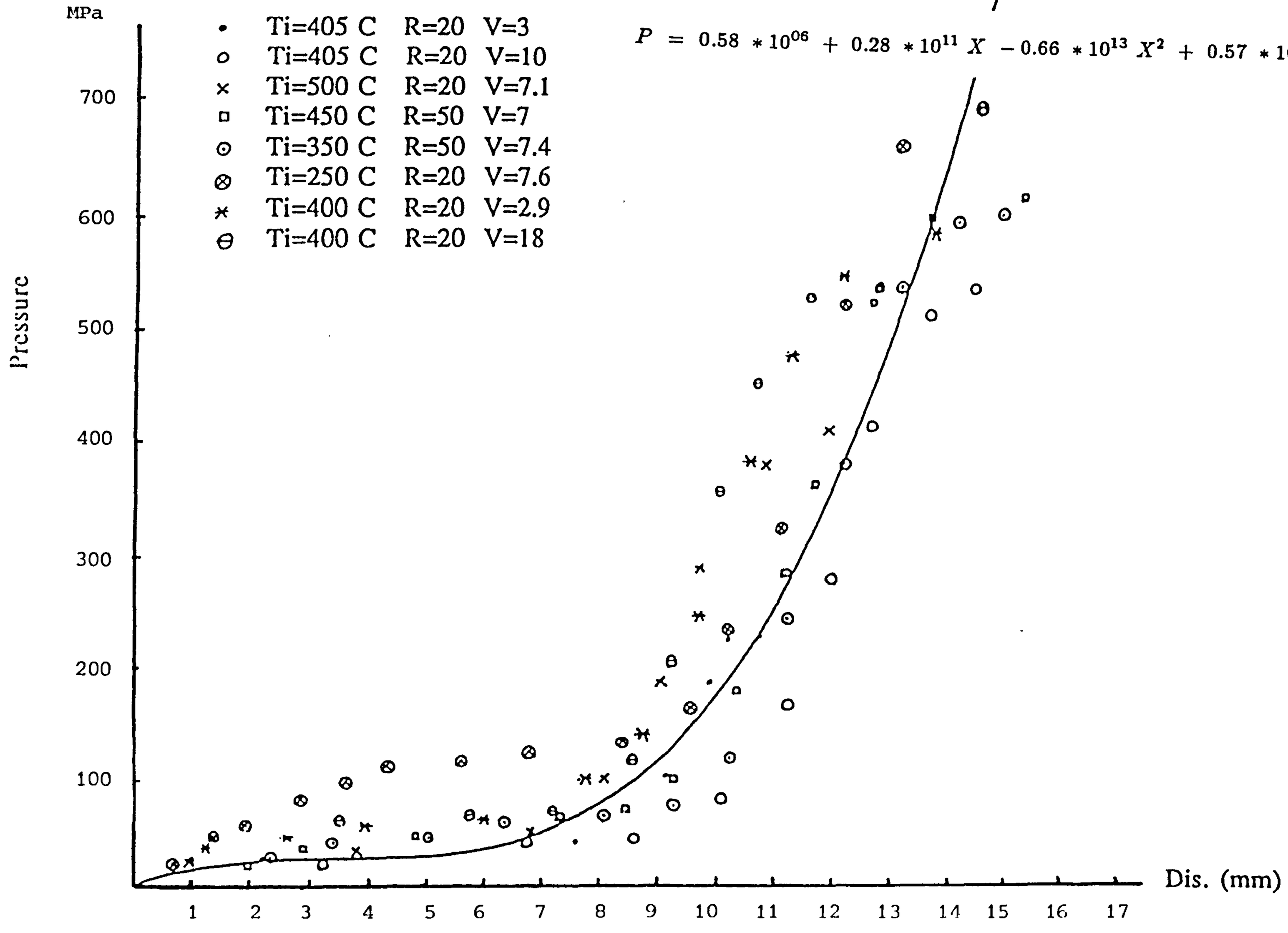

Fig.4.5 Pressure versus ram displacement for solid extrusion

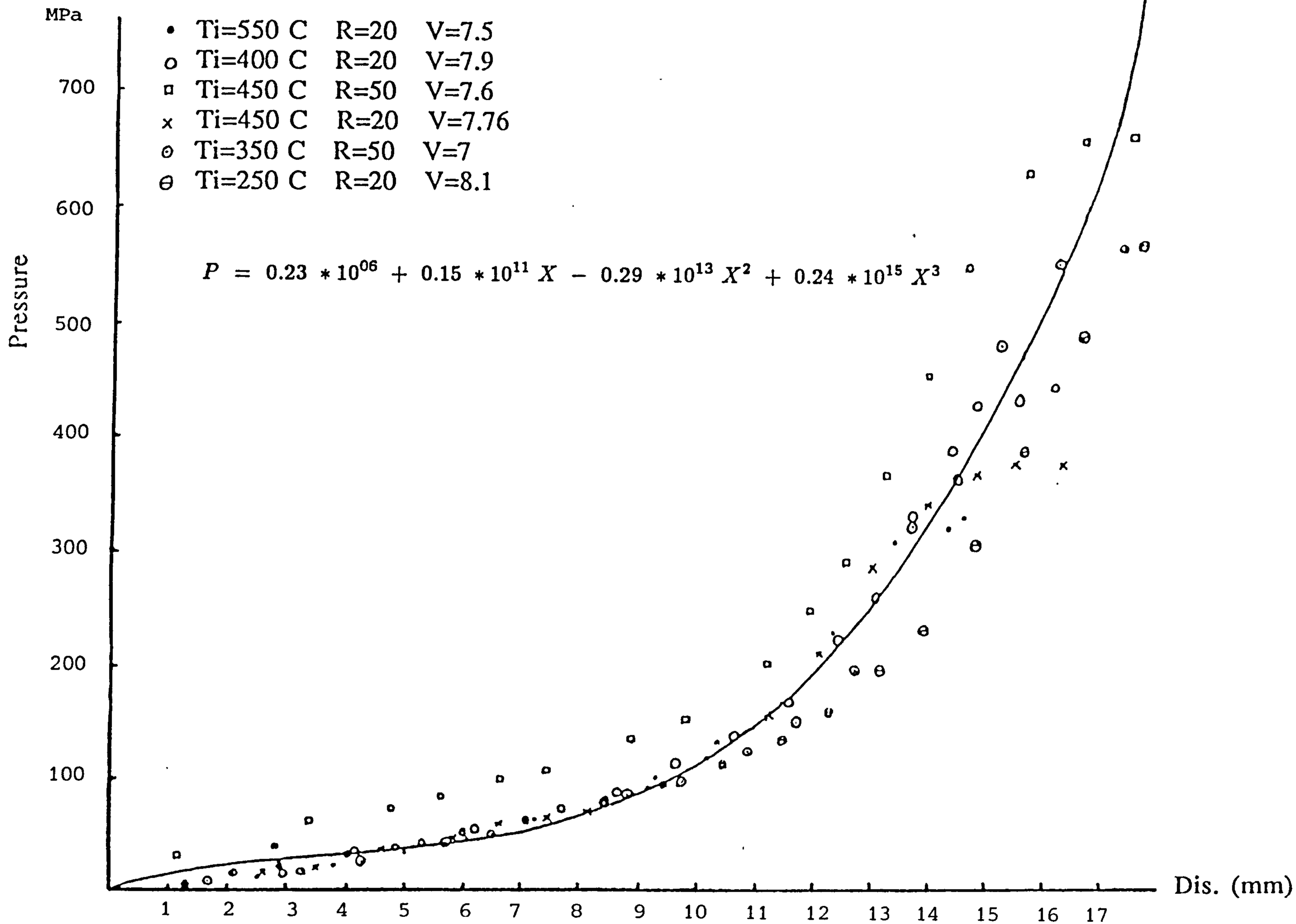

Fig.4.6 Pressure versus ram displacement for powder extrusion

4.2.3 Temperature change during upset

During extrusion the temperature changes occur in two distinct stages: (1) the upset stage where heat is generated by mechanical work and conducted to or from the container depending on the relative temperatures. (2) the steady-state stage where the deformation zone is established and extrusion begins.

When a heated billet is suddenly put into a container (usually preheated), any difference in temperature between the billet and the container will cause conductive heat flow and the billet temperature will be changed unless both billet and container have the same temperatures, a situation which is very rare in industry.

Now it is necessary to calculate the conductive heat flow and combine it with the mechanical heat input to obtain the temperature change during compaction.

Carslaw and Jaeger's [35] mathematical integration [35] previously mentioned has the following details. Consider a cylinder of radius, a, in a medium of thermal diffusivity, α'. At time $t = 0$, the cylinder is suddenly brought to temperature corresponding to a temperature difference, T_0, above the surroundings and maintained at this level. The question is in what manner does the temperature difference, T, between any point in the medium and surroundings depend on the time, t, and the distance, r, of that point from the axis of the cylinder ($r > a$). They obtained the integration.

$$\frac{T}{T_0} = 1 + \frac{2}{\pi}\int_0^{\infty} exp^{(-\alpha' u^2 t)} \frac{J_0(ur)N_0(ua) - J_0(ua)N_0(ur)}{J_0^2(ua) + N_0^2(ua)} \frac{du}{u} \qquad (4.7)$$

where

u — is a variable having the dimension of a reciprocal length extending from zero to infinity.

J_0, N_0—are Bessel functions of the first and second kind both of zero order

Gemant [36] applied this integration to heat flow caused by the conduction into an infinite medium from a cylindrical heat source. The integration was not entirely

suitable for numerical calculations and was expanded to a series and integrated by terms. This produced a series of curves to represent the heat flow which are now well-established for non-steady heat flow. By substitutions of the following into equation (4.7):

the dimensionless time function:

$$\tau = \alpha' \, t/r^2$$

where

t— compaction time, $t = X/V$

and

$$\alpha' = \frac{g}{\rho C_p}$$

and instead of u

$$v = ua$$

Remembering the general relation of any Bessel function:

$$Z_0' = -Z_1$$

With these substitutions and when $r = a$,

$$\alpha' u^2 t = \alpha' t \frac{v^2}{a^2} = \tau v^2$$

$$\frac{Q}{T_0 g} = 4 \int_0^\infty exp^{(-\tau v^2)} \frac{J_1(v)N_0(v) - J_0(v)N_1(v)}{J_0^2(v) + N_0^2(v)} dv \qquad (4.8)$$

From this expression families of curves can be presented. One of the curves is shown in Fig. 2.4 which was constructed by actually calculating numerically the integration of equation (4.8). The dimensionless heat dissipated $\frac{Q}{T_0 g}$ is plotted versus τ, from which Q is obtained for any specific case and at any given time.

The situation in extrusion is quite similar to Gemant's solution so it can be directly used for the conduction of heat between billet and container during the

upset stage in extrusion. Singer and Al–Sammrrai [20] have directly applied Gemant's graphical solution to their work concerning heat flow between billet and container during extrusion. Akeret [19] has found his numerical analysis of temperature change during extrusion is in agreement with Singer and Al–Sammarrai's [20]. Greasley [37] has used Gemant's solution in a graphical fashion to predict the temperature during upset stage. However in this work the integral has been numerically solved more accurately and conveniently numerically within the computer program used to predict the temperature changes during the upset stage.

A particular industrial practice which is used on the extrusion press used makes Gemant's solution particularly useful. The die and the pressure pad are always preheated to 400°C, but the container is usually kept between 150°– 300°C, hence the approximation of only radial heat flow is applicable. The total heat loss is dependent on the length of the body and the thermal contact with the container. When the billet is placed into the container, the diameter of billet is smaller than the container and an air gap exists. Hence the heat transfer is mainly convective and radiative. After the billet is upset to contact the container the heat transfer is wholly conductive but the contact length reduced. Hence the average billet length (half the sum of the billet lengths before and after upset) is taken and because aluminium is more conductive than steel, thermal gradients within the billet are ignored.

The numerical calculation of equation (4.8) is performed by a computer program written in Fortran 77 (see Microfiche at the end of thesis) on a SUN 3/180 computer. (flow chart see Fig.4.7)

With this program, any combination of billet and container temperature can be used to give Gemant's heat flows. Fig. 4.8 illustrates the heat changes with different temperature gradients between the billet and the container. Curves above the time axis indicate heat loss from the billet to the container when the billet temperatures are higher than the container. Curves below the time axis are for the billet gaining heat from the container when the billet temperatures are lower than the container. In addition to this heat flow, the ram travels a limited dis-

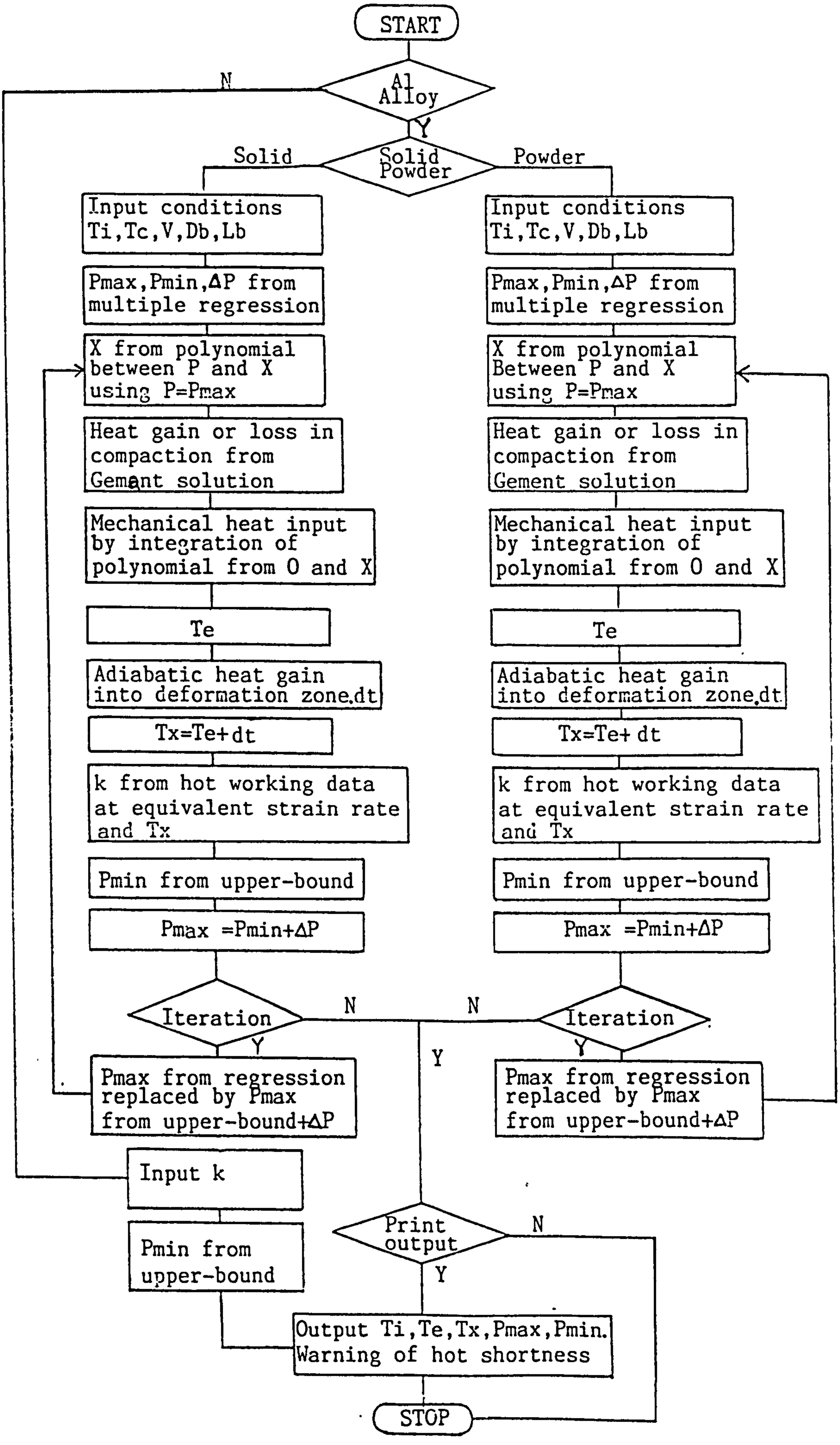

Fig.4.7 Flow chart of the program

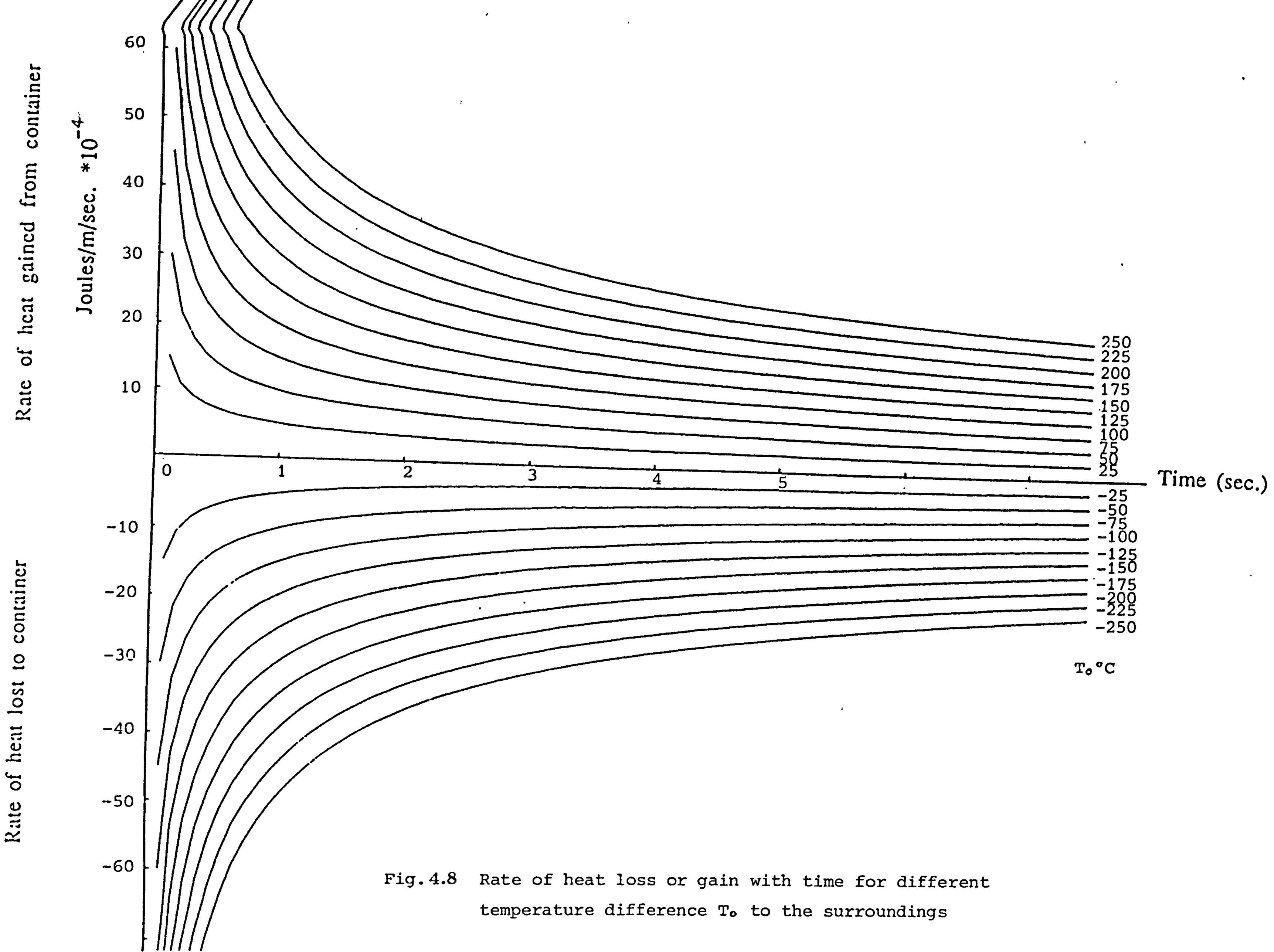

Fig. 4.8 Rate of heat loss or gain with time for different temperature difference T_o to the surroundings

tance during compaction and produces a certain amount of mechanical work. 95% of this mechanical work is converted to heat and raises the billet temperature [3,142,23,17].

The relationships between the extrusion pressure and ram travel distance have been expressed in equations (4.3) and (4.6). Having obtained the maximum extrusion pressure from equation (4.1) or equation (4.4) with any particular extrusion conditions, the distance of ram travel, X, during compaction can be obtained within the program by solving equation (4.3) or equation (4.6) for ingot and powder extrusion respectively. The mechanical work input is obviously a function of force and distance. By integration of equation (4.3) or equation (4.6) within the limits of compaction, the total mechanical work is obtained:

$$W = A \int_0^X P(X)\, dX \tag{4.9}$$

The rise in temperature, of course, is a function of the specific heat c_p of the material, and the mass M of the material being compacted.

$$\Delta T = \frac{H}{M c_p} \tag{4.10}$$

where

$$H = W \times 95\%$$

By combining the conduction of heat between the billet and the container, and the heat generated from the mechanical work, a nett heat change is obtained. Fig. 4.9 shows the rate of heat loss to the container and the heat gain from the mechanical work, when a billet temperature of 370° C, a container temperature of 350° C, a ram speed at 7.46 mm/sec. and an extrusion ratio of 20 is used. Figure 4.10 shows the resulting nett heat flow obtained from the curves in Fig. 4.9. Hence the temperature, Te, at the start of extrusion is obtained.

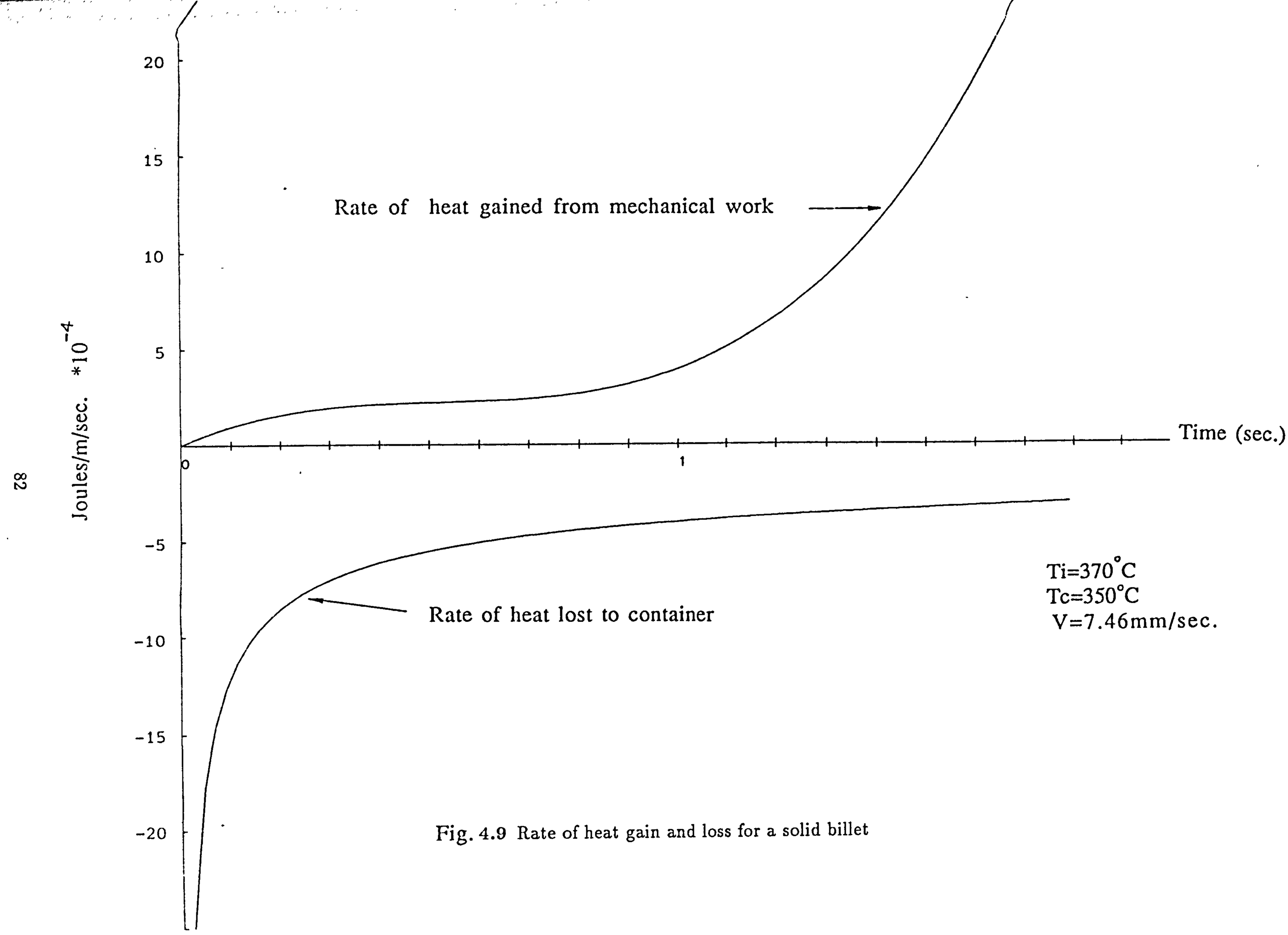

Fig. 4.9 Rate of heat gain and loss for a solid billet

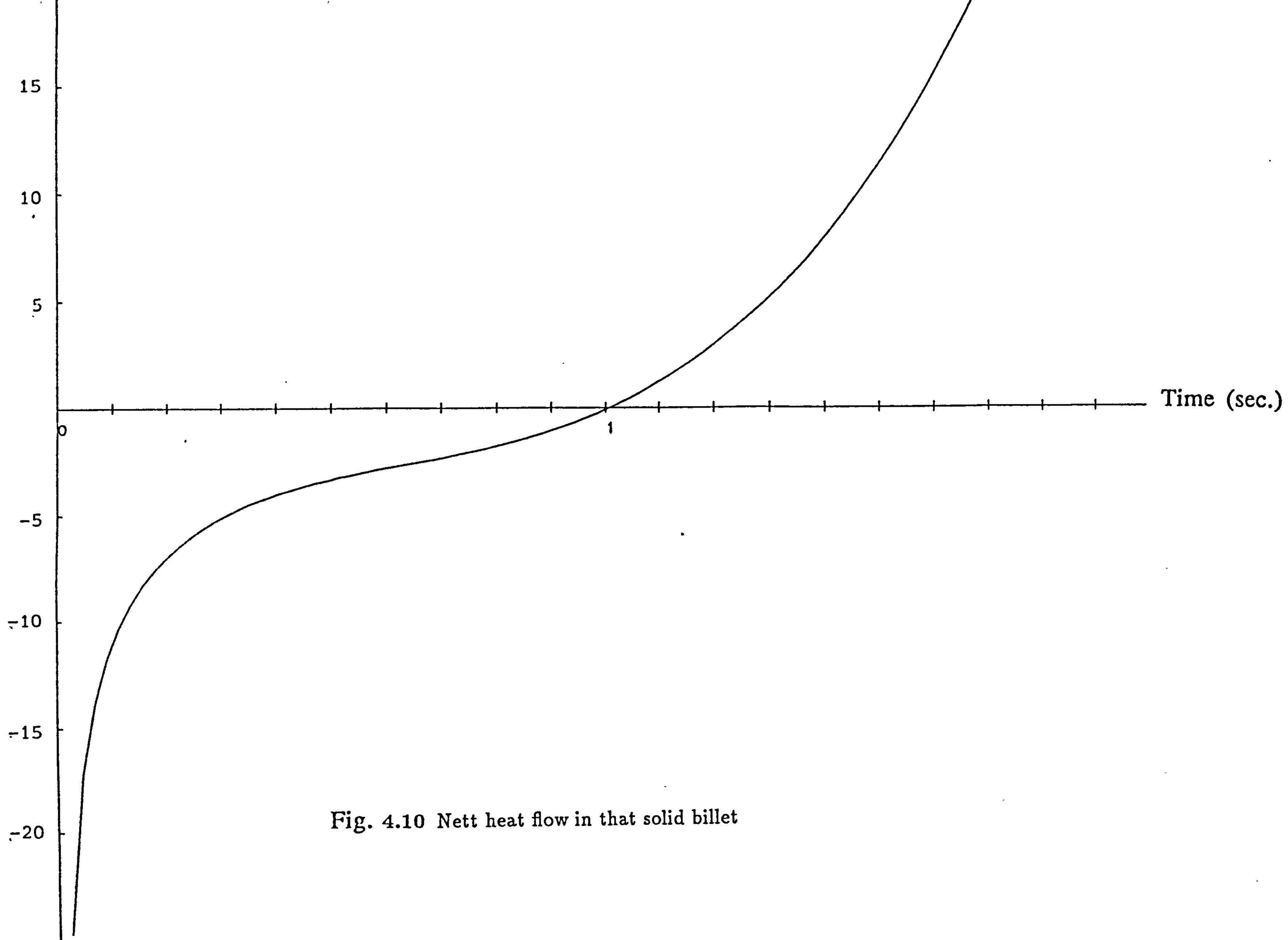

Fig. 4.10 Nett heat flow in that solid billet

4.2.4 Prediction of temperature at the start of steady-state conditions

As shown in Section 3.5 the deformation zone is an upturned frustum of a cone above the die exit and the dead metal zones can be considered as an extension of the tooling. The heat flow between the billet and tooling mean that their temperatures converge during the compaction stage. Hence there is only a minor temperature difference between the deformation zone and surrounding materials after the compaction stage [19]. So adiabatic heating is considered here and the temperature of the billet at some distance from the deformation zone is but little affected by the heat generated by plastic deformation. The heat transformed from the deformation energy is considered as only affecting the material in the deformation zone and the material which is pushed into the deformation zone during the stage when the pressure falls from Pmax to Pmin. Ashcroft and Lawson [6] have measured that temperature rise during compaction as about 10°C. But when the thermocouple moves into the deformation zone, there is a more rapid rise in temperature and they find that when an initial temperature is 300°C, a temperature rise of 170°C is measured in the product for an extrusion ratio of 200. This indicates that temperature rise mainly occurs in the deformation zone.

From the diagram in Fig.4.1, it is clear that after the maximum pressure, there is usually a drop in pressure, whilst the ram travels a short distance. As long as the ram moves under a pressure, a certain amount of mechanical work is done and is converted to heat which raises the temperature of the deformation zone. This temperature rise is critical in extrusion as it happens at the start of the steady-state condition. This temperature determines whether or not a satisfactory extrusion can be obtained and the microstructure and properties of the first part of the extrusion. After this critical stage the extrusion process is in the steady-state stage where the temperature changes are less dramatic [17]. Examination of many hot short extrusions in this work demonstrated that hot shortness (or tearing) started about 50-150 mm from front of the extruded products which are extruded at higher initial billet temperatures. This indicates that for the extrusions on the

hot–shortness boundary the maximum billet temperature occurs in front part (about 10 – 20% of the length of extruded product). As the billet temperature falls slightly due to the continuing heat loss to the container and the lower heat input rate once the pressure has fallen from the maximum the hot shortness disappears and the surface finish is therefore improved.

So the temperature at the start of steady-state stage is very important for the extrusion process. The work put into the deformation zone is related to the maximum pressure, the minimum pressure and the distance the ram travels between the two. The minimum pressure is clearly related to the same extrusion parameters as the maximum pressure. Although analytical methods are available to predict this pressure they depend on a knowledge of the billet temperature for an accurate input of the material flow stress. This has not yet been established. The rate at which the pressure decays from Pmax to Pmin has also been found to depend on the basic extrusion parameters and the maximum pressure. This rate which is manifest as the distance, x , also affects the billet temperature. The distance, x , (as shown in Fig. 4.1) which is the distance the ram moves during the fall in pressure from Pmax to Pmin is even more complicated because it does not only depend on the extrusion parameters, but also depends on the press and in particular the hydraulic control system of the press. There is no analysis for predicting this distance. Hence in this part of the program both Pmin and x are found by regression analysis.

For round dies and solid extrusion:

$$Pmin = 85 - 10.1\, ln\, R + 4.2\, ln\, Ti - 12.1\, ln\, V + 0.833\, Pmax \quad (4.11)$$

with correlation coefficient $r = 99\%$

and the distance, x, is given by:

$$x = 8.61 - 0.32\, ln\, R - 0.00143\, Ti + 0.0581\, V + 0.106\, Pmax - 0.116\, Pmin \quad (4.12)$$

with correlation coefficient $r = 87.7\%$

For shaped dies and solid extrusion:

$$Pmin = 12 - 5.2\,ln\,R + 15.5\,ln\,Ti - 45.5\,ln\,V + 0.931\,Pmax \quad (4.13)$$

with correlation coefficient $r = 97.4\%$

$$x = -23.4 + 0.64\,ln\,R + 0.0213\,Ti + 0.498\,V + 0.0282\,Pmax - 0.001\,Pmin \quad (4.14)$$

with correlation coefficient $r = 87.6\%$

For round dies and powder extrusion:

$$Pmin = 489 + 44.2\,ln\,R - 78.3\,ln\,Ti - 29.1\,ln\,V + 0.821\,Pmax \quad (4.15)$$

with correlation coefficient $r = 99.9\%$

$$x = -52.4 - 4.26\,ln\,R + 0.0615\,Ti + 1.22\,V - 0.113\,Pmax + 0.17\,Pmin \quad (4.16)$$

with correlation coefficient $r = 94.8\%$

For shaped dies and powder extrusion:

$$Pmin = -391 - 10.2\,ln\,R + 76.3\,ln\,Ti - 15.4\,ln\,V + 0.934\,Pmax \quad (4.17)$$

with correlation coefficient $r = 99.5\%$

$$x = -3.64 - 18.6\,ln\,R + 0.1109\,Ti + 0.21\,V - 0.0359\,Pmax + 0.108\,Pmin \quad (4.18)$$

with correlation coefficient $r = 99.7\%$

During the period whilst the pressure is falling and the deformation zone is being established the mean pressure is the average of Pmax and Pmin and hence the mechanical work done is given by:

$$W = P \times A \times x \quad (4.19)$$

where

P— mean pressure

95% of this work is converted to heat and this heat is only dissipated in the deformation zone where adiabatic heating occurs [19]. Hence the temperature rise, dt , is given by:

$$dt = \frac{H}{V_D \times \rho \times c_p} \tag{4.20}$$

where

$$H = W \times 95\%$$

Obviously as the ram advances hot material is forced out of the zone and cooler material enters. When the ram travels distance, x , it pushes a disc of material of thickness x into the deformation zone. So the heat is considered to be expended on a disc of material next to the deformation zone with a thickness x and the material in the deformation zone. A very rigorous analysis of this event, even under adiabatic conditions should take into account the fact that material is entering and leaving the zone at slightly different temperatures. However as will be shown in Chapter 7 the temperature rise predicted by this model agrees well with the literature [6,2,11] if hot shortness is used as a criterion.

If this temperature rise is considered with the temperature change during compaction, the real temperature, Tx , at the start of steady–state condition is found and this critical temperature determines the occurrence of hot shortness and influences the microstructure of the product in the early part of the extrusion.

It is reported that the deformation zone geometry changes with billet temperature [10]. At low temperature the deformation zone is restricted to the die mouth region while at higher temperature the deformation zone penetrates towards the rear of billet. It is also observed [53,43,137,140] that the deformation zone depends on the extrusion ratio, coefficient of friction on the die face, geometry of the die and strain hardening characteristics of the material. It is claimed that there is a relationship between deformation zone angle, ω, and extrusion ratio [10]:

$$\omega = 54.1 + 3.45 \, ln \, R$$

The volume of this truncated deformation zone is defined as [3]:

$$V = \frac{\pi h}{3}(\frac{D^2}{4} + \frac{D_e^2}{4} + \frac{D\ D_e}{4}) \tag{4.21}$$

for a 45° semicone angle.

Examination of the partial extruded billets from ingot and powder shows that the deformation zones are different. For ingot extrusion in round dies the deformation zone has been found to be an upturned frustum of a cone where the height "h" is fixed and the deformation angle, ω , changes accordingly as shown in Plate 2.

Examining the deformation zones which are obtained from different extrusion ratios, it is found that the height of deformation zone, h , is almost constant with a value of $h = 28\ mm$. Equation (4.21) then can be rewritten:

$$V = \frac{7\ \pi\ D_e^2}{3}(\ R + \sqrt{R} + 1\ ) \tag{4.22}$$

For shaped die extrusion, the deformation zone is not a cone frustum. It has a shaped top (rectangular, square or more complicated shape) and a circular bottom, so it is necessary to use a prismoidal rule to find the volume:

$$V = \frac{h}{6}(\ A + 4\ A_2 + A_e) \tag{4.23}$$

where

A— the area of cross section of billet

A_e—the area of cross section of extrusion (eg. a square with side length of l_e)

A_2—the area of a cross section at the middle of the total height of deformation zone and is expressed:

$$A_2 = \frac{L}{2}(D - l_e) + \frac{L^2}{4} + \frac{\pi}{16}(D - l_e)^2 \tag{4.24}$$

For powder extrusion, it is found that the dead metal zone does not extend to the die mouth and the shape is shown in Plate 2. The height of the deformation

zone is 20 mm. With this height, a dead metal zone is formed, having an angle of 45°. So the diameter of the top circle of the frustum is $D_t = D - 2 \times 20$ (D is the diameter of the billet). The volume of the deformation zone is:

$$V = \frac{h}{3}(A + A_t + \sqrt{AA_t}) \tag{4.25}$$

where

h—height of deformation zone = 20 mm

A—area of cross section of billet

A_t—area of the top of the frustum.

4.3 Limitations of regression analysis

The prediction of extrusion pressure has been studied by many workers as has been described in Section 2.1.4. However these predictions are confined to predicting extrusion pressure in the steady-state condition. It is however most important to predict the maximum extrusion pressure which determines whether or not the required pressure for an extrusion is within the capacity of the press. It also is a major influence on the temperature changes. There is little available literature for prediction of maximum extrusion pressure from analytical solutions. The use of upper-bound solutions is still confined to predicting the minimum extrusion pressure during steady-state conditions in extrusion and to use an upper-bound solution needs the actual temperature at which the material is deformed in order to obtain the shear stress of the material. If the actual temperature is not known the shear stress cannot be accurately put into the solution.

Temperature changes during compaction depend on the maximum pressure. The rate at which the pressure falls from maximum to minimum determines the heat input to the billet and the temperature when steady-state condition starts. However this rate is not predicable from fundamental data.

Regression has to be used to predict maximum extrusion pressure and the rate of fall in pressure from maximum to minimum so that the temperature during compaction and at the start of steady-state can be predicted. Once obtained the

shear yield stress under these working conditions can be obtained. This method is used in both powder and solid extrusions.

However, regression has its limitations. It is based on practical data when one variable depends upon others. The accuracy of this analysis is given by the correlation coefficient. If the values of the variables are close, covering a narrow range, a high correlation coefficient can be obtained. But in industry, when data is collected from an operational extrusion press low correlation coefficients can be expected. In practice, the variables are interdependent, but the analysis takes them as independent and the signs and values of some coefficients in the equation cannot always be given physical significance.

The extrusions in this investigation were performed on The Harwell Laboratory press. Although this is a research press the reproducibility of extrusion procedures may not be as high as that on a production press. For instance the times taken from billet removal from the furnace to the start of compaction varied slightly and this is reflected in the correlation coefficients. If similar formulae were established in other situations, where conditions were automated, it could make a considerable difference to the correlation.

4.4 Upper-Bound solutions within the temperature rise model

The upper-bound technique is applied to plane strain deformation caused by pure shear. An external force is imposed on a perfect rigid plastic body causing continuous plastic deformation. It assumes that an increment of mechanical work done by the external force produces an increment of strain of an element in that body. This element has maximum resistance to the deformation under the stress system and must also conform to the kinematic condition.

The upper-bound technique is built up by a trial and error process based on previous experience and now is well-established for estimates of the total mechanical work during deformation.

The upper-bound solution overestimates the pressure [38,2].

Although upper-bound techniques are for plane strain deformation it is found that axisymmetric processes have much in common with plane strain processes [2,38,137]. The pressure required in plane strain deformation is always slightly less than axisymmetric pressure [38]. Hence the overestimate tends to counteract the difference.

The load for a deformation process is found from the rate of energy dissipation [3,39,38]. The rate of energy dissipation at each velocity discontinuities is given by the product of the length of the velocity discontinuity boundary, s, the magnitude of the velocity discontinuity, u, and the shear yield strength of the material, k. Hence the total is given by summing these:

$$\frac{dW}{dt} = \sum k\, u\, s \tag{4.26}$$

The load L over half the billet using the detail of Fig. 4.11 can be shown to be [104,37]:

$$L = k(2m + \frac{2am}{R_e} + \frac{2a^2}{m \sin^2 \omega} + \frac{2aR_e}{m \sin^2 \psi} - 3a \cot \omega - 3a \cot \psi) \tag{4.27}$$

Since the extrusion load is certainly less than that predicted by $\sum kus$, this expression must be minimized. As m, ω, ψ are not independent, it is necessary to differentiate each of them. By differentiating equation (4.27) with respect to m,

$$\frac{dL}{dm} = k\,(\,2 + \frac{2a}{R_e} - \frac{2a^2}{m^2 \sin^2 \omega} - \frac{2aR_e}{m^2 \sin^2 \psi})$$

At the minimum L , this equation must be equal to zero.

$$2 + \frac{2a}{R_e} - \frac{2a^2}{m^2 \sin^2 \omega} - \frac{2aR_e}{m^2 \sin^2 \psi} = 0$$

then

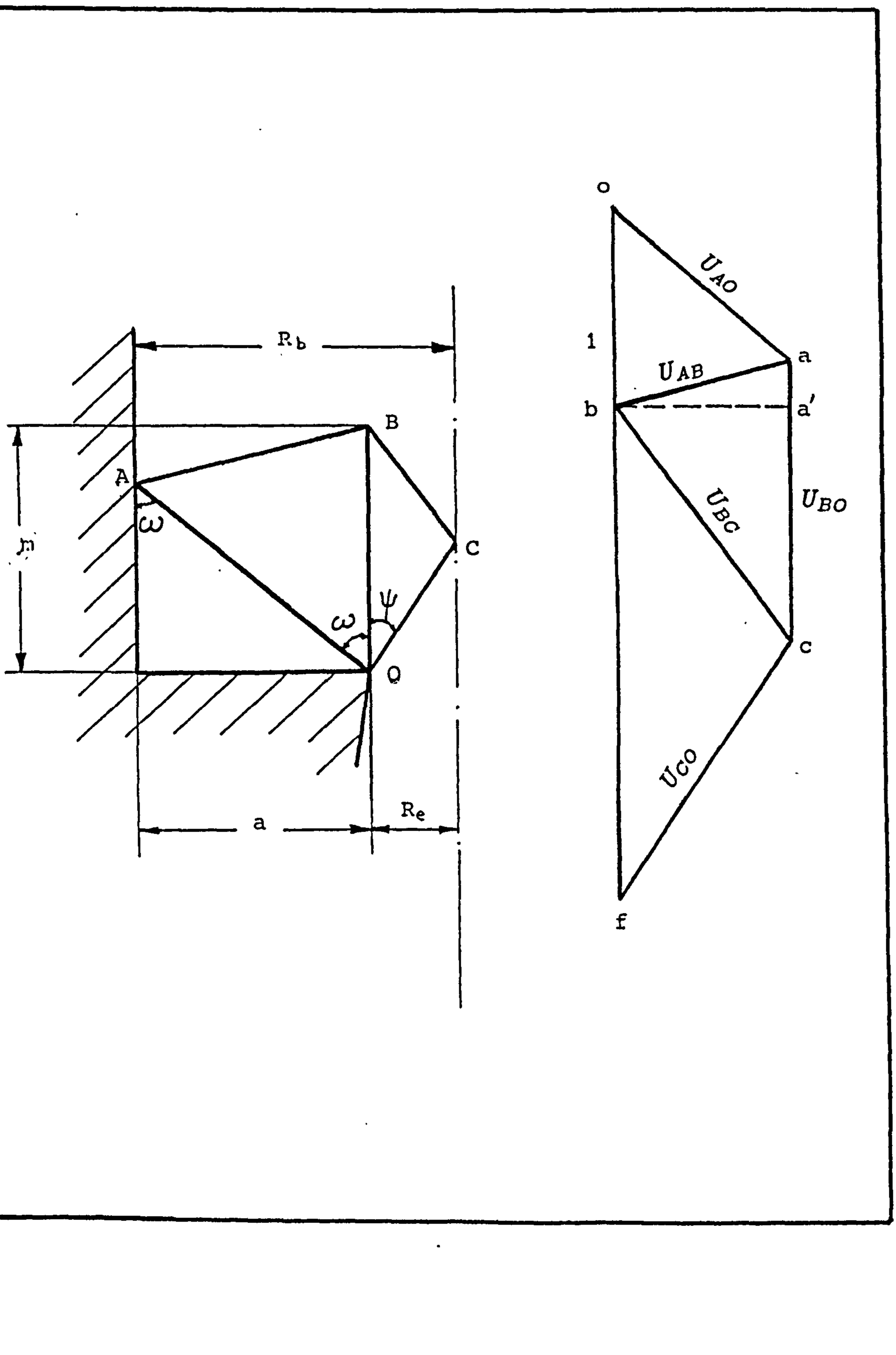

Fig. 4.11 A physical plane and corresponding hodograph during extrusion

$$m^2 = \frac{\frac{a^2}{\sin^2\omega} + \frac{aR_e}{\sin^2\psi}}{1 + \frac{a}{R_e}} \tag{4.28}$$

Differentiate with respect to ω, ψ:

$$-\frac{4a^2\cos\omega}{m\sin^3\omega} + \frac{3a}{\sin^2\omega} \doteq 0$$

$$\frac{3a}{\sin^2\psi} - \frac{4aR_e\cos\psi}{m\sin^3\psi} = 0$$

then

$$\cot\omega = \frac{3m}{4a} \tag{4.29}$$

$$\cot\psi = \frac{3m}{4R_e} \tag{4.30}$$

Obviously, ω and ψ are not independent of m, so an iteration is required to obtain accurate minimized value for ω, ψ and m, hence the minimized load. A subroutine in the computer program performs this minimization process. The value of ω, ψ and m for different extrusion ratios are given in Table 4.1. It has been assumed [2,1,39,38] that in plane strain extrusion at the extrusion ratio of 2, the angle of dead-metal zone boundary is 45°C. Here the value of ω and ψ calculated are 41.4°, close to the value of 45°C.

Using the values of ω, ψ and m to equation (4.27) the half load can be obtained:

$$L = k\,C$$

The extrusion pressure is often expressed as:

$$\frac{P}{2k} = C^*$$

Johnson [105] has made theoretical and experimental work on plane-strain extrusion in order to obtain the value of C^*. The value of C^* obtained from this calculation is consistent with Johnson's solution which is shown in Fig. 4.12 [37].

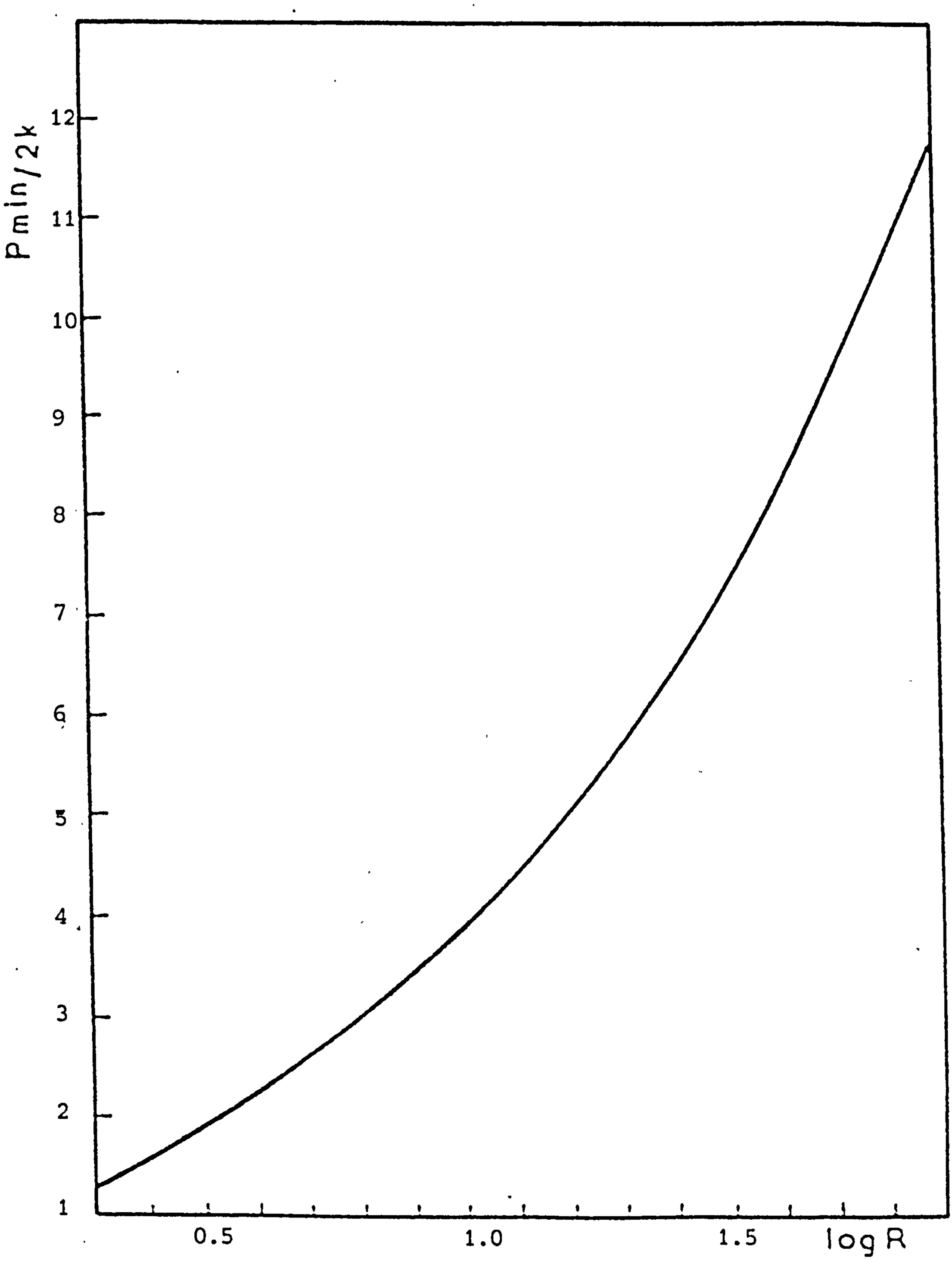

Fig. 4.12 Minimized upper-bound solution (after Johnson)

Extrusion ratio R	m	ω	ψ	C^*
2	30.2371	41.4097	41.4097	1.32288
2.2	30.1118	44.012	38.8368	1.44914
2.3	29.9787	45.1584	37.7218	1.50831
2.5	29.6261	47.2060	35.7571	1.62019
3	28.5078	51.2780	31.9481	1.87083
4	26.1861	56.7892	26.9841	2.29129
5	24.1896	60.4492	23.7956	2.64575
10	18.1422	69.2953	16.3820	3.96863
15	15.0849	73.1409	13.2628	4.94975
20	13.1800	75.4187	11.4381	5.76628
25	11.8504	76.9682	10.2052	6.48074
30	10.8554	78.1097	9.30075	7.12390
35	10.0748	78.9957	8.60075	7.71362
40	9.44144	79.7091	8.03823	8.26136
45	8.91415	80.2997	7.57337	8.77496
50	8.46631	80.799	7.18083	9.26013

Table 4.1 Values of m, ω, ψ, C^*

Table 4.1, clearly illustrates that when extrusion ratio changes, the value of ω, ψ, m and hence C^* are changed. It seems reasonable that if the extrusion ratio changes, the deformation zone shape and height change.

C^* can be computed for any ratio and typical values are shown in Table 4.1.

Summary:

The program uses regression equations based on Harwell data to find Pmax, P at any compaction distance, x, and ΔP to be obtained from the basic input data. The Gemant analysis and adiabatic heating during compaction and formation of the deformation zone allow Te and Tx to be estimated. The program then calls up C^* from the minimised upper-bound solution and is then in a position to calculate Pmin once the shear flow stress has been supplied from the stored metalworking data as shown in the next Chapter.

Chapter 5

MATERIAL PROPERTIES FOR INPUT INTO MODELS

5.1 Torsion tests and experimental observations

The flow stress of a material is related to both material properties such as chemical composition, metallurgical structure, phase morphology, grain size and to the deformation parameters [142,144,143]. These are the temperature of deformation, T, strain or degree of deformation, $\bar{\epsilon}$, and strain rate or rate of deformation, $\dot{\bar{\epsilon}}$ [91,92].

In summary:

$$\overline{\sigma} = f(T, \bar{\epsilon}, \dot{\bar{\epsilon}}, St)$$

where

St represents the microstructural condition.

In torsion testing the strain and strain rate of a solid cylindrical specimen vary linearly from zero at the centre to maximum at the surface [145]. Nadai [3,146] has given a graphical analysis for determining the value of shear stress from the type of curve shown in Fig. 5.1. The twist moment, M ,is a function of the amount of twist, θ. $M = F(\theta)$. The shear stress is a function of shear strain, γ,

$$\tau = f(\gamma)$$

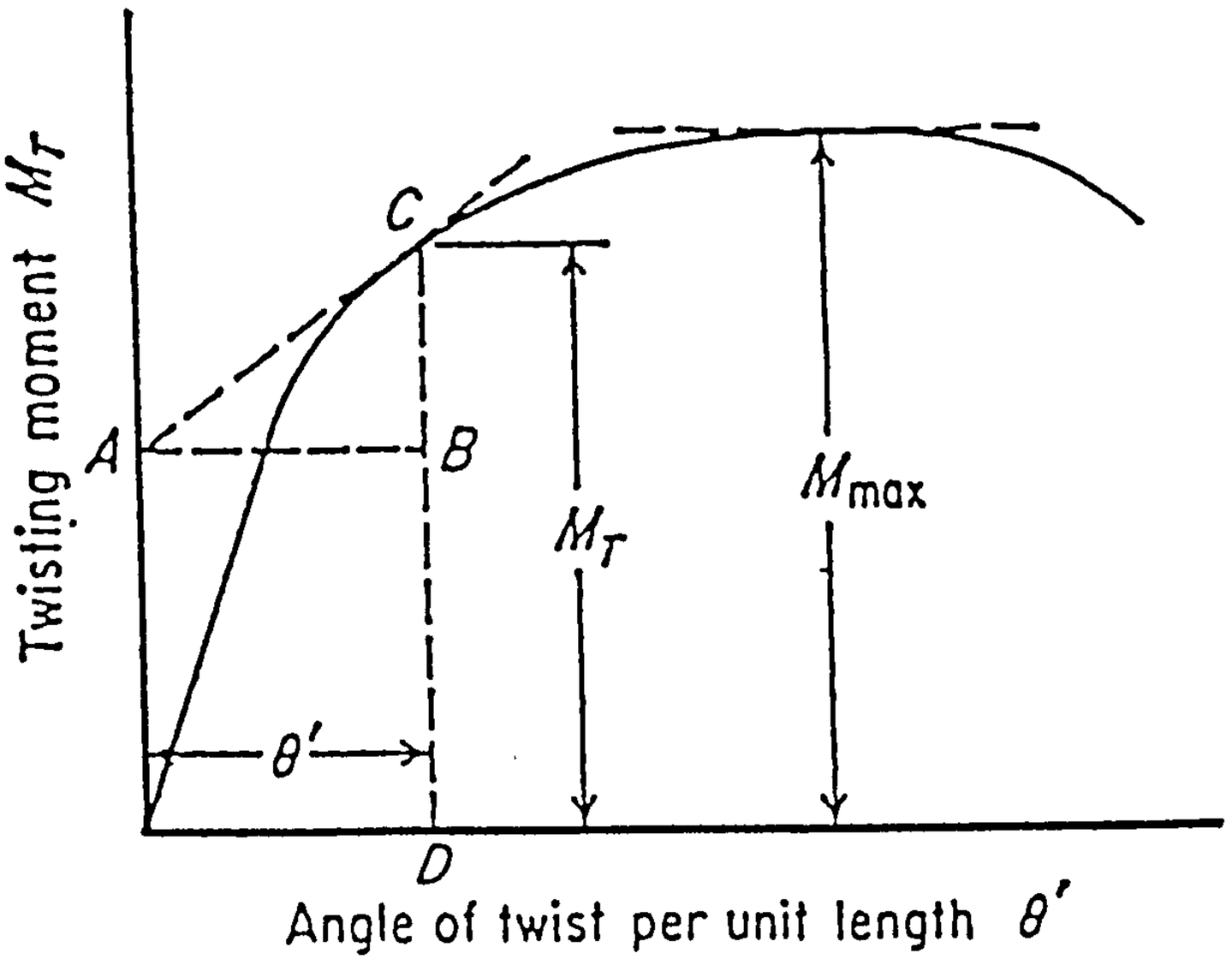

Fig. 5.1 Method of calculating shear stress from torque-twist diagram. [3]

. where

$$\gamma = r\theta$$

The twist moment, M, is given by

$$M = 2\pi \int_0^a \tau r^2 \, dr \cdot \tag{5.1}$$

With substitution of $r = \gamma/\theta$, $dr = d\gamma/\theta$,

$$M = \frac{2\pi}{\theta^3} \int_0^{\gamma_a} f(\gamma)\gamma^2 \, d\gamma$$

$$M\theta^3 = 2\pi \int_0^{\gamma_a} f(\gamma)\, \gamma^2 \, d\gamma \tag{5.2}$$

Since

$$\gamma_a = a\theta$$

M is also a function of θ. And

the maximum shear stress in the specimen at the outer fiber is

$$\tau_a = f(\gamma_a) = f(a\theta)$$

Differentiating equation (5.2) with respect to θ

$$\frac{d}{d\theta}(M\theta^3) = 2\pi f(a\theta)a^3\theta^2$$

With

$$\frac{d}{d\theta}(M\theta^3) = 2\pi a^3\theta^2\tau_a$$

$$\tau_a = \frac{1}{2\pi a^3\theta^2}\frac{d}{d\theta}(M\theta^3) \tag{5.3}$$

The shearing stress, τ_a, corresponding to the unit shear $\gamma_a = a\theta$ being proportional to the quantity dependent on θ, and according to Fig. 5.1.

$$\frac{1}{\theta^2}\frac{d}{d\theta}(M\theta^3) = \theta\frac{dM}{d\theta} + 3M = \overline{CB} + 3\overline{CD} \tag{5.4}$$

The shear strain, γ , and strain rate, $\dot{\gamma}$, are

$$\begin{aligned} \gamma &= \frac{a}{l}\theta \\ \dot{\gamma} &= \frac{a}{l}\dot{\theta} \end{aligned} \tag{5.5}$$

where

M— maximum torque

a— radius of the specimen

l— gauge length of the specimen

θ— amount of twist in the specimen

The torque versus twist curves in the torsion tests presented show that the magnitude of $\overline{CB}$ in equation (5.4) does not take great proportion compared with the maximum torque. So the shear stress is obtained by using a simplification of the Fields-Backofen relation [3,147,148].

$$\tau = \frac{3M}{2\pi a^3} \tag{5.6}$$

Torsion data have been shown in Figs. 3.2 – 3.12. All of the curves demonstrate an initial peak in flow stress followed by a 'steady-state' condition in which the strain rate, temperature and flow stress are approximately constant. The height and width of the peak increase markedly with increasing strain rate and decreasing temperature and are insignificant at the highest temperatures and lowest strain rates. The time and strain taken to reach the maximum value of the torque increase with increasing strain rate at a given temperature. At higher strain rates it requires more strain to reach the peak flow stress [69]. At higher strain rates the dislocation generation rate is fast enough to initially outweigh the recovery process and the recovery process does not balance the work hardening rate until higher dislocation densities have been achieved. Once the recovery process balances the work hardening rate at high dislocation densities it then momentarily outweighs it and

the flow stress falls to the steady-state value. At temperatures below 400°C, (see Fig.3.2 – Fig.3.4) the magnitude of the peak increases with increasing strain rate and gives more evidence of this effect. The strain for the occurrence of the onset of the steady-state deformation increases with increasing strain rate and decreasing temperature. The total strain to failure is highly dependent on the metallurgical condition. Fig. 3.14 shows the total strain as a function of temperature at various strain rates. It shows that the material can undergo the largest strain at temperatures around 400°C regardless of strain rate. This phenomenon indicates that the material has a ductility maximum at about 400°C. This maximum is due to microstructure changes and will be discussed in Chapter 8.

The shear yield stress and strain obtained from torsion tests are commonly converted to tensile stress and strain using Von Mises yield criterion [99,149,150,151].

$$\begin{aligned} \sigma &= \sqrt{3}\tau \\ \epsilon &= \gamma/\sqrt{3} \\ \dot{\epsilon} &= \dot{\gamma}/\sqrt{3} \end{aligned} \tag{5.7}$$

5.2 Plane strain compression tests and experiment results for solid and powder

The specimens machined from hot compacted powders showed insufficient resistance to the strain imposed in torsion testing and failed before flow stresses could be established.

Hence plane strain compression tests were used. Compression stress, strain and strain rate are obtained from the tests [3] as:

$$\begin{aligned} \sigma_c &= \frac{L}{Bb} \\ \epsilon_c &= ln\frac{h_0}{h_1} \\ \dot{\epsilon}_c &= \frac{V_c}{h_0} \end{aligned} \tag{5.8}$$

The flow stress, true strain, strain rate and temperature rise are evaluated

from the transient measurements made during tests. Computer control of V_c enabled constant strain rates to be achieved. The curves obtained from plane strain compression tests present the features of hot deformation of powder billets well. Fig. 3.23 shows the compression stress vs. strain curves with different temperatures at the highest strain rate of 6.9/sec.. The stresses increase sharply with decreasing testing temperatures. The main feature of these curves is that there is a rapid rise in stress to the maximum, then a drop, followed by the steady-state conditions. However, at this high strain rate the magnitude of the drop in stress decreases with decreasing temperature. At the lowest temperature, the drop is not significant at all and is followed by an "apparent" strain softening. This could be due to a significant temperature rise because the energy input into this specimen is the highest and it occurs at the highest strain rate. At lower strain rates the opposite effect occurs (Fig. 3.21, Fig. 3.22). Peaks are observed at the lower temperatures and not the high temperatures. The highest drops (relatively) occur at the highest temperatures and highest strain rate. After the drop the flow stress usually increases gradually with strain in the steady-state stage.

Fig. 3.13 shows the data extracted from the stress strain curves for powder compression replotted as the maximum stress versus strain rate at various temperatures. For most results the maximum stress was indistinguishable from the steady-state stress. At temperatures above 500°C and strain rates above 3.4 the flow stresses recorded no longer follow the general trends of increasing flow stress with increasing strain rate and decreasing temperature. This is thought to be due to the onset of incipient melting and is discussed later in Section 8.2.2. At the two highest testing temperatures the expected increased strain rate dependence is seen.

The compression stress and strain can be converted using the Von Mises criterion [170,179].

$$\sigma = \frac{\sqrt{3}}{2}\sigma_c$$

$$\epsilon = \frac{2}{\sqrt{3}} \epsilon_c$$

$$\dot{\epsilon} = \frac{2}{\sqrt{3}} \dot{\epsilon}_c \tag{5.9}$$

5.3 Combining torsion and compression data

Flow stresses for solid material are obtained from both torsion and compression testing. Although hot torsion and plane strain compression tests are recommended as standard testing methods, there are some disadvantages for each testing method. In hot torsion testing, when a specimen is twisted, specimen tends to be shortened but the two ends of the specimen are fixed, so an axial tensile stress exists in the specimen. This is often ignored. In compression testing the effect of friction between platen and specimen spread and barrelling have to be accounted for. However, shear stresses for solid material obtained from hot torsion tests and compression tests are in good agreement as shown in Fig. 3.12 and Table 5.1. Von Mises criterion is used for the combination.

Plane strain compression test data for powder is listed in Table 5.2 and is plotted in a similar form as Fig. 3.13.

5.4 The power law relationship between stress and strain rate

The characteristics of the relationship between stress and strain rate has been extensively investigated by numerous workers [60,73,152]. The results from present work are in agreement with the others and follow the established relationships.

At low stress, a power law relationship is followed:

$$\dot{\epsilon} = A_1 \sigma^n \tag{5.10}$$

where

A_1, n are constants.

Code	T°C	$\dot{\gamma}$	Γ NM	τ MN/m^2	σ MN/m^2	Z	sinh($\alpha\sigma$)
6	550	0.864	1.47	16.39	28.39	$6.76e^{09}$	0.32
8	550	3.456	1.59	17.67	30.60	$2.70e^{10}$	0.34
5	500	0.864	2.23	24.83	43.00	$3.06e^{10}$	0.49
4	500	1.728	2.16	24.01	41.58	$6.11e^{10}$	0.47
3	500	3.456	2.52	28.13	48.73	$1.22e^{11}$	0.56
2	497	6.912	3.18	35.48	61.45	$2.69e^{11}$	0.72
10	450	0.864	2.82	31.42	54.43	$1.70e^{11}$	0.64
9	450	1.728	3.20	35.59	61.64	$3.40e^{11}$	0.73
2-1	450	3.456	3.31	36.87	63.90	$6.81e^{11}$	0.76
1	450	6.912	3.68	40.96	70.95	$1.36e^{12}$	0.86
11	394	1.728	4.22	46.94	74.24	$3.16e^{12}$	1.02
12	411	3.456	4.14	46.10	79.83	$3.10e^{12}$	1.00
13	400	6.912	5.32	59.20	102.5	$9.79e^{12}$	1.38
14	400	13.82	5.95	66.30	114.8	$1.96e^{13}$	1.63
18	375	1.728	5.02	56.00	97.00	$7.36e^{12}$	1.28
17	382	3.456	5.37	59.80	103.6	$1.07e^{13}$	1.40
16	375	6.912	5.56	61.90	107.2	$2.94e^{13}$	1.47
15	375	13.82	5.94	66.20	114.7	$5.89e^{13}$	1.62
19	350	1.728	6.08	67.70	117.3	$2.42e^{13}$	1.68
20	350	3.456	6.78	75.50	130.8	$4.83e^{13}$	2.00
20C	350	11.90		68.66	118.9	$1.66e^{14}$	1.71
22	350	13.82	8.30	92.45	160.1	$1.93e^{14}$	2.82
25	300	3.456	9.1	101.3	175.53	$7.12e^{14}$	3.37
19C	300	5.889		103.5	179.27	$1.21e^{15}$	3.52
18C	300	11.95		105.0	181.87	$2.46e^{15}$	3.63
16C	250	1.386		156.0	270.20	$7.03e^{15}$	9.74
17C	250	11.95		166.9	289.15	$6.06e^{16}$	12.0
27	250	6.912	14.64	163.0	282.3	$3.50e^{16}$	11.14
26	250	13.82	15.57	173.4	300.3	$7.01e^{16}$	13.59

C means from compression test.

Table 5.1 Solid torsion and compression data

No.	T°C	$\dot{\bar{\epsilon}}$	$\bar{\epsilon}$	k MN/m^2	$\bar{\sigma}$ MN/m^2	Z	sinh($\alpha\sigma$)	ΔT^*
1	550	0.8	0.8	4.5	7.79	$6.01e^{07}$	0.12	0.5
2	550	3.4	1.6	18.94	32.8	$2.56e^{08}$	0.52	1.37
3	550	6.9	2.4	17.75	30.74	$5.19e^{08}$	0.48	1.29
4	500	0.8	0.8	17.	29.44	$1.94e^{08}$	0.46	1.23
5	500	3.4	1.6	33.75	58.46	$8.26e^{08}$	1.00	2.45
6	500	6.9	2.4	28.89	50.04	$1.68e^{09}$	0.83	2.09
7	400	0.8	0.8	36.37	62.99	$3.42e^{09}$	1.10	2.64
8	400	3.4	1.6	43.035	74.54	$1.45e^{10}$	1.38	3.12
9	400	6.9	2.4	45.78	79.3	$2.95e^{10}$	1.51	3.32
10	300	0.8	0.8	57.74	100.01	$1.64e^{11}$	2.16	6:19
11	300	3.4	1.6	63.75	110.42	$6.90e^{11}$	2.56	5.62
12	300	6.9	2.4	68.26	118.23	$1.42e^{12}$	2.91	7.3
13	250	0.8	0.8	77.	133.37	$1.98e^{12}$	3.70	8.25
14	250	3.4	1.6	88.	152.42	$8.42e^{12}$	4.97	9.43
15	250	6.9	2.4	92.08	159.49	$1.71e^{13}$	5.54	9.86

* Δ T is temperature rise due adiabatic heating.

Table 5.2 Powder compression test data

By plotting $ln\dot{\epsilon}$ versus $\ln\sigma$ at constant temperature, the value of n which is a measure of the strain rate sensitivity can be obtained.

Fig. 5.2 is the power law plot of torsional flow stresses for solid at low stresses and high temperatures. The constant n obtained is 5.52.

Fig. 5.3 shows the power law expression of the compression flow stress data at high temperatures and low stresses. The constant n is obtained to be equal to 5.51. The data at 550°C is a poor fit and is considered to be influenced by incipient melting. If the best set of parallel lines (n is constant) is drawn through the data, good agreement in the values of n is obtained between the two test methods and materials.

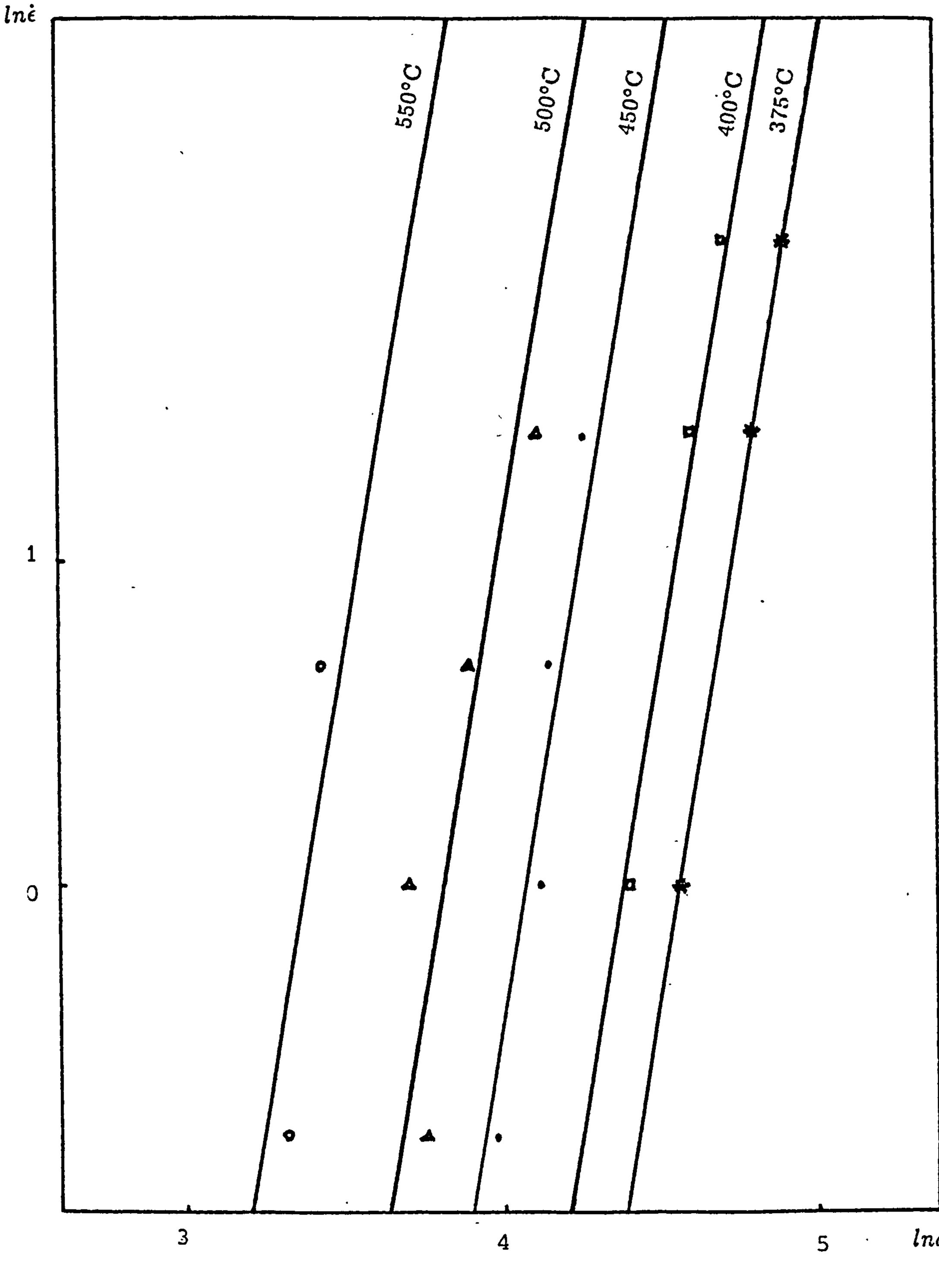

Fig.5.2 The power law expression of torsional flow stress data (solid)

5.5 Exponential relationship between stress and strain rate

Results from torsion and plane strain compression tests can also be modeled by the established exponential relationships.

$$\dot{\epsilon} = A_2 exp^{\beta\sigma} \tag{5.11}$$

where

A_2, β are constants.

By plotting $ln\dot{\epsilon}$ versus σ, parallel straight lines can be obtained for different temperatures and β is the slope.

Fig. 5.4 is the exponential expression of torsion and plane strain compression flow stress data for solid material. β is obtained to be 0.06.

Fig. 5.5 is the exponential expression of plane strain compression flow stress data for powder material. β is equal to 0.08. The agreement between material types is not as good. The particulate nature appears to lessen the strain rate effects at low temperature.

5.6 The general relationship of flow stress and strain rate

As the flow stress changes with temperature and strain rate, a more general relationship covering a wide range of stress and temperature is given by Sellars and Tegart [152,136]

$$\dot{\epsilon} = A_3[\sinh(\alpha\sigma)]^{n'} exp(-\frac{\Delta H}{RT}) \tag{5.12}$$

where

A_3, α, n'—constants.

ΔH— activation energy

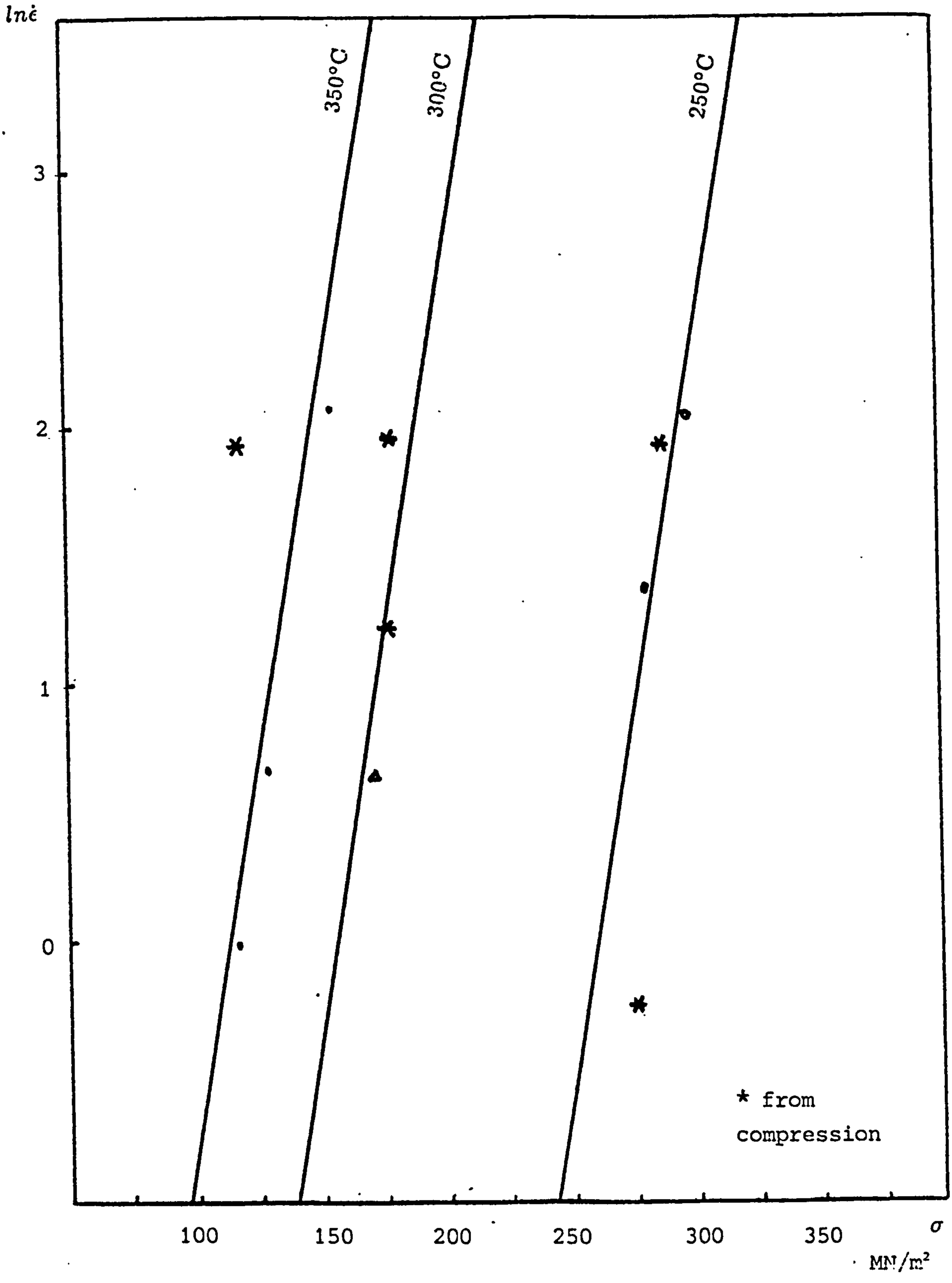

Fig. 5.4 The exponential expression of torsion and compression flow stress data (solid)

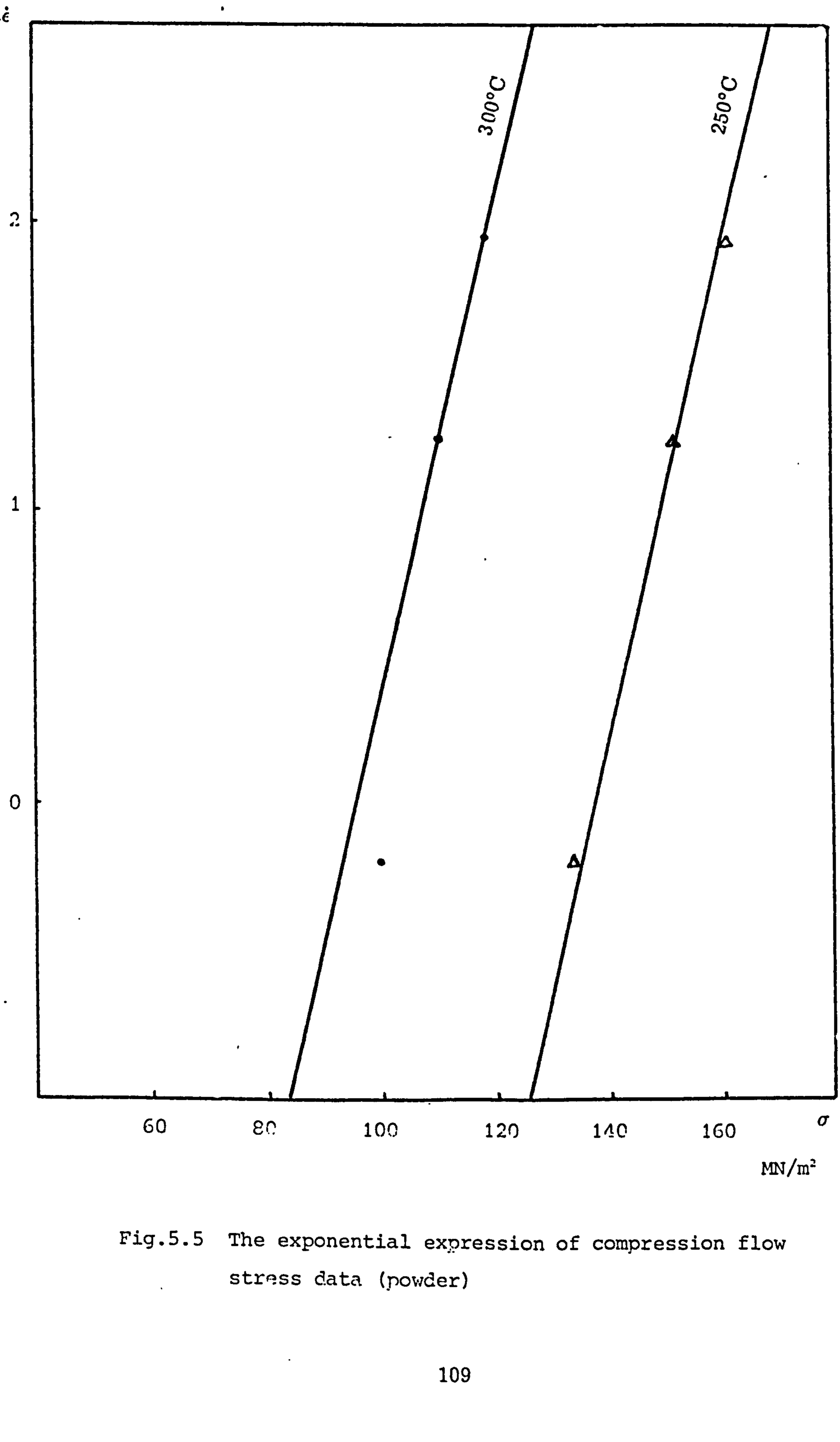

Fig.5.5 The exponential expression of compression flow stress data (powder)

R— Gas constant

At low stress ($\alpha\sigma < 0.8$) [3,78,60,156,170] equation (5.12) approximates to equation (5.10) representing the power law relationship.

$$\begin{aligned} \dot{\epsilon} &= A_3\sigma^n exp(-\frac{\Delta H}{RT}) \\ &= A_4\ \sigma^n \end{aligned}$$

At high stress ($\alpha\sigma > 1.2$) equation (5.10) approximates to the exponential relationship, equation (5.14).

$$\begin{aligned} \dot{\epsilon} &= A_3 exp^{\beta\sigma}\ exp(-\frac{\Delta H}{RT}) \\ &= A_4 exp^{\beta\sigma} \end{aligned}$$

Since

$$sinh(\alpha\sigma) = \frac{e^{\alpha\sigma} - e^{-\alpha\sigma}}{2}$$

when

$$\alpha\sigma > 1.2$$

$$e^{-\alpha\sigma} \rightarrow 0$$

so

$$sinh(\alpha\sigma) \simeq \frac{e^{\alpha\sigma}}{2}$$

Hence

$$\dot{\epsilon} = A_3[sinh(\alpha\sigma)]^n\ exp(-\frac{\Delta H}{RT})$$

becomes

$$\dot{\epsilon} = A_4[\frac{e^{\alpha\sigma}}{2}]^n$$

and

$$\dot{\epsilon} = A_5[e^{\alpha\sigma}]^n$$

This is of the same form as

$$\dot{\epsilon} = A_4 exp^{\beta\sigma}$$

therefore

$$n\sigma = \beta$$

and

$$\alpha = \frac{\beta}{n}$$

with

$$\alpha = 0.011 \qquad for\ solid$$

$$\alpha = 0.015 \qquad for\ powder$$

This expression indicates that hot working mechanisms are thermally activated processes and the value of ΔH indicates the type of mechanism [69].

In equation (5.10), assuming that the hot working is performed under constant flow stress and the activation energy is constant covering a wide range of temperature, then equation (5.10) can be expressed as:

$$\begin{aligned} \dot{\epsilon} &= A_3 f(\sigma) exp(-\frac{\Delta H}{RT}) \\ &= A_4 exp(-\frac{\Delta H}{RT}) \end{aligned}$$

hence

$$ln\dot{\epsilon} = lnA_4 - \frac{\Delta H}{R}\frac{1}{T}$$

A plot of $ln\dot{\epsilon}$ versus $\frac{1}{T}$ can be obtained from the experimental data and the slope is $\frac{\Delta H}{R}$. ΔH can then be obtained.

Fig. 5.6 is the plot for solid material from experimental data which shows strain rate as a function of reciprocal absolute temperature at a constant flow stress. It can be seen that the data fits the linear relationship as expected. The activation energy obtained from these torsion and compression tests for solid aluminium alloy 2014 is 159.6 kJoule/mole.

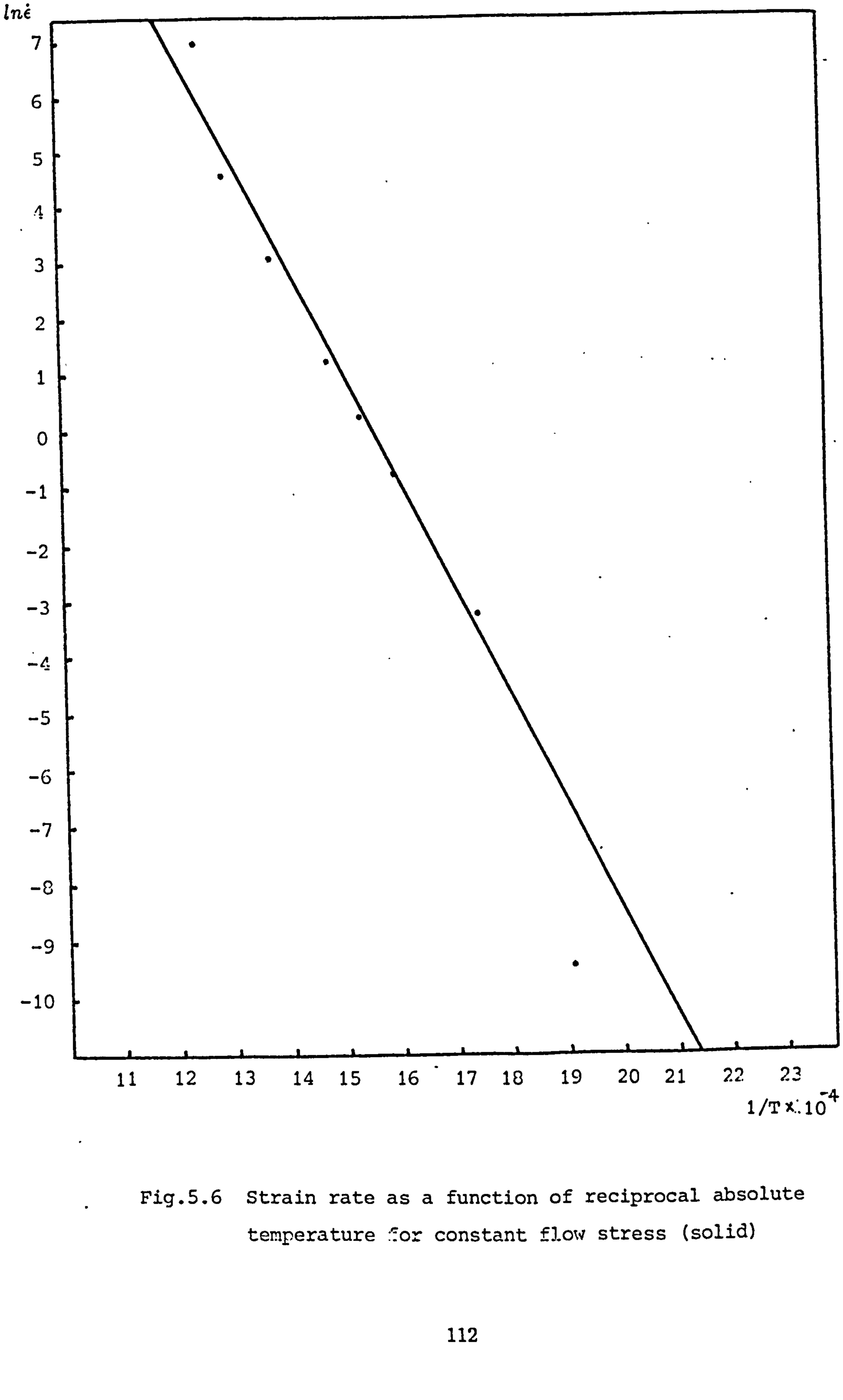

Fig.5.6 Strain rate as a function of reciprocal absolute temperature for constant flow stress (solid)

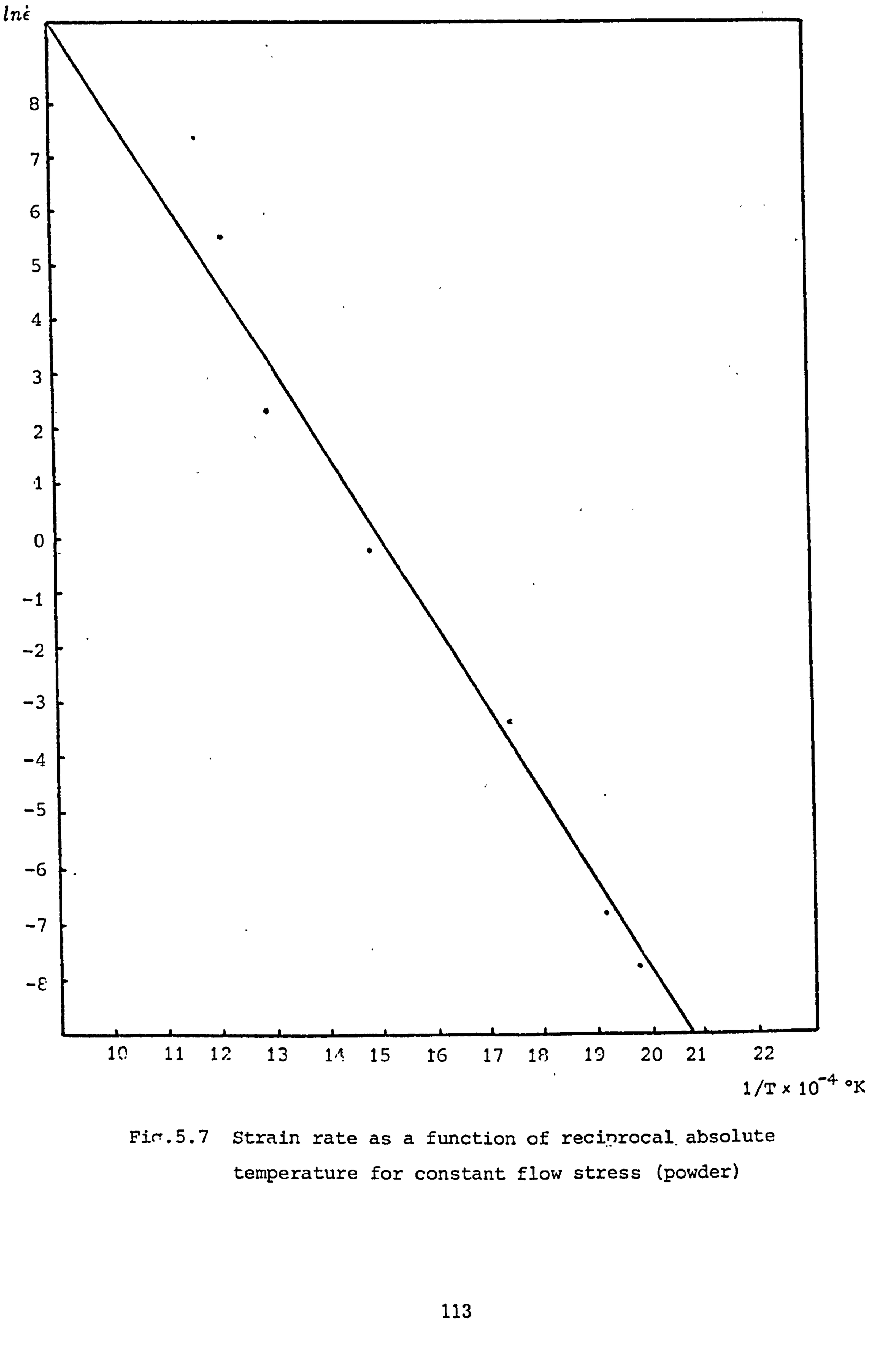

Fig.5.7 Strain rate as a function of reciprocal absolute temperature for constant flow stress (powder)

Fig. 5.7 is a similar plot for the data from compression tests as the powder alloy. Here $\Delta H = 124.1\ kJoule/mole$. These values agree with the extensive previous work that has been done in this area (Table 5.3). The values are all in a very narrow band around 138.1 kJoule/mole (self-diffusion in aluminium [78,171,60,156]). This indicates that the hot deformation of aluminium and aluminium alloy is a thermally activated process similar to that occurring in creep and the mechanism of deformation is also diffusion based. The rate controlling process is either the climb of edge dislocations or the cross-slip of screw dislocations [165,167].

5.7 Zener–Hollomon parameter in hot deformation

Equation (5.10) can be made even more general by introducing the Zener–Hollomon parameter, Z, [153] which is the temperature corrected strain rate [69] and is constant in a hot working test since $\dot{\epsilon}$ and T are held constant. Many workers [60,81,22,32,54,69] have found that the effects of temperature and strain rate can be combined using:

$$Z = \dot{\epsilon}\, exp(\frac{\Delta H}{RT})$$

Since the activation energies for solid and powder materials have been obtained and the deformation temperature has been obtained in Section 4.2.4, estimating the strain rate for an extrusion allows Z to be found.

During extrusion, the mean strain rate is obtained from [139,54,3,43]:

$$\dot{\epsilon} = \frac{6V \tan\omega\ lnR\ D^2}{(D^3 - D_e^3)} \qquad (5.13)$$

The variables in this formula are all given by the extrusion conditions, so the strain rate, $\dot{\epsilon}$, can be easily calculated.

The value obtained for Z in this work is more accurate than most previous work because the extrusion temperature can be predicted from the computer model with its iteration.

Alloy	Activation energy (kJoule/mole)	References
Pure Al	174.9(Extrusion)	[81,171]
Al-Alloy	156-164	[22]
Al-Alloy	160 (Extrusion)	[32]
Pure Al	146-151 (Creep)	[171]
Al	148.5 (High temp.creep,self-dif.)	[172]
Al	117 (Low temperature creep)	[172]
Pure Al	156 (Compression,creep,torsion)	[85,54]
Al	138-151 (Creep)	[60,156,78]
Al	155 (Hot working)	[60,78]
Al	125.5-182 (Hot working)	[156]
Al	183-229 (Recovery)	[156]
Al	142-250 (Recrystallization)	[156,78]
Al-5Mg	161.2	[76]
Pure Al	155	[136]
Al	125.5-180 (Torsion)	[58]
Al	155 (Creep)	[58]
AA 1100	162.8	[157]
AA 2014	134.4	[157]
Al-Si	140	[158]
AA 5083	162.8 (Torsion)	[59,159]
Al	150	[53,59]
Al-5Mg-0.8Mn	162 (Extrusion)	[59]
Al-5Mg-0.8Mn	178 (Tensile)	[59]
Pure Al	214	[119]
Al	146 (Torsion)	[160,164]
Al 2014	142 (Torsion)	[12]
Pure Al	158.7 (Torsion)	[155]
Al	150 (Creep)	[165]
Al	146.6 (Self-diffusion)	[165]
Pure Al	148.5 (High temperature creep)	[167]
Pure Al	115 (Low temperature creep)	[167]
Al-Mg	159 (Torsion)	[154]
Al	150 (Torsion)	[140]
Pure Al	138 (Self-diffusion)	[78,171,60,156]
Al-4Mg	137 (Compression)	[168]
AA 3003	165 (Torsion)	[166]
AA 3004	193.8 (Torsion)	[166]
Al	156.5 (Extrusion)	[54]
Al	154 (Compression)	[54]

Table 5.3 Activation energy of aluminium alloys

This value represents the temperature compensated strain rate at the particular given strain rate and the working temperature in the extrusion.

Since:

$$Z = \dot{\epsilon}\, exp(\frac{\Delta H}{RT}) \ .$$

and

$$\dot{\epsilon} = A_3[\sinh(\alpha\sigma)]^{n'} exp(-\frac{\Delta H}{RT})$$

Hence

$$Z = A_3[\sinh(\alpha\sigma)]^{n'} \qquad (5.14)$$

This equation represents the relationship between stress, strain rate and Z. Z and α have been obtained already.

Taking natural logarithm of equation (5.14)

$$\ln Z = \ln A_3 + n' \ln [\sinh(\alpha\sigma)]$$

By plotting $\ln Z$ versus $\ln [\sinh(\alpha\sigma)]$ from the experimental data, the constants A_3 and n' can be obtained.

Fig. 5.8 is the plot for solid material which represents the relationship between flow stress and temperature compensated strain rate. This figure displays that the data fits a linear relationship between the Zener–Hollomon parameter and the flow stress which can cover a wide range of temperatures. Hence the data from a modest number of metalworking tests can be extrapolated and stored numerically using the constants.

From Fig.5.8 A_3 and n' for solid are:

$$A_3 = 2.38 * 10^{12}$$

$$n' = 5.1$$

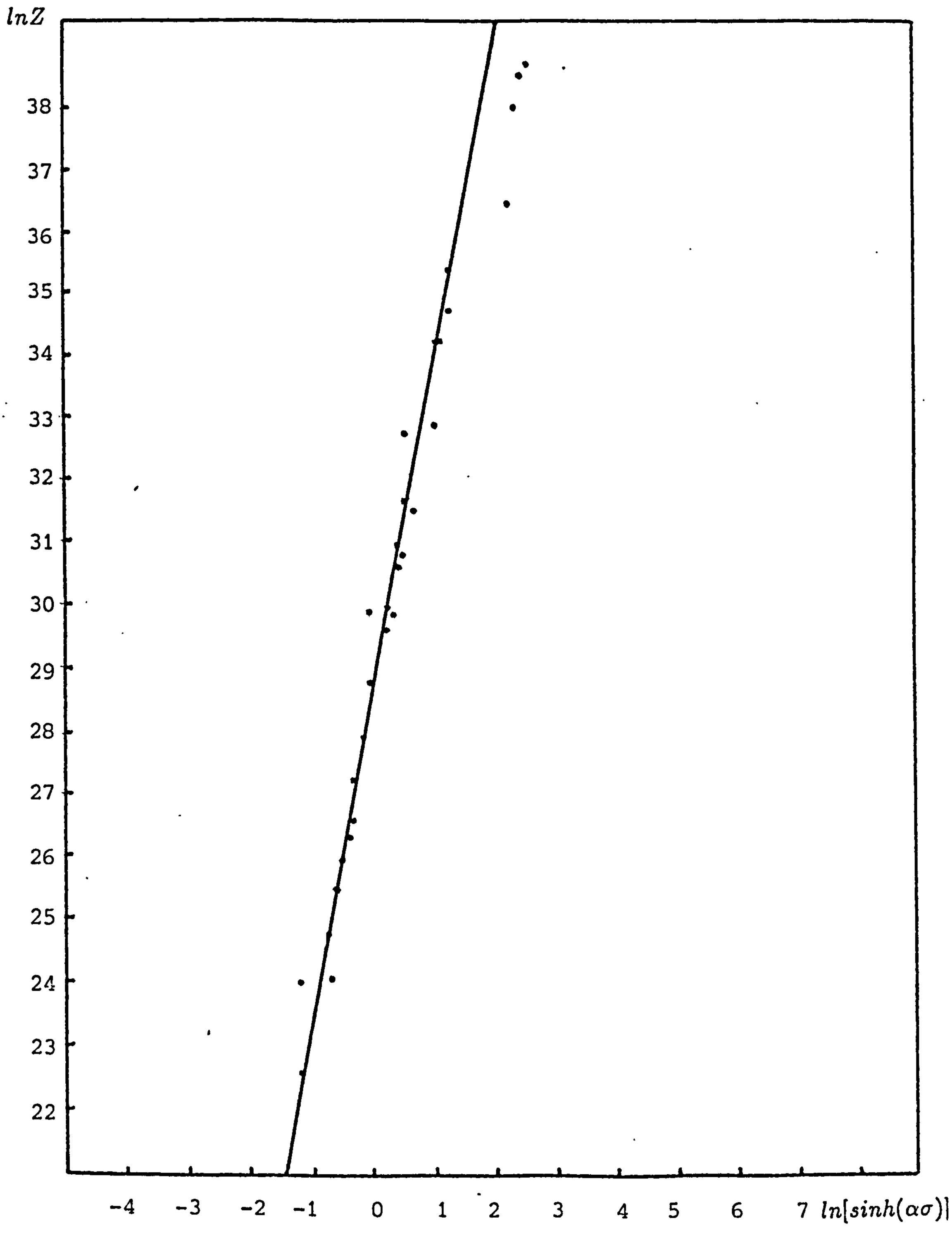

Fig.5.8 The relationship between flow stress and temperature compensated strain rate (solid)

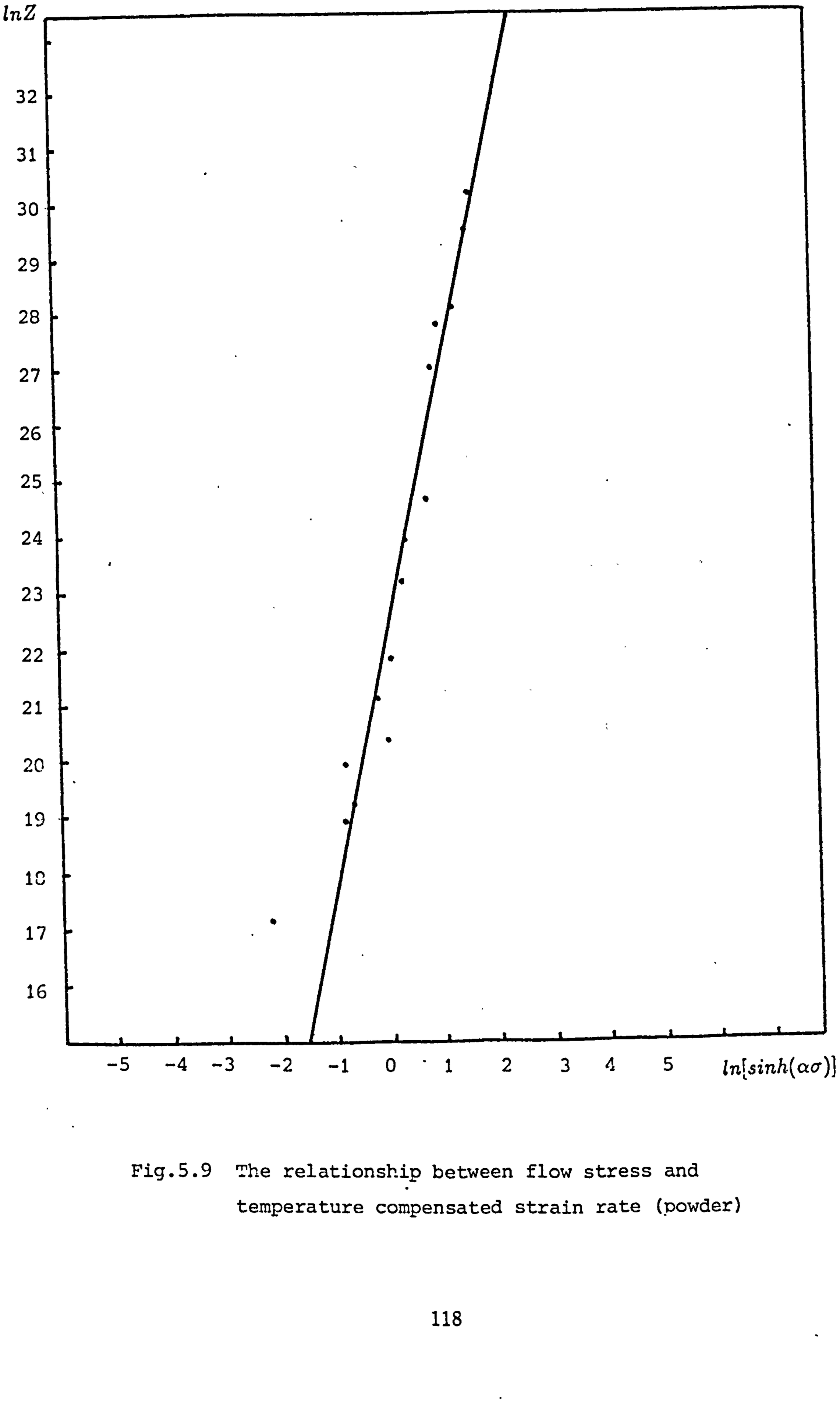

Fig.5.9 The relationship between flow stress and temperature compensated strain rate (powder)

Alloy	n	$\beta\ (m^2/MN)$	$\alpha\ (m^2/MN)$	n'	ref.
Al	5			4.67	[60]
Al	4.7			4.55	[152]
Al			0.0883	3.05	[8]
Pure Al				4.45	[171]
Pure Al	4.6			4.6	[136]
Al-2014			0.03251	3.35	[12]
Al-2014(s)	5.52	0.06	0.011	5.1	Here
Al-2014(p)	5.51	0.08	0.015	4.5	Here

Table 5.4 Value of constants

Fig.5.9 is the $\ln Z$ versus $\ln[sinh(\alpha\sigma)]$ plot for powder and A_3, n' are obtained as:

$$A_3 = 5.91 * 10^9$$

$$n' = 4.5$$

Table 5.4 compares the values for the relevant constants in this and other work.

Although the temperature changes in extrusion have been calculated the temperature changes in hot working tests have been ignored for the following reasons. It is well known that during deformation that the major part of mechanical work is converted to heat and adiabatically heats the specimen. It is reported [151] that a 15°C increase in temperature can occur in torsion testing. In the present work calculations based on adiabatic conditions, even ignoring heat losses to the specimen ends gives the maximum temperature rise as 25°C. It was therefore ignored.

In compression tests, a proportion of the mechanical work is also converted to heat and assumed to heat the specimen adiabatically. This temperature rise is also listed in Table 5.2 as ΔT^* . It is less than 10°C and therefore all temperature rises were ignored.

5.8 Calculation of shear stress at any temperature and strain rate

Since ΔH, A_3 and n' have been obtained for both solid and powder material their values can be used to obtain the flow stress at any strain rate and temperature by using the equation:

$$Z = A_3 \sinh(\alpha\sigma)^{n'}$$

From this equation, the value of $\ln[sinh(\alpha\sigma)]$ can be found.

Remember:

$$\sinh(\alpha\sigma) = \frac{e^{\alpha\sigma} - e^{-\alpha\sigma}}{2} \tag{5.15}$$

and the solution to this equation is [37]:

$$\sigma = \frac{1}{\alpha} \ln(e^v + \sqrt{e^{2v} + 1}) \tag{5.16}$$

Where

$$v = \ln[\sinh(\alpha\sigma)]$$

This flow stress can then be converted to shear stress using Von Mises criterion as before and the shear stress can be used in the upper-bound solution for the prediction of extrusion pressure. The program performs all the calculations.

5.9 The effects of data "smoothing"

The constants A_1, A_2, A_3, n, β, α, n', ΔH obtained by converting the experimental data to the hot working equations may demonstrate the effect of data smoothing. Once obtained these constants are used to calculate the shear stress at any particular temperature and strain rate as described in Section 5.8. The graphical methods used to determine these constants mean that the data is smoothed. To check this the interpolated and extrapolated data is compared with the actual data in Figs. 5.10 and 5.11. The graphs for both solid and powder materials show

that the calculated shear stresses are quite close to the actual shear stresses. Since both sets of data are close to a 45°line this indicates that no systematic errors have been introduced in the data processing and that the equation is accurate over the range of shear stresses employed.

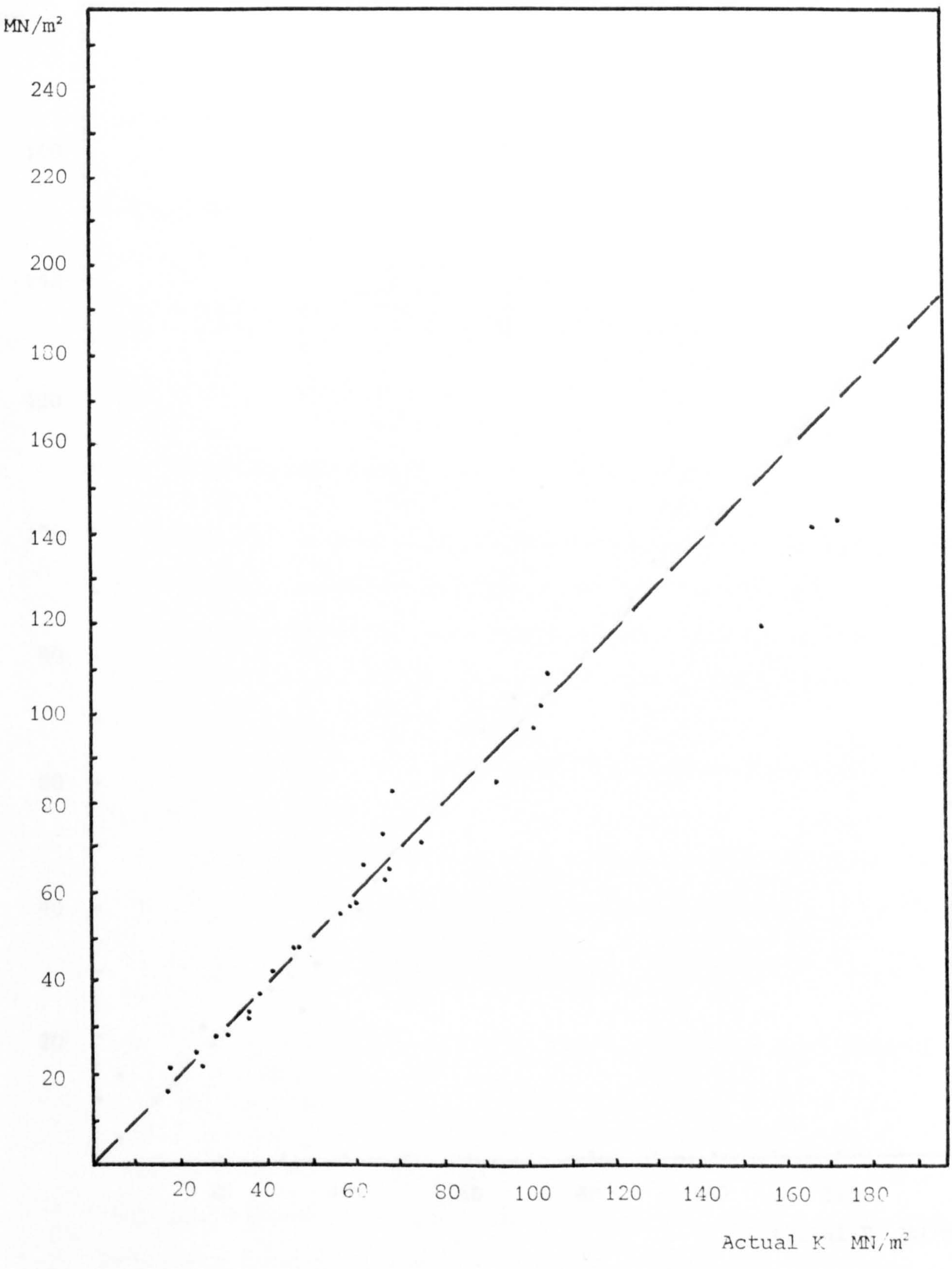

Fig. 5.10 Comparison of calculated k with actual k (solid)

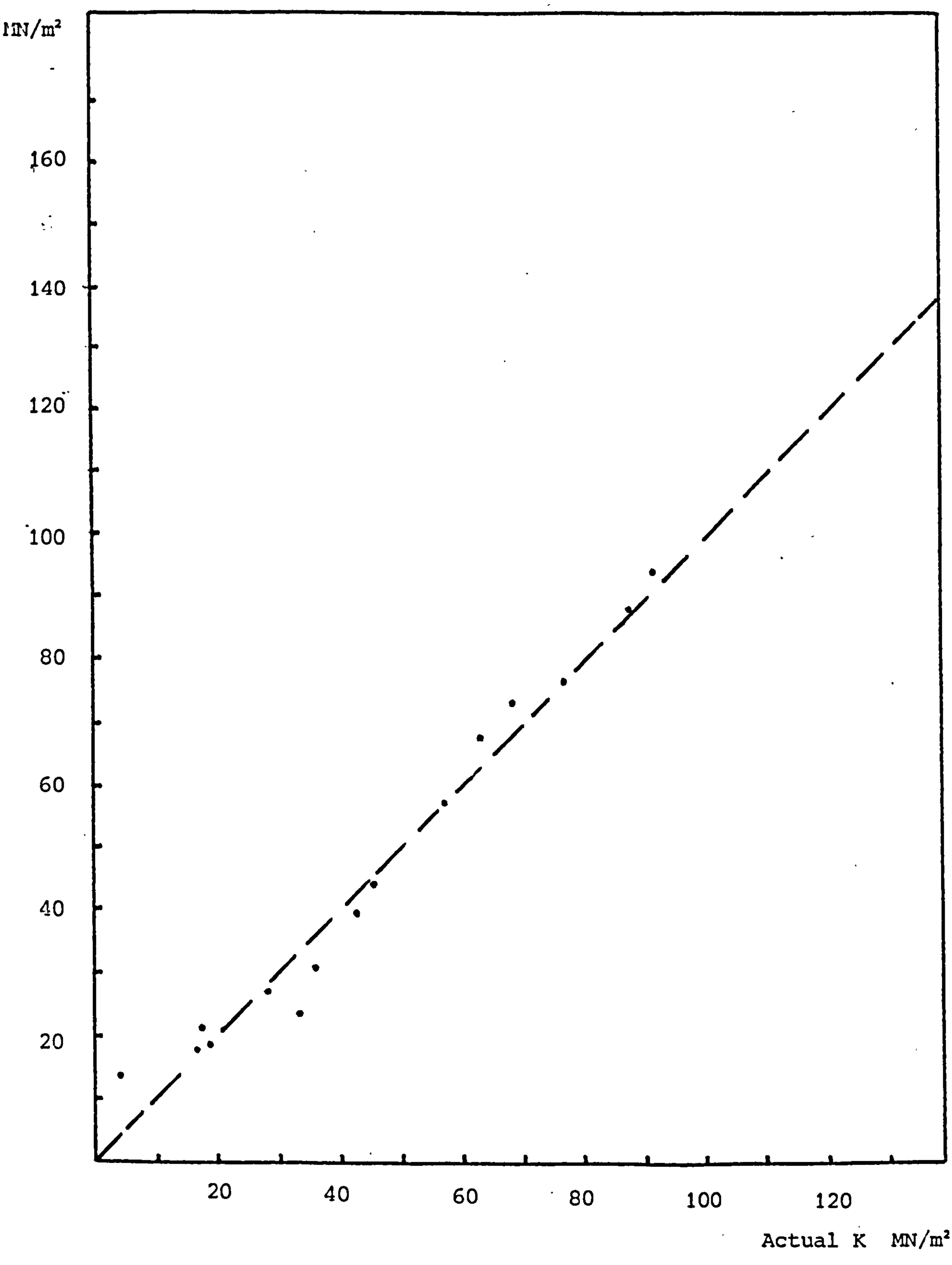

Fig.5.11 Comparison of calculated k with actual k (powder)

Chapter 6

APPLICABILITY OF MODELS

6.1 Independant checks on the model

The usefulness of the model which combines regression analysis, thermal analysis, upper-bound solutions and metalworking data has been monitored in several ways.

1. Comparison of microstructures in extruded products with those from metalworking test specimens using the thermal model to link the detail observed (Chapter 8 and 9).

2. Examination of the exact temperature Tx which is associated with the hot shortness limit (Chapter 7).

3. Comparison of how the shear yield stress from metalworking tests and upper-bound solutions relate to the actual steady-state extrusion pressure (this Chapter).

6.2 Comparison of upper-bound solutions and steady-state pressure

Minimised upper-bound solutions have been accepted as accurate estimates for axisymmetric extrusion steady-state pressure [38,2]. Most accurate comparisons have been at low actual temperatures using lead as the material. This is because difficulties in the estimation of the deformation temperature in hot extrusion makes selection of the appropriate flow stress of the material difficult. The minimised

upper-bound solutions need the thermal model to select the flow stress from the torsion and compression data. Hence comparison of the predicted Pmin with actual steady-state pressure gives an estimate of the accuracy of the thermal model.

As shown in Fig. 6.1 the model slightly overestimates the actual pressure for solid material. This indicates that the thermal model slightly underestimates the deformation temperature. Fig.6.2 shows that for the powdered material gives excellent agreement. In both these comparisons only good extrusions are compared with theory. It is not obvious why the powder material gives better agreement. It may be accumulation of a number of effects such as the better fit of the billet compaction curve (Fig. 4.5 and 4.6), the more realistic model of heat transfer length for long powder billets.

6.3 Model for other materials

This program is based on the experimental data of aluminium alloy 2014 in solid and powder form. The shear stresses were obtained from hot torsion and compression tests.

For other materials, if the flow stress of the material is available, this model can be used to predict the minimized extrusion pressure using upper-bound solution for a particular extrusion ratio. The temperature changes during upset stage and steady-state condition can also be predicted if an experimental program has been conducted to give regression equations for the prediction of Pmax and the change in pressure during the upset stage.

The need for this data is an obvious limitation of the model. However work is in progress on finite element analysis of powder compaction [192] and other finite element analysis models [189,190,191] and these models could be combined. However analytic prediction of Pmax requires much further work.

The use of the model to relate microstructures and rationalize hot shortness limits as is done in the next Chapters could also be done with other materials.

The numerical results of the model are shown tabulated in Table 6.1 – 6.4 and

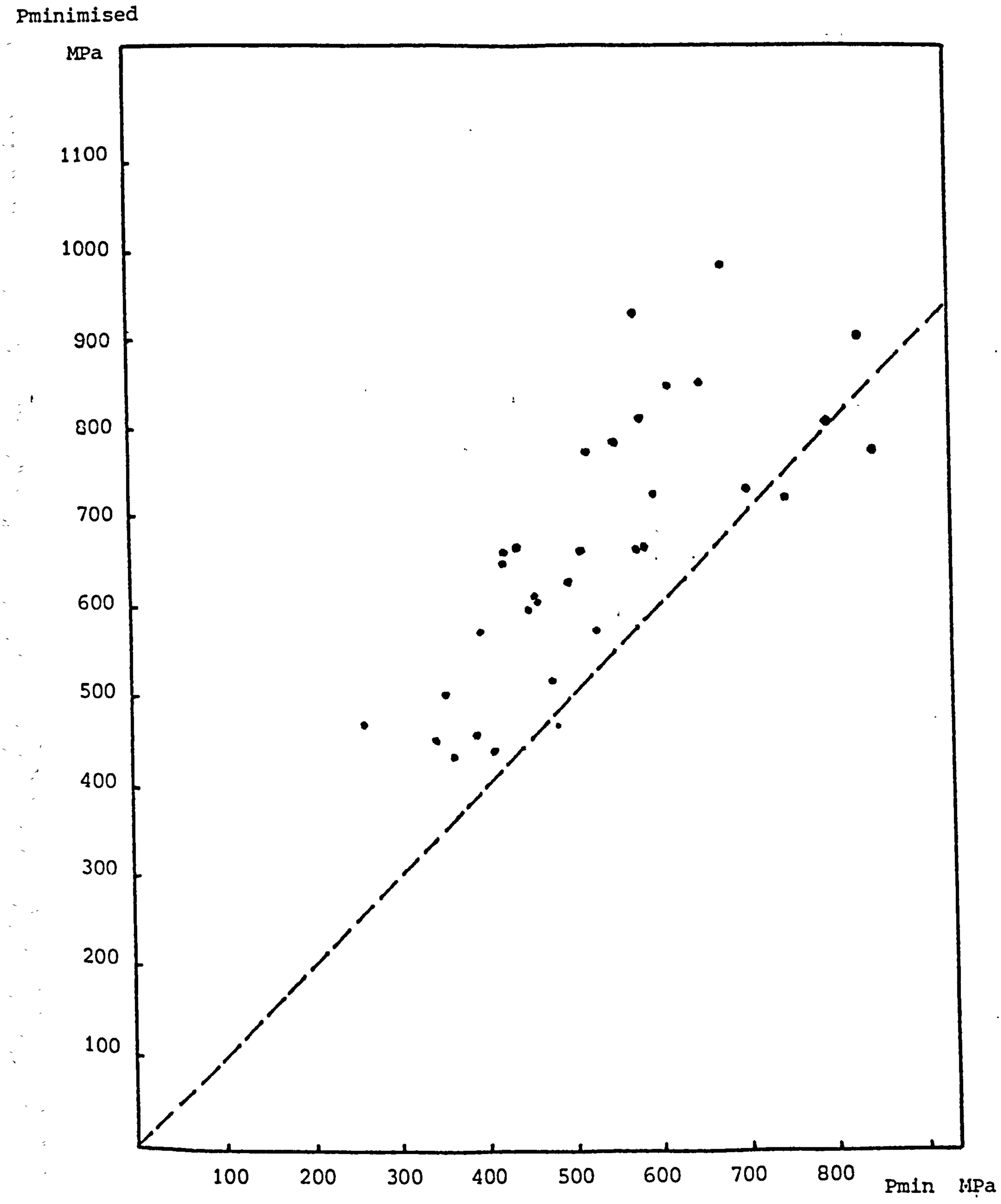

Fig. 6.1 Comparison of Pmin (actual) with Pminimised (Solid)

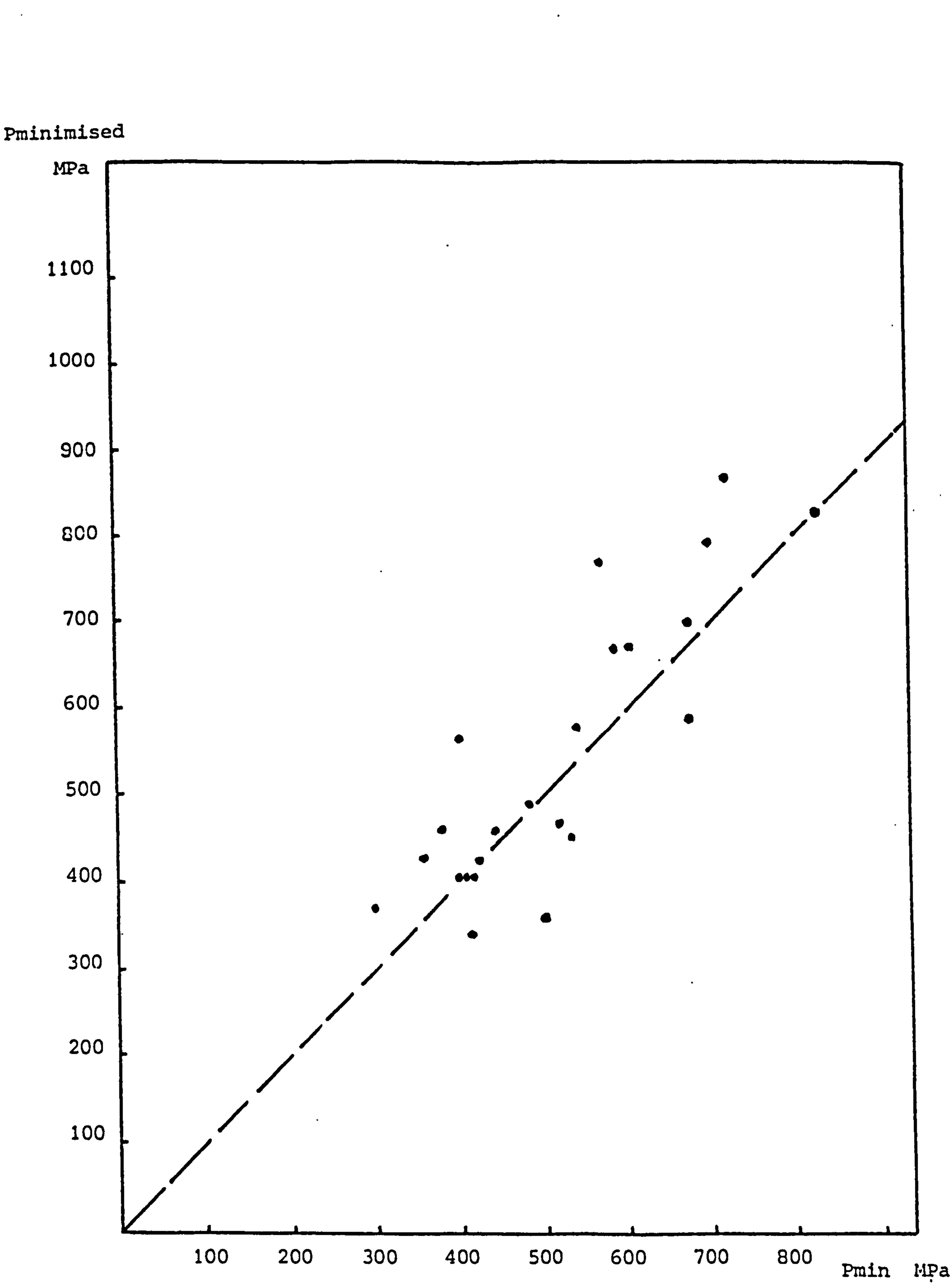

Fig. 6.2 Comparison of Pmin (actual) with Pminimised (Powder)

some typical output of the model is listed in the Microfiche.

R	Ti°C	V(mm/s.)	Act.Pre.(MPa)		Reg.Pre.(MPa)		Up-b.(MPa)	Ub+Reg.(MPa)	Te°C	Tx°C	Result	k(MN/m^2)
			Pmax	Pmin	Pmax	Pmin	Pmin	Pmax				
20	370	7.46	520	510	544.5	508.9	665.3	722.6	306.5	378.5	good	58.1
20	289	7.9	810	750	706.2	641.9	719.8	784.3	260.7	367.3	good	62.8
20	553	7.04	330	320	281.1	292.0	454.3	443.5	421.8	436.4	HS.f	39.7
20	505	15.6	202	187	331.7	324.1	416.9	424.5	430.3	472.9	HS	36.4
20	375	9.7	515	479	532.7	496.0	627.9	664.5	319.8	393.7	good	54.8
20	375	23.8	566	529	522.5	476.4	572.1	617.9	344.4	430.7	good	49.9
20	500	13.8	361	330	339.7	332.2	430.4	437.8	421.1	463.1	HS	37.6
20	470	14.2	369	342	380.0	365.1	467.8	482.6	400.7	450.2	HS	40.8
20	300	22	683	579	669.9	599.5	672.5	724.9	286.2	401.2	good	58.7
20	250	17.1	777	705	792.6	704.0	732.4	821.1	246.7	381.1	good	63.9
30	375	7.08	560	550	571.0	527.3	785.4	829.1	307.4	389.2	good	54.7
10	375	6.87	474	473	481.9	464.8	515.3	532.4	306.2	354.8	good	64.9
20	375	7.15	431	427	536.1	502.6	665.6	699.2	308.0	377.1	good	58.1
20	544	4.37	339	346	297.3	311.2	456.5	442.7	403.4	423.4	good	39.8
20	472	15.4	382	362	376.3	361.1	441.2	456.3	417.1	462.4	good	38.5
20	496	11.3	367	348	347.2	340.9	419.5	421.3	427.4	461.3	cr.f	36.8
20	472	16.3	399	374	375.6	359.8	445.4	450.8	416.3	466.7	cr.f	38.0
20	524	6.8	321	325	316.9	322.8	469.2	464.2	404.4	430.1	HS.f	41.0
20	447	31.4	428	396	403.9	375.3	457.9	486.6	410.1	476.8	crack	40.0
20	447	23.8	411	388	407.1	381.2	463.1	489.0	404.2	466.7	good	40.4
20	550	6.81	266	266	285.1	295.6	300.6	290.1	481.1	503.9	V.HS	26.2

Table 6.1 Extrusion conditions and comparisons for solid round die

R	Ti°C	V(mm/s.)	Act.Pre.(MPa)		Reg.Pre.(MPa)		Up-b.(MPa)	Ub+Reg.(MPa)	Te°C	Tx°C	Result	k(MN/m^2)
			Pmax	Pmin	Pmax	Pmin	Pmin	Pmax				
53	550	5.85	268	250	365.9	354.8	698.5	709.6	411.7	451.2	HS.f	36.7
53	525	12.1	352	325	388.1	364.3	645.6	669.4	427.7	485.7	HS.f	33.9
53	475	12.0	505	469	454.0	418.9	720.4	755.5	394.1	466.2	HS	37.8
53	450	12.1	496	470	489.5	448.2	716.9	806.3	375.1	456.5	HS	40.1
20	420	41.5	431	405	441.6	403.0	498.6	537.2	389.2	469.7	HS	43.5
20	400	31.3	484	443	476.9	435.7	534.1	575.4	366.8	449.3	crack	46.6
20	450	6.87	415	400	399.9	392.4	578.5	585.9	342.6	379.1	good	56.5
20	230	13.5	1055	851	850.1	754.3	778.1	873.8	222.9	366.6	good	67.9
20	440	44.5	435	400	410.3	376.3	469.1	503.1	406.9	482.3	HS	40.9
20	350	27.4	497	458	566.2	511.0	612.8	668.0	324.1	423.0	good	53.5
20	350	37.4	472	453	562.6	504.3	602.1	660.4	330.0	434.0	good	52.6
20	425	27	550	483	438.8	405.9	501.1	534.2	384.4	456.2	HS	43.7
20	375	30.7	530	484	519.5	471.1	571.0	619.4	346.3	437.4	v.f.cr.	49.8
20	300	44.3	650	583	661.9	584.4	668.6	746.2	291.5	419.7	good	58.4
20	325	52.6	400	392	607.4	537.2	633.1	703.4	314.3	433.8	v.f.cr.	55.3
20	250	7.25	805	733	802.4	722.5	803.4	883.3	220.6	348.0	good	70.1
20	500	7.2	271	264	347.1	346.2	470.7	471.5	399.1	431.4	good	41.1
20	450	31.3	417	390	399.5	371.7	462.9	490.7	407.1	474.0	HS	40.4
20	350	79.5	588	516	554.6	488.6	583.2	649.2	340.2	459.4	cr.mr	51.0
20	400	7.2	430	440	493.7	467.4	674.9	701.2	317.3	375.9	good	58.9
20	550	4.27	637	625	290.4	305.7	617.7	602.4	366.4	378.7	HS.f	53.9
20	450	14.4	378	356	408.3	388.4	504.4	524.4	382.6	438.6	good	44.0

Table 6.1 continued

R	Ti°C	V(mm/s.)	Act.Pre(MPa)		Reg.Pre.(MPa)		Up-b.(MPa)	Ub+Reg.(MPa)	Te°C	Tx°C	Result	k(MN/m^2)
			Pmax	Pmin	Pmax	Pmin	Pmin	Pmax				
20	405	7.45	470	462	533.0	494.0	605.1	643.8	327.9	394.7	good	51.9
20	500	7.14	421	407	457.0	428.7	444.9	473.2	384.9	441.0	good	38.5
50	405	10.	568	522	605.0	543.2	774.8	836.6	340.5	444.4	good	41.7
50	450	7.	644	589	578.2	536.1	726.1	768.2	351.9	445.0	good	39.1
50	350	7.4	636	574	668.8	614.0	941.8	996.6	294.4	405.6	good	50.7
20	250	7.58	717	612	710.0	650.9	862.6	921.8	235.1	339.1	good	73.6
20	400	2.9	604	582	569.4	570.9	822.0	820.5	268.8	328.9	good	71.1
20	400	18.	560	480	508.0	430.7	473.2	550.5	356.0	456.0	good	40.9
50	500	11.3	467	421	523.5	465.2	522.4	580.7	410.6	515.5	V.HS	28.1
50	475	18.3	506	434	526.0	444.5	509.0	590.5	413.8	536.1	V.HS	27.4
50	275	67.5	812	684	683.3	523.2	990.8	1150.9	275.3	453.0	HS	53.4
50	550	5.0	637	624	515.7	496.3	606.0	625.4	384.3	465.3	HS.f	32.6
50	550	6.4	298	267	507.4	477.4	520.0	550.0	416.7	498.4	crack	28.0
50	525	12.4	485	397	502.4	442.0	484.2	544.6	429.3	532.1	V.HS	26.1
50	475	13.1	540	466	537.2	470.1	604.2	671.3	398.0	495.0	crack	32.5
50	450	11.8	554	475	560.6	495.8	670.0	734.8	374.1	473.1	crack	36.1
50	425	17.1	621	524	569.3	486.3	692.5	775.5	369.9	478.9	crack	37.3
50	400	16.4	688	561	593.1	509.5	754.3	837.9	349.6	462.8	s.cr.f	40.6
50	450	9.4	567	500	568.4	513.7	708.5	763.2	361.2	457.2	v.f.cr	38.2
20	400	6.87	418	418	540.4	504.6	650.5	686.2	314.8	381.1	good	56.2
50	375	21.8	633	566	607.2	508.5	786.0	884.6	339.6	464.0	v.f.cr.m	42.3

Table 6.2 Extrusion conditions and comparisons for solid shaped die.

R	Ti°C	V(mm/s.)	Act.Pre.(MPa)		Reg.Pre.(MPa)		Up-b.(MPa)	Ub+Reg.(MPa)	Te°C	Tx°C	Result	k(MN/m^2)
			Pmax	Pmin	Pmax	Pmin	Pmin	Pmax				
50	350	19.6	750	650	636.1	539.2	858.1	954.9	317.8	445.6	good	46.2
50	325	22.	883	833	659.5	554.6	909.9	1014.9	301.4	438.4	good	49.0
50	300	20.2	767	675	691.8	587.4	998.6	1103.0	277.8	420.7	good	53.8
50	300	35.4	633	575	673.0	544.3	943.6	1071.3	288.0	444.0	f.cr.	50.8
50	525	6.0	505	477	526.7	497.5	633.2	662.3	379.5	463.2	cr.f	34.1
50	450	13.7	600	522	555.7	484.6	655.6	726.7	380.0	481.1	f.cr.	35.3
50	550	2.27	325	400	542.1	556.8	1050.4	1035.8	279.1	362.3	good	56.6
50	550	5.2	343	300	514.4	493.0	625.3	646.4	380.9	461.9	HS.f	33.7

Table 6.2 continued

R	Ti°C	V(mm/s.)	Act.Pre(MPa)		Reg.Pre.(MPa)		Up-b.(MPa)	Ub+Reg.(MPa)	Te°C	Tx°C	Result	k(MN/m^2)
			Pmax	Pmin	Pmax	Pmin	Pmin	Pmax				
20	552	6.87	407	405	383.1	384.9	405.2	403.3	393.3	395.0	good	35.4
20	553	15.6	320	312	381.8	359.9	303.6	325.5	453.3	475.7	HS.f	26.5
20	472	14.6	433	421	419.9	405.5	392.8	407.3	391.0	424.6	cr.fm	34.3
20	450	16.7	422	410	431.2	414.6	406.5	423.1	377.8	422.7	good	35.5
20	531	12.4	325	321	391.8	377.8	349.9	363.8	414.0	440.6	HS	30.5
20	446	14.4	452	444	433.5	421.5	461.9	473.9	366.0	394.6	good	40.3
20	548	10.9	541	500	384.3	373.0	360.9	372.3	410.0	430.3	good	31.5
20	500	14.4	272	299	406.1	390.1	375.1	391.1	397.0	432.2	good	32.7
53	500	14.5	396	383	686.8	663.9	395.7	418.6	395.5	533.9	HS	20.8
20	405	15.3	403	403	456.6	446.2	563.3	573.7	328.3	360.4	good	49.2
20	405	42.7	388	384	455.6	415.5	375.5	415.6	364.3	470.1	crack	32.8
20	385	25.8	436	415	468.2	444.6	433.5	457.1	336.0	424.1	good	37.8
20	400	24.6	415	401	459.1	435.5	404.5	427.6	353.0	436.1	good	35.3
20	400	30.6	422	395	458.9	428.9	395.3	424.7	358.4	448.2	f.cr.f	34.5
20	375	39.5	561	500	474.1	439.0	412.8	447.8	339.2	448.8	f.cr.	36.0
20	350	43.5	592	533	490.6	455.1	432.4	467.8	321.2	442.5	f.cr.	37.7
20	425	29.3	400	383	444.4	413.5	382.5	412.7	370.0	453.2	f.cr.	31.5
20	325	48.5	580	533	508.2	472.3	451.4	487.4	305.7	437.2	good	39.4
20	550	16	229	230	383.1	360.6	317.9	340.4	436.7	467.6	HS fm	27.7

Table 6.3 Extrusion conditions and comparisons for powder round die.

R	Ti°C	V(mm/s.)	Act.Pre.(MPa)		Reg.Pre.(MPa)		Up-b.(MPa)	Ub+Reg.(MPa)	Te°C	tx°C	Result	k(MN/m^2)
			Pmax	Pmin	Pmax	Pmin	Pmin	Pmax				
20	500	7.5	382	382	381.2	377.5	460.9	464.5	348.4	378.0	good	39.9
20	550	7.5	358	358	327.1	334.3	429.6	422.4	375.6	389.2	good	37.2
20	400	7.9	493	481	508.0	478.2	492.8	522.6	301.0	367.1	good	42.6
50	450	7.6	696	670	564.7	531.4	590.2	623.5	321.5	425.3	good	31.8
20	450	7.76	419	410	441.1	424.9	341.6	357.7	325.0	430.1	good	29.5
50	350	7.	631	565	706.6	646.0	773.4	834.5	272.0	375.5	good	41.6
20	250	8.1	674	582	774.7	691.0	669.3	752.9	234.0	315.4	good	57.9
20	400	2.3	572	537	499.6	489.4	578.6	588.9	192.0	310.7	good	50.0
20	411	7.44	530	513	492.2	466.5	468.4	494.2	313.0	374.4	good	40.5
50	500	14.8	471	433	509.5	477.6	467.5	499.8	389.0	493.8	crack	25.2
50	400	10.7	637	600	633.8	581.7	674.0	726.2	308.0	412.8	good	36.3
50	400	21.3	700	625	638.5	575.4	622.0	685.1	339.0	451.0	f.cr.	33.5
50	450	26.7	517	465	573.2	520.0	509.1	562.4	387.0	499.1	f.cr.	27.4
50	350	22.9	768	666	714.7	635.3	697.9	777.3	314.0	430.6	good	37.6
50	300	28.	783	700	803.4	703.4	795.4	895.5	284.0	411.7	good	42.8
50	271	29.5	820	716	861.4	749.0	870.1	982.6	259.0	395.4	good	46.9
50	450	25.3	618	539	572.9	520.5	487.4	539.8	394.5	506.6	cr.mr	26.2
50	550	7.0	321	332	450.3	441.1	482.3	491.5	360.5	459.8	f.cr.	26.0
50	525	11.7	430	405	480.2	457.6	453.6	476.2	388.8	490.6	crack	24.4
50	300	18.6	912	821	800.7	707.1	827.3	920.9	276.0	392.0	good	44.5

Table 6.4 Extrusion conditions and comparisons for powder shaped die.

HS — Hot short
HS f — Hot short front
HS fm — Hot short front and middle
V.HS — Very hot short
cr.f — cracks front
v.f.cr. — very fine cracks
cr.mr — cracks middle and rear
s.cr.f — slight cracks front
f.cr.mr— fine cracks middle and rear
f.cr. — fine cracks
cr.fm — cracks front and middle
f.cr.f — fine cracks front

Table 6.5 Abbreviations for Table 6.1 – 6.4

Chapter 7

HOT SHORTNESS LIMITS

7.1 Theory and practical data

In an extrusion the capacity of the press is usually fixed and the extrusion ratio is also often fixed by the product. So the remaining parameters are the ram speed and the billet temperature. These then are of prime importance in controlling the temperature cycle of the microstructure and unless there are phase morphology or subgrain size limitations in the product then the upper thermal limit is the onset of hot shortness. As stated before the maximum extrusion temperature is 400°C – 480°C for Al–Cu–Mg–Si alloy [173].

The ram speed and initial billet temperature are linked through the actual extrusion temperature at the critical part of the process. For hot extrusion this is Tx. It is the rate of extrusion that is of most commercial concern. High melting point low yield strength alloys are less sensitive to deformation rate. For example copper alloys are extruded as fast as 200 mm/sec. [1]. However, aluminium, magnesium and some other alloys are distinctly sensitive in respect of the rate at which deformation is carried out on them. If a certain critical speed, which depends on the alloy, the temperature and the shape of the extruded part, is exceeded, characteristic faults ranging from roughened, torn or repeatedly cracked surface and even complete disintegration are exhibited and often attributed to hot shortness.

There are several explanations of hot shortness. Bishop [16] states that hot

shortness is caused by the temperature rise due to plastic deformation. It is thought that a very small amount of a grain boundary film of a low-melting constituent melts and hot shortness occurs [3,14,170] or that the variable flow velocities between the material at the centre of the die and the periphery result in longitudinal tensile stresses when the extrusion passes through the die, causing cracks to open. Usually fir-tree cracking occurs in the circumference of the surface of extruded material [170,1,3]. Pearson [1] states that the reason for hot shortness is that differential stresses are set up due to the unequal distribution of flow through the die aperture, the temperature rise of the metal due to the heat generated by internal and external friction in deformation. Strain hardening caused by working which is not sufficiently removed by recovery and recrystallization adds to the problem. Sheppard [46] points out that hot shortness occurs when excessive localized heating of the surface takes place because of the high strain rate history of this region. This causes liquation of low temperature phases. The friction in the die land area results in material exhibiting low flow stress being unable to resist the imposed shear stress. He also points out that cracking is particularly sensitive to extrusion speed. He and Paterson [157] state that surface cracking occurs when the tensile stress caused by friction stresses generated in the die area just exceeds the material's hot yield stress and in Al-2014 it is a major problem.

Most of the heat generated from deformation energy is in the zone where deformation is most severe, in the region near the entry to the die and in the very heavily worked zone near the surface of the section, where there is also friction at the bearing surface of the die. When the metal is extruded slowly, the generation of high local temperature tends to be prevented by the dissipation of heat into the surrounding mass and into the tools. However, if the extrusion rate is high, when the heating is greater due to the enhanced pressure required, the temperature may easily be raised far enough to bring the surface layer to the point where hot shortness develops. Akeret [19] stated that the temperature of the extrusion when it leaves the die should not exceed a certain value. Ashcroft and Lawson [6] found that hot shortness occurs when the temperature reaches at a critical value and the

emergent temperature from the die should not exceed 480°C for Al–Zn–Mg–Cu alloy.

Examinations of the extrusion in the present work demonstrated that the initial billet temperature was a very important relative to the occurrence of hot shortness. Ram speed and the extrusion ratio, which both determine the strain rate, also play an important role. Among about 120 extrusions in this investigation, it was observed that when the initial billet temperature reaches 550°C, most of the extrusions were hot short unless a slow ram speed was employed. Hot shortness occurred mostly in the front part of the extrusion just after the pre-extrusion. The surface finish gradually improved as the process proceeded. Die shape was shown to be important too. Square cornered dies produced extensive hot shortness whereas round dies gave good products under otherwise identical conditions. Large increases in ram speed caused hot shortness even at low temperature. This kind of hot shortness usually occurred in the middle and rear part of extrusion which was evidence of increasingly adiabatic conditions.

It was considered important to establish the relationship between these variables and to find out the critical value of the temperature, Tx, which was considered to be of more fundamental value than Ti.

7.2 Limit diagrams and model

Attention has been paid in this work to find the hot shortness boundaries relative to the initial billet temperature and ram speed for a particular extrusion ratio. Extrusions were performed at particular extrusion ratios close to the hot shortness boundary to produce cracks in the front part of the extrusion. The program was then used to calculate Tx at the start of steady-state condition for these hot short extrusions. According to the experimental data, the temperature Tx which causes hot shortness for solid extrusion through round dies was found to be in the range 438°C – 461°C, and 453°C – 461°C for solid extrusion through shaped dies.

Fig. 7.1 and 7.2 are the limit diagrams for round die with extrusion ratio of

20 and shaped (square) die with extrusion ratio of 50 for solid extrusion. Fig. 7.3 and 7.4 are the limit diagrams for round die with extrusion ratio of 20 and shaped die with extrusion ratio of 50 for powder extrusion. The container temperature was 200°C for all the extrusions. The left side of the boundaries indicates where good extrusions can be obtained. The right sides indicate the danger of obtaining hot short extrusions. Along the boundaries, the numbers on the left side are the calculated temperature when extrusion starts, Te, and the right side numbers are the calculated temperature at the start of steady-state condition, Tx. It can be seen that the initial billet temperature is not a useful control over hot shortness at all. Hot shortness can be produced at any initial billet temperature. Te is not much better. Hot shortness was produced over a 100°C range in Te. Tx on the other hand represents a much better guide, so long as it can be calculated. The model used in this work produced answers that were consistent over a 20°C range in temperature around 470°C. This temperature is slightly lower than the critical temperatures reported in other work on comparable alloys [137,173].

It was significantly below the melting point of any of the phases present in this alloy [124] (see Table 7.1). The incipient melting observed in the very high temperature torsion and compression tests was not seen in this extruded material. Hence it is proposed that when the secondary tensile stresses exceed the high temperature yield stress of the alloy, hot shortness occurs.

It was considered that the use of the model and metalworking data to predict such a consistent hot shortness criterion ($Tx < 470°C \pm 20°C$) represents an advance over most practice. If other critical temperatures are known for any alloy system under investigation, for example precipitation temperatures, onset of recrystallization and grain growth then the model could also be used to control these phenomena.

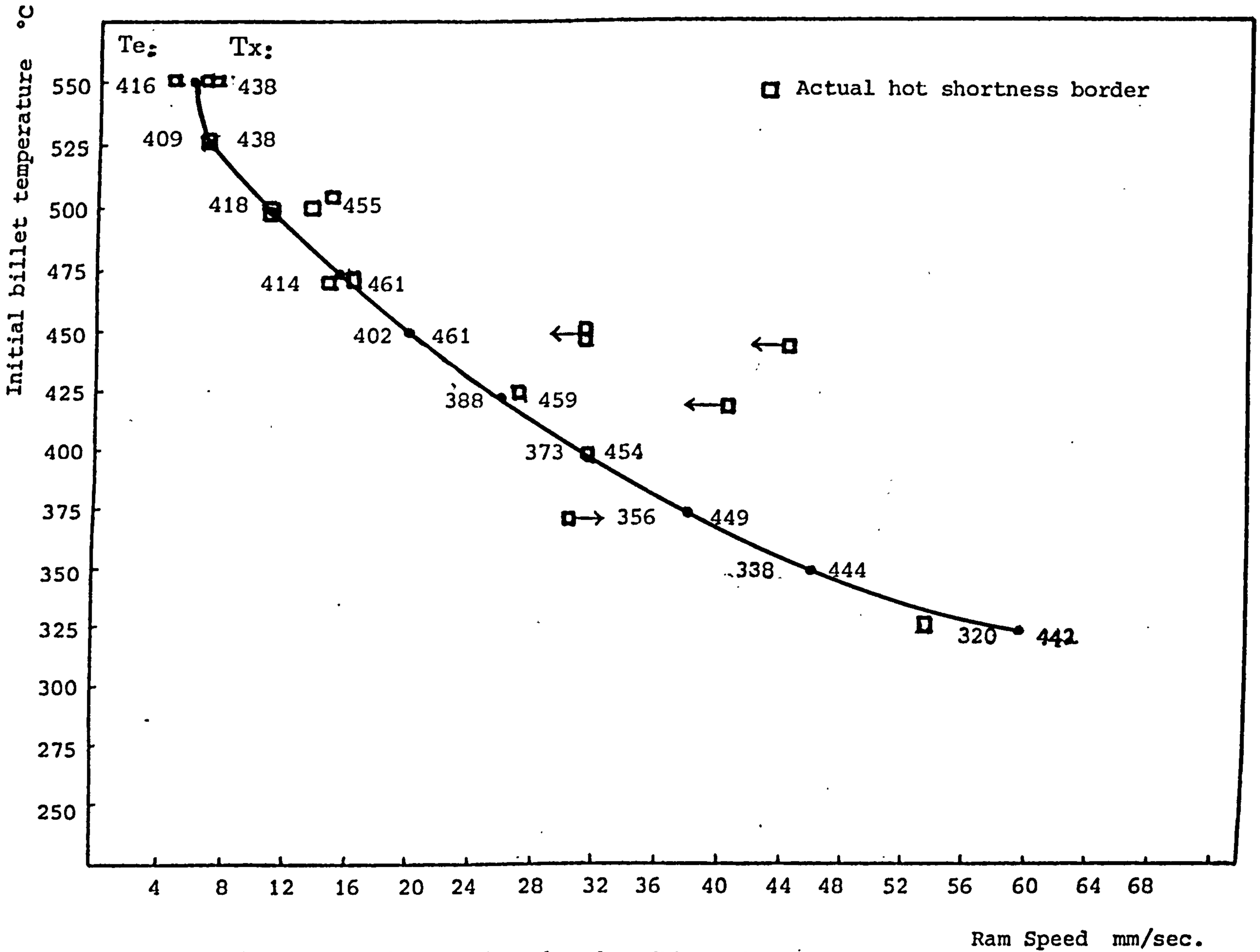

Fig. 7.1 Hot shortness boundary for solid round die R=20

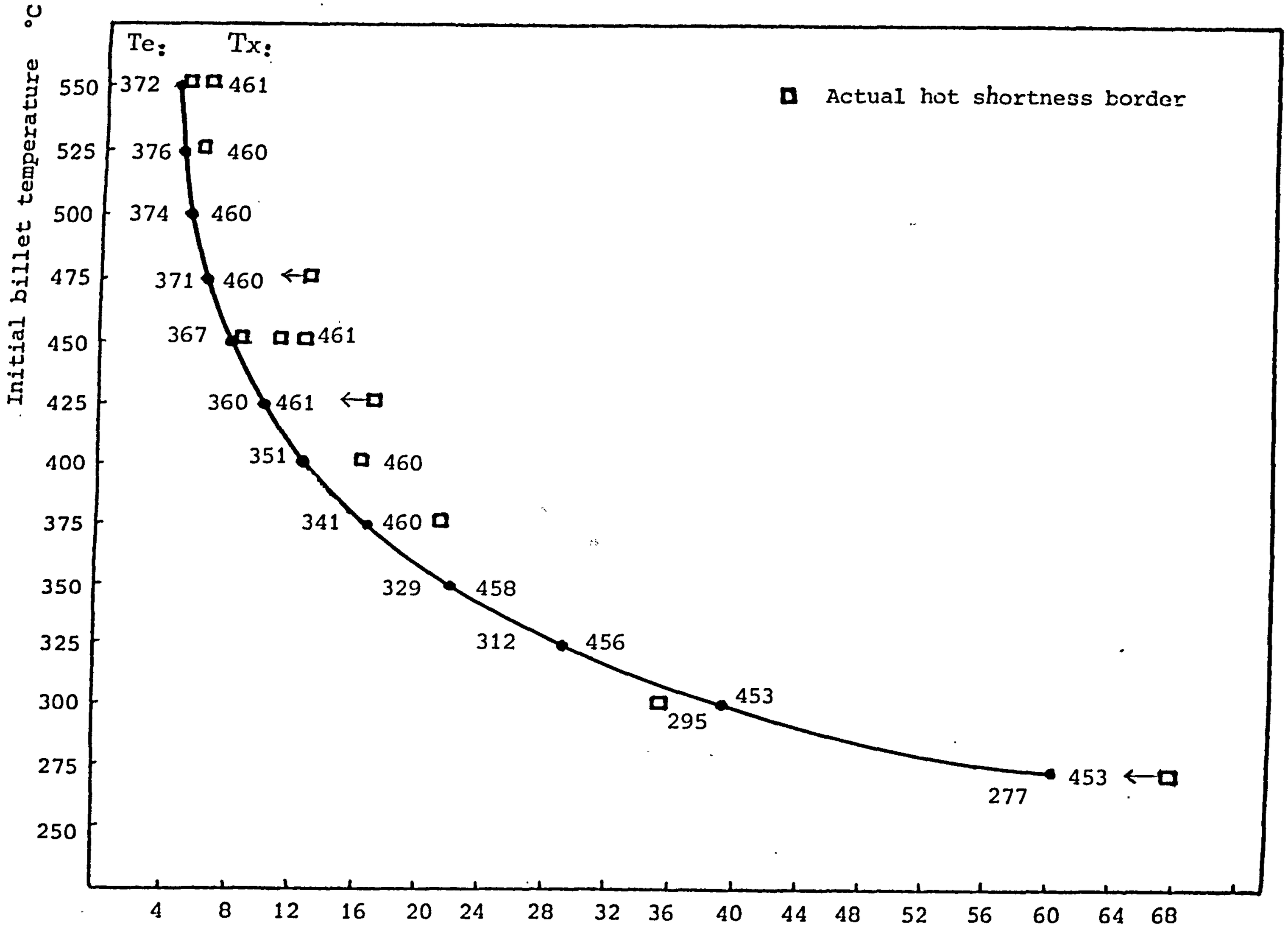

Fig. 7.2 Hot shortness boundary for solid shaped die R=50

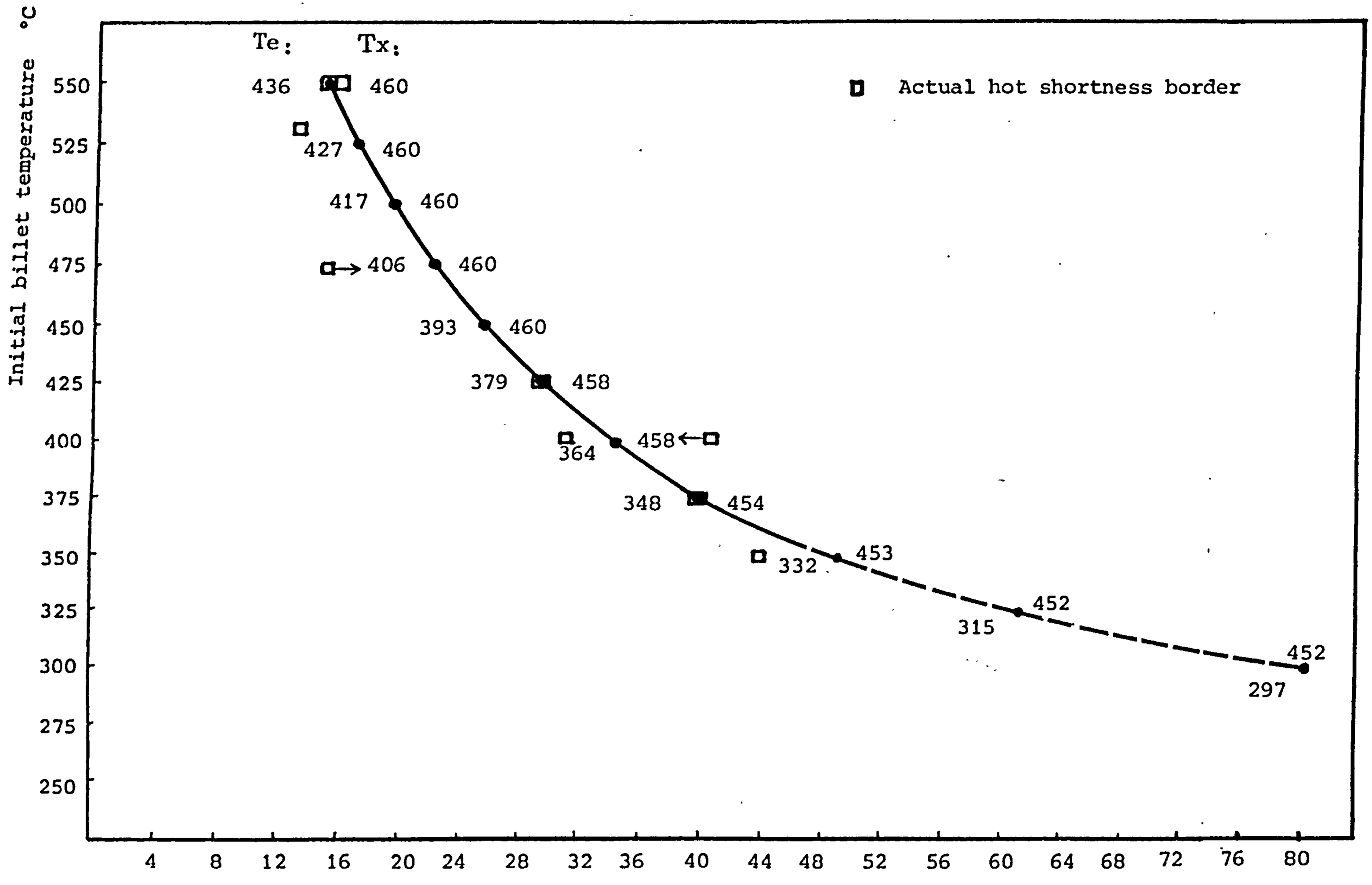

Fig. 7.3 Hot shortness boundary for powder round die R=20

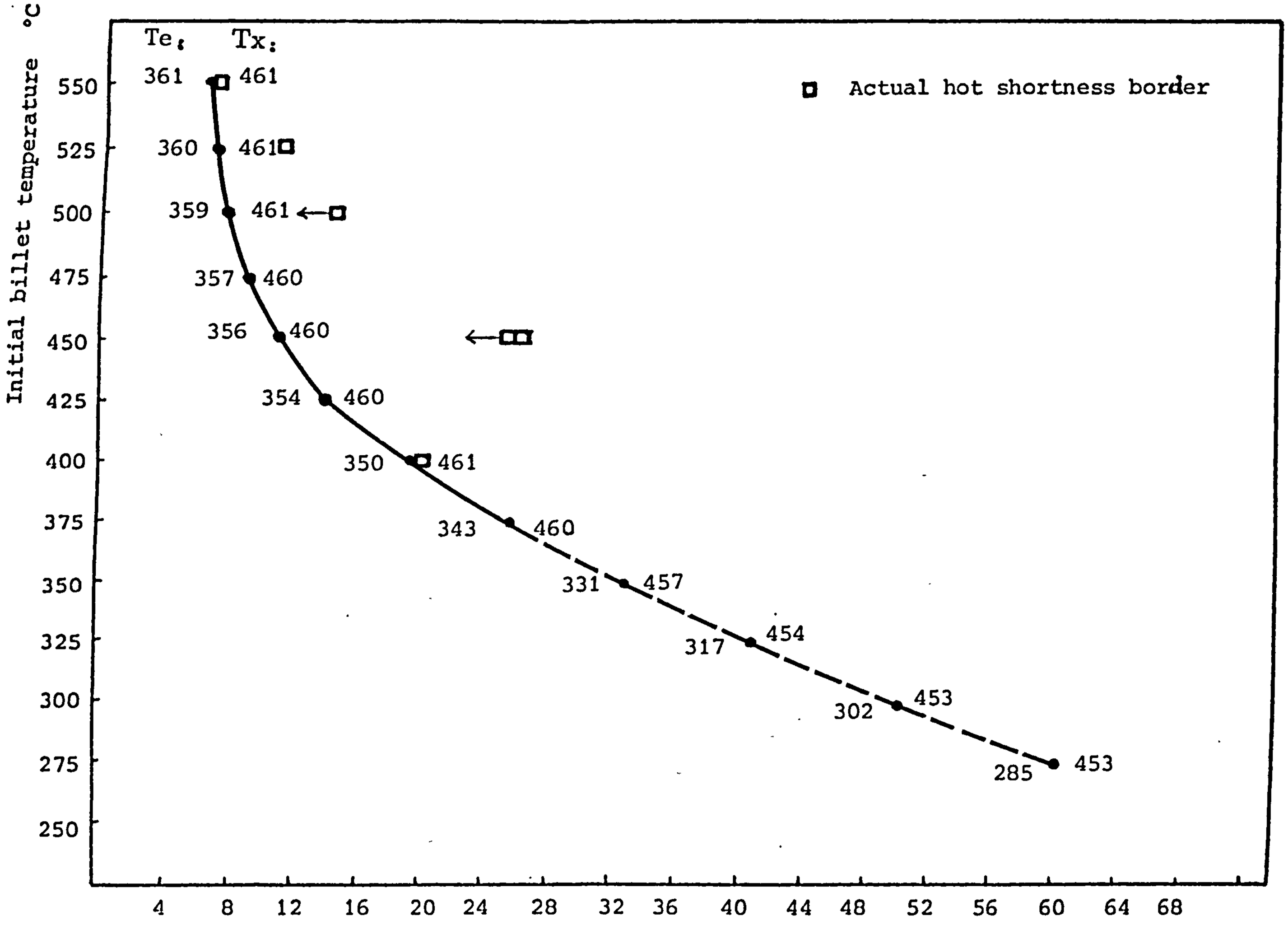

Fig. 7.4 Hot shortness boundary for powder shaped die R=50

Reactant	Possible phase reaction	T (°C)
Liq. →	Al+CuAl_2	548
Liq. →	Al+MnAl_6	658
Liq. →	Al+Si	577
Liq. →	Al+Mg_2Si	595
Liq. →	Al+Mg_2Si+Si	555
Liq. →	Al+CuAl_2+Si	525
Liq. →	Al+CuAl_2+Mg_2Si	515
Liq. →	Al+FeAl_3	655
Liq. →	Al+CuAl_2+Cu_2FeAl_7	545
Liq. →	Al+CuAl_2+Si+$Cu_2Mg_8Si_6Al_5$	507
Liq.+Mg_2Si →	Al+CuAl_2+$Cu_2Mg_8Si_6Al_5$	512
Liq.+Mg_2Si+Si →	Al+$Cu_2Mg_8Si_6Al_5$	529

Table 7.1 Possible phase reaction temperatures

Chapter 8

DEPENDENCE OF MICROSTRUCTURE ON DEFORMATION PARAMETERS

8.1 Analysis of microstructure in torsion tests

Since torsion testing is a laboratory testing method, the parameters can be controlled precisely. These controlled conditions can be used to produce reference microstructures which can be compared with those in extruded sections.

8.1.1 Microstructural analysis of as received ingot material

The billets for extrusion were produced from as received ingot which was in the TB condition (solution treated, quenched and naturally aged). Hence the torsion specimens were taken from ingot in the same condition. The billets for extrusion and hence the specimens for torsion test are all initially heated to a required temperature then deformed at that temperature. During the preheating period, the microstructure changes and the materials were deformed with this starting microstructure. To examine this microstructure a series of heat treatments were applied to the as received ingot material.

Plate 3 shows the as received TB condition. Its microstructure can be seen to consist of elongated grains and coarse constituent particles formed during solidification and aligned in the direction of subsequent hot working. The elongated grains are about 660 μm in length and 26 μm in width with an aspect ratio

of 25:1. The subgrains are approximately $2 - 4\ \mu m$ diameter. The high magnification optical micrograph shows equiaxed recrystallized grains with high angle boundaries between them. The small equiaxed grains with precipitates on their boundaries have formed on the original grain boundaries. These are evidence that static recrystallization must have occurred after hot working since these small grains are not deformed.

	Billet(quenched)	Torsion tested at surface $\dot{\gamma}$=3.45		
T°C	Hv(tran)	Hv(tran)	Strain to fail	Subg.dia. μm
received	160	no test	no test	5(no-test)
250	166.	166.5	no record	4.5
300	113	122	3.73	3.75
350	92.6	99	12.06	1.29
400	89.76	120*	13.4*	1.85*
450	116.25	124.75	11.4	2.4
500	145	149.25	3.45	3

* Tested at 411°C.

Table 8.1 Microhardness and subgrain size

The TEM picture in Plate 3 shows the elongated original grains with equiaxed subgrains within them. These subgrains are indicative of recovery in the hot worked billet material. The TEM also shows fine dispersoids of transition metal rich particles formed during homogenization or hot working by solid state reaction distributed in the matrix. The microhardness for this material is 160. (see Table 8.1)

8.1.2 Microstructure before deformation begins

To examine the microstructure before extrusion and torsion testing specimens were produced by heating as received material to 250, 300, 350, 400, 450 and 500°C for half an hour then water quenching. Thin foils for TEM examination and optical microstructures were analysed as soon as possible after quenching to minimise natural ageing phenomena.

Plates 4 – 6 show the results of this work. At 250°C the structure shows little

change from the as received condition. However, at higher magnification, more precipitate particles can be seen on grain and subgrain boundaries and within grains. The TEM picture shows a network of θ' and possibly some Q phase particles of 0.1 μm diameter which can be compared with slightly larger precipitates at 400°C which were examined by STEM. The shape of these particles agrees with other observations [34,188].

At 300°C grain boundaries are clearer at low magnification as even coarser precipitates decorate them. All precipitates seem larger than at 250°C, especially the θ' precipitates in the TEM picture.

At 350°C the original grain boundaries are not as clear as at lower temperatures but at higher magnification coarsened precipitates decorating grain boundaries and precipitate free zones are evident. These light etching zones are evident in all the optical micrographs at this temperature and appear as a sub-structure within the grains at the lowest magnification. Hence they are associated with the recovered substructure boundaries. The θ' seem to have all grown to θ which first appear here as long rod like particles in the TEM picture. Dislocation loops are also evident.

At 400°C larger precipitates and wider precipitate free zones can be seen even at low magnification. Longitudinal sections take on a definite banded appearance. The TEM picture shows large precipitates. STEM analysis of this structure confirmed that the long rod like precipitates are $CuAl_2$ (θ). The large dark particle consists of Al-Cu-Mg-Si and is most probably $Al_5Cu_2Mg_8Si_6$, the "Q" phase. Other particles containing Al-Cu-Mg-Mn-Si-Fe and Al-Cu-Mn-Si-Fe were detected.

At 450°C even wider precipitate free zones are evident. Dissolution of precipitates occurs even more at this temperature. Precipitates within grains begin to dissolve too. This causes the zones to be distinct. The θ rods have coarsened significantly.

At 500°C precipitate free zones are not evident because precipitates have extensively dissolved and only coarse constituent particles remain. Extensive grain growth occurs. The TEM structure indicates fine insoluble dispersoids within the

large grains.

Table 8.1 lists the results of microhardness test of billets after quenching from different temperatures. With increasing temperature the precipitates coarsen and so the hardness decreases until 400°C. After that precipitates start to dissolve and the hardness increases by solution hardening.

The following observations are useful thermal markers in non-deformed solid material:

1. At 250°C fine networks of θ' in a recovered subgrain structure remain.
2. At 300°C θ' has coarsened.
3. At 350°C precipitate free zones first appear, rod like θ appears.
4. At 400°C significant banding begins in microstructure following original hot working direction.
5. At 450°C extensive particle dissolution occurs. θ rods are much coarser.
6. At 500°C full particle dissolution and grain growth occurs.

8.1.3 Microstructural changes after deformation in torsion

As described in Section 3.3 torsion tests were carried out at various temperatures and twisting rates. This section deals with specimens deformed at constant twisting rates. However, the strain and strain rate vary from zero at the specimen centre to a maximum on the surface. So microstructural changes with strain and strain rate can be examined in one specimen. The key for Plates 7 – 12 shows how samples were taken.

The specimen tested at 250°C and surface strain rate of 3.45 (Plate 7) shows almost the same structure as the specimen before testing (Plate 3). Original grains

remain and the billet deformation direction is still obvious in the tangential section. In the transverse section the grain size is slightly decreased on the edge of the specimen. Precipitate particles pinning boundaries can be seen at higher magnification. A high dislocation density can be seen in the TEM picture with precipitates on the subgrain boundaries. Microhardness and grain size were measured at the edge of torsion specimen and are listed in Table 8.1. The microhardness and grain size have not significantly changed from the original which indicates that recovery processes counteract work hardening effects even at this low temperature.

Similar effects are seen at 300°C (Plate 8). However the higher strain to failure makes the effects more pronounced. As in the comparative ingot material larger and more precipitate particles are distributed on grain boundaries and in the matrix. There is some evidence that precipitate free zones start to accompany the precipitate coarsening process. This occurs at a slightly lower temperature than in the undeformed ingot. This suggests that the strain assists the diffusion process. The coarse constituent particles follow the deformation. In the TEM picture, θ' phase can be seen within subgrains as expected [133]. The microhardness is softer than the specimen tested at 250°C and comparable to the equivalent quenched ingot material (see Table 8.1). This is again caused by particle coarsening. The subgrain size is reduced but this has little effect on the hardness.

Plate 9 is for the specimen tested at 350°C and shows more coarsened precipitates and other intermetallic particles. The specimen edge shows such severe shear that original grain boundaries are obliterated. The banding that occurs in the microstructure is obvious in the tangential section and this occurs 50°C lower than in the undeformed material. The TEM picture shows subgrains, large precipitate particles and dislocations. Softening by precipitate coarsening continues and the subgrain size decreases further due to the increased strain to failure. The light etching precipitate free regions are more extensive and distinct than at 300°C.

The specimen tested at 411°C (Plate 10) shows the same low magnification features. On the edge, the specimen was severely distorted and original grain boundaries cannot be seen at all. In the longitudinal and tangential sections the

elongated grains in the twisting direction give a fibrous structure. The TEM picture shows long rod-like precipitates and other particles, and only a few dislocations. This testing temperature seems a critical temperature at which the microhardness and subgrain size start to increase again (see Table 8.1). The final strain to failure is 13.4, larger than any others. The maximum amount of particle coarsening without significant solution hardening seems to occur here. This gives rise to the ductility maximum in torsion. The higher temperature now appears to overcome the effects of increased strain and the subgrain size starts to increase. The strain causes solid solution hardening to begin at about 50°C lower than in the strain free ingot material. The precipitate free zones are most distinct at this temperature.

In Plate 11 the specimen tested at 450°C the optical microstructure is again similar. Precipitate free zones are still very clear. The TEM picture shows some large precipitates and other second phase particles. Second phases start to dissolve extensively and because of this the material is much harder. It only shows 11.4 strain to failure. Since the temperature is high, dislocation cross-slip and climb are rapid which increases the subgrain size and sharpens the subgrain boundaries.

In Plate 12 specimen tested at 500°C little bulk deformation is evident. This is due to the low strain to failure as shown in Table 8.1. Original grains containing subgrains remain. Precipitate free zones on subgrain boundaries are so clear that they can be seen optically at low magnification. At higher magnification incipient melting is detected. The TEM picture shows the well-defined subgrains with many dislocations which are helical and due to quenching. In this microstructure, less second phase particles are present indicating more alloying elements have been dissolved into matrix. This solute hardening causes the room temperature hardness to return to almost the as supplied level. The subgrain size appears to still be increasing but it is thought that it is little changed from the original size due to the small strain to failure at this temperature.

It has been reported that subgrain size increases with increasing deformation temperature and inversely with the Zener–Hollomon parameter and flow stress

[81,171,69,73,85,60,64,55,65,71,59,156]:

$$Z = \dot{\epsilon}\, exp(\frac{\Delta H}{RT})$$

$$d^{-1} = a + b \ln Z$$

$$\sigma = \sigma_0 + k d^{-m}$$

In this work subgrain size was measured by using average linear intercept method [175,176,162]. However the additional variables of solute dissolution, different strain to failure and the exact location of the specimen in the strain gradient make comparisons with previous work unreliable. The subgrain sizes obtained in torsion testing are plotted in Fig. 8.1

Ductility maxima have been reported before [178] but no direct comparisons with this alloy, which shows a maximum at 400°C are possible.

It is difficult to locate TEM specimens with equivalent strain histories from samples tested at the same temperature but different strain rates, due to the strain gradients across the specimen. However Plate 13 is provided as some evidence that at 350°C the strain rate influences the dislocation networks as may be expected, with more complex networks at high strain rates.

In summary for torsion testing of solid material, dynamic recovery is considered to be the sole restoration process. Even at the high temperature of 500°C only subgrains contained in the original grains are displayed (see Plate 12). The received material consists of numerous fine dispersoids evenly distributed in a structure containing subgrains. The substructure of the deformed material appears finer at lower temperatures as described in Section 8.1.3. The subgrain size decreases until 350°C and then begins to increase again. This minimum coincides with the softest quenched hardness (Table 8.1) and coarsest θ precipitation and the ductility maximum. The softening process is still dynamic recovery as no new recrystallized grains are found. The reason for this is that as aluminium has a high stacking fault energy, dislocation climb and cross-slip are easy, leading to

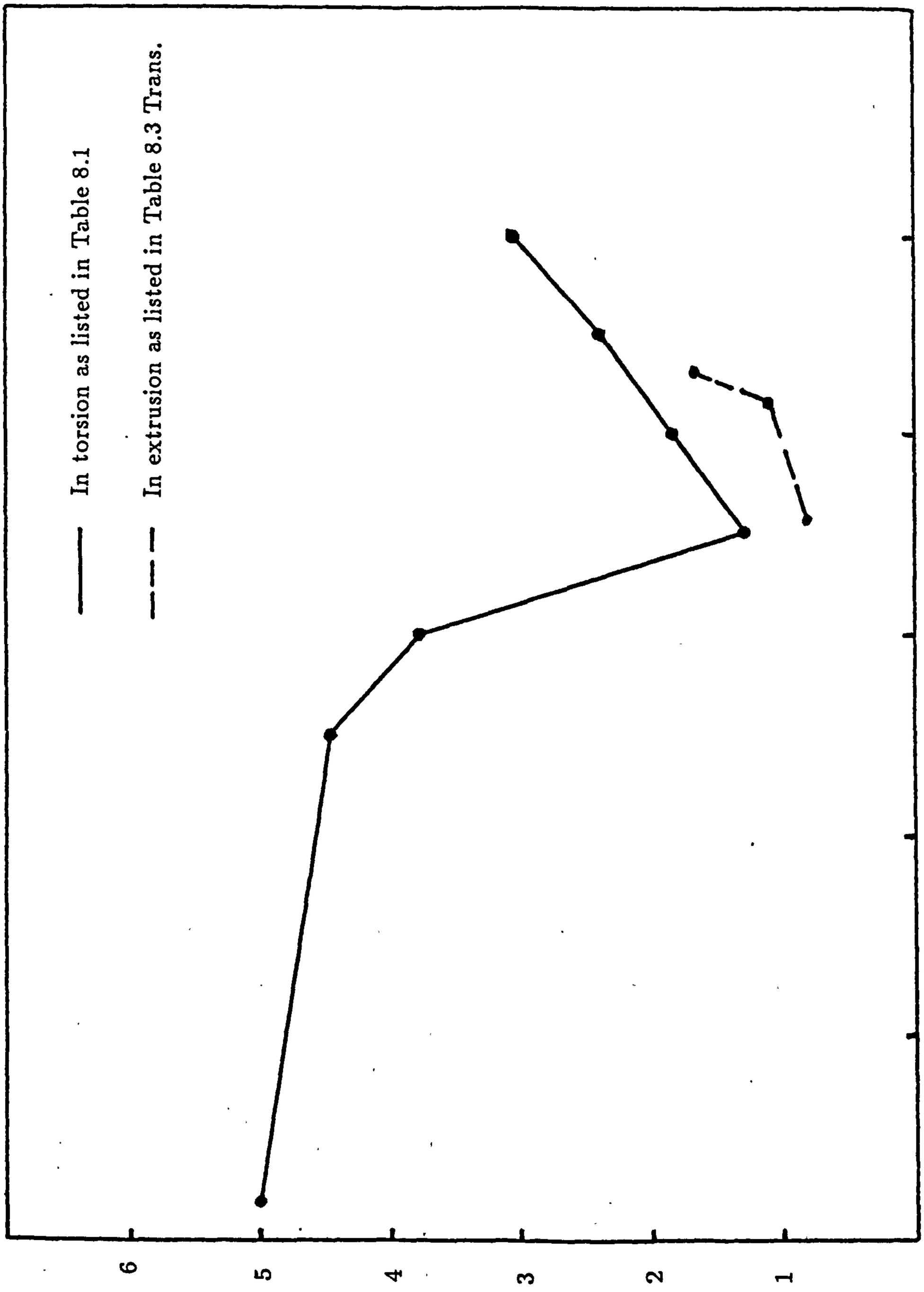

Fig. 8.1 Subgrain size versus temperature in torsion and extrusion

a high degree of dynamic recovery which retards dynamic recrystallization. In addition, the evenly distributed fine dispersoids in the matrix may also retard recrystallization by pinning grain boundaries.

Thermal markers in torsion tested solid material are:

1. At 300°C precipitate free zones start to form.
2. At 350°C banding and extensive precipitate free zones appear.
3. At 411°C severely distorted grains, lower dislocation density in subgrains and large rod like θ precipitates indicate that the material is in its softest state.
4. At 450°C extensive precipitate dissolution and heavily banded microstructure present.
5. At 500°C specimen is unrepresentative due to small strain to failure.

8.1.4 Limit of torsion test temperature

Three specimens tested at 545, 550 and 552°C at shear strain rates of 0.8, 1.7 and 3.4 respectively failed after little strain (Plate 14). Plate 15 shows typical longitudinal microstructures in such material. Most of the second phases have dissolved, some insoluble constituents formed during solidification remain in the matrix aligned in the original hot working direction. However also obvious are regions of incipient melting, especially at grain boundaries.

So the temperature of 550°C is not a useful testing temperature due to the onset of incipient melting which produces the fibrous failure effect. This temperature represents an absolute upper thermal limit to processing. It will be shown later that in extrusion the more aggressive stress system on die exit reduces this thermal limit significantly.

8.2 Analysis of microstructure in compression tests

8.2.1 Microstructure analysis of as received powder

Powder material is usually produced by gas atomization with cooling rates of $10^4 - 10^6$ K/s. As the powder is atomized from molten liquid to produce solid, undercooling occurs, resulting in a fine cast structure. Optical and scanning microscopy show mostly round particles with fine dendritic or cellular microstructure and segregation at the submicron level which is in agreement with other work [110,28]. Plate 16 shows the fine and coarse powder materials. Dendritic or cellular solidification structures are shown throughout the particles. No outer rim of fine cells can be seen at the periphery compared with other observations [90,27]. This demonstrates that the cooling rate must be very high so that the nucleation of dendrites at the oxide film and within the liquid droplet occurs almost concurrently. These high cooling rates also provide that a great amount of the alloying elements are in solid solution and other second phases are of very fine structure. Compositions for the coarse and fine powders have been listed in Table 2.4.

8.2.2 Microstructure of compression tested specimens

The microstructural change from the hot compacted structure to a fully hot worked structure can be examined in the hot compression test specimens. Coarse powder was used for the compression tests. The procedure and shape of the test specimen have been described in Section 3.4 and the flow stress relationships have been analysed in Section 5.4 and 5.5.

As a control, several solid specimens were also tested in plane strain compression, even though hot torsion data was available. The data obtained is comparable whatever the test method, as shown in Section 5.5. Plate 17 shows the powder specimens. Each column shows specimens tested at same strain rate and final strain but different temperatures. Because the powder compact has low resistance to secondary tensile forces, cracks and breaks occur outside the compressed regions. The cracking increased with increasing strain and strain rate as shown in

each row. It is thought that the accomplished strain effects predominate. There appears to be a similar ductility maximum to that observed in the torsion testing of solid material between 400 and 500°C and at the highest strain rates it occurs closer to 400°C.

The compression specimens were preheated for half an hour at the testing temperature.

Plate 18 is the microstructure taken from the non-deformed part of a compression test piece after being heated to the highest test temperature of 550°C and quenched. Even at this temperature the original powder particles are clear. Grains within each powder particle can be seen. However the dendritic or cellular cast structure has disappeared. Most of the alloying elements in the fine interdendritic segregation have been dissolved into solid solution except some which form insoluble second phases during solidification. There is also some evidence of fine dispersoids in the microstructure.

Plate 19 and 20 show medium and high magnification microstructures of specimens tested at different temperatures and strain rates. Plate 21 shows a low magnification survey of the specimen from the medium strain and strain rate tests. Different strain rates ($\dot{\epsilon}$) are also associated with different final strains (ϵ). At 250°C the second phases from the as cast structure (Plate 16) are distributed throughout the matrix after modest amount of strain (0.8). Some of the powder particles, separated by aluminium oxide film remain obvious but most of the powder particles have been welded together. By a strain of 1.6 the prior particle boundaries are destroyed and the aluminium oxide films have been fragmented. Further strain (2.4) gives a similar but more uniform structure. At 300°C the situation is comparable. Some second phase particles seem to have coarsened.

At 400°C and low strain (0.8) the powder particle boundaries are very evident probably due to coarsening of precipitates on them. However, at a strain of 1.6 the microstructure starts to take on a banded appearance (see later in Plate 21) where some finer particles have been taken into solution. Coarse constituent particles have aligned in the deformation direction and other large and small second phase

particles are distributed randomly in the matrix.

Up to this temperature no new grains can be seen in the structure. However this test configuration allows analysis of the microstructure at high strains and high temperature. At temperature of 500°C and a strain of 0.8, a new structure which has never appeared before is displayed (see Plate 20). Powder particles remain as usual at low strain but grains within powder particles have appeared. At a strain of 1.6 the powder particles are so elongated that a banded fibrous structure is formed (see Plate 21). Recrystallized grains can be seen and the second phase particles are evenly distributed in the matrix. This indicates that at this temperature and strain, dynamic recrystallization has begun. At a strain of 2.4 fragmented aluminium oxide film can be seen along the powder particle boundaries and dynamic recrystallization is so extensive it refines the structure.

At 550°C a similar situation arises but more recrystallized grains are present. There are regions within the specimen that exhibit regions of incipient melting (bottom centre). However elsewhere (bottom right) fully equiaxed recrystallized grains are formed.

In summary prior powder particle boundaries are destroyed by a strain of 1.6 at all temperatures. Banding begins at 400°C. This feature is displayed extensively at lower magnification in Plate 21. Dynamic recrystallization begins at 500°C producing equiaxed new grains. Incipient melting occurs at 550°C.

Plate 22 shows the effect of temperature on the subgrain form, precipitate structure and dislocation structure in the powder at medium strain (1.6) and strain rate (3.4 /sec). The two specimens tested at 250°C and 300°C, possess a subgrain structure. Some high angle powder particle boundaries are also present which may be decorated with alumina [182,183]. The subgrains are formed within the original grains. This is indicative of a dynamic recovery process. Because the temperatures are low, only dynamic recovery has occurred and dynamic recovery rates are slow so a small subgrain size is produced.

The specimen tested at 400°C demonstrates a slightly different feature. The microstructure again shows subgrains with low contrast (this can be compared

with the specimens tested at 550°C and 500°C later). The lack of good contrast between the subgrains gives an indication that they are subgrains with low misorientations between them. A significant level of precipitates remain in the specimen of $\approx 0.1\ \mu m$ size. In the range 250 to 400°C the recovery processes are more effective. The driving force for recovery is the reduction in strain energy which is accompanied with dislocation rearrangement and hence a decrease in dislocation density [181]. The amount of recovery is a balance between the generation and annihilation rate of dislocations. At lower temperature, when strain is applied, dislocation density increases, dislocations get tangled, dislocation mobility and rearrangement ability decrease so the rearrangement of dislocation subboundaries is limited. Since the temperature is low, dislocation climb and cross-slip are not easy, hence the microstructures show only a poorly recovered structure and small subgrain size. At higher temperatures dislocation cross-slip and climb processes proceed faster, thus facilitating dislocation subboundary rearrangement. So the rate of annihilation increases and leads to a higher amount of recovery. After this extensive dynamic recovery, substructures become more fully polygonized and subgrain boundaries are narrower and well defined. The subgrain size therefore increases with increasing temperature.

At 500 and 550°C dynamic recrystallization has occurred. The grains show good contrast which indicates that they are recrystallized grains. At 550°C the recrystallized grains are slightly elongated. At these higher temperatures, firstly dynamic recovery occurs and subgrains form. As strain proceeds, dislocation density increases. Dislocations are further attracted to such subboundaries whose misorientation gradually increases until they build up a high misorientation and can migrate freely. Some become active nuclei for dynamic recrystallization to form new, comparatively perfect grains. Then, in the newly formed grains, dynamic recovery continues to take place as the deformation continues and new recrystallized grains eventually form again [75]. Finally, when the deformation has finished, the structures may be recrystallized but with some evidence of recovery. Because the compression test pieces were quenched with water inside the press immediately

after testing, there is little time for static recrystallization. So dynamic recovery and recrystallization are the operating softening processes here. At 500°C the structure looks similar but with less well defined dislocation networks and perhaps some residual precipitates.

Some conclusions can be drawn from these compression tests for powders:

1. Powder particle boundaries remain at low strains (0.8) at all temperatures.
2. High strains (2.4) remove powder boundaries at all temperatures.
3. At medium strain (1.6) powder boundaries remain below 300°C.
4. These critical strains compare well with extrusion work.
   Chare [107] reported a critical extrusion ratio which must be exceeded and McShane et al [103] reported that a natural strain of 2.3 was necessary to obtain complete welding between particles for commercially pure aluminium powder and this value should be applicable for aluminium alloy.
5. The operative mechanisms in powder deformation are dynamic recovery and recrystallization. At 400°C and below dynamic recovery is the main deformation mechanism. The lower the temperature the less well defined are the subgrain structures and dislocation rearrangements. At 500°C and above dynamic recrystallization dominates although it may begin slightly at 400°C.
6. Modest strain, localised variations in degree of recrystallization and grain growth produce very banded microstructures in the range 500°C – 550°C.
   At 400°C banding just begins.
7. At 550°C incipient melting is observed.
8. In the range of 400°C – 500°C the rapid recovery and modest recrystallization effects coupled with the concentration of most solutes in coarse precipitates (i.e. no significant solution hardening) produce a ductility maximum in plane strain

compression. This is of little consequence in extrusion but would be very important in powder forging.

9. Dynamic recrystallization is triggered in these tests because high strains can be achieved at high test temperature. These combinations were not possible in the torsion testing of solid material.

Thermal markers in hot plane strain compression tests are:

1. At 400°C banding begins.
2. At 500°C extensive banding by recrystallization and grain growth begins. Most soluble particles dissolved.

8.3 Analysis of microstructure of extruded solid product

8.3.1 Microstructure changes with temperature

Most aluminium alloy products are produced by hot working. The properties of such hot deformed material are very dependent upon the characteristics of the microstructure formed by the hot working process. It is essential to know the final microstructure of the product in order to understand its properties. It is also important to know how the microstructures change before, during and after extrusion in order to describe how the process influences the properties of the product. The microstructure of the "as received" ingot has been described in Section 8. 1. 1 and extrusion conditions have been described in Section 3. 1. 2. Five typical extrusions extruded at different temperatures but identical ram speed and same extrusion ratio are chosen for comparison. The extrusion conditions are listed in Table 8. 2 and are chosen to cover the range from good extrusions to

No.	Ti (°C)	Vr (mm/sec.)	R	$\dot{\epsilon}$	Te (°C)	Tx (°C)
1	250	7.25	20	1.65	218.5	355.9
2	400	7.20	20	1.64	317.3	415.8
3	450	6.87	20	1.56	344.0	432.0
4	500	7.20	20	1.64	398.0	477.0
5	553*	7.04	20	1.60	427.9	497.5

* Container temperature was estimated at 180°C.

Table 8.2 Extrusion conditions of five solid extrusions

ones where hot shortness occurs as shown in Plate 23. This range was chosen to demonstrate the full thermal effects on microstructure.

Plate 23 shows the extrusions listed in Table 8.2 numbered 2 – 5. There is marked difference in the surface quality among these extrusions. When lower temperatures are employed the surface quality is good. At billet temperatures below 450°C an acceptable good surface condition can usually be obtained unless extremely high ram speed is imposed. At the higher billet temperature of 500°C the extrusion is severely surface cracked. At the highest temperature the extrusion is split for nearly half of the length.

Plate 24 is for the five extrusions listed in Table 8.2 at very low magnification. The microstructural changes across half sections can be seen. Specimens were cut 30% from front. Because No.5 was split, the specimen was taken slightly further back. A very interesting phenomenon is noticeable that in the transverse section at all temperatures. The deformation area is divided into several regions as two distinct rings can be seen. The outer ring relates to the intense shear that occurs at the edge of the dead metal zone. This region contains higher dislocation density and more deformation energy. Inwards the section has less shear except for another intense shear region, a ring near the inner core. The outer skin of the billet contained large grains as shown in Plate 2. These arose during initial hot working. The shear is sufficient to obliterate these grains as shown at the lowest temperature of 250°C. However at higher temperatures recrystallization

and grain growth restore an outer layer of larger grains. The precise origin of the inner high shear ring is unknown but this also causes a ring of large grains at high temperature. Hence in solid extrusion the final microstructure is non-uniform. These different shear regions were not observed in powder extrusion which indicates that powder extrusion can provide a more uniform structure.

Hence for solid material with an initial billet temperature of 250°C, (Tx=356°C), produces a very fine structure. When higher initial billet temperatures are employed, the microstructures change dramatically. By 400°C, (Tx=416°C), the outer ring of the extrusion has a surface layer of recrystallized grains present. They are most probably formed statically during cooling after the extrusion left the die. Recrystallization occurs preferentially in regions where the deformation was severe. In addition, the friction between the billet and container wall enhances the local temperature in this region [23]. Dynamic recovery occurs first in this region. However the fine second phase particles pin dislocations and subgrain boundaries and retard dynamic recrystallization. After the extrusion exits the die the stored plastic strain energy can cause static recovery followed by static recrystallization. At the extreme surface the strain rate should be at the highest and this results in finer grains and smaller grain size. Inside the core of the extrusion the rate of dislocation generation and annihilation is in equilibrium and dynamic recovery has sufficiently reduced most of the deformation energy provided by the external force.

At an initial billet temperature of 450°C, (Tx=432°C), Plate 24 illustrates that more static recrystallization has occurred at the periphery and the recrystallized layer is deepened. Recrystallized grains have grown and elongated in the extrusion direction. In the core a fibrous recovered structure is present.

When the initial billet temperature has been raised to 500°C, (Tx=477°C), a fully recrystallized structure becomes apparent. It is accompanied by hot shortness since the surface layer is cracked when the product exits the die. Because the temperature is so high static recrystallization follows recovery throughout the whole cross section. Recrystallized grains have completely replaced the recovered

structure, hence the fibre structure has disappeared. At the centre of the extrusion some recrystallized grains are large because of the slow cooling and lower strain rate.

At 553°C, (Tx=497.5°C), large recrystallized grains occur in the surface layer and in the inner high shear annulus. Because this sample was very hot short the specimen was taken further back along the extrusion. It is therefore representative of the structure between 450°C and 500°C where a mixed microstructure results. This is dynamic recovery with static recrystallization in the highly strain regions.

Plates 25 – 27 show higher magnifications of inner core microstructures for these extrusions. The fibrous structure results from the elongated original high angle boundary grains after the severe shear.

At higher magnification coarse precipitates are randomly distributed in the matrix and coarse intermetallic constituent particles remain from casting, aligned in the extrusion direction. Particle coarsening and dissolution follow the trends established in Section 8.1.2 and 8.1.3. No recrystallization and detailed grain or subgrain structure can be seen in the optical micrograph. The absence of recrystallization indicates that even static recrystallization did not occur as the extrusion was not quenched after the extrusion exited from the die. However the electron micrographs in plate 28 reveal the further microstructural detail. At 250°C, very fine equiaxed subgrain structure is present in the transverse section while in the longitudinal section a band of subgrains contained in an elongated grain can be clearly seen. The subgrains are aligned in the extrusion direction and are bounded by original grain boundaries of high angle. In spite of this, the subgrains are almost equiaxed indicating that these subgrains are formed dynamically. The ragged subgrain boundaries indicate that the subgrains are poorly recovered subgrains. The absence of static recrystallization is indicative that dynamic recovery is the only dynamic softening process. Many fine dispersoids and other second phase particles are evident. Plate 29 reveals the dislocation and precipitate structure. Many dislocations are attracted to the subgrain boundaries forming dislocation walls. This high dislocation density is consistent with the poorly recovered subgrains.

At 400°C the fibrous structure is still present. Banding is more extensive (Plate 25) and compares well with that in torsion (Plate 10). This fibrous structure may show a possibility that the bands may be caused by alternating recrystallized grains and deformed structures. Higher magnification reveals this structure (Plate 26). It can be seen that some tiny recrystallized grains have nucleated in both transverse and longitudinal sections. The dark area consists of many tiny recrystallized grains. The great number of grain boundaries etched forming the shading. Examination of this area carefully shows that these recrystallized grains occur preferentially at coarse constituent particles and probable original grain boundaries. Obviously these coarse constituent particles provide nuclei for this static recrystallization. Because these particles are aligned in the extrusion direction so the recrystallized grains follow this pattern, thus fibre is formed. The light area is the deformed structure, where there is lack of coarse constituent particles, i.e. a lack of nuclei so recrystallization does not occur. At this temperature it still can be seen that even in the light area, if there are some large particles, recrystallized grains have formed there. The fibre structure is sandwiched by banded regions of recrystallized grains which appear dark and regions of recovered structures which appear light. This recrystallization must be static and commence immediately after the extrusion emerges from the die or even in the die–land region where the temperature is high. As the temperature drops recrystallization ceases and results in tiny recrystallized grains alongside recovered structures. Coarse constituent particles again align in the extrusion direction. Electron micrographs (Plate 28) reveal the subgrain structure. The lack of contrast between the subgrains again indicates that they are of low misorientation. In the recrystallized area there are no small grains and dislocations can hardly be seen. The subgrain size is increased and the subgrain wall has been improved. Subgrain boundaries are well defined and narrower as a result of enhanced thermal activation. This is indicative of greater recovery. The subgrains are almost equiaxed even in the longitudinal section even though the materials have undergone ten, twenty or more times elongation. It has been proposed [171,156,64,60,85,81] that the subgrain boundaries

have to disintegrate and reform at the equilibrium spacing continually in order to relocate themselves. Dislocations are pushed out of subgrain boundaries by the external stress and become mobile. The mobile dislocations intersect and disrupt the subgrain boundaries. So the subgrains are broken up by the flux of dislocations. Then dislocations are attracted to the area where dislocations are dense in a climb-controlled process and annihilate there. The remaining dislocations rearrange themselves (repolygonization) forming new subgrain boundaries at the equilibrium spacing with approximately constant dislocation density and misorientation. So long as the rate of generation and annihilation are balanced, dislocation density and subgrain size remain constant. It is also suggested [171,60,81] that the high concentration of vacancies produced by the strain during deformation, enhances dislocation climb and hence recovery. In Plate 29 the dislocation array forms neatly on the subgrain boundary and the other area is nearly dislocation free indicating that the dislocations generated within subgrain tend to move towards an existing subgrain or to form a subgrain boundary. The individual dislocation spacing is larger than at lower temperatures. Precipitates are also larger giving evidence of the higher deformation temperature.

At 450°C wider banding occurs and some recrystallized grains are larger. It can be seen in Plate 26 that the shaded area is associated with significant numbers of the coarse constituent particles while the light area has less of coarse particles and so no recrystallized grains. Plate 28 (bottom right) shows the subgrain structure. A series of subgrains within an original grain can be seen. Precipitates are quite coarse. Dislocations are extensively pinned by precipitates showing how precipitates act to inhibit dynamic recrystallization. Plate 29 (bottom) shows even wider dislocation spacing and coarse particles.

At 500°C the extrusion has recrystallized (Plate 25). This can be compared with the torsion test at 500°C (Plate 12) which also displayed clear precipitate free zones. This indicates that at this temperature (the calculated temperature at steady state is Tx=477°C) precipitates start to dissolve into the matrix forming wide precipitate free zones. Both specimens show that precipitate dissolution is

almost complete. The white etching precipitate free zones are obvious in both specimens. This indicates that the deformation temperature Tx is certainly $\leq$500°C. If it were significantly higher then the extrusion would look like the one extruded at Ti=553°C and not like that torsion tested at 500°C. This is again a useful check on the thermal model.

The final microstructure on Plates 24 – 27 which was selected further down the extrusion with much lower actual temperatures than those quoted consists of a mixture of recrystallized grains and deformed structure. Since the temperature is high, dynamic recovery has occurred rapidly. This rapid recovery expended most of the stored energy at the centre of the extrusion. The larger recrystallized grains (Plate 24) may result from different nucleation and growth conditions than those which prevailed at Ti=500°C.

In summary, the above examinations show that aluminium alloys which have high stacking–fault energy only undergo dynamic recovery during hot working condition as has been well documented [70,55,68,52,66,73]. In addition, the material in this investigation, has got numerous fine dispersoids which can pin the dislocations and subgrain boundaries to impede subgrain migration and hence inhibit dynamic recrystallization. This phenomenon has been investigated by many researchers [186,119,120,177,121,66] who suggest that the fine dispersoids ($< 0.1\mu m$) can retard recrystallization. They interfere with dislocation movement and inhibit grain growth and migration. There are also some large size particles produced during solidification. These large particles ($> 1\ \mu m$) generally act as sites for the nucleation of recrystallization. So the nett effect of particles depends on their size and spacing, initial grain size and deformation mode [186]. In this material the small particles are present in large numbers and are very closely spaced which can inhibit dynamic recrystallization. So that the only dynamic softening is dynamic recovery. Dynamic recovery leads to formation of subgrains and the subgrain size increases with increasing temperature and is a basic function of the Zener-Hollomon parameter, the temperature compensated strain rate.

$$d^{-1} = a + b \log Z$$

Ti (°C)	Tx (°C)	Trans.	Long.
		subg.dia. μm	subg.dia. μm
250	355.9	0.84	0.85
400	415.8	1.12	1.17
450	432.0	1.67	1.72

Table 8.3 Subgrain sizes at different temperature

$$Z = \dot{\epsilon}\, exp(\frac{\Delta H}{RT})$$

Plate 28 is a good example of the subgrain size increases with increasing temperature. Subgrain sizes were measured by using an linear intercept method and are shown in Table 8.3.(also see Fig. 8.1) It is clear that with increased temperature, the value of Z decreases and subgrain size increases but flow stress decreases.

After the extrusion exits from the die, static recovery and partial or full static recrystallization occurs. Because static recovery and recrystallization are thermally activated processes they are dependent on temperature, previous strain and previous strain rate. They occur preferentially at surface layers where the strain and temperature are highest. It is reported [74] that 50% or more of the total stored energy can be released during recovery. Afterwards depending upon the total stored energy, temperature and cooling rate static recrystallization may follow static recovery.

8.3.2 Microstructural changes due to temperatures generated by increased strain and strain rate

It is important to know how various deformation parameters affect Tx and hence the microstructure. As an example two billets with the same initial temperature have been selected. The precise extrusion extrusion conditions are listed in Table 8. 4.

Plates 30–34 are for these extrusions. The upper photos are at the lower strain and strain rate. The changes in structure are very obvious. When the extrusion

No.	Ti (°C)	Vr (mm/sec.)	R	$\dot{\epsilon}_f$	Te (°C)	Tx (°C)
1	375	6.87	10	1.225	306.4	382.4
2	375	7.08	30	1.82	307.	411.0

Table 8.4 Extrusion conditions for two solid extrusions

ratio is low, i.e. the strain rate is low, the result is a very fine structure with severe shear on the periphery. The structure is predominantly recovered. Subgrain boundaries within the dark etching grains are revealed but not those within the original white (unetched) grains (Plate 32). At the high magnification some static recrystallized grains can be seen optically. Transmission electron micrographs (Plate 34) reveal the subgrain and dislocation structures. Neat dislocation arrays form at subgrain boundaries.

At the higher strain and strain rate (lower photos) a different fully recrystallized structure is seen except at the centre. This is due mainly to the higher temperature Tx generated during extrusion. The high degree of deformation also accelerates recrystallization and increases the number of nuclei. When this extrusion left the die, the stored energy was much higher than the former one. Static recovery and recrystallization occurred rapidly and the extrusion is nearly fully recrystallized. In the longitudinal section the recrystallized grains are elongated in the extrusion direction. Sellars et al [177] have annealed hot rolled aluminium alloy at 600°C for six days and the recrystallized grains were still slightly elongated in the original hot working direction. Paterson et al [34] have solution treated Al-2014 extrusion at 500°C for half an hour and obtained elongated recrystallized grains. After such static recrystallization, the temperature is still high so grain growth may occur. However, as this material has got numerous fine dispersions which can pin grain boundaries and impede grain growth, abnormal grain growth may occur especially if some grains can overcome the local pinning and migrate. Plate 32 and 33 show a large recrystallized grain that has swept to another area in order to reduce the grain boundary area and hence reduce the energy.

Plate 34 shows subgrains taken from the recovered parts of both extrusions.

No.	Ti (°C)	Vr (mm/sec.)	R	$\dot{\epsilon}$	Te (°C)	Tx (°C)
1	250	8.10	20	1.83	232.1	347.1
2	400	7.90	20	1.79	300.7	359.6
3	450	7.76	20	1.76	324.0	376.8
4	500	7.50	20	1.70	347.7	396.7
5	550	7.50	20	1.70	374.3	421.4

Table 8.5 Extrusion conditions of fine powder extrusions

There seems to be a slightly reduction in subgrain size at the higher strain rate.

8.4 Microstructures in extruded powder product

Powder material is usually extruded into engineering materials such as wrought bars since fully densification can be obtained during extrusion. Some of the bars go to further fabrication and the remainder go into service as extruded. 2014 powder material used in the present investigation is a candidate matrix for metal matrix composites. It is therefore important to know the microstructures of typical extruded products.

For the fine powder extrusions, five extrusions extruded at different temperature and same extrusion ratio with identical ram speed are selected for comparison. (see Table 8.5) All surface finish conditions were good unlike the solid material under almost identical conditions. Specimens were cut from the extrusion products at 30% along the length from the front. Under different extrusion conditions, the products show different structures. Microstructures were all taken from the centre of the extrusion. However this was not essential as the extensive structure variations observed in solid extrusion were not seen in the powder product. This is considered to be a distinct advantage in high performance alloys.

Plates 35 – 36 are for these extrusions. All extrusion microstructures show fine structures. (compared with solid extrusions) The structure is homogeneous across the whole cross section. Powder particles are completely welded together because the minimum strain (1.6) is exceeded at this extrusion ratio (R=20). The oxide

No.	Ti (°C)	Vr (mm/sec.)	R	$\dot{\epsilon}$	Te (°C)	Tx (°C)
1	411*	7.44	20	1.67	313.4	371.5
2	552**	6.87	20	1.56	391.0	462.9

* Container temperature estimated at 180°C, die shape rect. 25 x 10mm.
** Container temperature measured at 234°C, die shape ϕ18mm.

Table 8.6 Extrusion conditions of coarse powder extrusions

film is fragmented and aligned in the extrusion direction. At 250°C, no detail of structure can be seen except some big intermetallic particles and some fragmented oxide aligned in the extrusion direction. No recrystallized grains can be seen. This indicates that at this low temperature static recrystallization did not occur.

At 400°C, a fine structure is also obtained. Careful examination of the matrix revealed some small recrystallized grains. This recrystallization probably occurred during cooling and was rather static than dynamic. Because the temperature is not high static recrystallization ceased quickly resulting in a finer structure with some recrystallized small grains. In Plate 39 (top right) the TEM picture shows the subgrain and dislocation structure. The subgrains are nearly equiaxed indicating they are formed by dynamic recovery.

At 450°C, local recrystallization occurred producing banded microstructures. At even higher temperatures (500°C and 550°C), a nearly fully recrystallized structure is present. However, these recrystallized structures are different from those produce in compression tests at and above 500°C. As the calculated Tx for these two extrusions are only 396.7°C and 421.4°C respectively these structures are probably the result of static recrystallization.

Plate 37 and 38 are for the coarse powder extrusions listed in Table 8.6. Both surface finish conditions were good. These plates show much coarser structures compared with the fine powder extrusions.

At an initial billet temperature of 411°C the structure shows mainly a recovered structure with recrystallization confined to the very coarse particles. It is suggested

that the lower levels of alumina and other second phase particles in these regions promotes recrystallization. As the calculated temperature at the start of steady state is 371.5°C, we can compare this structure with the plane strain compressed structure at 400°C, this recrystallization may be static. Plate 39 right column bottom 2 pictures show the subgrain and dislocation structures. The subgrains are approximately equiaxed with almost evenly distributed second phase particles. The second phase particles are almost round in shape and some of them are on the subgrain boundaries where they pin the boundaries. Dislocations are clearly seen and tangled inside the grains. These grains must have formed dynamically. The subgrains are in poor contrast indicating the low misorientation between them. Precipitate free zones are also present.

The extrusion at 552°C shows more evidence of fine scale recrystallization. The fine recrystallized grains can be seen optically. In the longitudinal section, a large powder particle is elongated (Plate 37 right bottom). The severe shear has broken the oxide layer coating on the particle and exposed the nascent metal. The fragmented oxide film can be seen on the boundary of the particle. However a nearly complete powder particle is observed. This powder particle must have been elongated in the longitudinal direction. Inside the particle, recrystallized grains can be found. A similar phenomenon has been observed by other workers [185]. When they extruded powder billet at temperature of 390°C they were able to trace individual particles within the structure.

The TEM (Plate 39 left column) demonstrates the equiaxed recrystallized grains and dislocation structure. The recrystallized grains are very fine and almost equiaxed even in the longitudinal section (centre micrograph). These grains have good contrast indicating that they have high misorientation and probably possess high-angle boundaries. Whether these recrystallized grains are dynamically or statically formed is difficult to determine because the extrusion was not quenched after it exited from the die. Final microstructures are dependent on the extrusion condition also the cooling [155]. However, the dislocations inside the grains and the very neat dislocation network on the twist boundary in Plate 39

(bottom left) indicate that these grains may first dynamically recover, followed by subgrain growth or may partially recrystallize before static recrystallization occurs after the product leaves the die. Because there are great many oxide fragments and small dispersoids in this material, these small particles can effectively pin sub-grain boundaries, retard dynamic recrystallization and subgrain growth [186]. So dynamic recrystallization may be limited. Compare this with the microstructure from plane strain compression tests, the one tested at 500°C, strain of 1.6 and strain rate of 3.4 was dynamically recrystallized. Hence dynamic recrystallization may have occurred in this extrusion. The calculated temperature in the steady state regime is 462.9°C. At this temperature static recrystallization will definitely occur after the material leaves the die. These small particles and oxide fragments will act to prevent grain growth so the recrystallized grains are fine.

The fine powder extrusion structure is much finer than the coarse powder extrusion. This must be caused by the original microstructure of the fine powder particles. The fine powder provides a better distribution of aluminium oxide film. Also in the fine powder particles, the cellular cells are finer which will give finer second phase precipitates and greater distribution of the dispersion, leading to grain refinement. Clearly for high performance alloys the existence of areas of large grain size are to be avoided and the finer powders will give more uniform matrix properties.

In summary, powder particle boundaries which remain in the compacted billet are destroyed in both fine and coarse powder extrusions because the threshold strain has been exceeded. The destruction of the cast microstructure begins in the preheat and continues during the deformation as the particles are sheared during their passing through the deformation zone. Large static recrystallization regions were never observed as in solid material. Dynamic recovery was the predominant restoration process at low temperatures assisted by dynamic recrystallization at high temperatures. Static recrystallization may also occur after high temperature extrusion but the recrystallized grains are very small and uniform.

8.5 Comparison of solid and powder extrusion limits

Plate 40 shows solid and powder extrusions extruded at identical conditions. As previously described in Sections 2 .1 .6 and 2. 1. 7 and 8.4 this plate gives direct evidence that the extrusion limit for powder is widened. The solid one is split but the powdered one is sound. The extrusion pressure for powder is lower than that for the equivalent solid hence less heat is produced during extrusion. This means that the extrusion range is extended. This allows higher initial billet temperatures for the same extrusion ratio. This may be advantageous in that it gives better homogenization possibilities and more flexibility over the extruded microstructure. In this work only the powder route enabled recrystallization throughout the section without hot shortness on the surface. The uniformity of the product microstructure is also a distinct advantage of the powder route.

Chapter 9

CORRELATION OF EXTRUDED MICROSTRUCTURES WITH REFERENCE MICROSTRUCTURES USING Tx

9.1 Correlation for solid material

The microstructure analysis of torsion specimens provides an atlas of microstructure under hot working conditions for this aluminium alloy. Because the torsion specimens were quenched immediately to room temperature after deformation, this structure represents the real hot working structure. The analysis shows that dynamic recovery is the restoration process during hot working of solid material.

This atlas and the atlas from heat treatment of the alloy give a good guide to the microstructures in extruded materials. In extrusion the easiest parameter to change is usually the initial billet temperature. However this temperature is not a reliable control parameter because of the temperature changes that occur during extrusion. The model calculates the temperatures at the start of steady-state condition and provides a basis for control and comparison.

The use of the thermal model is best demonstrated with the lowest temperature extrusion. The structure from the solid extrusion at an initial billet temperature of 250°C (Plate 25) bears no resemblance to the torsion specimen tested at 250°C

(Plate 7). Extensive precipitation is visible in the optical micrographs of the extrusion but not in the torsion specimen. This is not surprising as the calculated temperature at the start of steady-state is 355.9°C. The microstructure compares very well with the specimen torsion tested at 350°C (Plate 9) in both optical and electron micrographs. The size of precipitate, the fibrous structure and the subgrain in transverse section are also quite similar. This indicates that the calculated Tx is more accurate than the initial billet temperature in predicting the microstructure that will be formed.

Further comparisons can be carried out for extrusions at higher temperatures. At an initial billet temperature of 400°C, the extruded structure is like that torsion tested at 400°C (Plate 10). Here Tx (416°C) is close to Ti(400°C) hence the comparison should be with that torsion tested at 400°C. The levels of banding in equivalent micrographs are similar as are the dislocation, precipitate and subgrain structures.

At an initial billet temperature of 450°C, the calculated Tx is 432°C. This microstructure compares well with the specimen torsion tested at 450°C (Plate 11), at lower magnification the elongated grains, the wider banding fibrous structure and the subgrains in the TEM micrograph are more or less similar. Without the thermal model correlation of Ti=450°C with the 500°C torsion structure might have been expected due to a temperature rise. However Plate 12 shows this is not to be the case. The optical micrographs at an extrusion temperature of Ti=500°C, Tx=477°C compare well with those on Plate 12 (500°C). The precipitate free zones at magnification of 108 (Plate 12) and those shown on Plate 26 are remarkably unique and similar.

The TEM at Ti=250°C, Tx=356°C (plate 28) compares well with the torsion test at 350°C (Plate 9). The basket work θ' precipitates evident at 300°C in the torsion tests (Plate 8) are not obvious in the extruded section. As predicted by the thermal modeld they have coarsened and changed morphology. Clear subgrain boundaries become obvious when Tx is 416°C (Plate 28) and this is also evident in torsion at 400°C (Plate 10). The precipitate in the extrusion (Tx=356°C,

Plate 29 top right) compares very well with the precipitate in material quenched from 350°C (Plate 5 bottom left). The large rod-like precipitates present in this extrusion did not occur in quenched material at 250°C but occurred at 350°–400°C. This indicates that the calculated Tx=355.9°C is more accurate than the initial billet temperature. The dislocation structure and subgrain structure at Tx=356°C (Plate 28) compares well with the torsion test at 350°C (Plate 9).

9.2 Correlation for powder material

Plane strain compression tests provide an atlas for powder materials. This can be used to interpret the microstructures of powder extrusions. As has been described in Section 8.4, for powder extrusions in the temperature range of 250 – 550°C, there is no evidence of the type of recrystallization shown in powder compression at and above 500°C as the calculated deformation temperature in extrusions were not this high.

At an initial billet temperature of 500°C, Tx is 396.7°C and banding just becomes obvious (Plate 35). This compares well with the compression specimen strained to 6.9 at 400°C (Plate 19). Without the thermal model it would not have been possible to predict and confirm that the dynamic recrystallization observed in compression testing would not be observed in extrusion even though initial billet temperatures covered the same range.

The model also allows quenched billet, extruded rod and compressed powder precipitate morphology to be compared (Plate 41). Here the precipitate morphology indicates that they are the same which in itself give the thermal model good credibility. The much bigger size of the precipitates in extrusion are thought to have occurred due to ripening which has been enhanced by the bigger strain (2.99) and slower cooling.

Chapter 10

CONCLUSIONS

This research programme on the extrusion of solid and powdered aluminium 2014 alloy has enabled the following conclusions to be drawn:

1. Successful prediction of microstructures and hot shortness limits in extrusion cannot be done from initial extrusion conditions.

2. It is possible to predict the critical temperature, Tx, during extrusion from upper-bound analysis, metal working data and some limited regression data obtained from the extrusion operations. This temperature is very useful in predicting extrusion limits.

3. Correlation of microstructural details between metalworking tests and extruded products has given an independent confirmation of the validity of the thermal model.

4. The extrusion range and the uniformity of product microstructure have been shown to benefit from the powder route.

5. This uniformity has been related to the different restoration processes that occur in the solid and powder materials.

6. Hot plane strain compression testing of partially consolidated powder material has been shown to be a useful alternative to hot torsion testing in the provision of metal working data.

Bibliography

[1] C.E.Pearson and R.N.Parkins "The Extrusion of Metals", Chapman and Hall, London, 1961

[2] G.W.Rowe "Principle of Industrial Metalworking Process", 1977

[3] G.Dieter "Mechanical Metallurgy" McGraw–Hill, 1976

[4] P.L.Charpentier et al *Metall. Trans.A 1986 Vol.17A P2227*

[5] S.Hirst and D.H.Ursell *Metal Treatment and Drop Forging 1958 Vol.25 P409*

[6] K.Ashcroft and D.Lawson *J. Inst. Metals 1960 Vol. 89 P369*

[7] B.J.Meadows, M.J.Cutler *J. Inst. of Metals 1969 Vol.97 P321*

[8] T.Sheppard and D.Raybould *J. of Inst. Of Metals 1973 Vol.101 P73*

[9] T.Sheppard and A.F.Castle *Proc. of 16th MTDR Conf. Manchester 1975 P535*

[10] M.G.Tutcher and T.Sheppard *Metals Technology 1980 Dec. P488*

[11] H.Stenger *Wire World Int. 1975 Vol.17 P54*

[12] S.J.Paterson PhD. Thesis University of London 1981

[13] A.R.E.Singer *Met. Industry 1962 Vol.100 P346*

[14] K.E.Hughes and C.M.Sellars *J. of the Iron and Steel Inst. 1972 Sept. P661*

[15] R.I.Tanner and W.Johnson *Int. J. Mech. Sci. 1960 Vol.1 P28*

[16] J.F.W.Bishop *Quart. J. of Mech. Applied Math 1956 Vol.9 P236*

[17] O.C.Zienkiewicz et al *Int. J. for Numerical Methods in eng. 1981 Vol.17 P1497*

[18] A.R.E.Singer and J.W.Coakham *J. of Inst. Metals 1960-61 Vol.89 P177*

[19] R.Akeret *Inst. of Metals 1967 P204*

[20] A.R.E.Singer and S.H.K.Al-Samarrai *J. Inst. Of Metals 1960 Vol.89 P225*

[21] F.W.Sharman *Metals Technology 1977 Vol.4 P91*

[22] A.F.Castle and T.Sheppard *Metals Tech. 1976 Oct. P454*

[23] T.Altan and C.H.Lee et al 'Approximate Calculation of Velocity and Temperature Distribution in Axisymmetric Extrusion and Drawing'.

[24] R.P.Vierod PhD.Thesis University of London 1983

[25] G.H.Tan and T.Sheppard *Mat. Sci. and Tech. 1986 Dec. Vol.2 P1233*

[26] G.J.Marshall et al *Powder Metall. 1986 Vol.29 No.1 P57*

[27] T.Sheppard and M.A.Zaidi *Matl Sci. And Tech. 1986 Jan. Vol.2 P69*

[28] G.H.Tan and T.Sheppard *Powder Metall. 1986 Vol.29 No.2 P143*

[29] T.Sheppard and R.P.Vierod *Mat. Sci. and Tech. 1987 April Vol.3 P285*

[30] N.C.Parson and T.Sheppard *Mat. Sci. and Tech. 1988 Sept. Vol.4 P816*

[31] G.H.Tan, M.A.Zaidi and T.Sheppard *Powder Metall. 1984 Vol.27 No.1 P3*

[32] A.F.Castle And T.Sheppard *Metals Technology 1976 Oct. P465*

[33] T.Sheppard and E.P.Wood *Metals Technology 1980 Feb. P58*

[34] S.J.Paterson and T.Sheppard *Metals Tech. 1982 Oct. Vol.9 P389*

[35] S.Carslaw and J.C.Jaeger *Phil. Mag. 1938 Vol.26 P473-95*

[36] A.Gemant *J. of Appl. Phiysics 1946 Vol.17 P1077*

[37] A.Greasley *PhD Thesis University of London 1976*

[38] W.Johnson and H.Kudo:"The Mechanics of Metal Extrusion" Manchester University press 1962

[39] J.F.W.Bishop *Metall. Rev. 1957 Vol.2 P361*

[40] W.J.McG.Tegart:"Elements of Mechanical Metallurgy" Macmillan New York 1966

[41] W.R.D.Wilson *Int. J. Mech. Sci. 1971 Vol.13 P17*

[42] A.W.Duffill and P.B.Mellor Proc. Inst. Mech. Eng. 1965-66 Vol.180 Pt.3 P260

[43] R.J.Wilcox and P.W.Whitton *J. of Inst. Metals 1958-59 Vol.87 P289*

[44] B.Avitzur: Metal Forming: Processes and Analysis 1968

[45] T.Sheppard et al *Metal Sci. 19798 Aug. P473*

[46] T.Sheppard *Metals Technology 1981 April P130*

[47] A.F.Castle And G.Lang *Aluminium 1976 Vol.52 P7-10*

[48] H.Kudo *Int. J. Mech. Sci 1960*

[49] J.Halling, L.A.Mitchell *Int. J. of Mech. Sci. 1965, Vol.7 No.4 P277*

[50] F.A.A.Crane:"Mechanical Working of Metals"

[51] L.C.Dodeja and W.Johnson *J. Mech. Phis. Solids 1957 Vol.5 P281*

[52] W.Johnson *J. Mech. Phys. Solids 1956 Vol.4 P191*

[53] M.M.Farag and C.M.Sellars *J. of Inst. Metals 1973 Vol.101 P137*

[54] W.A.Wong and J.J.Jonas *Trans ATME 1968 Vol.242 P2271*

[55] J.J.Jonas, H.J.McQueen and W.A.Wong *Special Report Iron and Steel Inst. 1967 P49*

[56] B.Avitzur *J. of Eng. for Industry 1965 Feb. p57*

[57] J.J.Jonas and T.Chandra *Metal Forming Interrelation between theory and practice 1971 P115*

[58] C.M.Sellars and W.J.McG Tegart *ACTA Metall. 1967 Vol.14 P1136*

[59] H.J.McQueen et al *Metal Sci. 1984 Aug. P395*

[60] J.J.Jonas, C.M.Sellars, W.J.McTegart *Met. Rev. 1969, Vol.14 P1-24*

[61] H.Ormerod and W.J.McG Tegart *J. of Inst. Metals 1963-64 Vol.92 P297*

[62] M.J.Luton and C.M.Sellars *ACTA Metall. 1969 Vol.17 P1033*

[63] H.J.McQueen *Micros. Sci. 1979 Vol.7 P71*

[64] J.P.Immarigeon, H.J.McQueen *Canadian Met. Quart. 1969, Vol.8 P25*

[65] T.Sheppard, M.G.Tutcher *Metals Tech. 1981, Aug. P319*

[66] H.M.Chan and F.J.Humphreys *ACTA Metall. 1984 Vol.32 No.2 P235*

[67] D.Harwick and W.J.McG Tegart *J. of Inst. Metals 1961 Vol.90 P17*

[68] H.P.Stuwe: Deformation under Hot-Working Conditions, Iron and Steel Inst. 1966 P1

[69] H.J.McQeen and J.J.Jonas *Metal Forming 1971 Vol.39 pt.3 P393*

[70] H.J.McQeen *Trans. JIM Vol.9 1968 P170*

[71] H.J.McQueen *Metall. Trans.A 1977, Vol.8A, June P807*

[72] P.Hollinshead and T.Sheppard *Mat. Sci. and Tech. 1987 Dec. Vol.3 P1019*

[73] W.A.Wong, H.J.McQueen and J.J.Jonas *J. of Inst. Metals 1967 Vol.95 P129*

[74] C.Yong et al *Mat. Sci. and Eng. 1986 81 P391*

[75] R.J.Arsenault:"Treatise on Materials Science and Technology" Vol.6 Academic press New York 1984

[76] T.Sheppard and M.G.Tutcher *Metal Sci. 1980 Vol.4 P579*

[77] T.Sheppard, N.C.Parson and M.A.Zaidi *Met. Sci. 1983 Oct. Vol.17 P481*

[78] W.J.McG.Tegart:"Ductility" Proc. of a Seminar of the American Society for Metals Oct 14-15 1967 P133

[79] T.Sheppard and D.S.Wright *Metals Technology 1980 July P274*

[80] P.Gay, P.B.Hirsch and A.Kelly *ACTA Metall. 1953 Vol.1 P315*

[81] H.J.McQueen, W.A.Wong and J.J.Jonas *ACTA Metall. 1967 Vol.15 P586*

[82] D.J.Abson and J.J.Jonas *Metal Sci. J. 1970 Vol.4 P24*

[83] J.Wert *Proc. of 6th Int. Conf. on Strength of Metals and Alloys(ICSMA 6) Australia 16-20 Aug. 1982 Vol.1 P339*

[84] J.J.Urcola and C.M.Sellars *ACTA Metall. 1987 Vol.35 No.11 p2649*

[85] H.J.McQueen and J.E.Hockett *Metall. Trans. 1970 Nov. Vol.1 P2997*

[86] D.Raybould and T.Sheppard *J. of Inst. Metals 1973 Vol.101 P65*

[87] A.Lawley and M.J.Koczak "A fundamental study of P/M processed at elevated temperature of aluminium alloys" 1984 Oct.

[88] R.D.Parkinson and T.Sheppard *Powder Metall. 1986 Vol.29 No.2 P135*

[89] S.C.Jha and R.Ray *Mat. Sci. and Eng. 1988 98 P475*

[90] M.A.Zaidi and T.Sheppard *Mat. Sci. and Tech. 1987 Feb. Vol.3 P146*

[91] T.Altan at al:"Metal Forming: Fundamentals and Application" American Society of Metals 1983

[92] H.Frost and M.F.Ashby "Deformation-mechanism Maps" pergamon Press 1982

[93] J.Weertman *J. of Applied Phys. 1955 Vol.26 Pt.10 P1213*

[94] D.Hughes et al *Mat. Sci. and Tech. 1988 Feb. Vol.4 P106*

[95] J.A.Walker and E.A Starke *Powder Metall. 1983 Vol.26 No.4 P185*

[96] T.Sheppard M.A.Zaidi and G.H.Tan *Powder Metall. 1983 Vol.26 No.1 P10*

[97] A.Lawley and M.J.Koczak: "A Fundamental Study of P/M Processed Elevated Temperature Aluminium Alloys" 1985

[98] *MPR April 1986 P294*

[99] F.F.Nia and B.L.Davis *Powder Metall. 1982 Vol.25 No.4 P209*

[100] L.Arnberg et al Int. J. of Rapid Solidification 1986 Vol.2 P55

[101] J.Duszczyk and P.Jongenburget *Rev. Powder Metall. Phy. Cer. 1985 Vol.2(4) P267*

[102] J.Duszczyk et al Proc. Conf. of Rapid Solidified Materials San Diego 1986 3-5 Feb. P57

[103] H.McShane, M.G.Tutcher and T.Sheppard *Powder Metall. 1978 No.2 P47*

[104] T.Sheppard and H.McShane *Powder Metall. 1976 No.3 P121*

[105] W.J.Johnson *J. of The Mechanics and Phys. of Solid 1956 Vol.4 P269*

[106] T.Sheppard and H.McShane *Powder metall. 1976 No.3 P126*

[107] T.Sheppard and P.J.M.Chare *Powder Tech. 1972 Vol.15 No.29 P17*

[108] P.J.M.Chare and T.Sheppard *Int. J. of Powder Metall. and Powder Tech. 1974 Vol.10 P203*

[109] M.Oyane et al *Bull. JSME 1973 Vol.16 P1254*

[110] R.D.Parkinson, T.Sheppard *Powder Metall. 1985, Vol.28 No.4 P189*

[111] P.D.Liddiard *Powder Metall. 1984 Vol.27 No.4 P193*

[112] E.C.Rollason:"Metallurgy for Engineers" Edward Arnold 1961

[113] T.Sheppard *Powder Tech. 1974 Vol.10 P257*

[114] U.V.Deshmukh et al: High Streng Powder Metallurgy Aluminium Alloys II, Proc. of a TMS-AIME Symposium on Al Powder Metall. 13-17 Oct. 1985 P100

[115] I.J.Polmear "Light Alloys" Edward Arnold, 1981

[116] Metal handbook Vol.7 P128

[117] A.R.Woodward "Aluminium and Aluminium Alloy Extrusion" Alcon Lab. Banbury, Oxon

[118] R.A.Ayres *Metall. Trans.A 1979 Vol.10A July P849*

[119] J.E.Hatch: "Aluminium Properties and Physical Metallurgy" American Society for metals 1984

[120] B.J.Dunwoody et al *J. of Inst. Metals 1973 Vol.101 P172*

[121] A.K.Gupta et al *Mat. Sci. and Tech. 1987 Dec. Vol.3 P1012*

[122] S.Ceresara and P.Fiorini *Powder Metall. 1981 No.4 P210*

[123] S.Lee and S.Wu *Metall. Trans.A 1987 Vol.18A Aug. P1353*

[124] L.F.Mondolfo:"Aluminium Alloys: Structure and Properties" Butterworths London 1976

[125] M.V.Lancker:"Metallurgy of Aluminium Alloys" Chapman and Hall London 1967

[126] H.J.Axon *J. of Inst. Metals 1952-53 Vol.81 P449*

[127] J.Nutting and M.A.P.Dewey *Heat Treat. Metals ISI 1966*

[128] C.V.Lynch *Int. Extru. Tech. Seminar 1969 March*

[129] A.G.Guy:"Physical Metallurgy for Engineers" Addison-Wesley 1966

[130] G.Thomas:"Transmission Electron Microscopy of Metals" John Wiley and Sons, London 1962

[131] R.B.Nicholson and J.Nutting *Phil. Mag. 1958 Vol.3 Pt.8 P531*

[132] J.Karov and W.V.Youdelis *Mat. Sci. and Tech. 1987 Jan. Vol.3 P1*

[133] J.Gronostajski and T.Tobota *Mat. Sci. and Tech. 1988 April Vol.4 P335*

[134] C.H.Samans:"Metallic Materials in Engineering"

[135] T.Sheppard et al:"Microstructural Control in Aluminium Alloys" Proc. of a Symposium of TMS in New York Feb.27 1985 P123

[136] C.M.Sellars *Alu. Transf. Tech. And Appli. 1978 P405*

[137] W.Johnson and P.B.Mellor:"Engineering Plasticity" Van Nostrand Reinhold London

[138] N.R.Draper and H.Smith:"Applied Regression Analysis"

[139] P.Feltham *Metal Treatment 1956 Pt.23 P440*

[140] J.H.Decroix et al: Deformation under Hot-Working Conditions, Iron and Steel Inst. 1966 P135

[141] J.F.Adie and J.M.Alexander *Int. J.Mech.Sci. 1967 Vol.9 P349*

[142] T.Altan and F.W.Boulger *J. of Eng. for Industry 1973 Nov. P1009*

[143] T.Altan and G.D.Lahoti *Annals. GIRP Vol.28(2) P473*

[144] J.F.W.Bishop and R.Hill *Phil. Mag. 1951 Vol.42 P414*

[145] D.S.Fields and W.A.Backofen *Proc-Amer. Soc. Test Mat. 1957 Vol.57 P1259*

[146] A.Nadai:"Theory of Flow and Fracture of Solid" McGraw-Hill 1950

[147] W.Precht and J.R.Pickens *Metall. Trans. 1987 Vol.18A Sept. P1603*

[148] R.Akeret et al:"Atlas of Hot Working Properties of Nonferrous Metals" Vol.1: Aluminium and Aluminium Alloys

[149] D.R.Barraclough et al *J. of Testing And Evaluation 1973 Vol.1 P220*

[150] F.A.Hodierne *J. of Inst. Metals 1962-63 Vol.91 P267*

[151] H.ormerod and W.J.McG.Tegart *J. of Inst. Metals 1960-61 Vol.89 P94*

[152] C.M.Sellars and W.J.McG.Tegart *Mem. Sci. Rev. Met. 1966 Vol.63 P731*

[153] C.Zener and J.H.Hollomon *J. Applied Phys. 1944 Vol.15 P22*

[154] M.Raghavan and E.Shapiro *Metall. Trans.A 1980 Vol.11A Jan. P117*

[155] I.Gutierrez et al *Mat. Sci. and Eng.A 1988 102 P77*

[156] H.J.McQueen *J. Metals 1968 Vol.20 pt.4 P31*

[157] T.Sheppard and S.J.Paterson *Metals Tech. 1982 July Vol.9 P274*

[158] F.J.Humphreys and P.N.Kalu *ACTA Metall. 1987 Vol.35 No.12 P2815*

[159] E.Evangelista et al: 4th Risϕ Symposium on Metal Sept. 1983.

[160] C.P.Hinesley and H.Conrad *Mat. Sci. and Eng. 1973 Vol.12 P47*

[161] R.A.Vandermeer and Paul Gordon Proc. Symposium "Recovery and Recrystallization of Metals" Gordon and Breach, New York, Feb.1962

[162] R.T.DeHoff and F.N.Rhines "Quantitative Microscopy" McGraw-Hill London, 1968

[163] T.S.Srivatsan and C.W.Meyers *Trans. of ASME 1987 Oct. Vol.109 P350*

[164] R.Medrano et al *Metal Forming Interrelation between Theory and Practice 1971 P85*

[165] T.Sheppard and D.S.Wright *Metals Technology June 1979 P215*

[166] P.Hollinshead, T.Sheppard *Mat. Sci. and Tech. 1987 Dec. Vol.3 P1019*

[167] O.D.Sherby et al *ACTA Metall. 1957 Vol.5 P219*

[168] K.P.Rao and Y.V.Prasad *J. of Mech. Working Tech. 1986, 13, P38*

[169] P.L.Morris and B.J.Duggan *Met. Sci. 1978 Vol.12 P1*

[170] C.M.Sellars and W.J.McG.Tegart *Int. Metall. Rev. 1972 Vol.17 P1*

[171] H.J.McQueen et al *Canadian J. of Phys. 1967 Vol.45 P1225*

[172] P.R.Landon et al *Trans. ASM 1959 Vol.51 P901*

[173] W.J.McG.Tegart *Special Report London(Iron and Steel Inst) 1968 No.111 P26*

[174] A.F.Castle "Temperature Change in the Extrusion of Aluminium"

[175] J.Hilliard *Metal Progress 1964 May Vol.85 P99*

[176] *Annal Book ASTM Standard 1984 P120*

[177] F.R.Fernandez and C.M.Sellars *Mat.Sci. and Tech. 1988 July Vol.4 P621*

[178] M.M.Farag and C.M.Sellars:Deformation under Hot-Working Conditions, Iron and Steel Inst. 1966 P60

[179] P.Moore:Deformation under Hot-Working Conditions, Iron and Steel Inst. 1966 P103

[180] A.H.Cottrell:"An Introduction to Metallurgy" Edward Arnold London 1967

[181] C.R.Borrett et al:"The Principles of Engineering Materials"

[182] N.Hansen *ACTA Metall. 1970 Vol.18 P137*

[183] T.Sheppard, M.A.Zaidi and G.H.Tan *Metal Sci. 1983 Dec. Vol.17 P563*

[184] R.W.Hains: Special report "Temperature Changes in the Extrusdion of Aluminium"

[185] M.J.Couper and R.F.Singer: High Strength Powder Metallurgy Aluminium Alloys II, Proc. of a TMS-AIME Symposium on Al Powder Metall. 13-17 Oct. 1985 P199

[186] N.Hansen and B.Bay *ACTA Metall. 1981 Vol.29 P65*

[187] T.B.Vaugham: Deformation under Hot-Working Conditions, Iron and Steel Inst. 1966 P68

[188] T.Sheppard: Special report "Metallurgical Aspects of Direct and Indirect Extrusion"

[189] K.Mori et al *Int.J.Mech.Sci. 1983 Vol.25(11) P775*

[190] O.C.Zienkiewicz et al Proc. Conf. Japan Sco. for Tech. of Plas. 1984 2 P1041

[191] A.Chandra et al *Int.J.Mech.Sci. 1984 Vol.26(11-12) P661*

[192] P.J.Kwan PhD Thesis North Carolina State University 1985

Plate 1

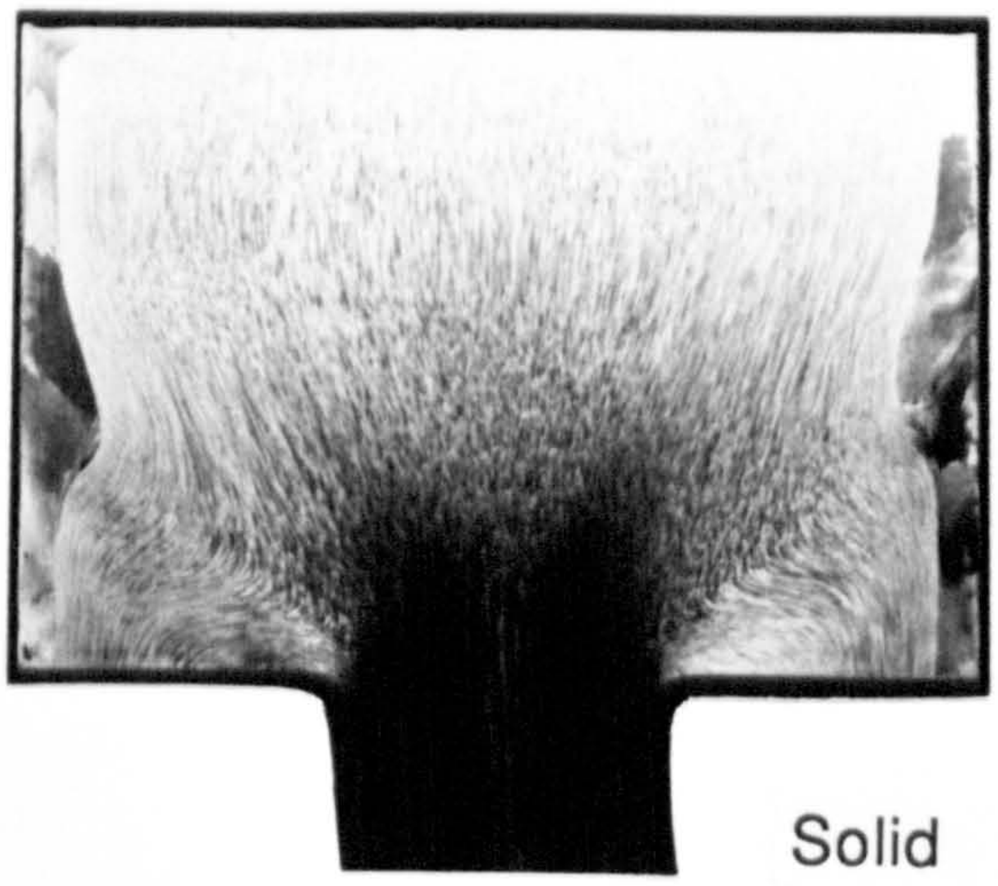

Solid

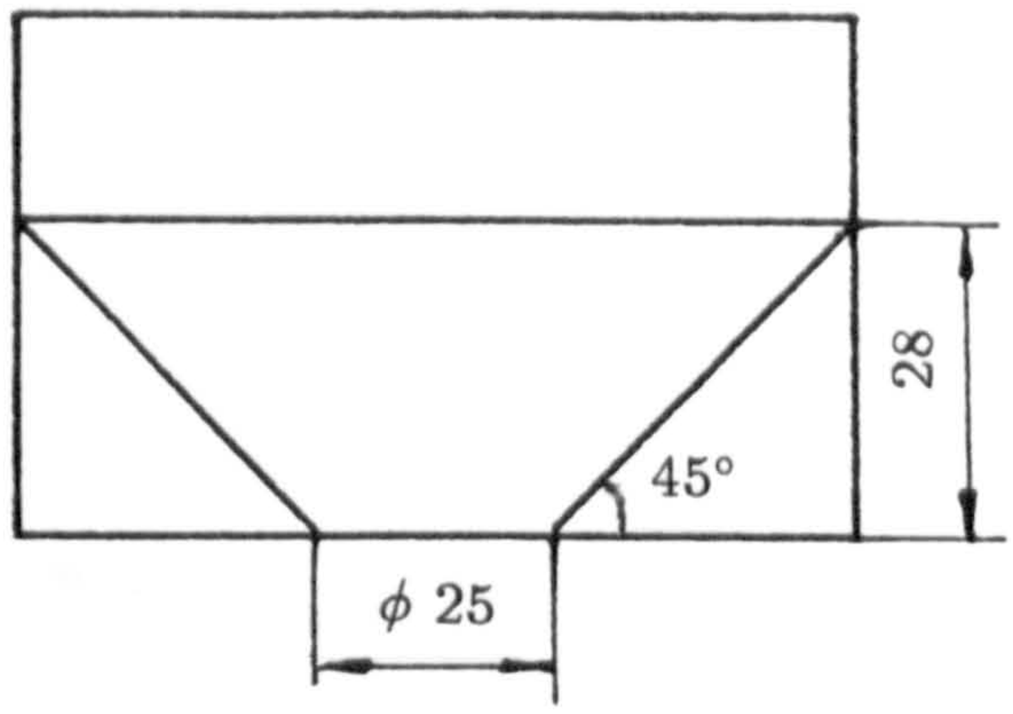

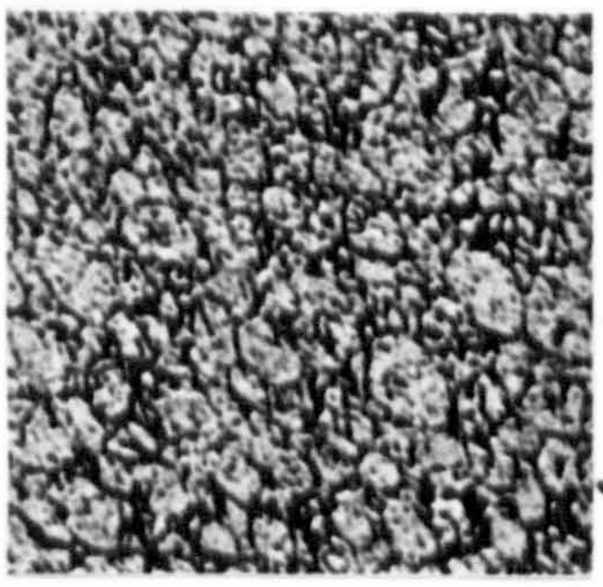

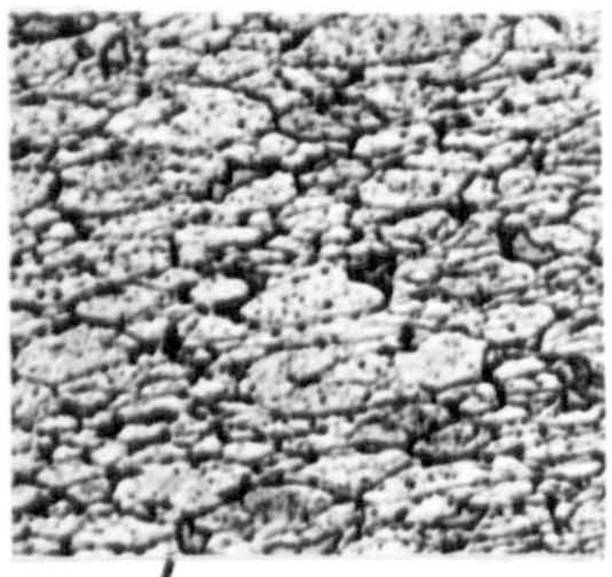

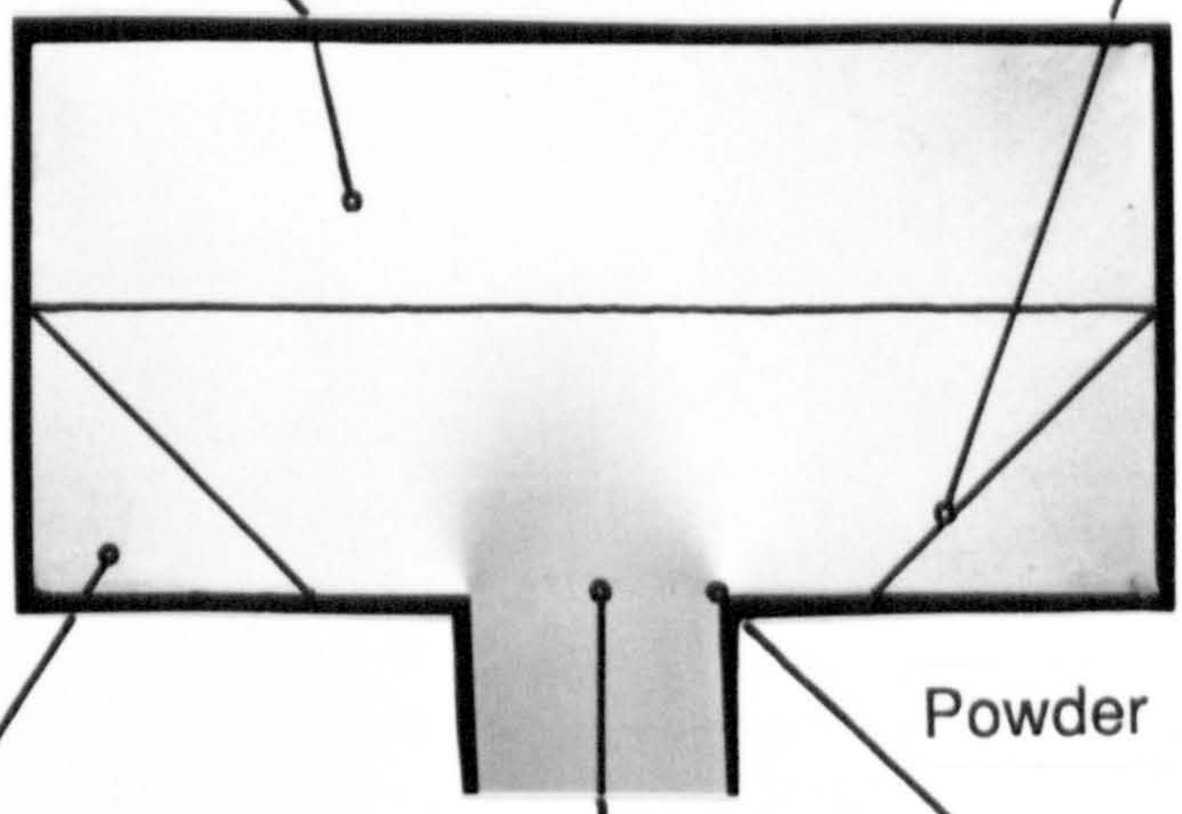

Powder

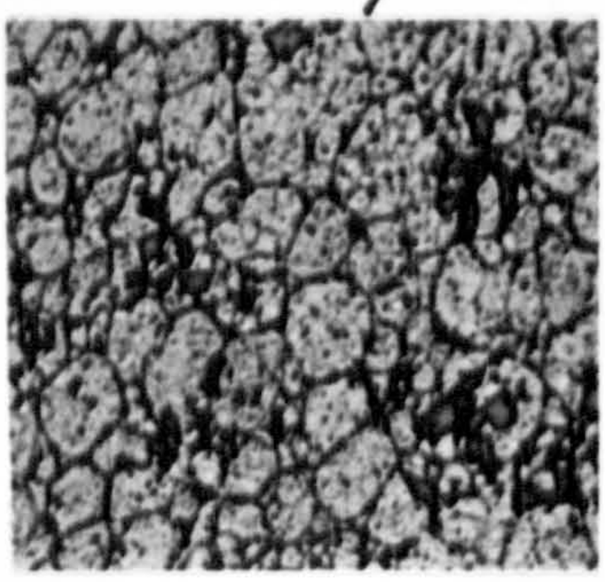

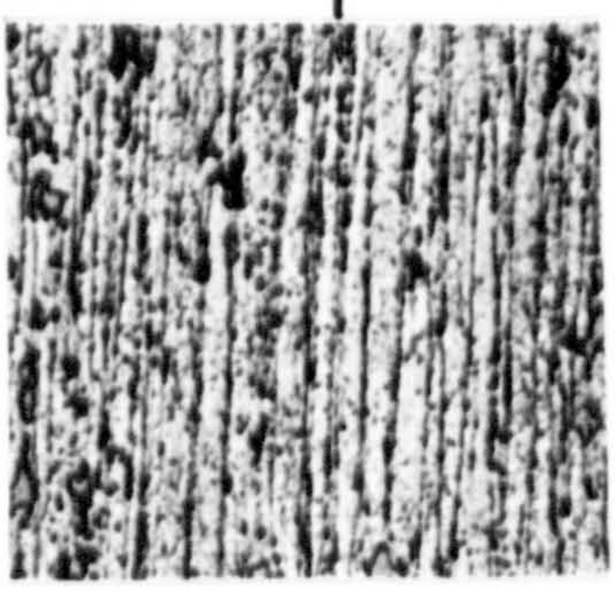

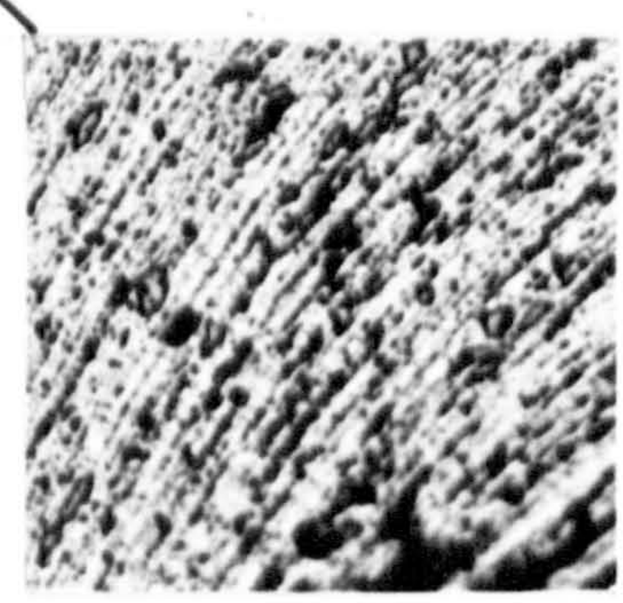

Plate 2

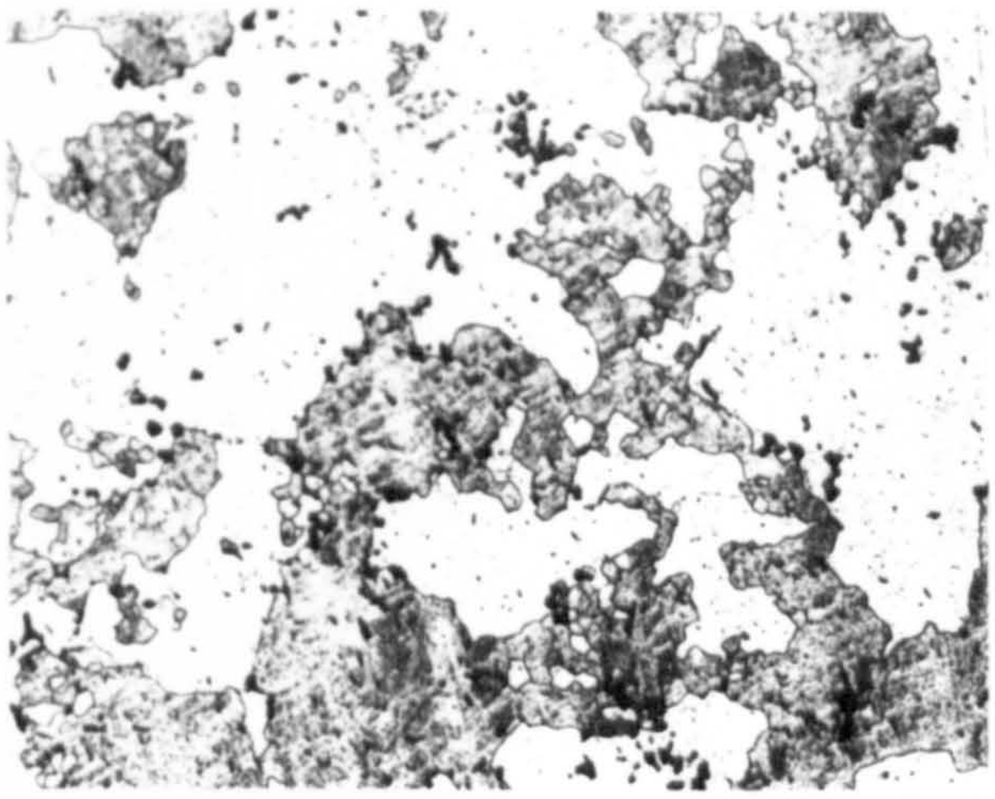

X168 Trans.

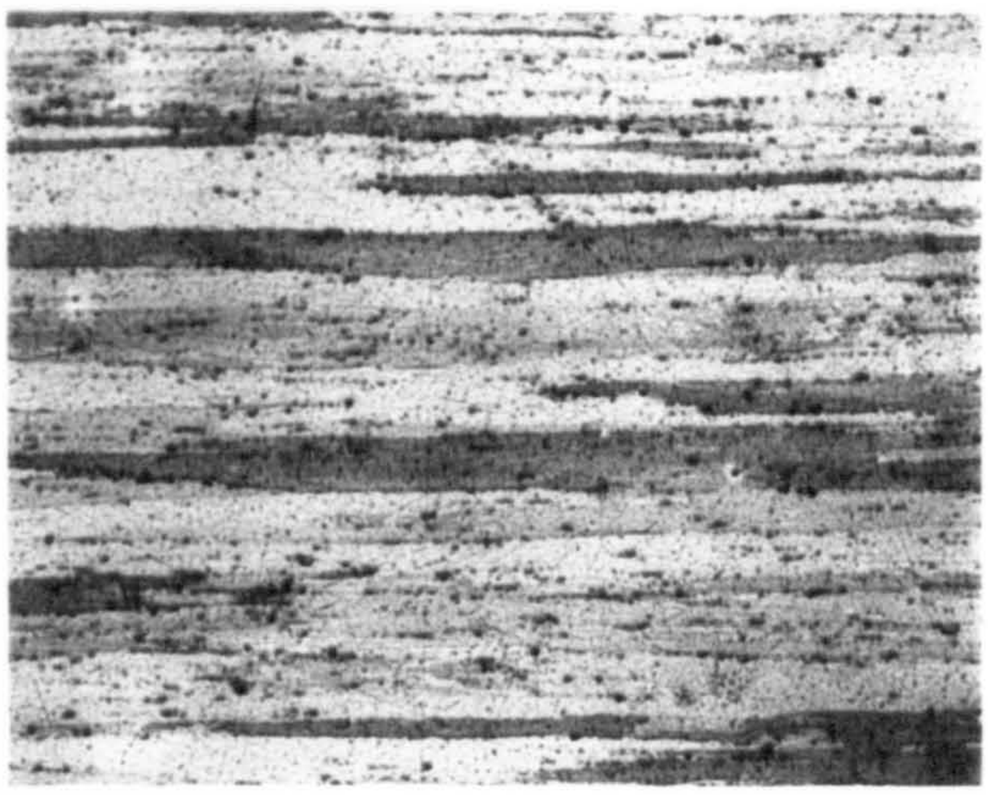

X54 Long.

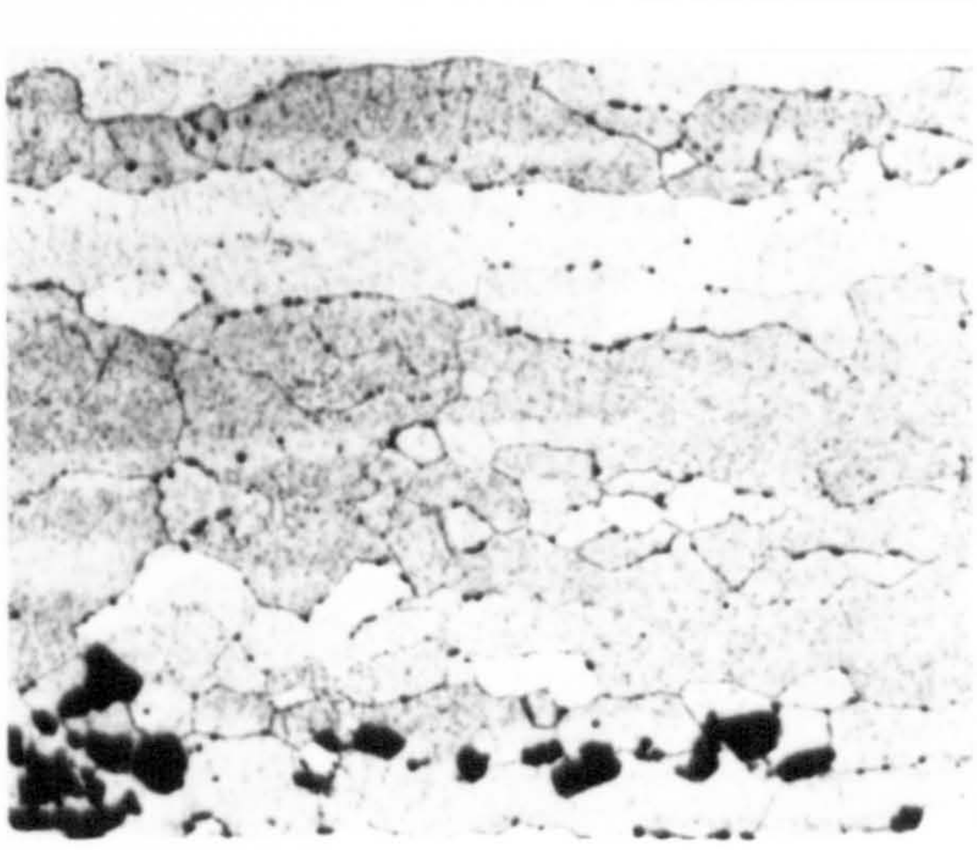

X843 Long.

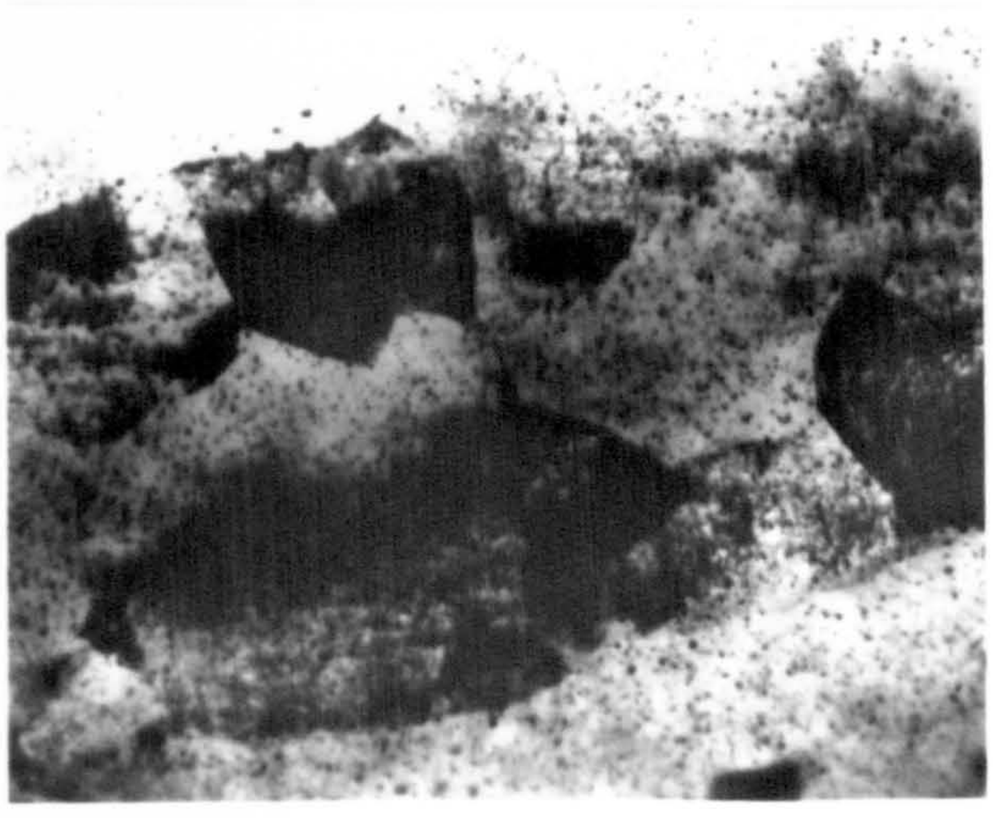

2 μm

Plate 3

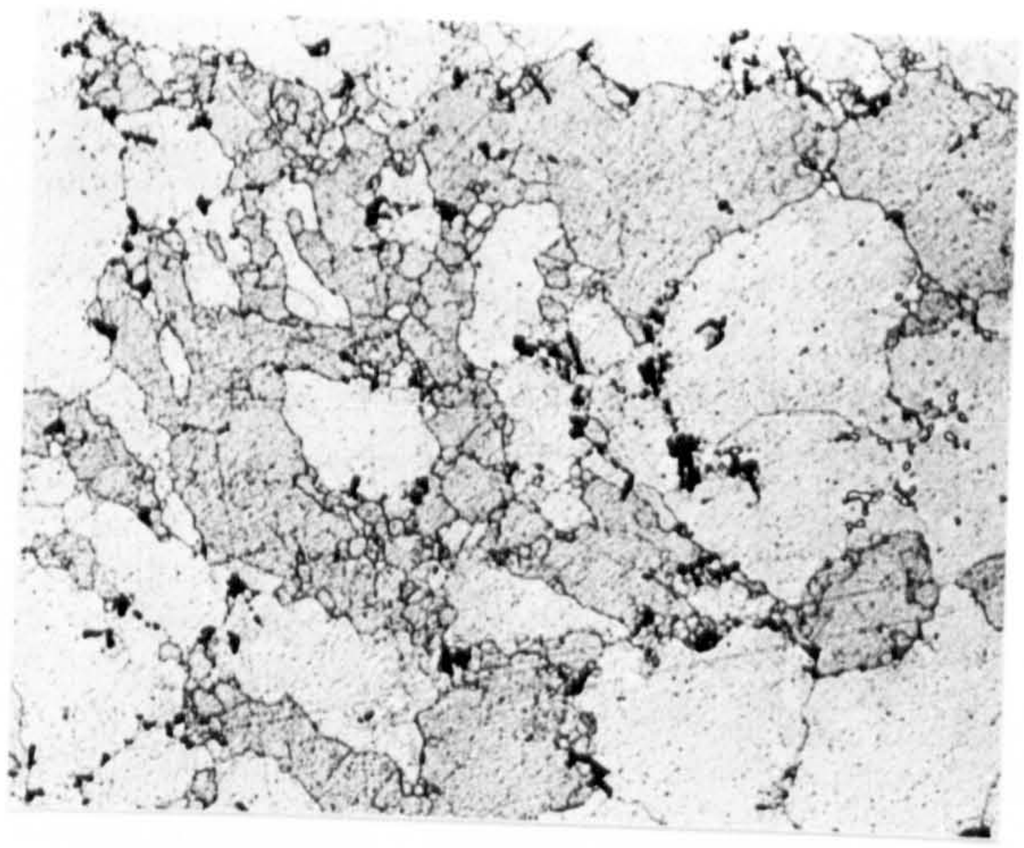

Trans.

X168

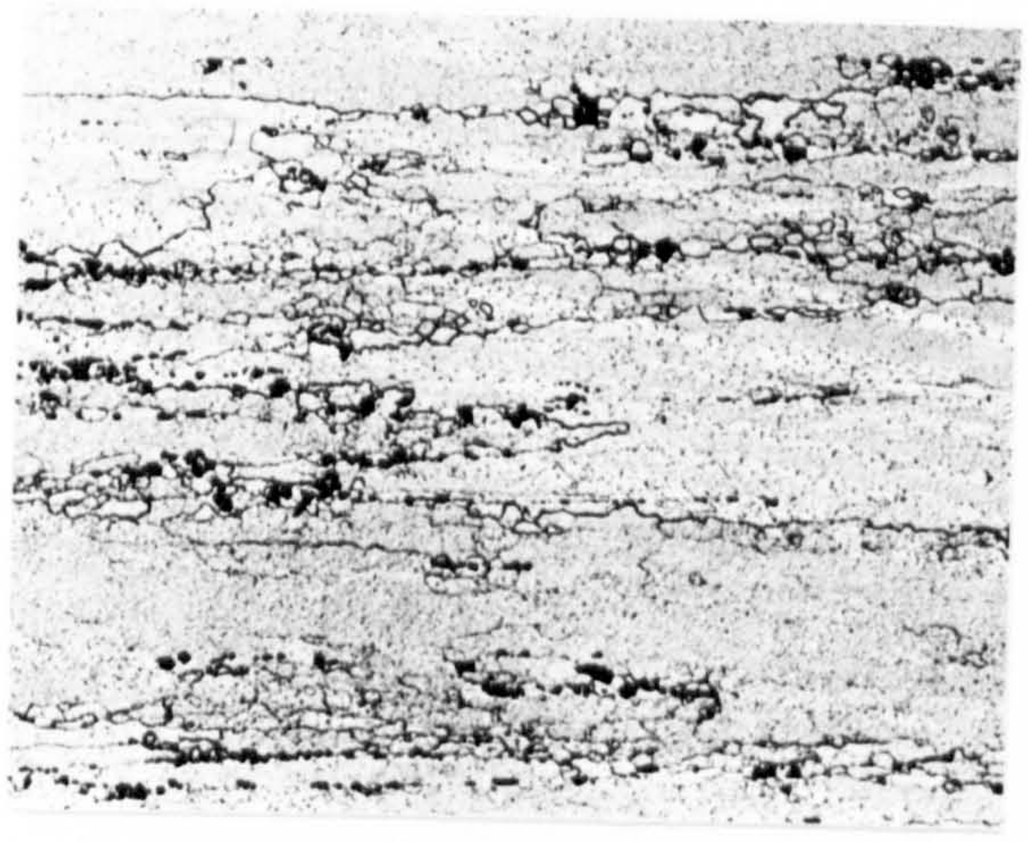

Long.

X168

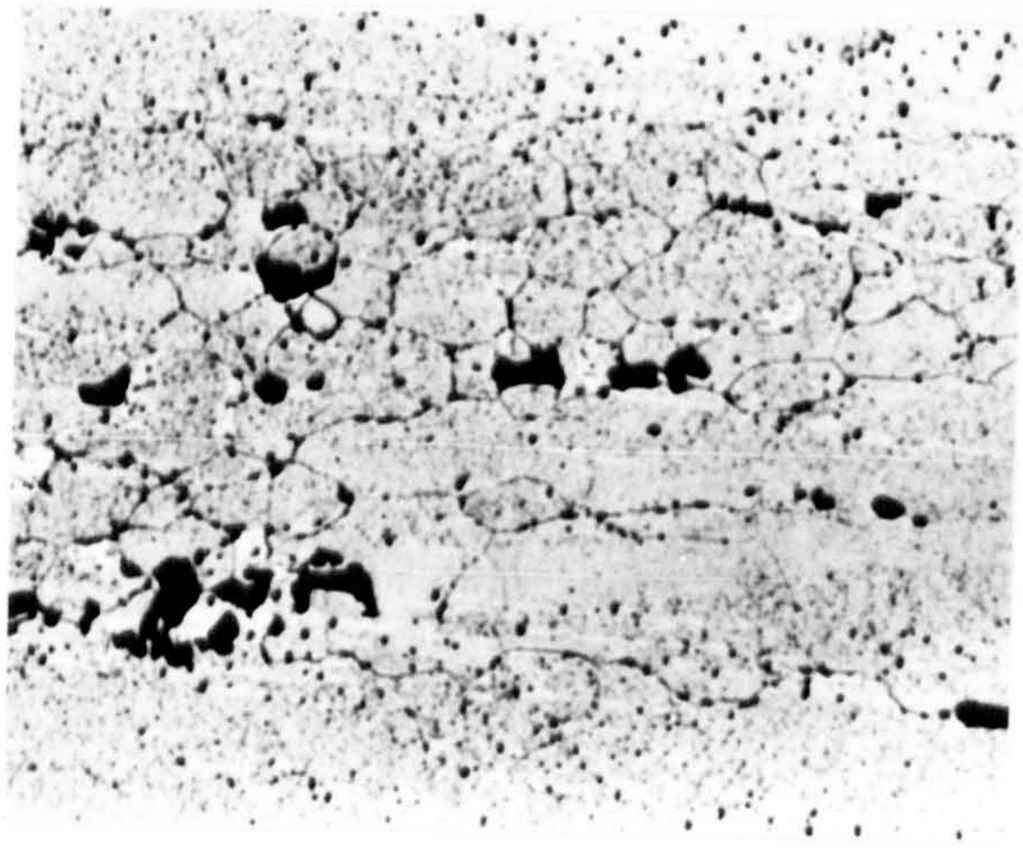

Long.

X843

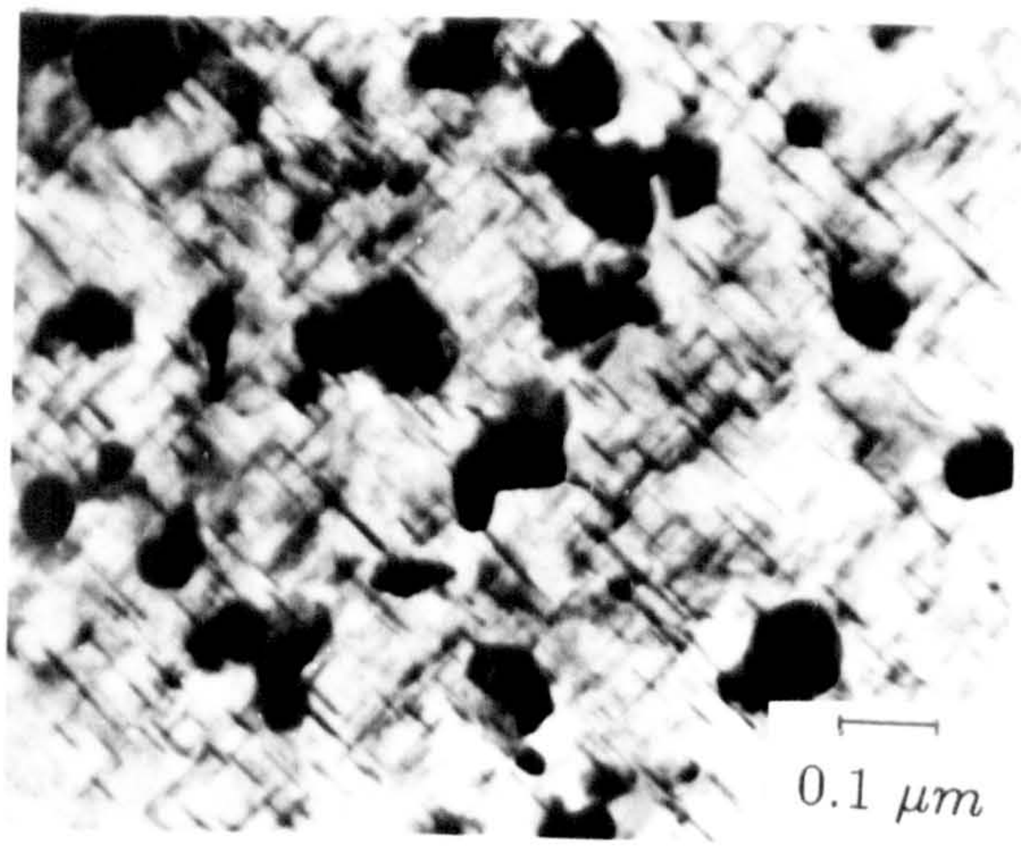

250°C

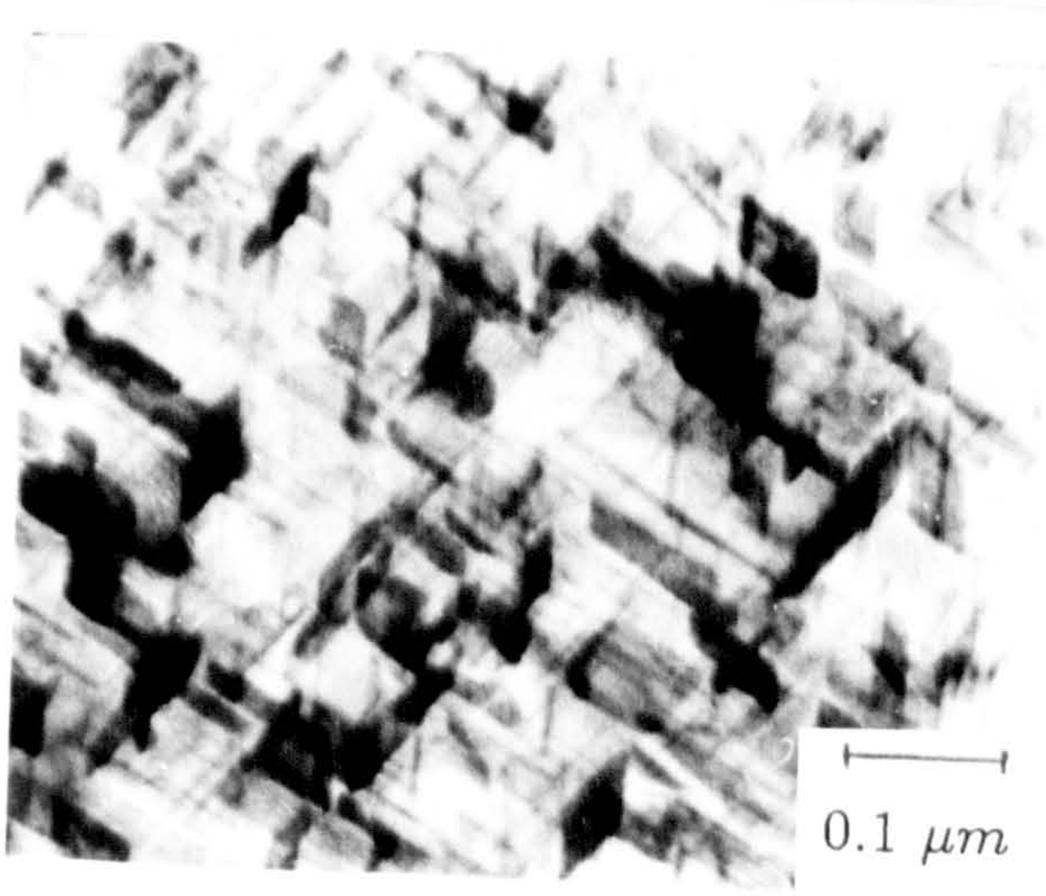

300°C

Plate 4

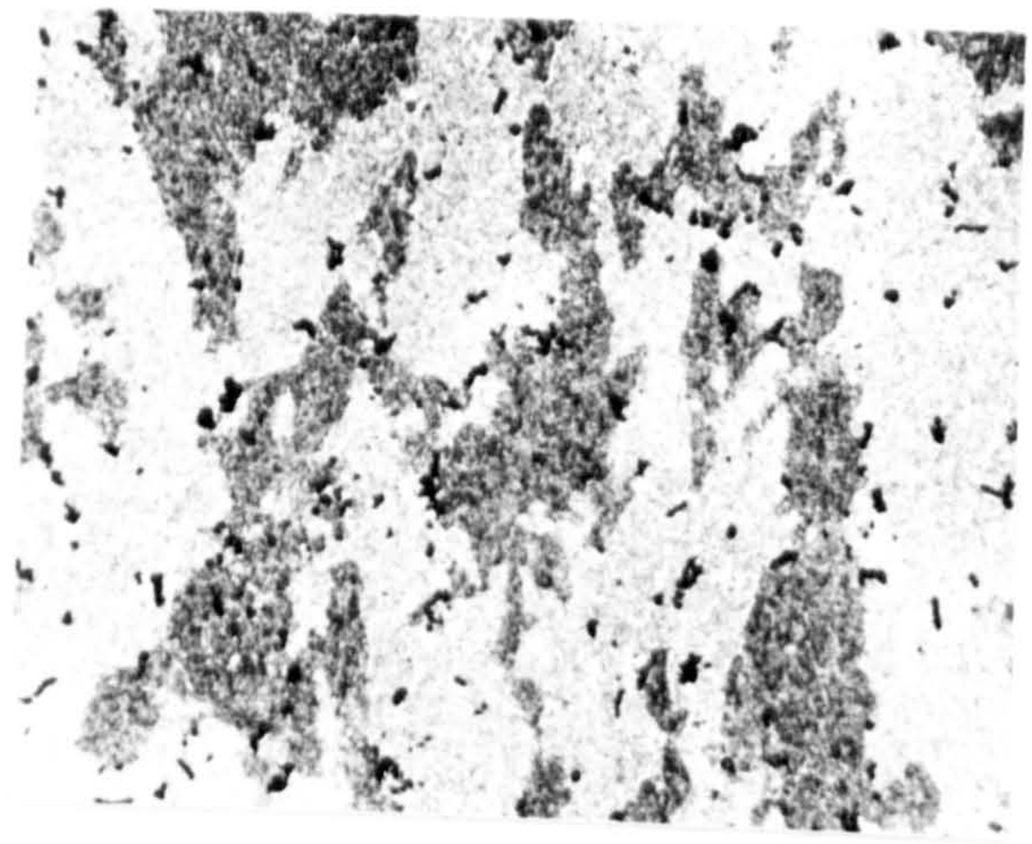

Trans.

X168

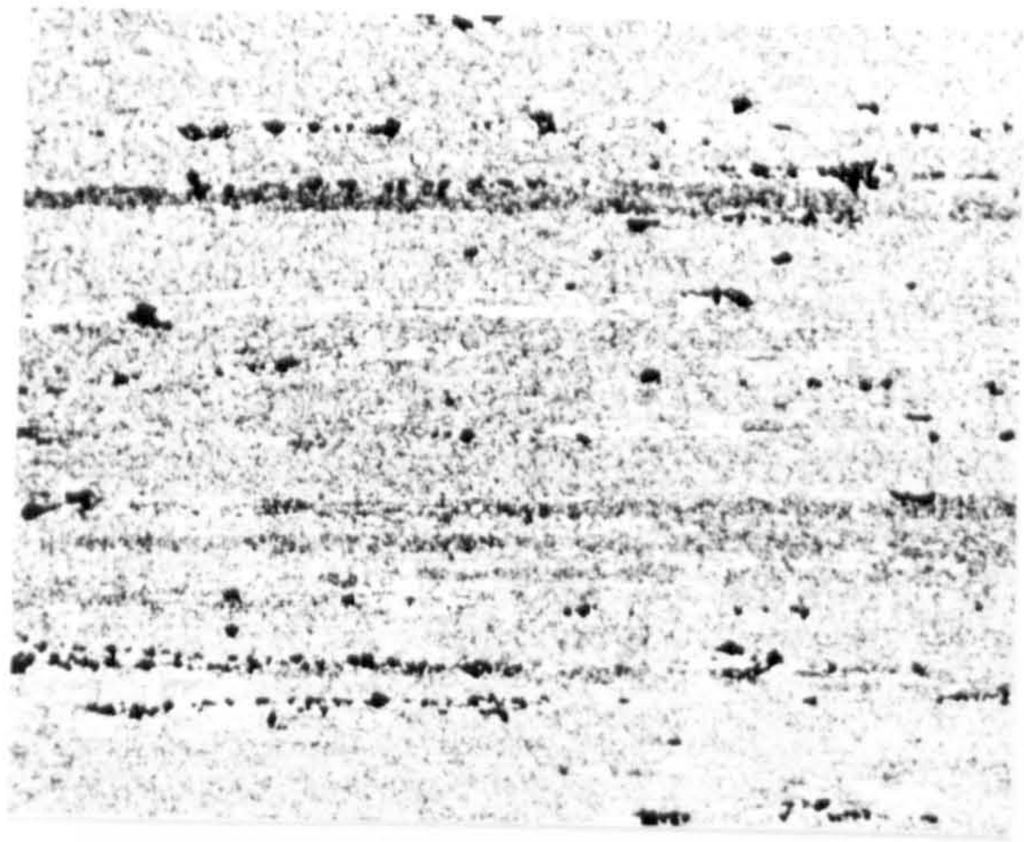

Long.

X168

Long.

X843

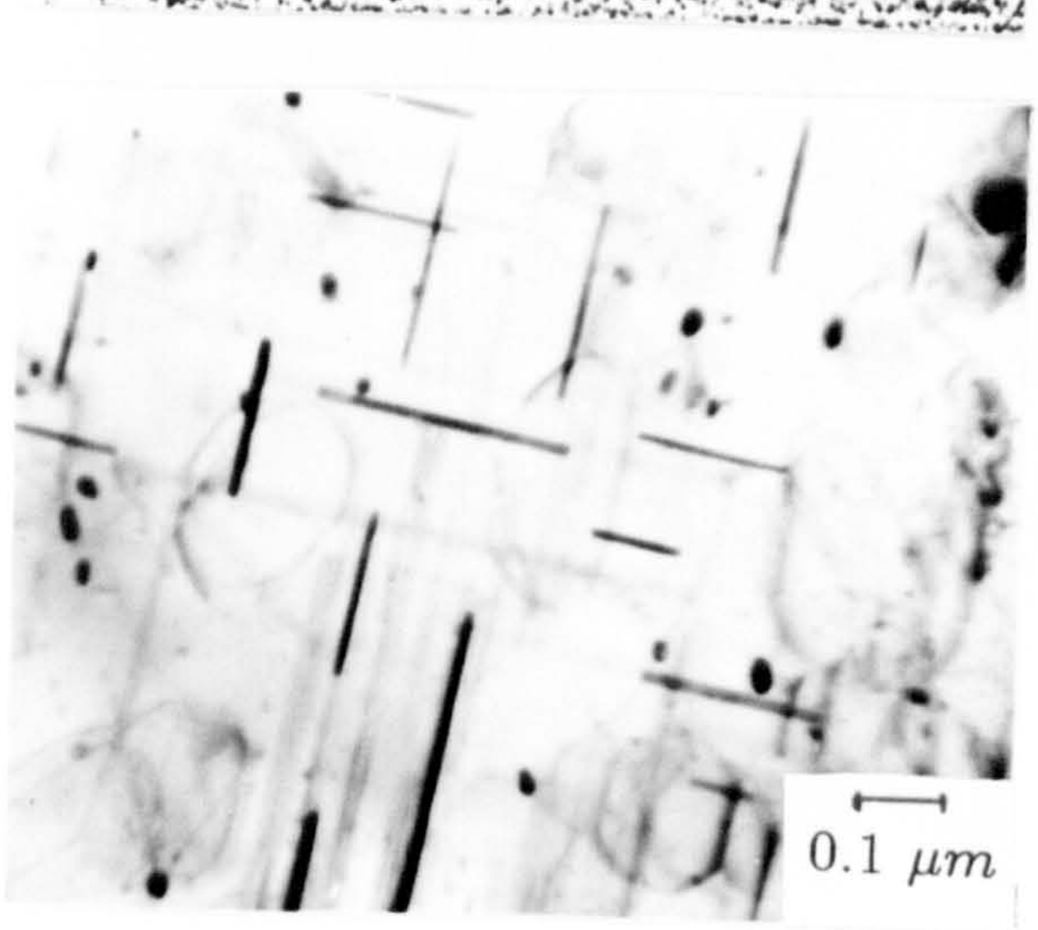

350°C

400°C

Plate 5

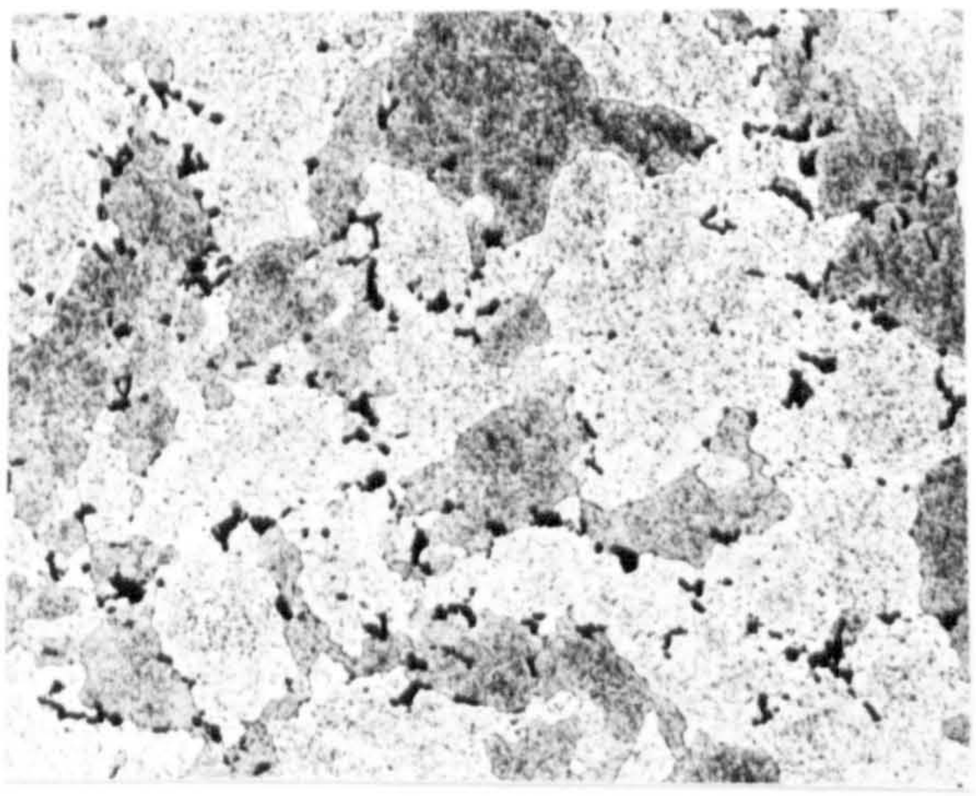

Trans.

X168

Long.

X168

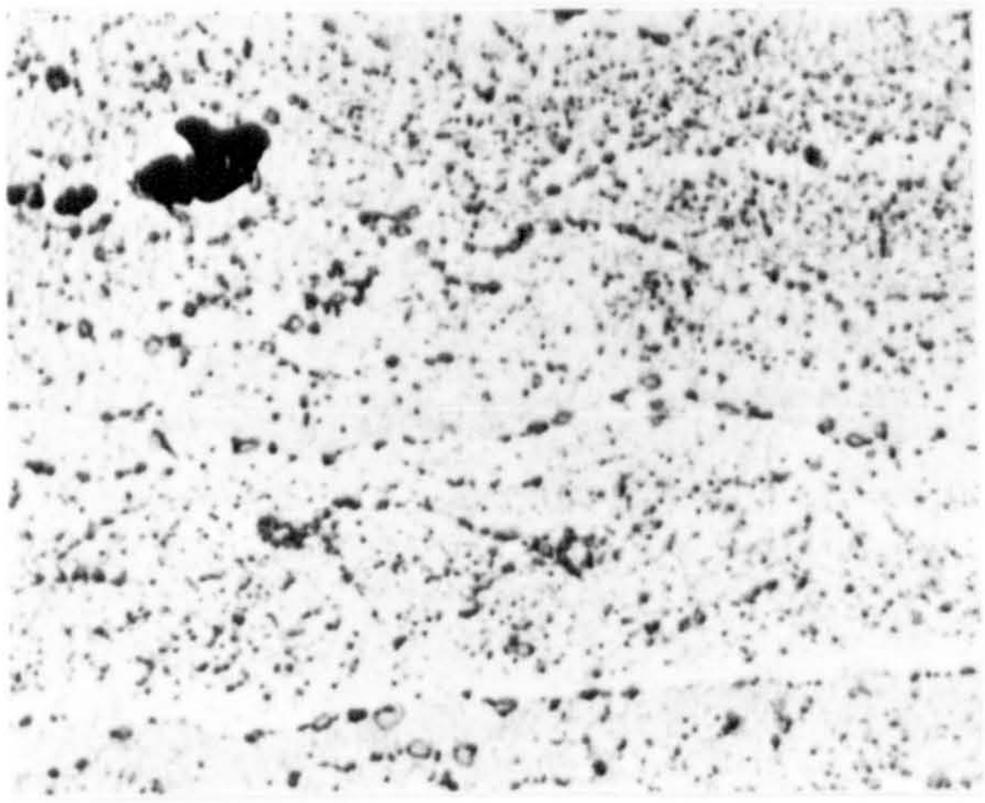

Long.

X843

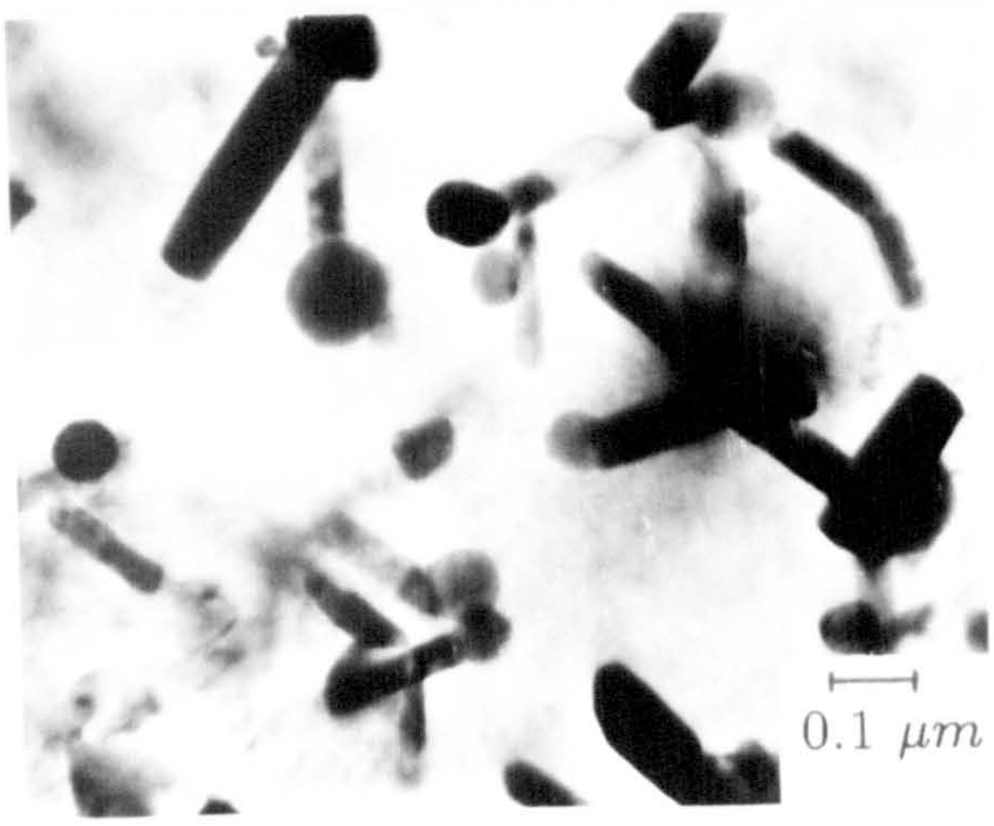

450°C

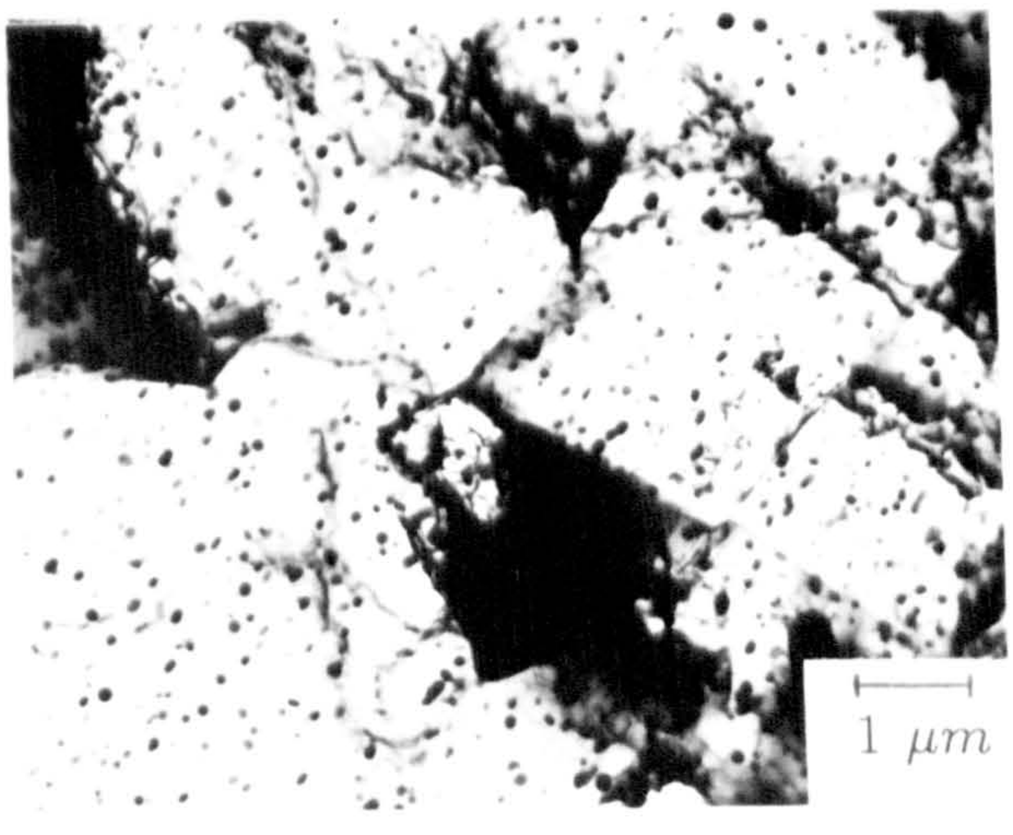

500°C

Plate 6

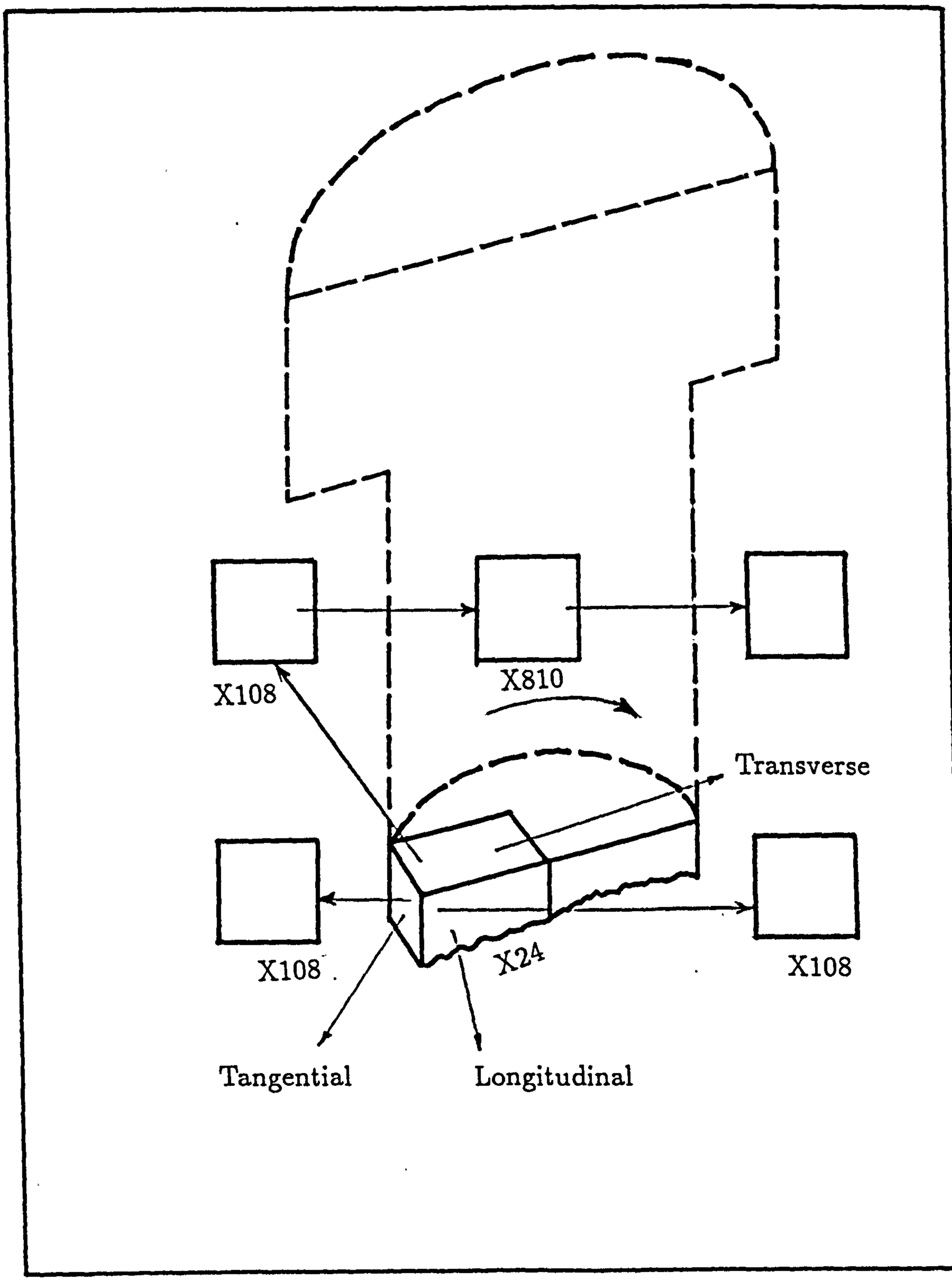

Key for Plates 7 – 12

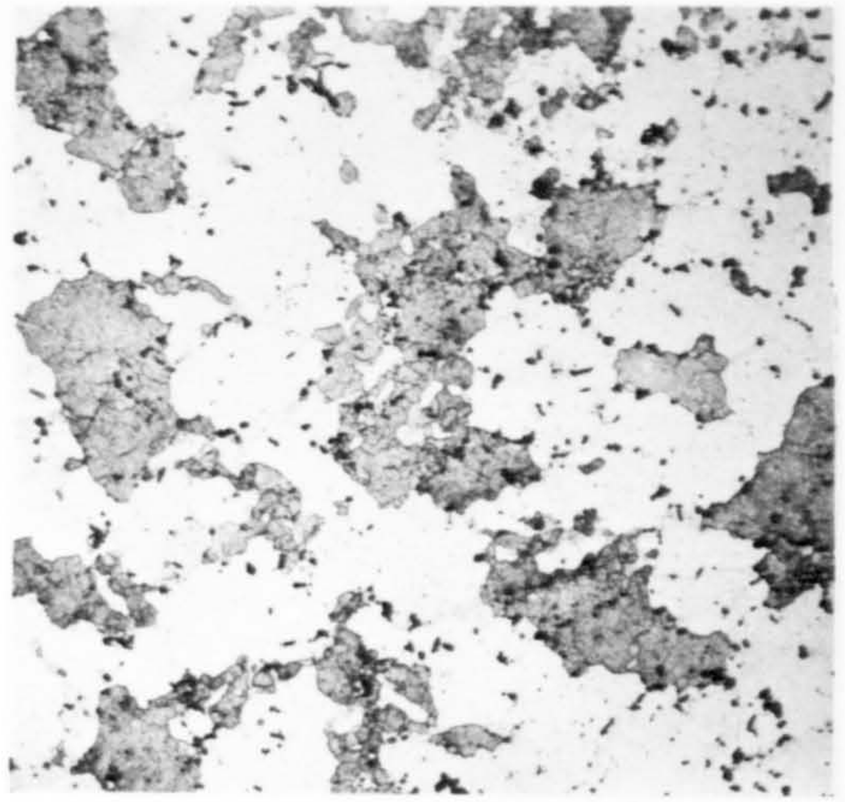

X108

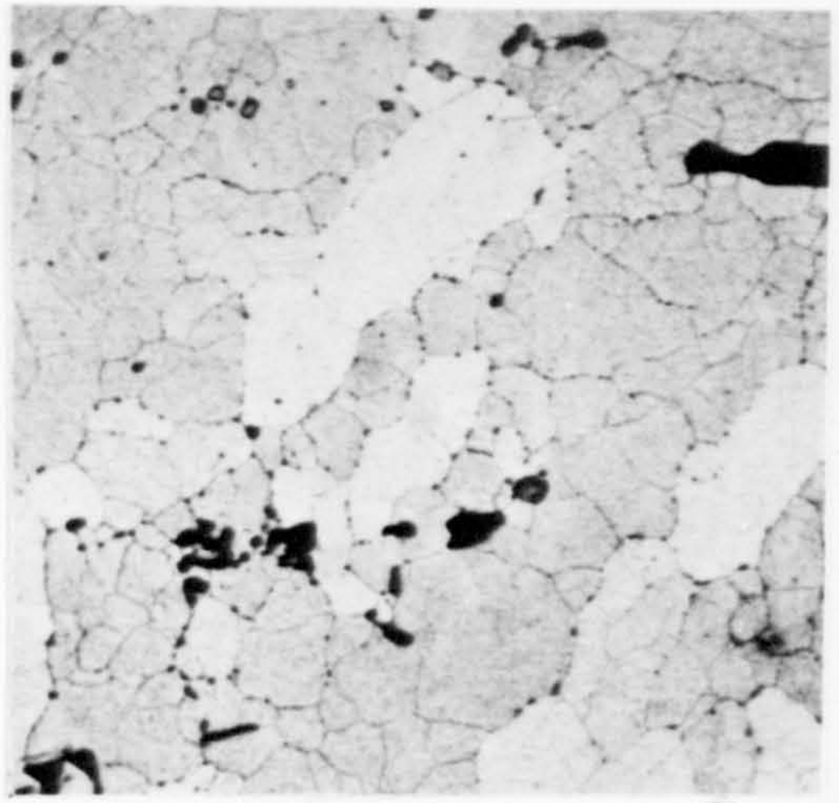

X810

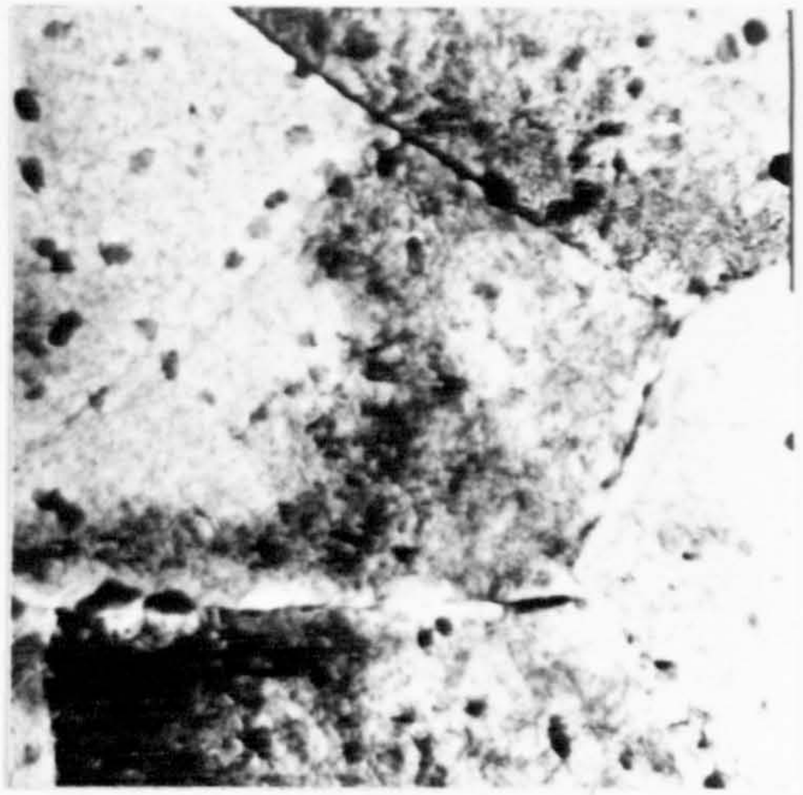

0.5 μm

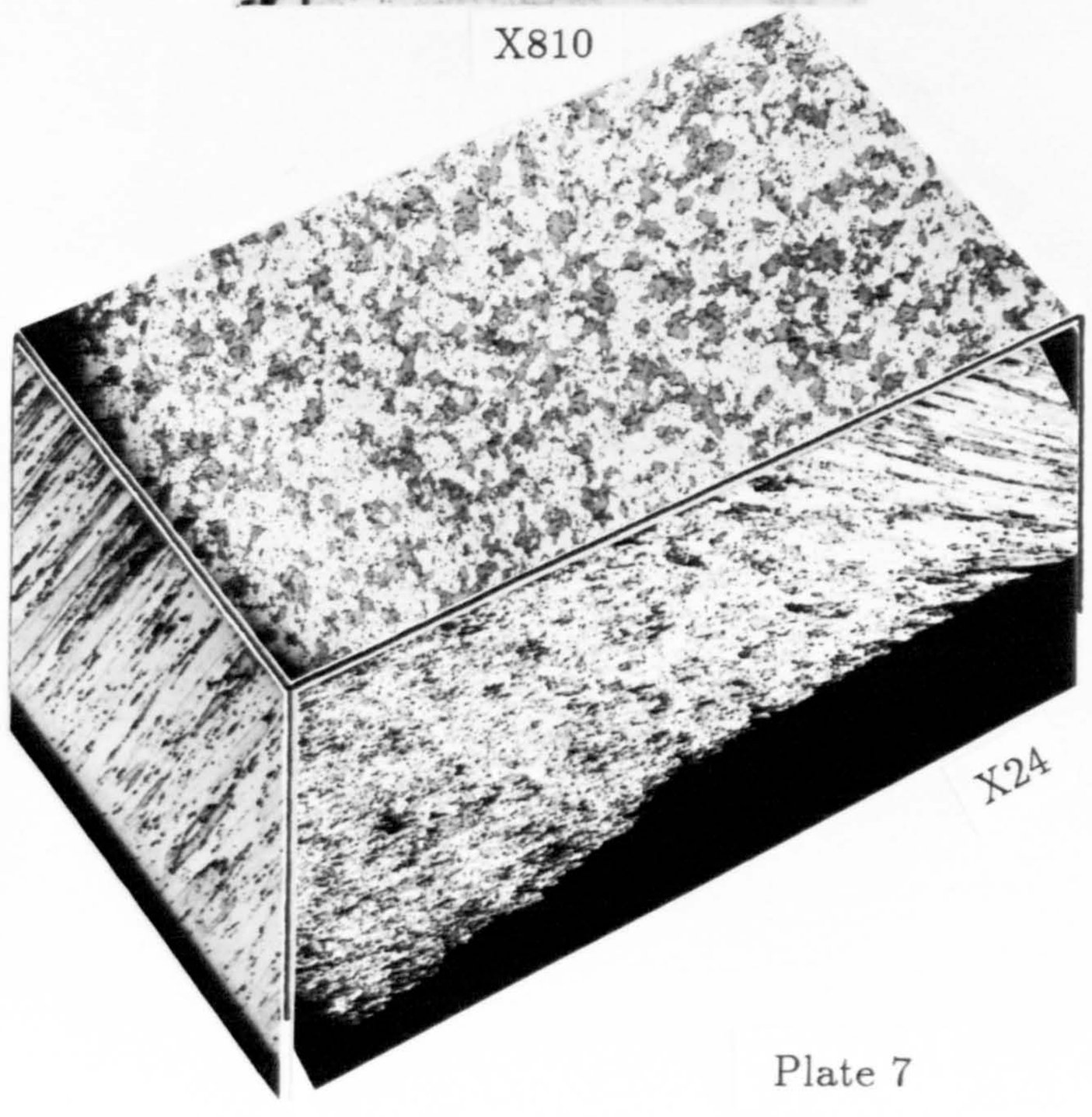

X24

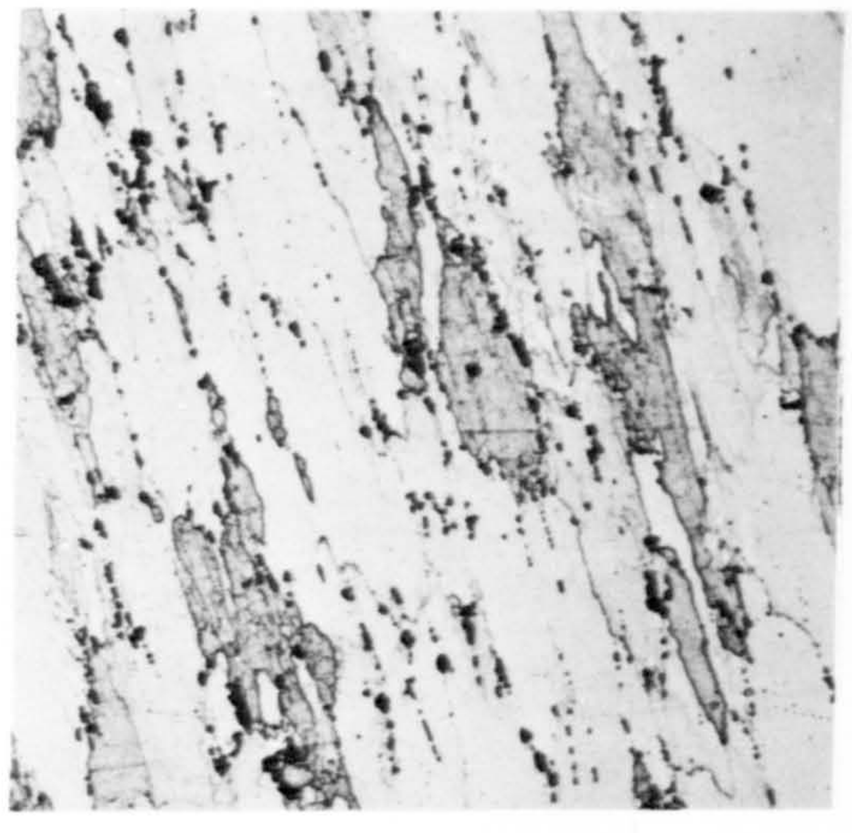

X108

X108

Plate 7

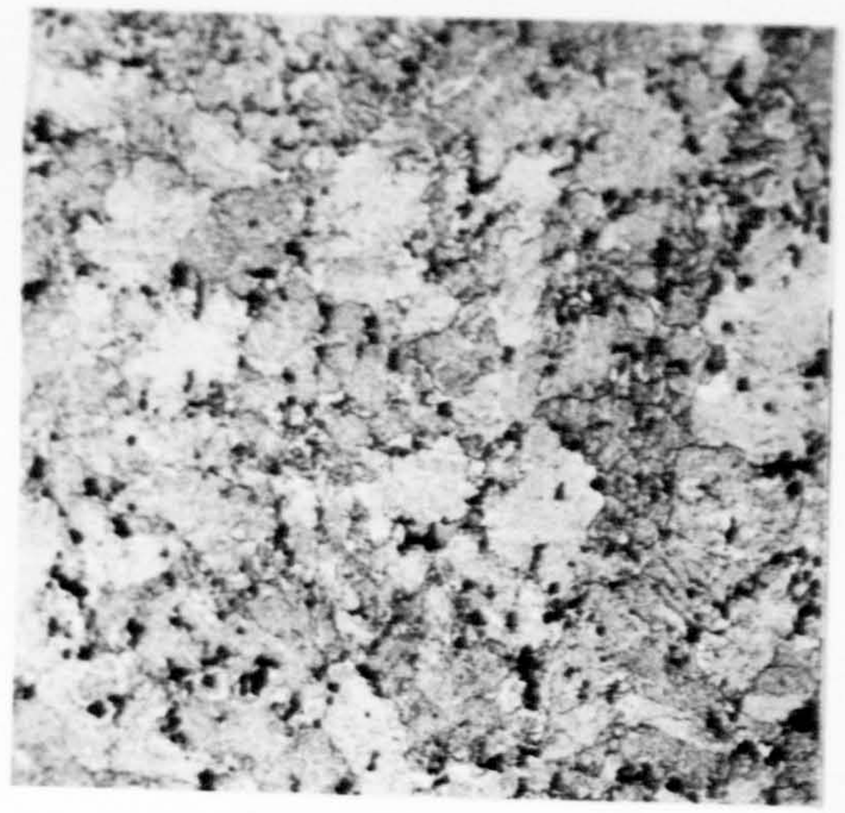

X108

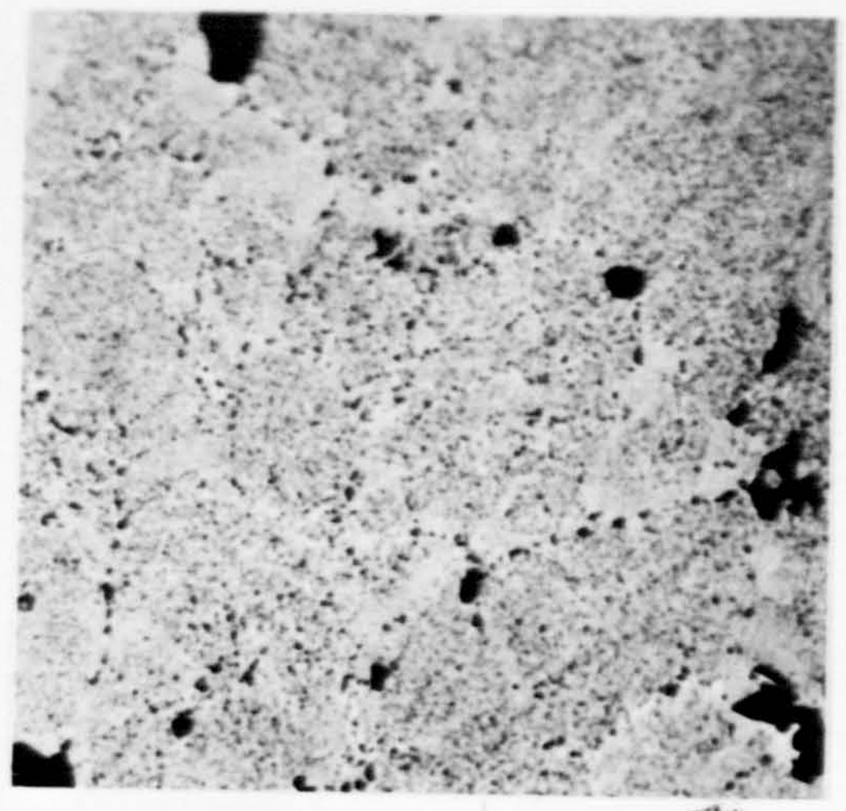

X810

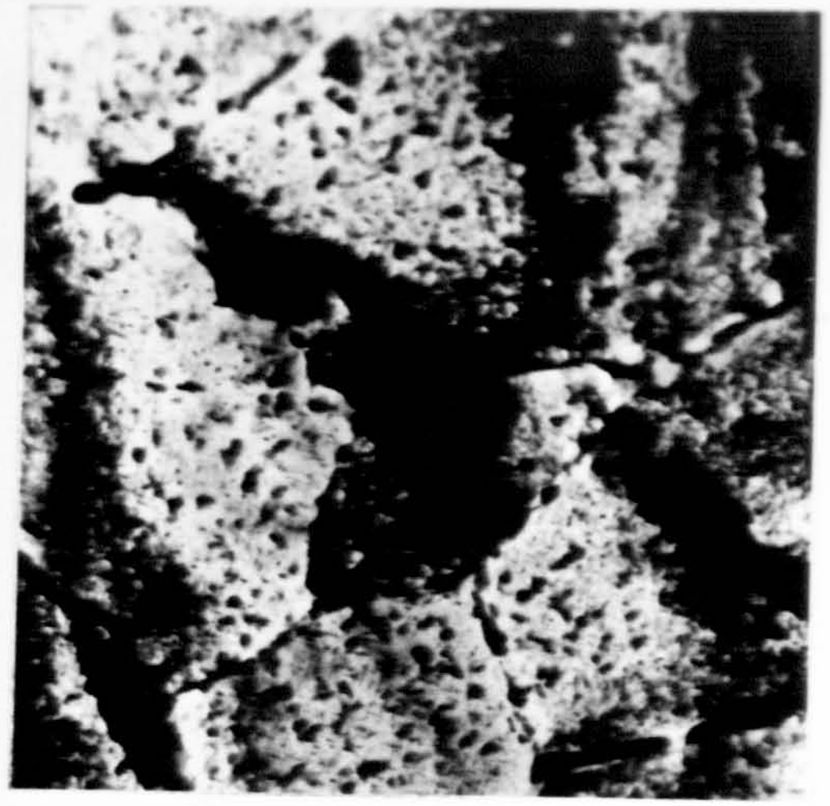

0.5 μm

X108

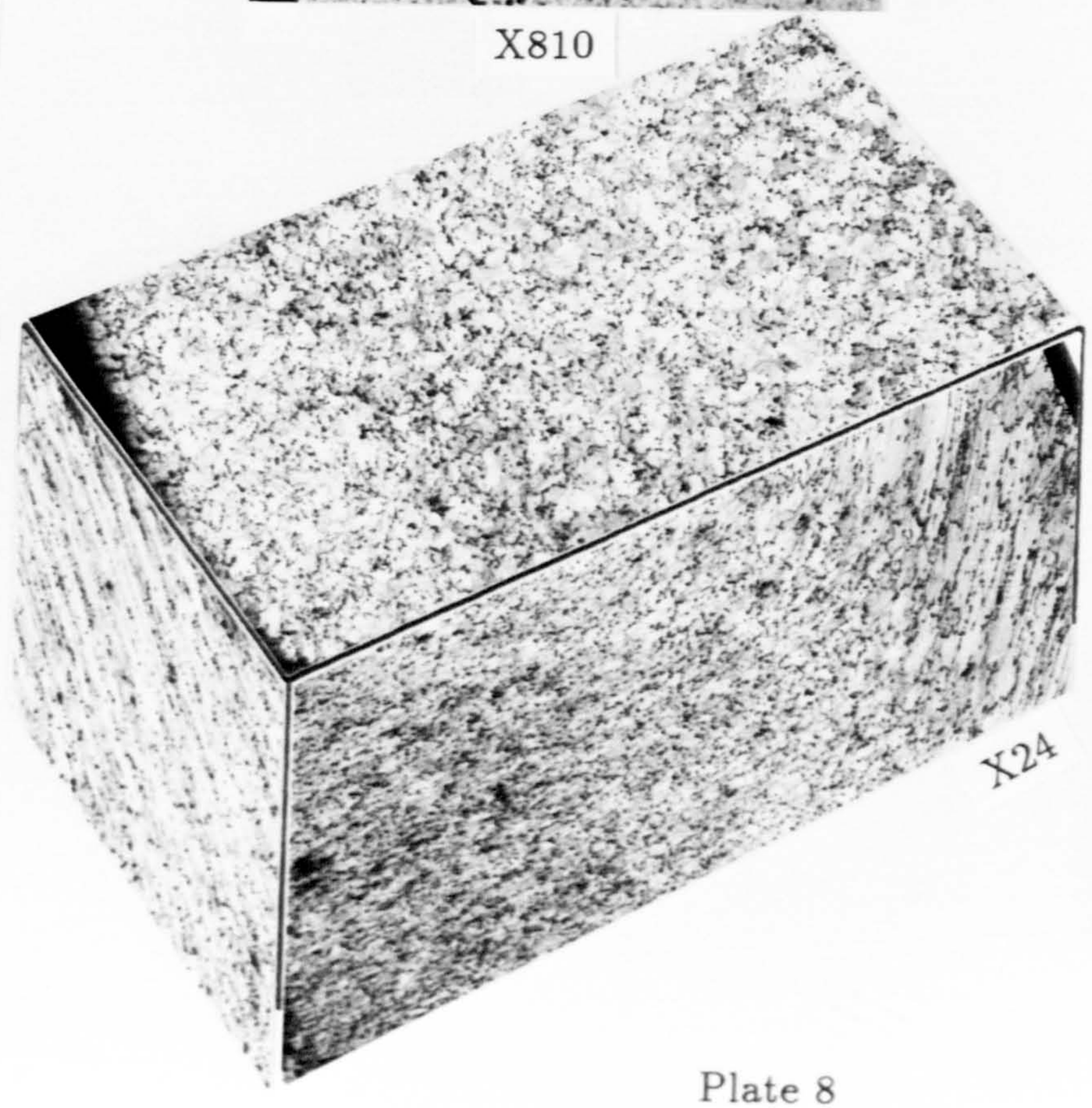

X24

X108

Plate 8

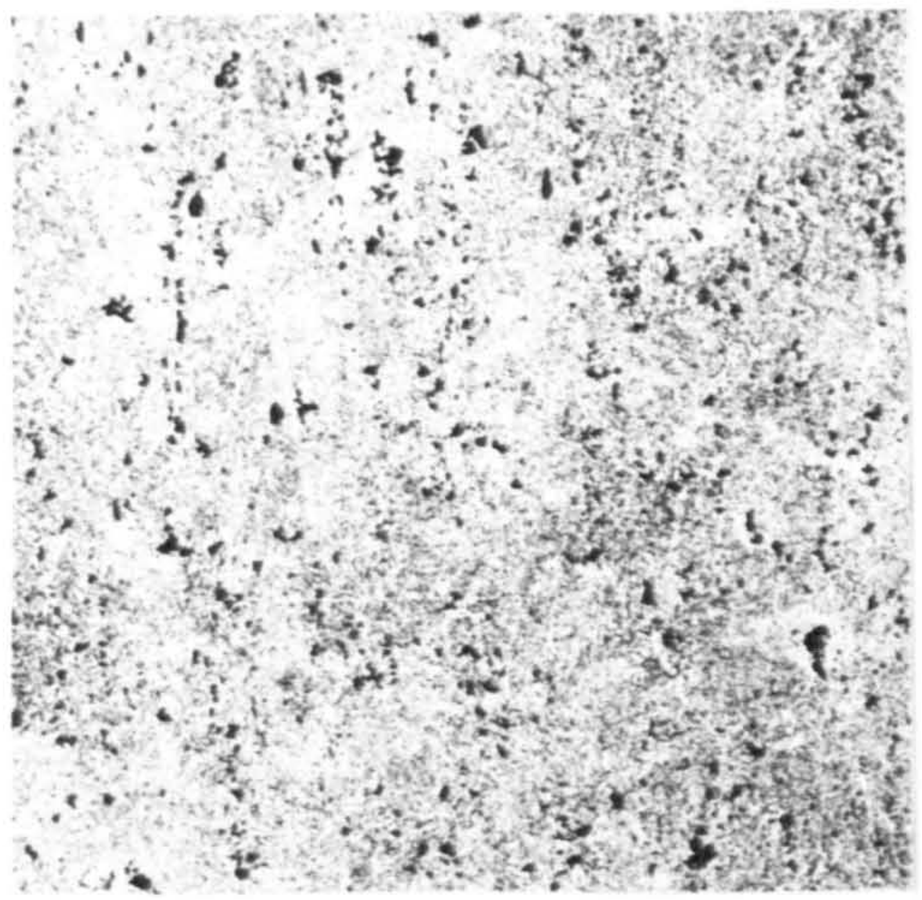

X108

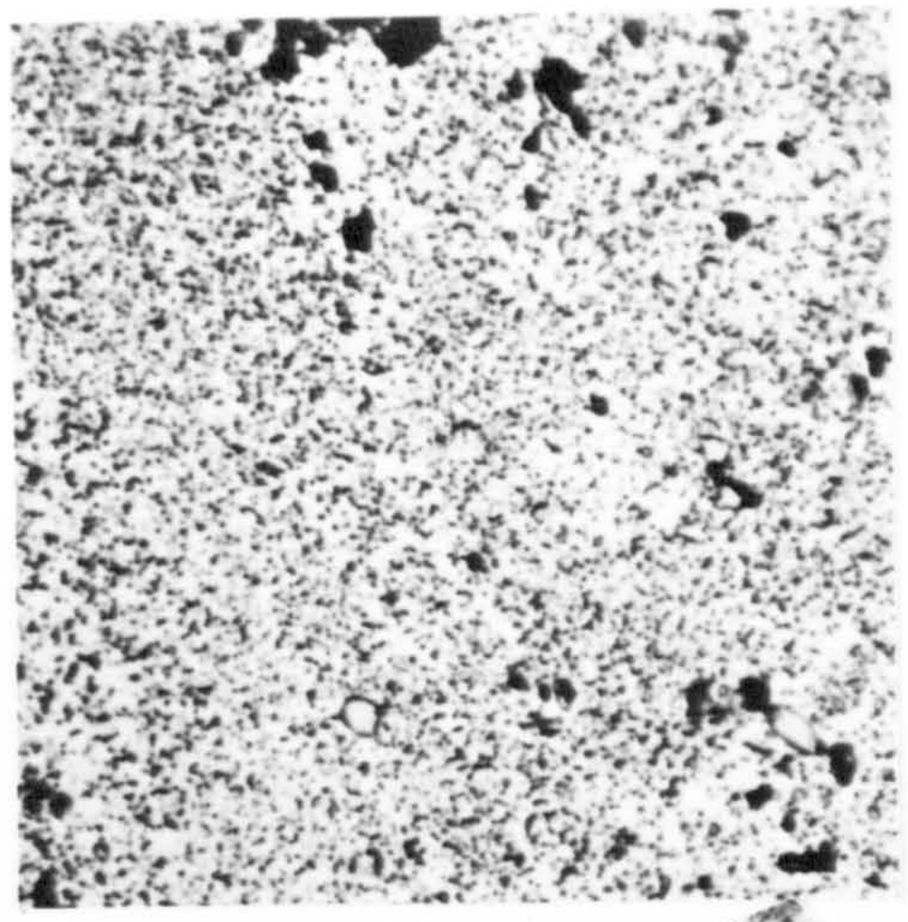

X810

0.5 μm

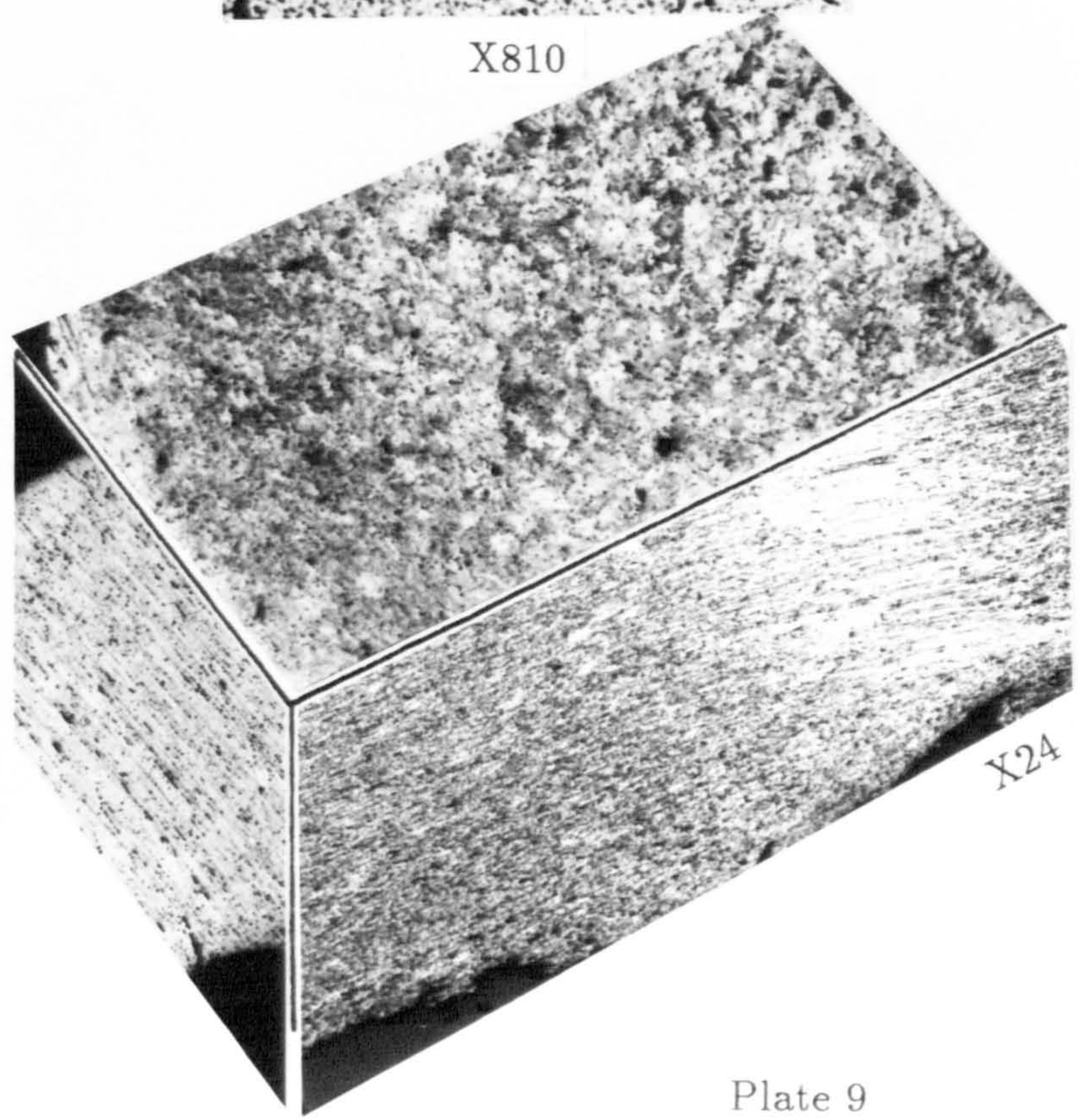

X24

X108

X108

Plate 9

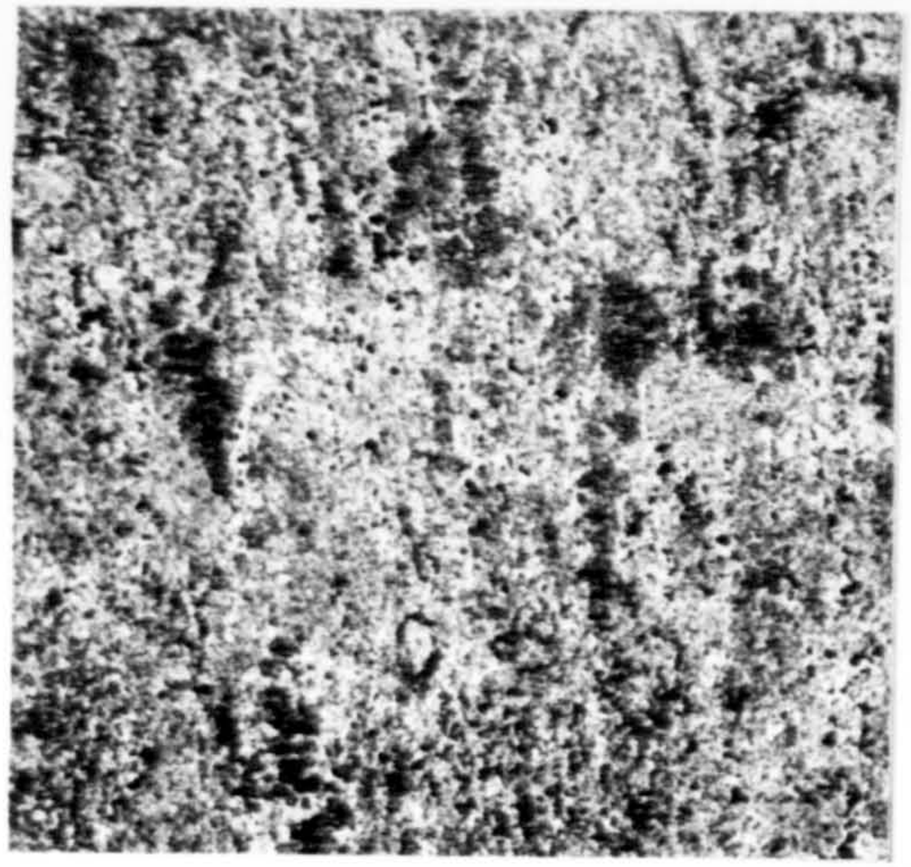

X108

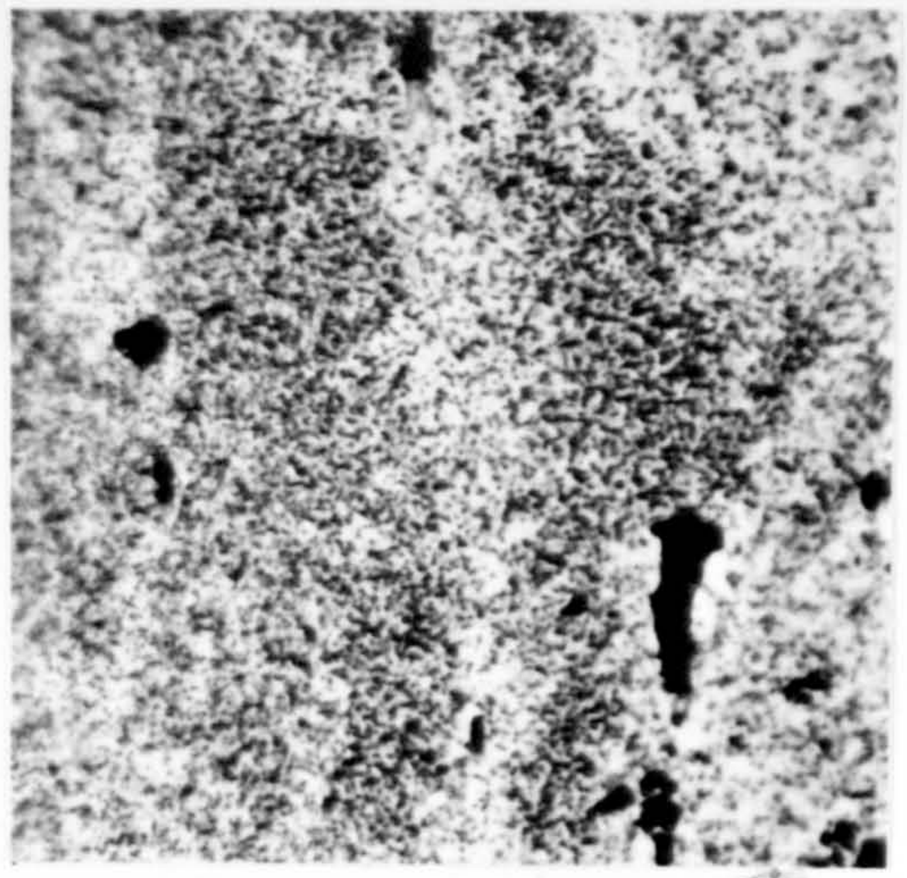

X810

0.5 μm

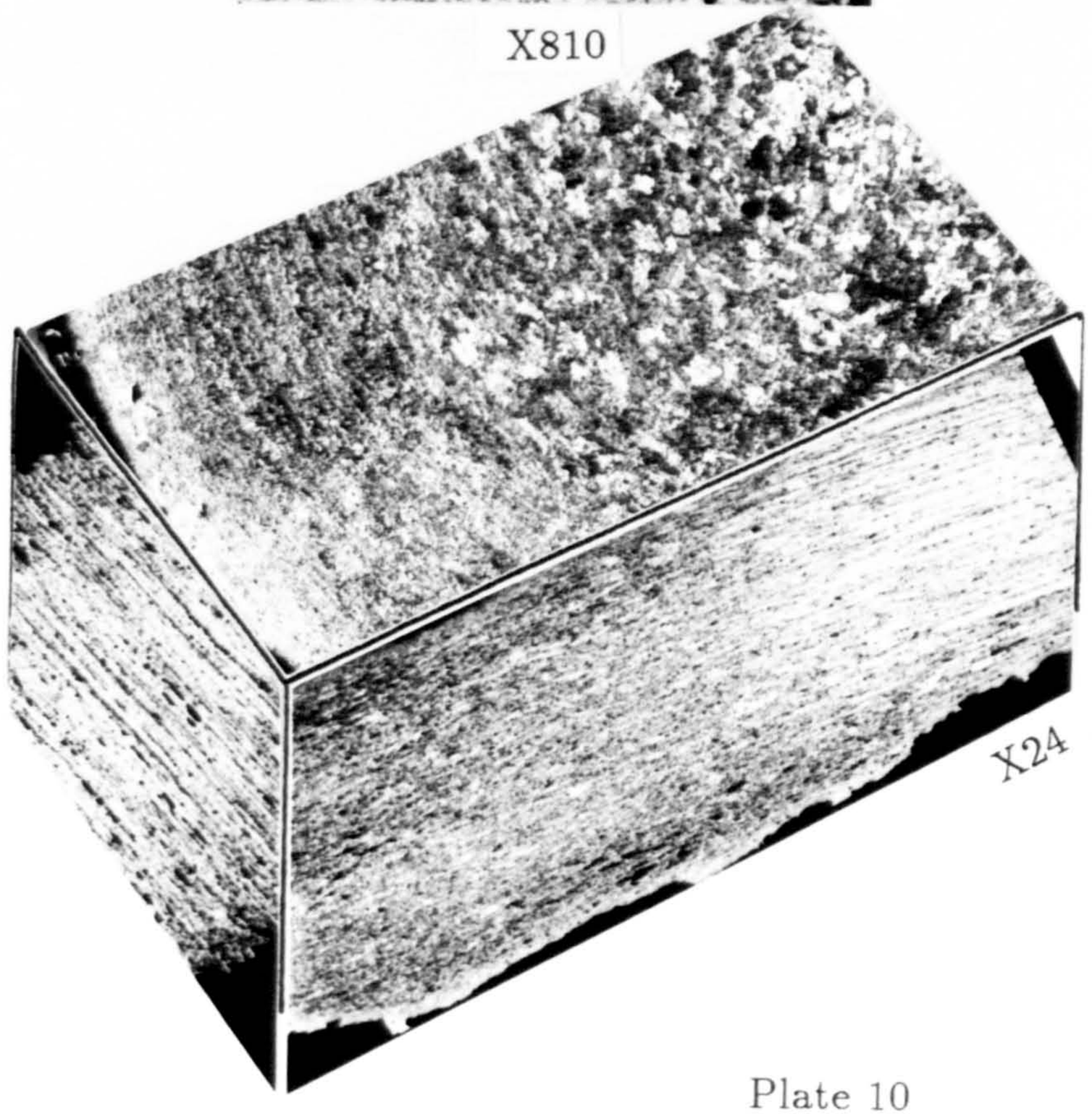

X24

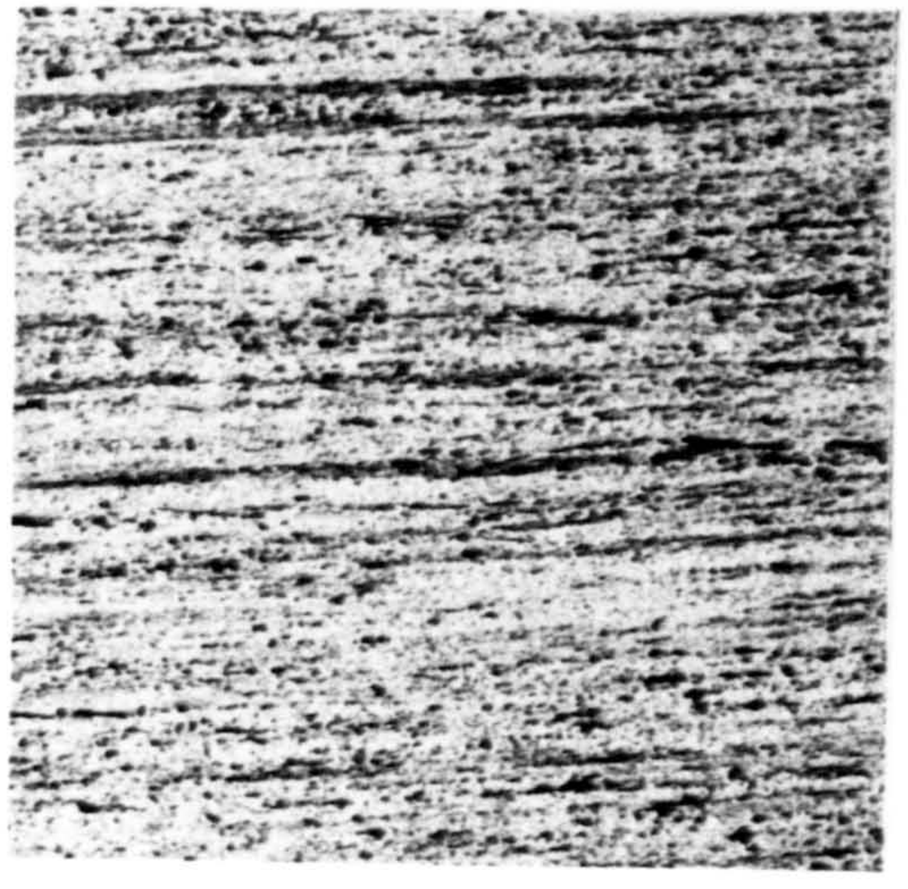

X108

X108

Plate 10

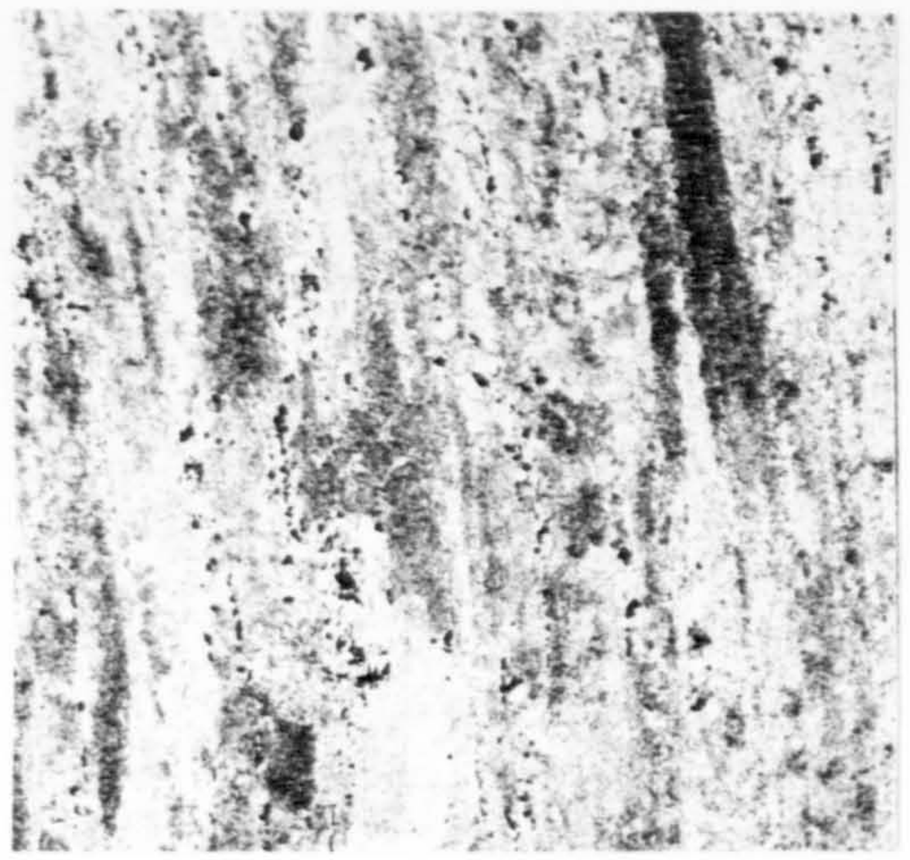

X108

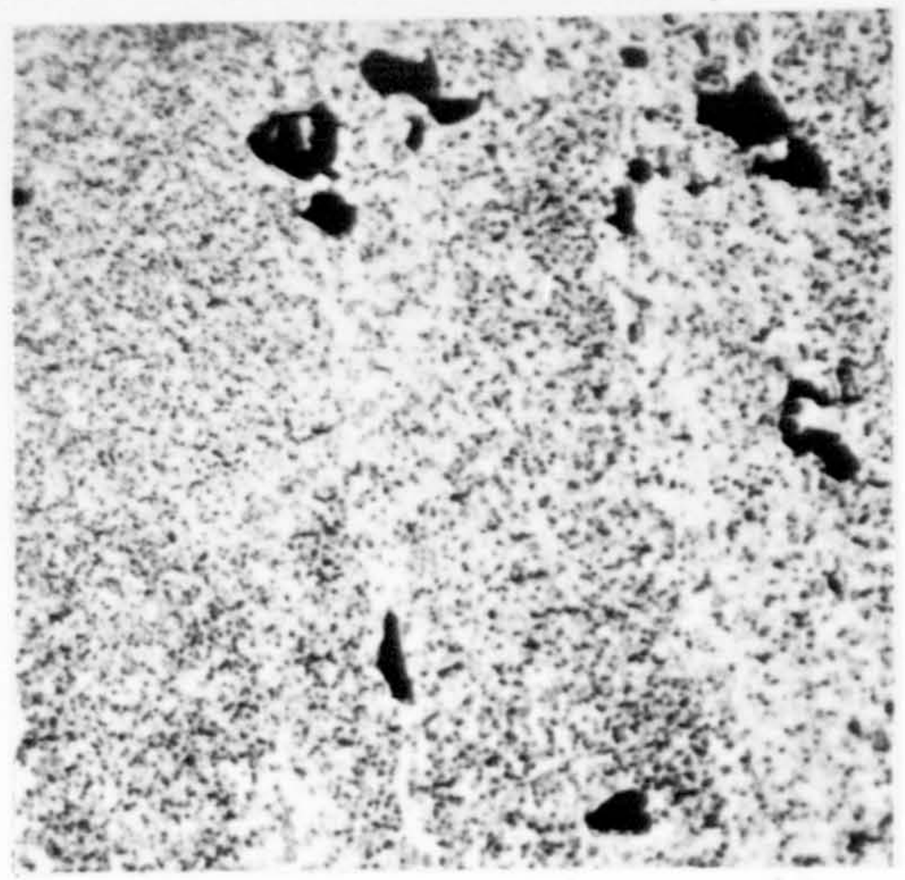

X810

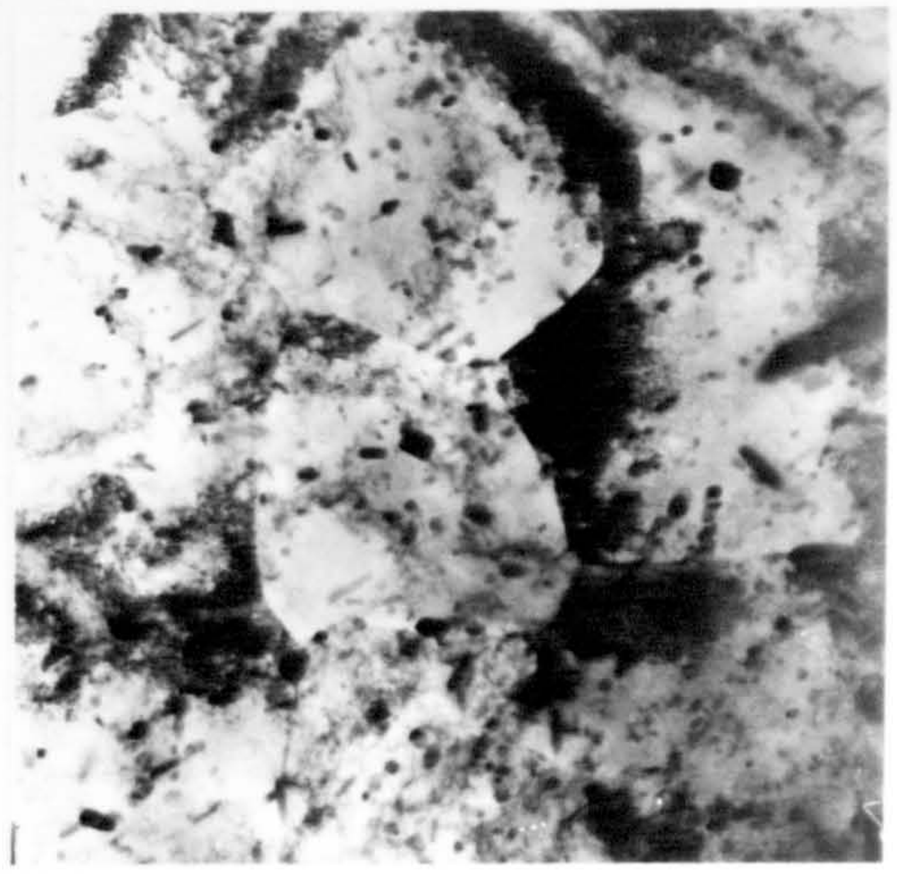

0.5 μm

X108

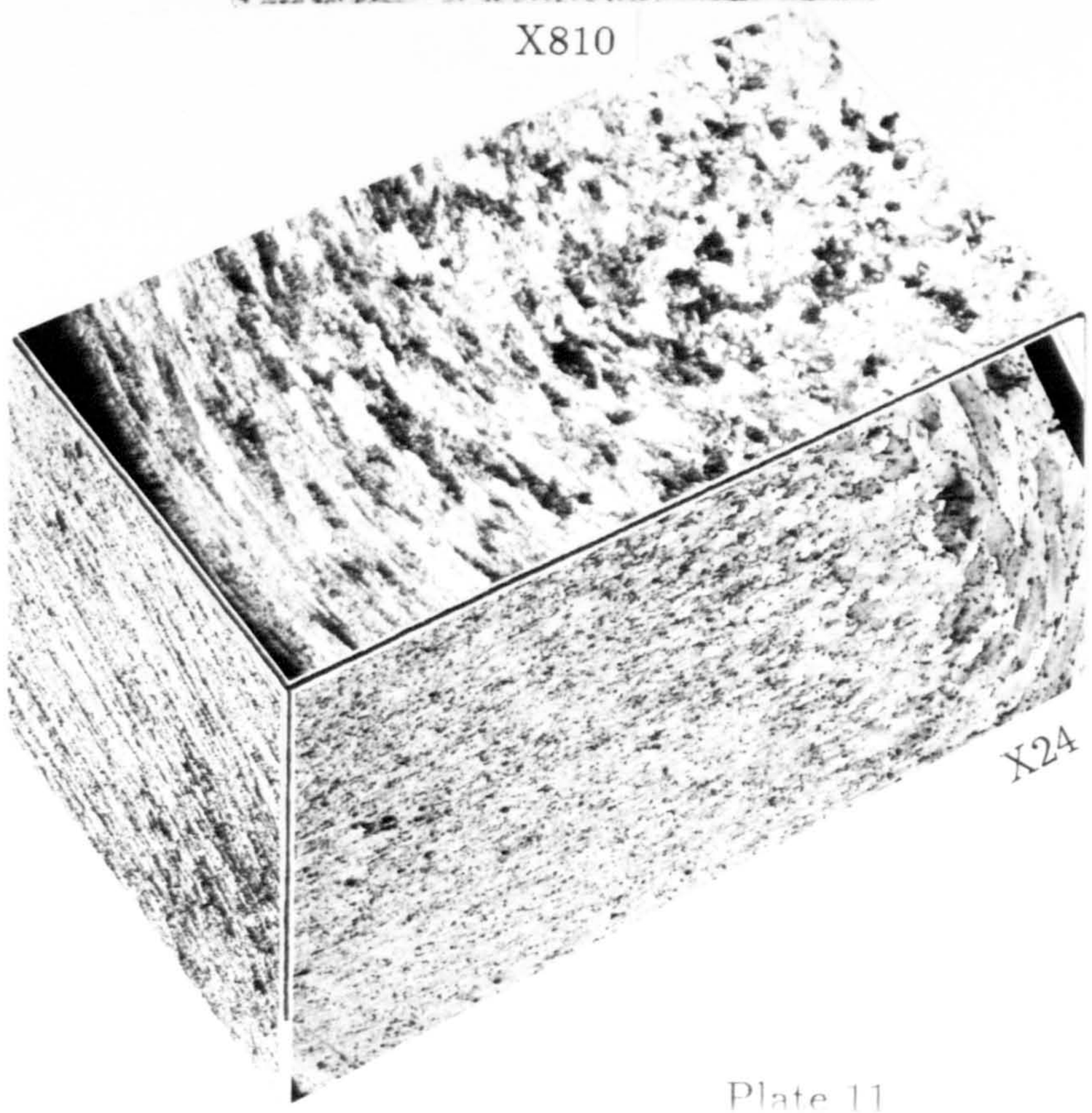

X24

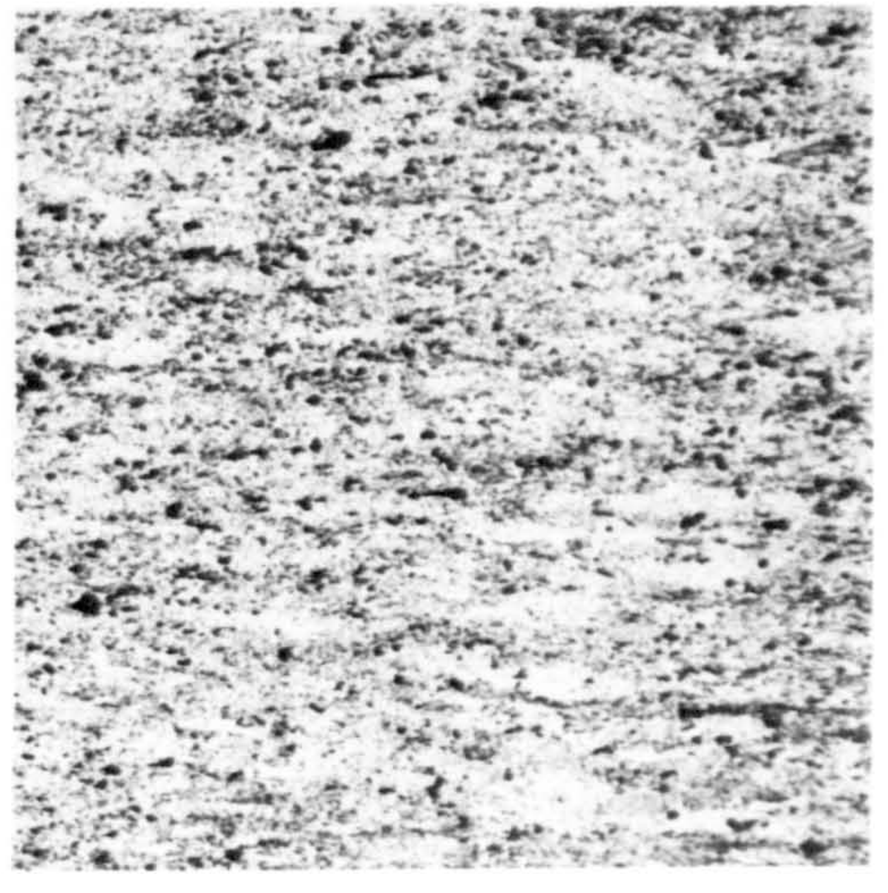

X108

Plate 11

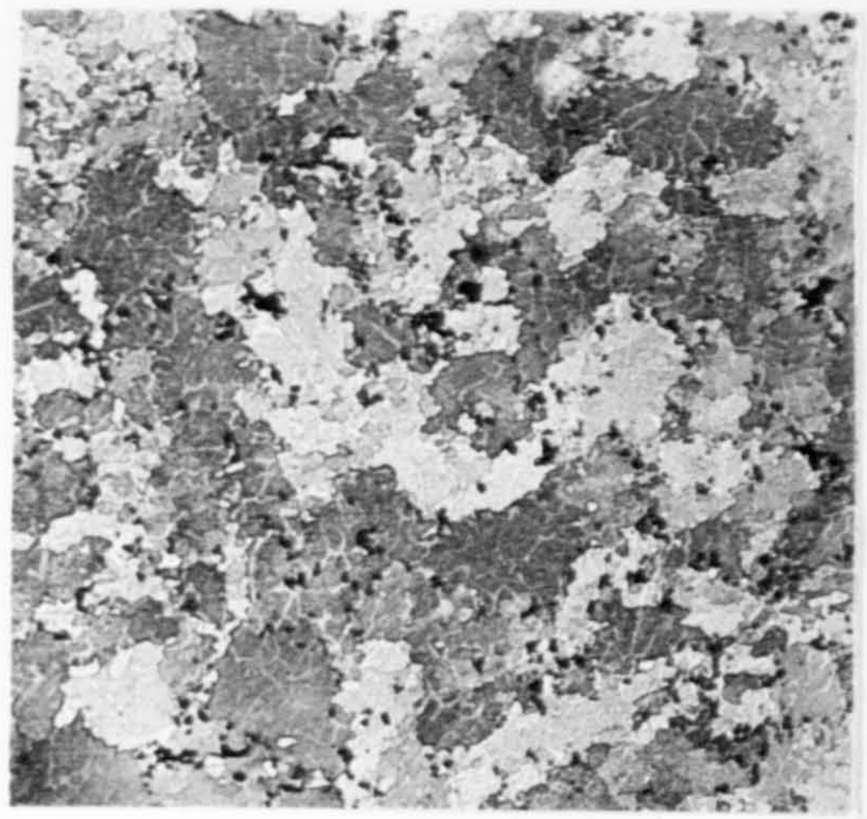

X108

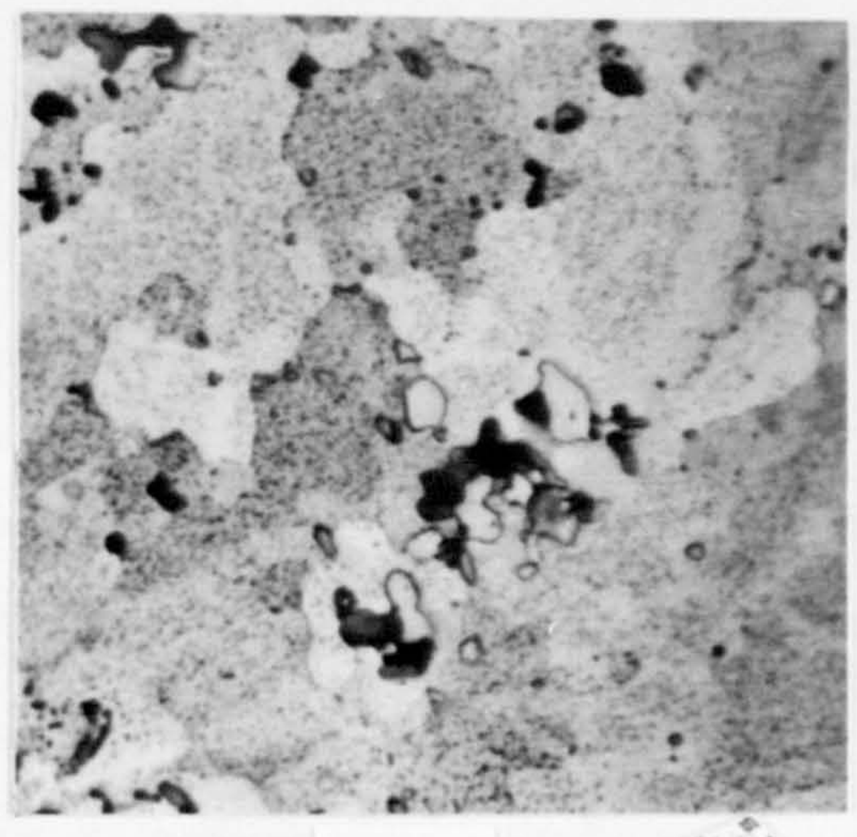

X810

1 μm

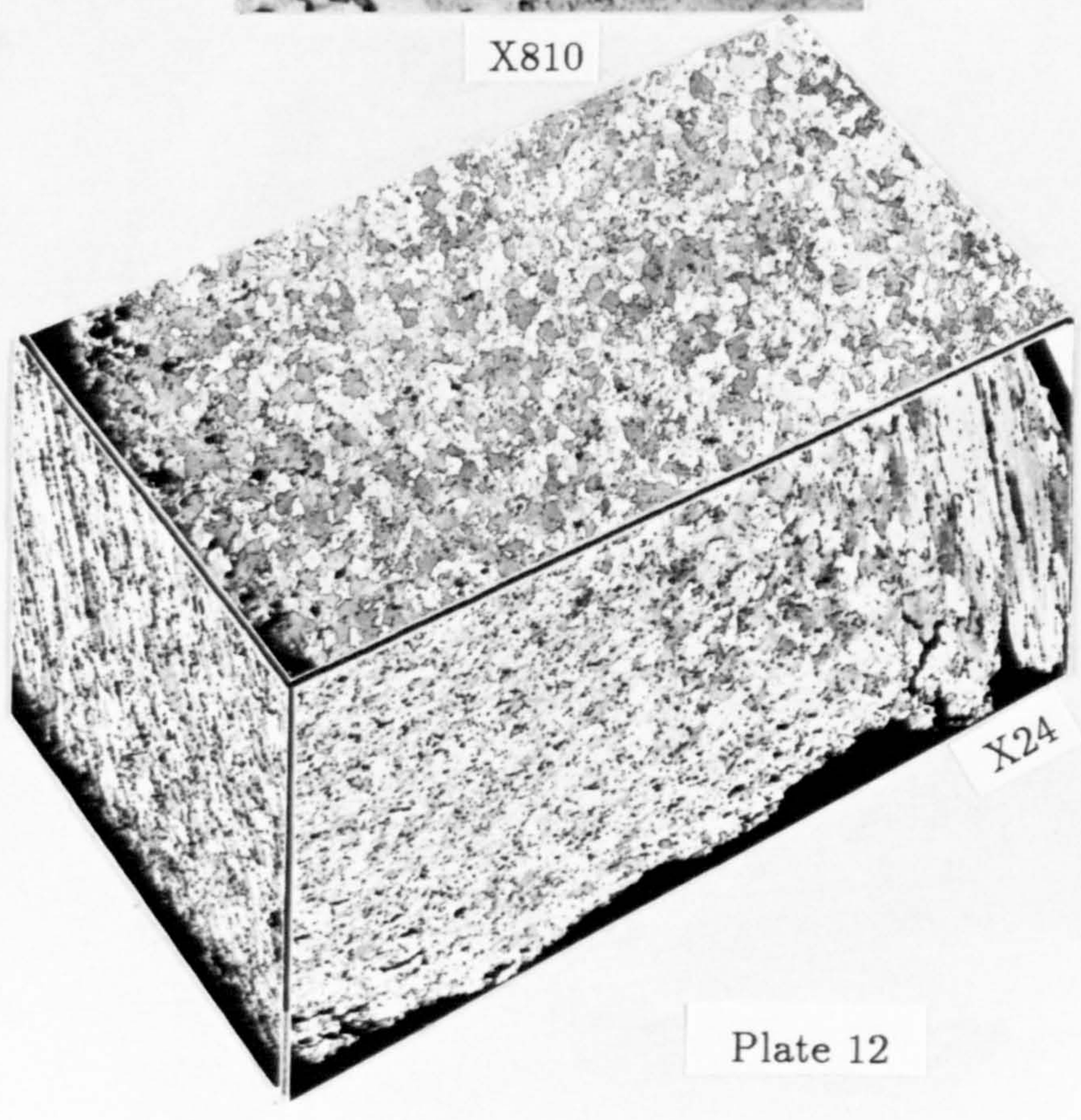

X24

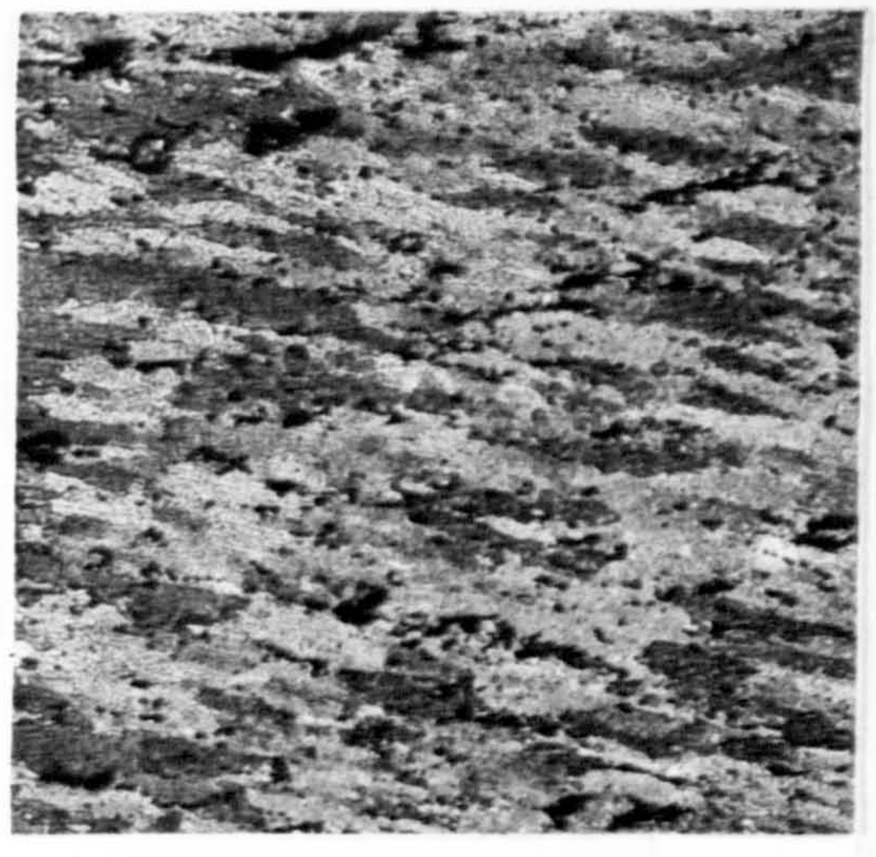

X108

X108

Plate 12

Plate 13

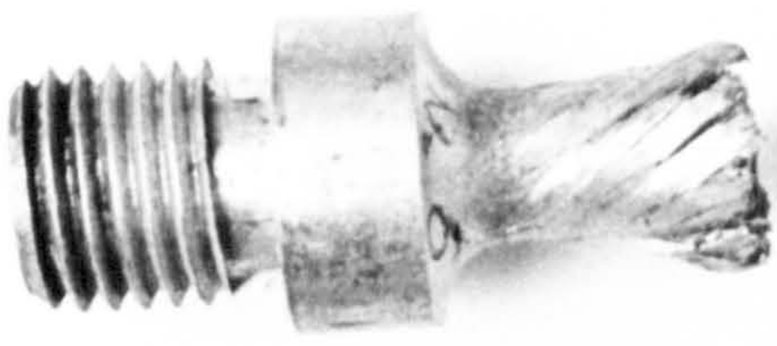

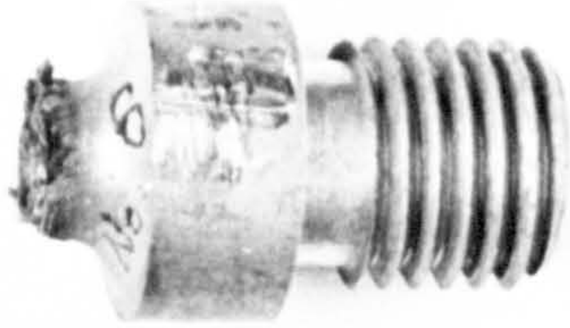

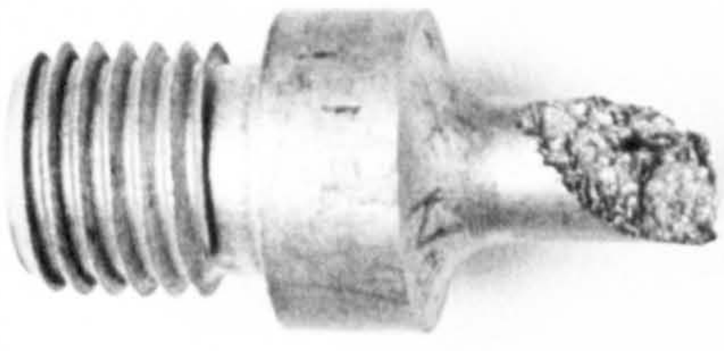

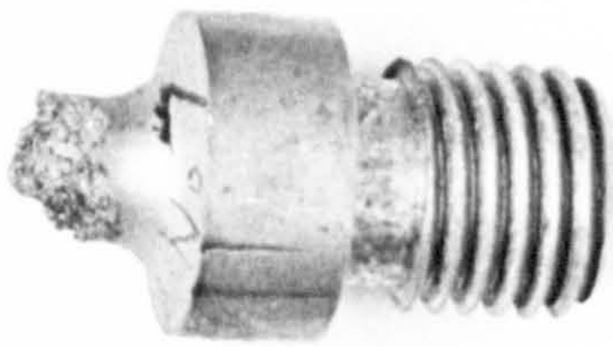

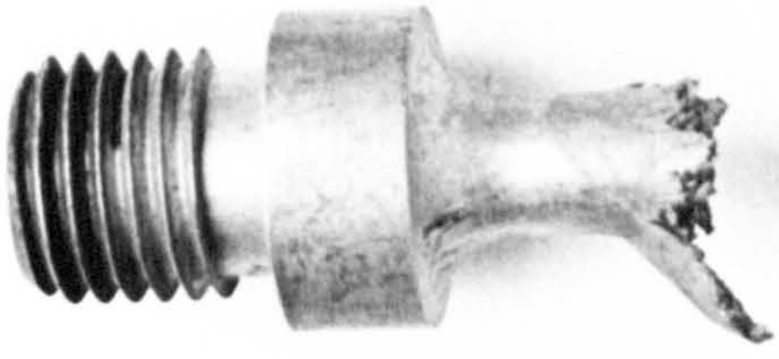

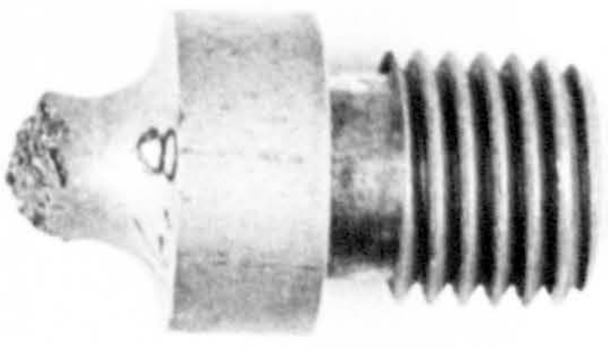

Plate 14

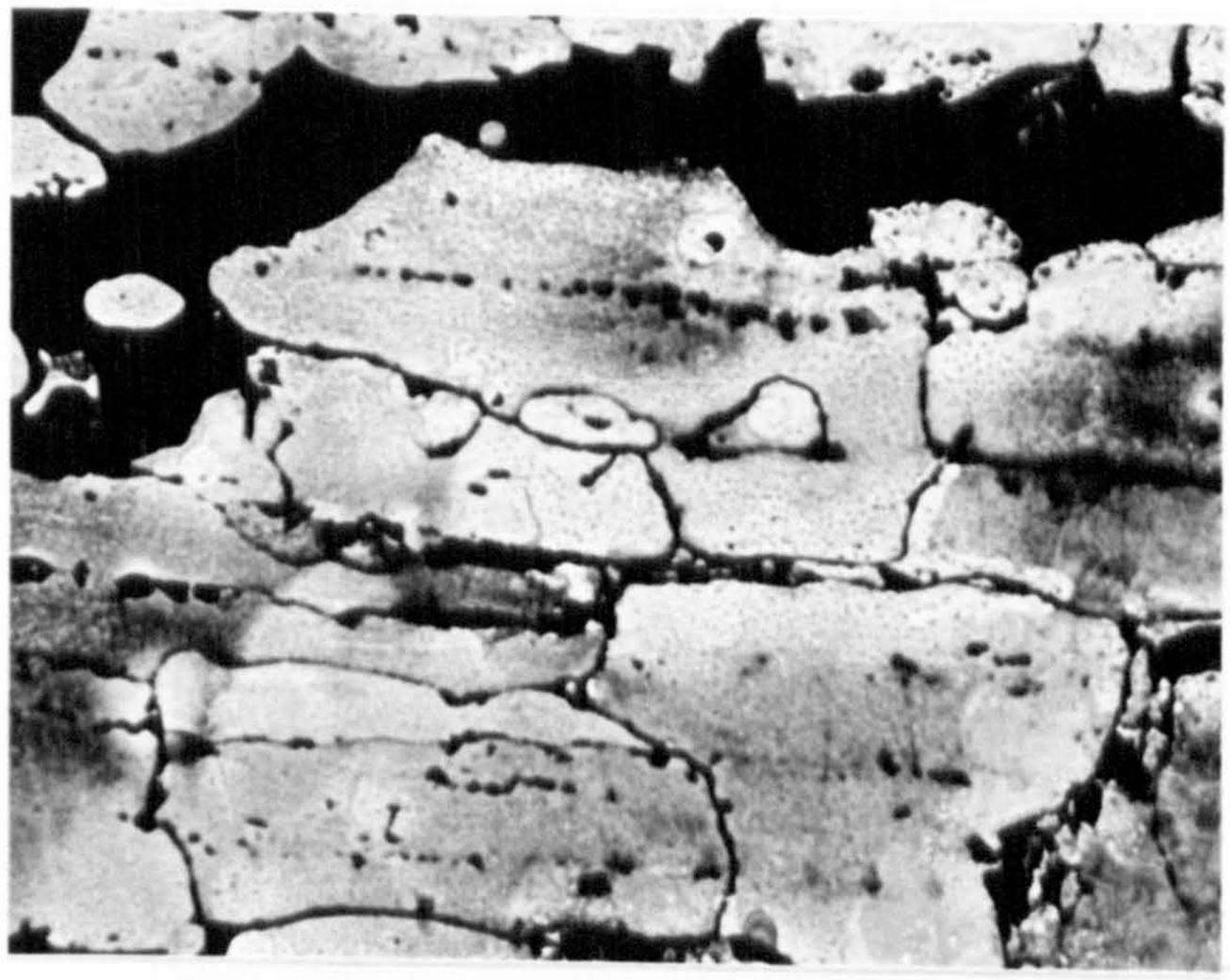

X135

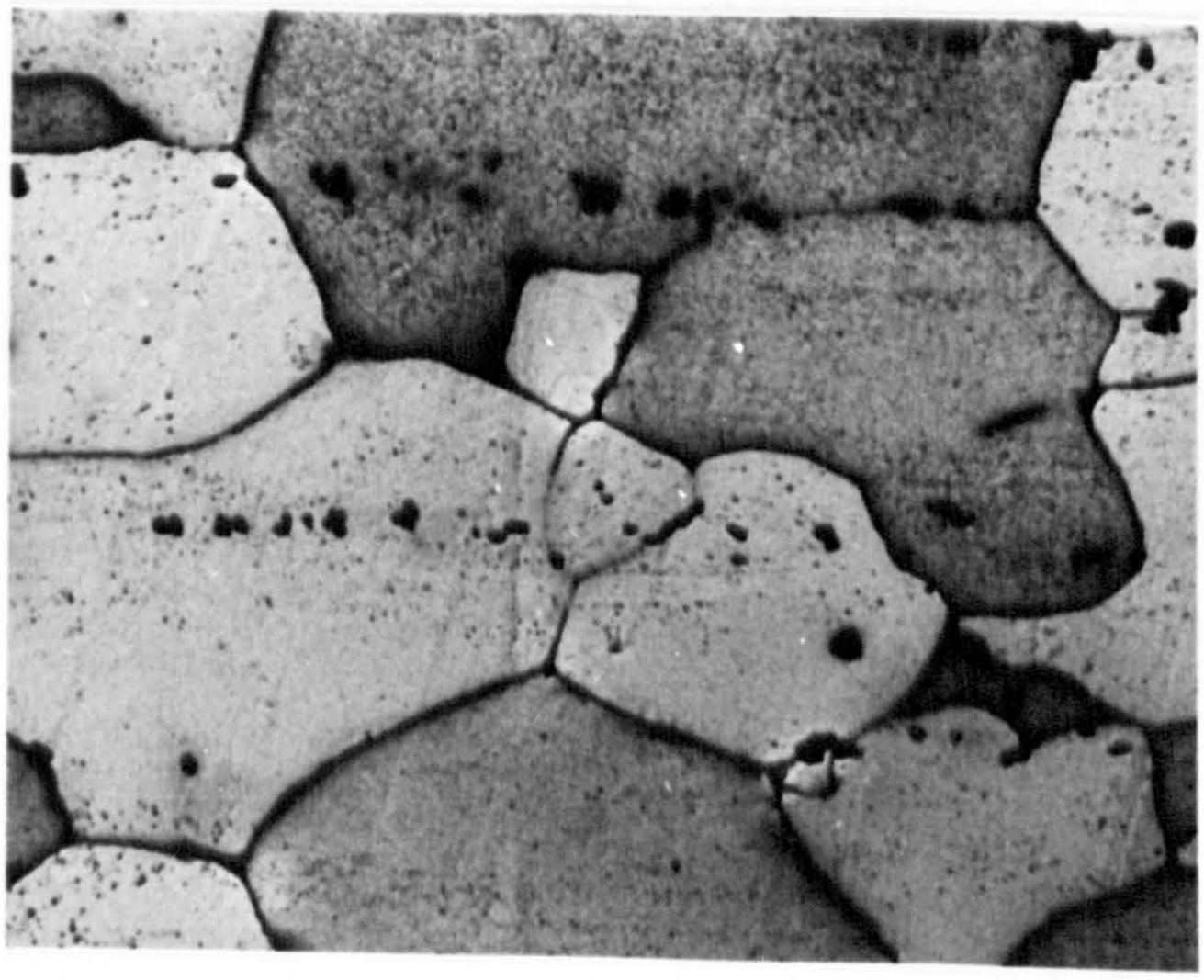

X225

Plate 15

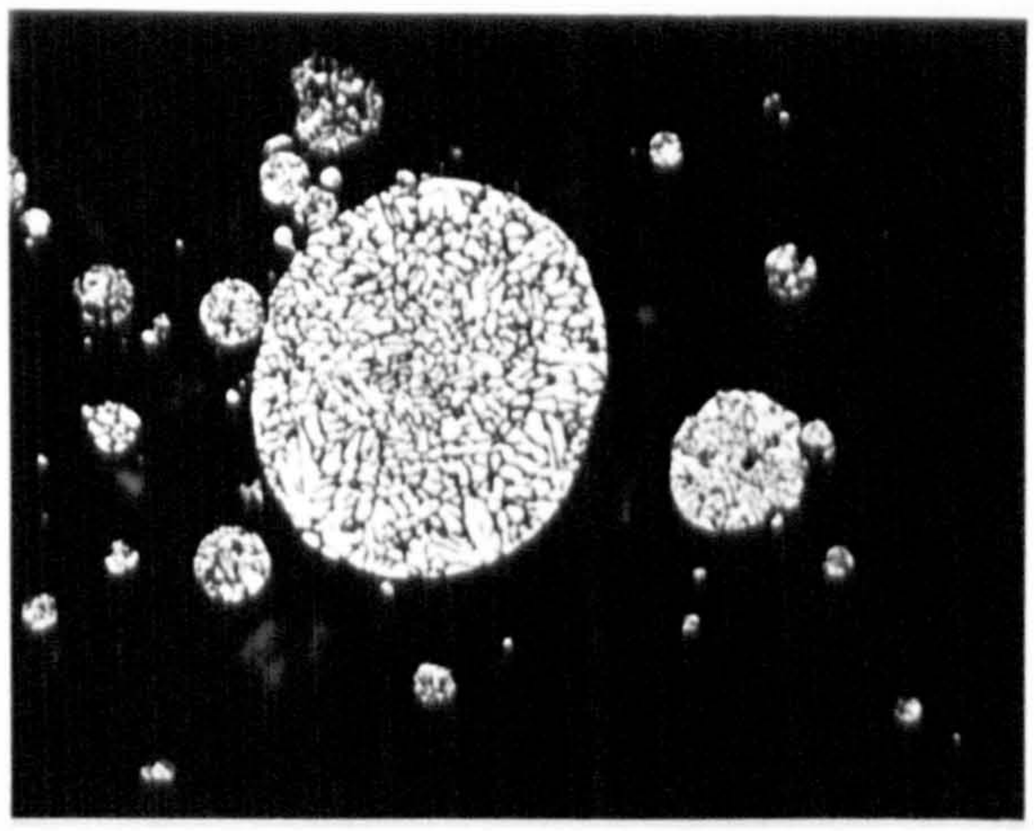

Fine

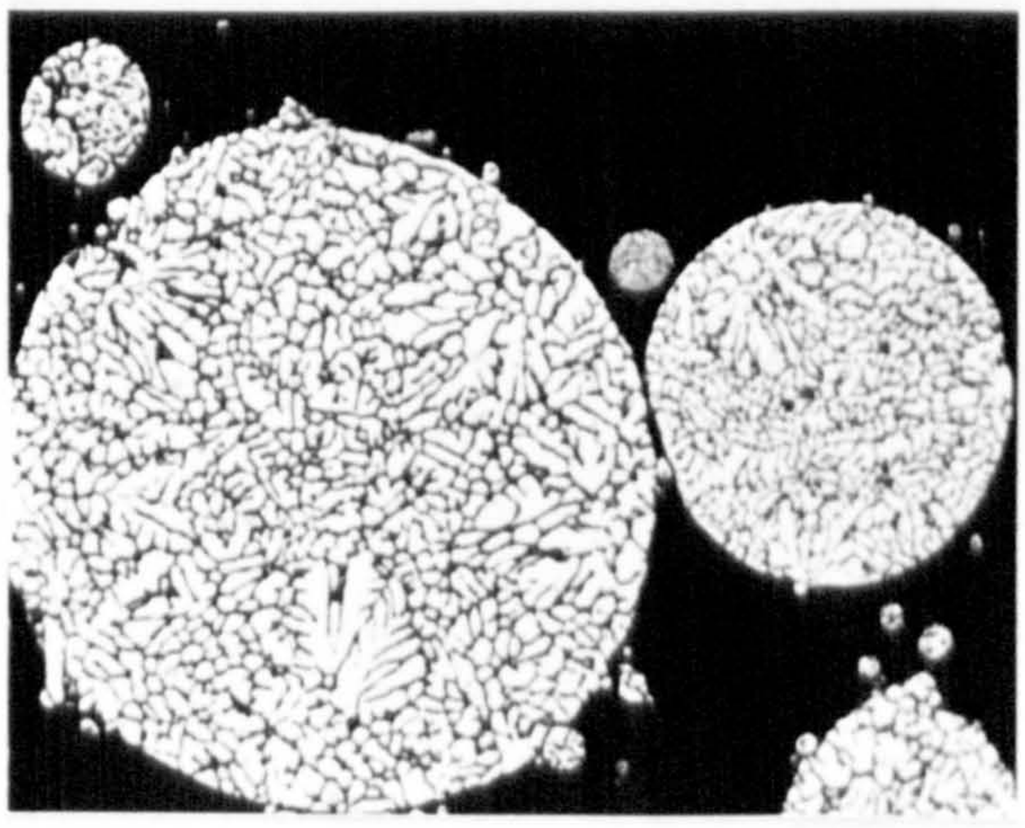

Coarse

X843

Plate 16

250°C

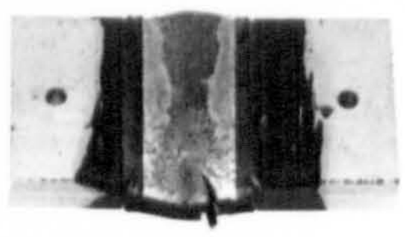

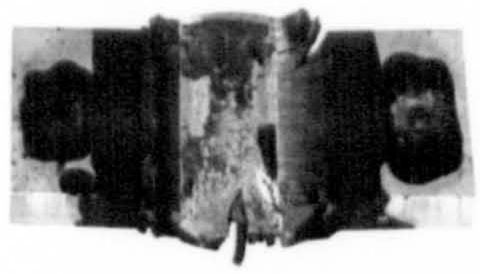

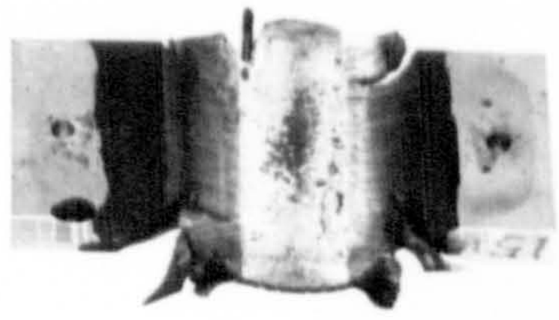

300°C

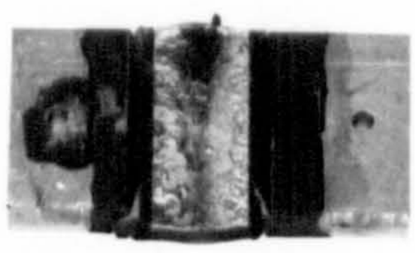

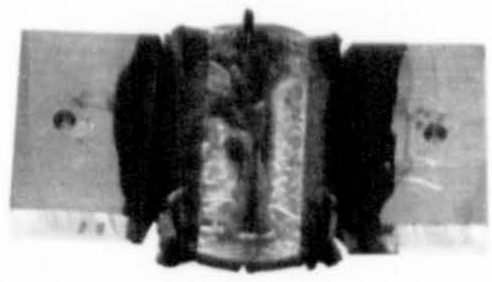

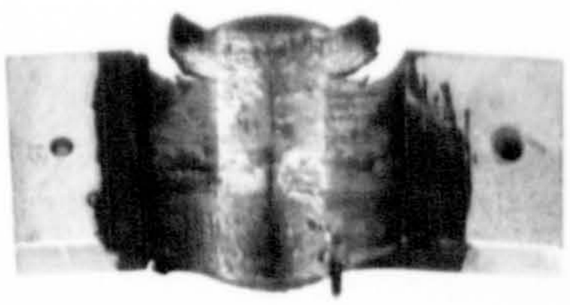

400°C

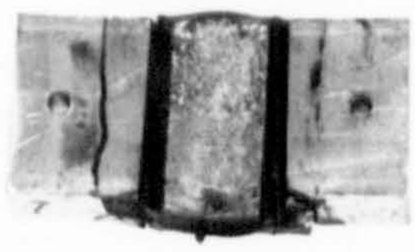

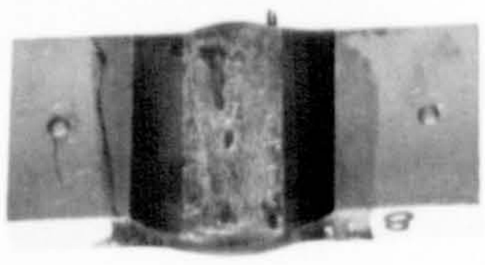

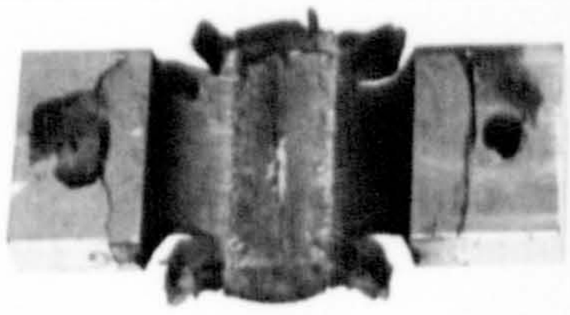

500°C

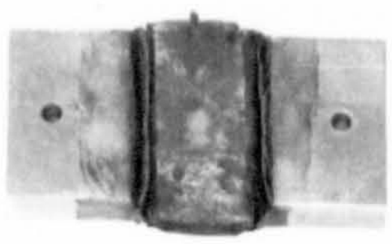

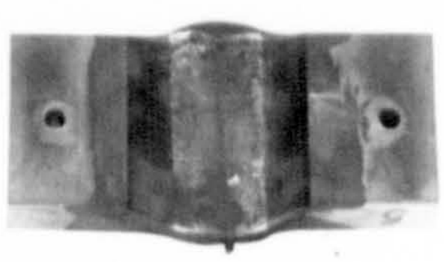

550°C

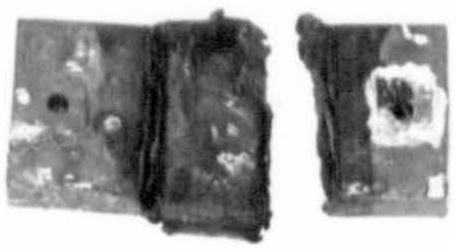

$\epsilon = 0.8 \quad \dot{\epsilon} = 0.8$

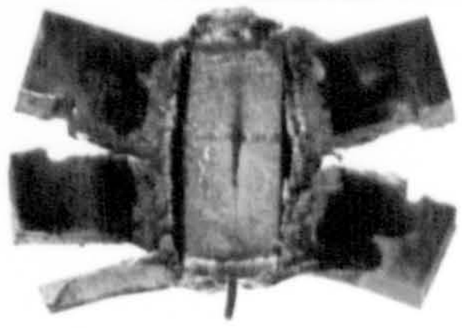

$\epsilon = 1.6 \quad \dot{\epsilon} = 3.4$

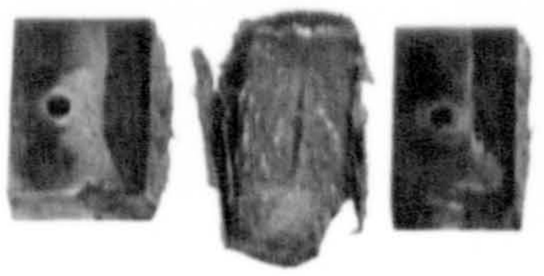

$\epsilon = 2.4 \quad \dot{\epsilon} = 6.9$

Plate 17

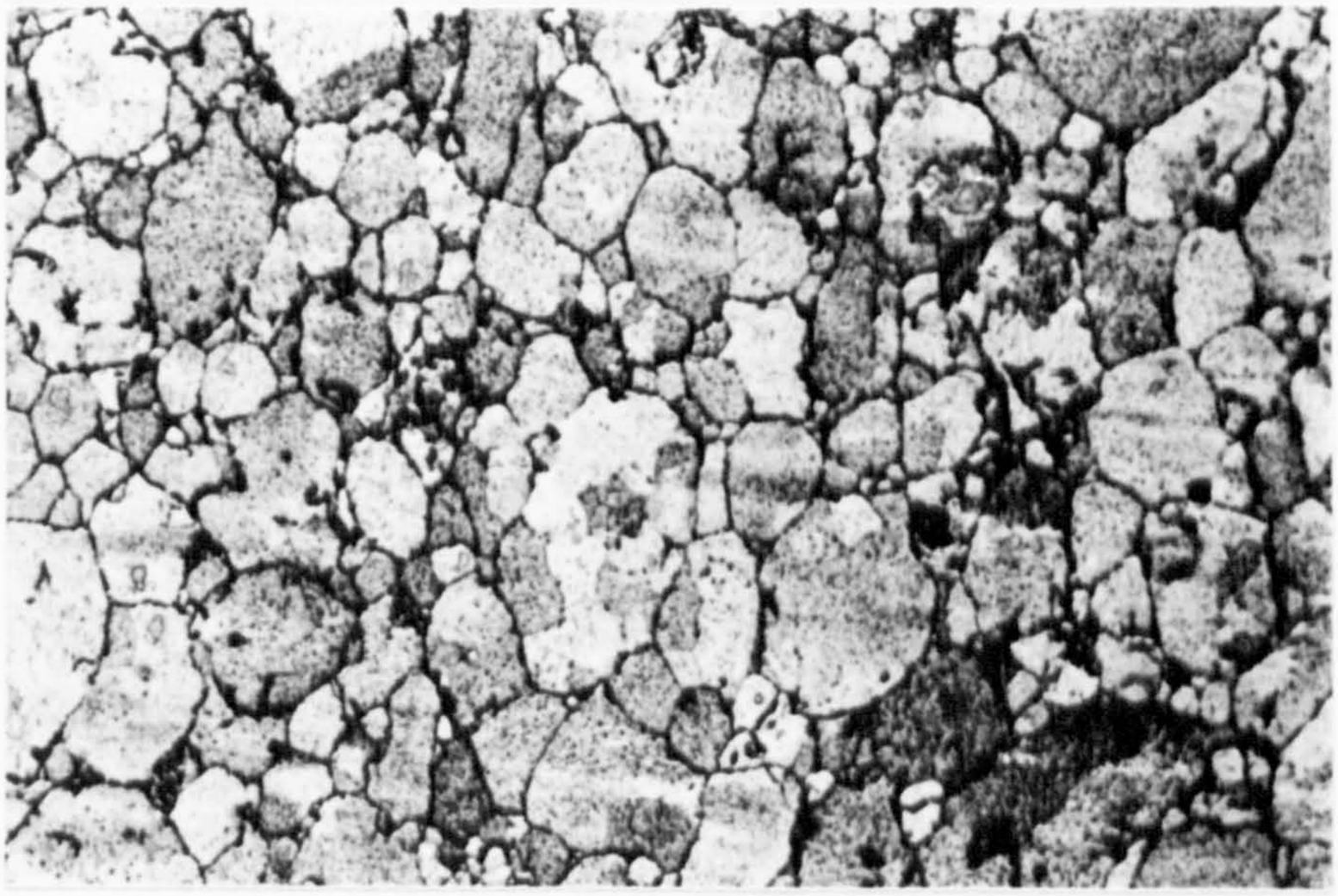

X675

Plate 18

250°C

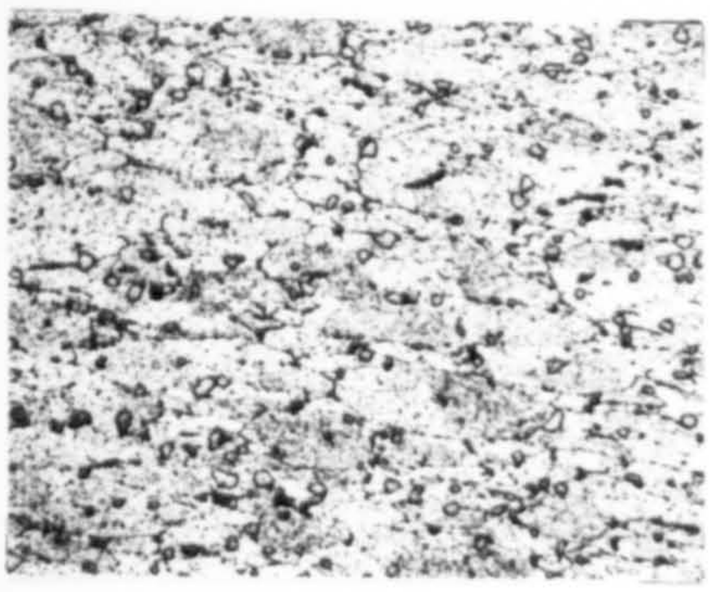

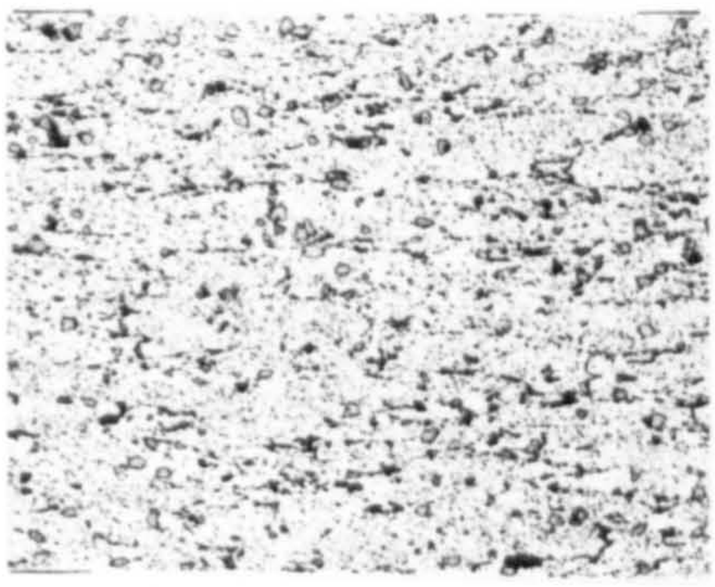

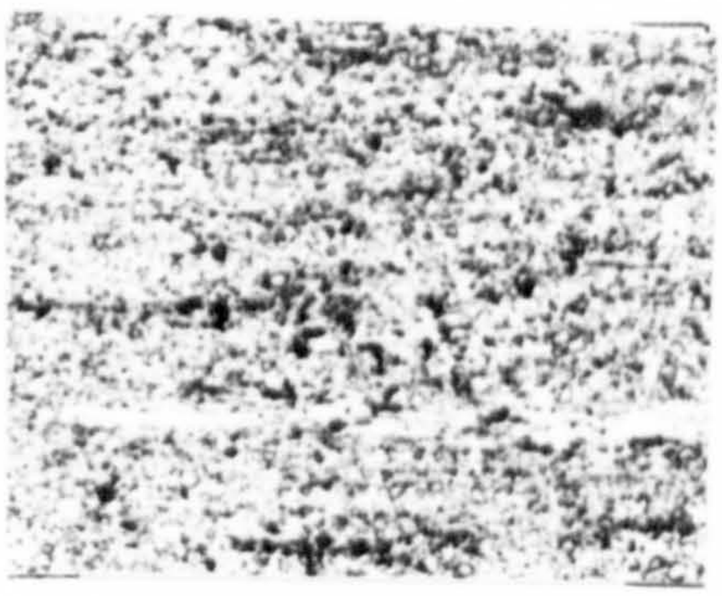

300°C

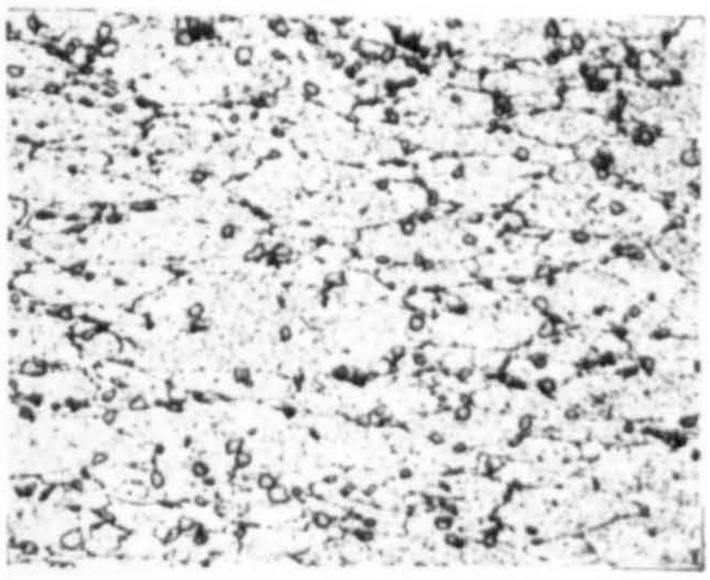

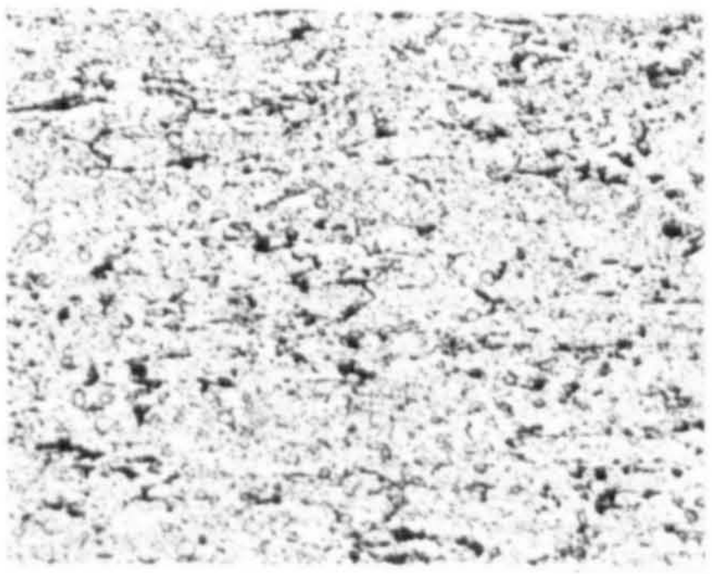

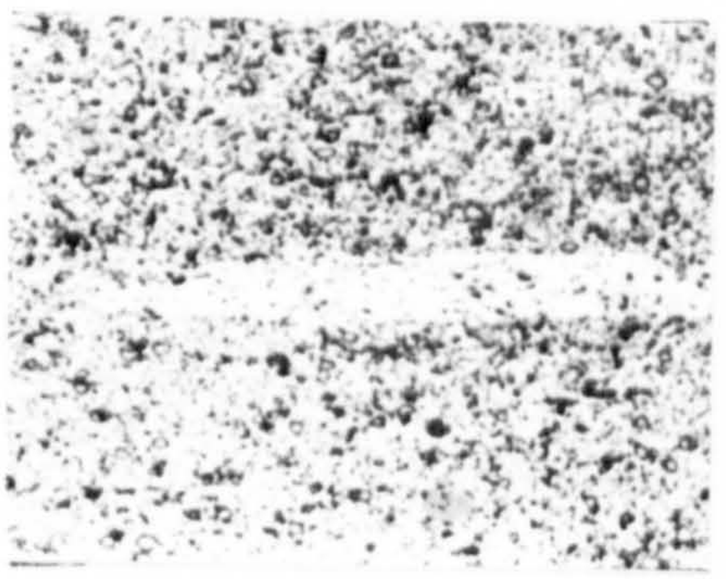

400°C

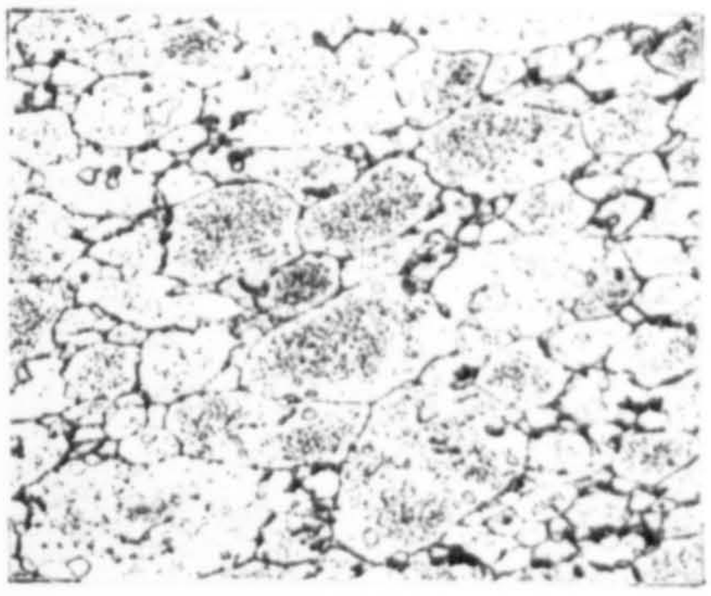

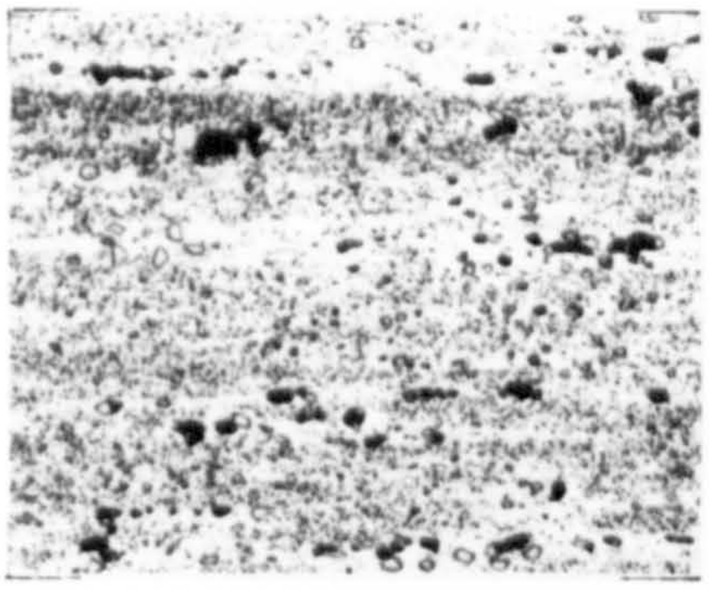

500°C

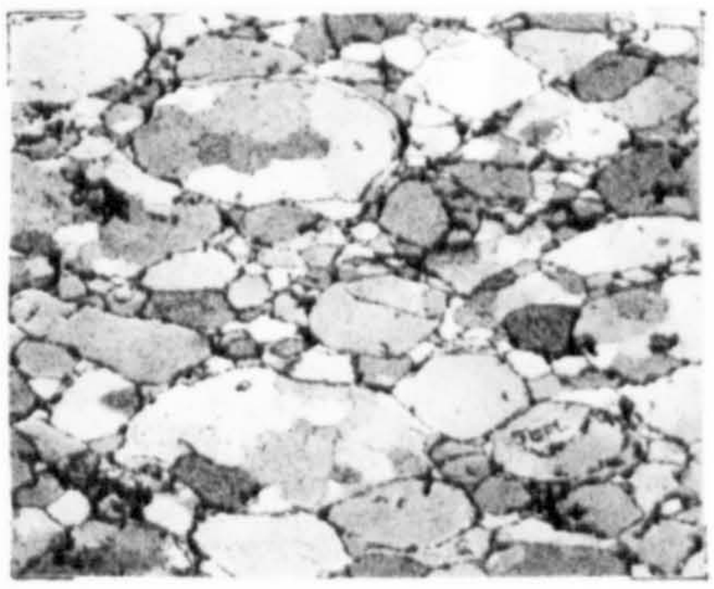

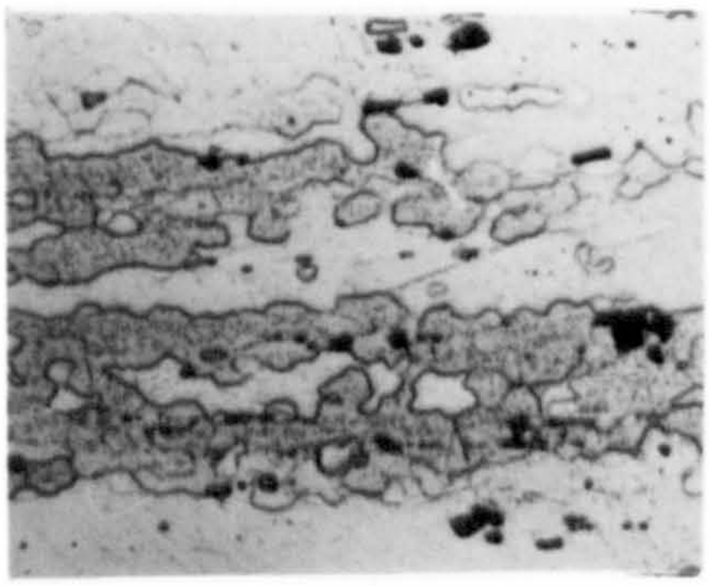

550°C

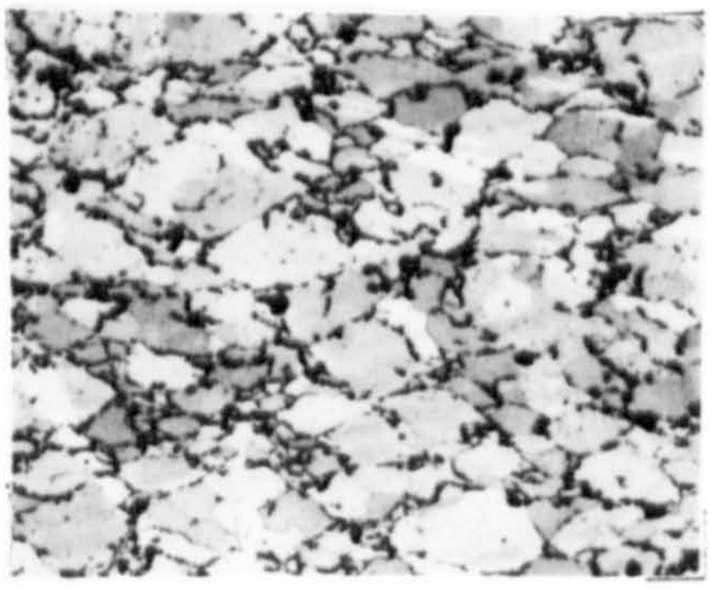

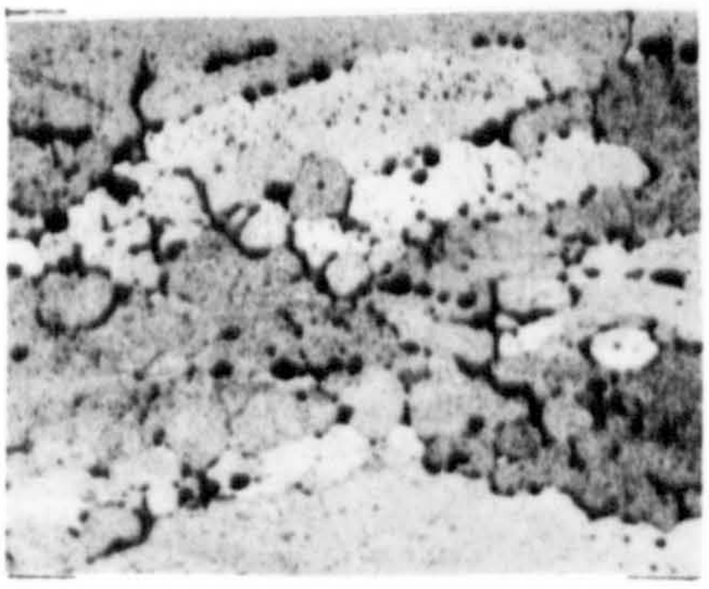

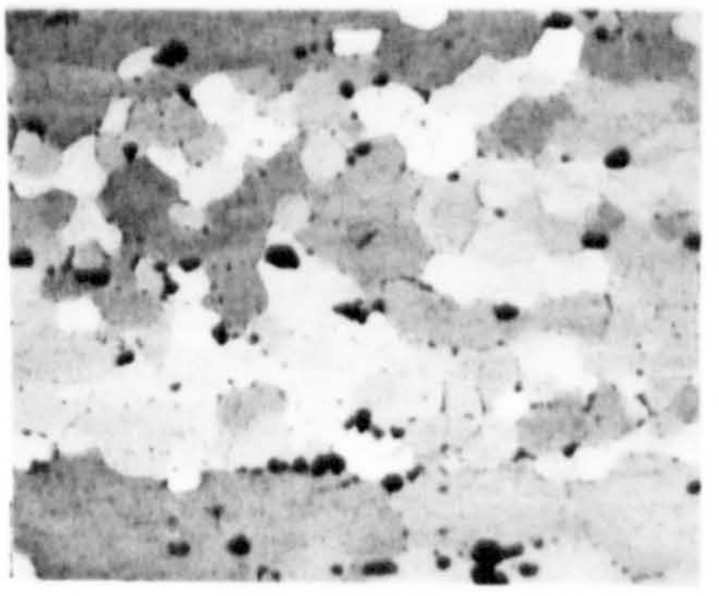

$\epsilon = 0.8, \dot{\epsilon} = 0.8$

$\epsilon = 1.6, \dot{\epsilon} = 3.4$

$\epsilon = 2.4, \dot{\epsilon} = 6.9$

Plate 19

X336

250°C

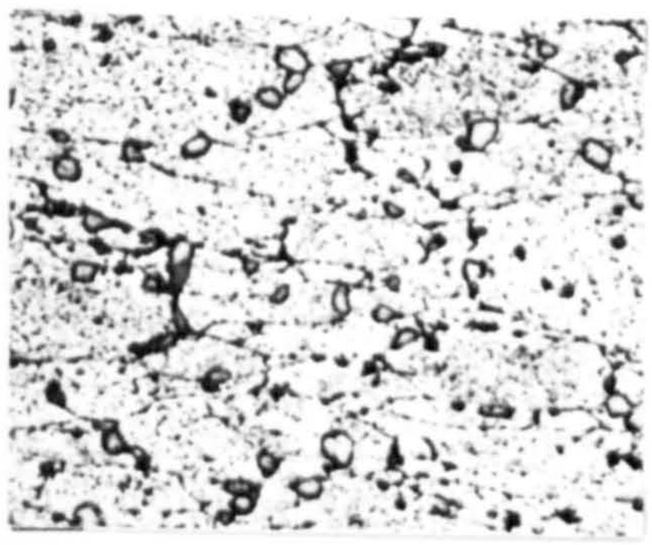

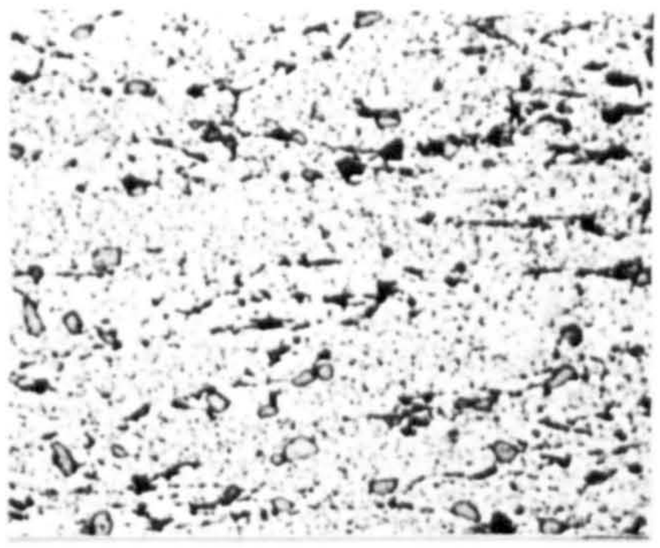

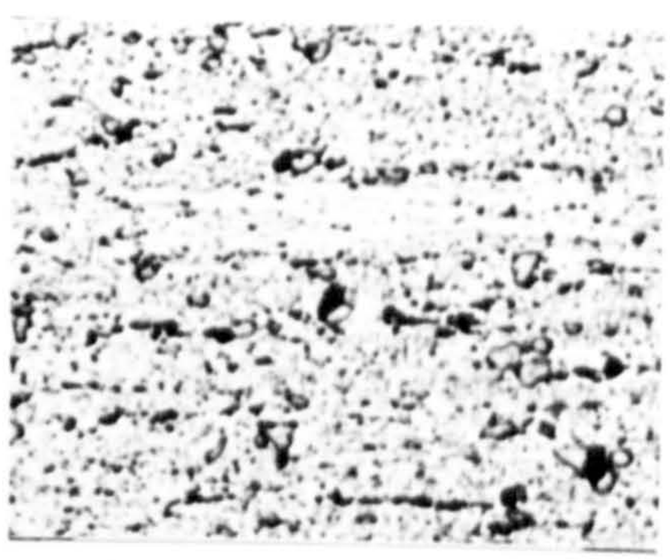

300°C

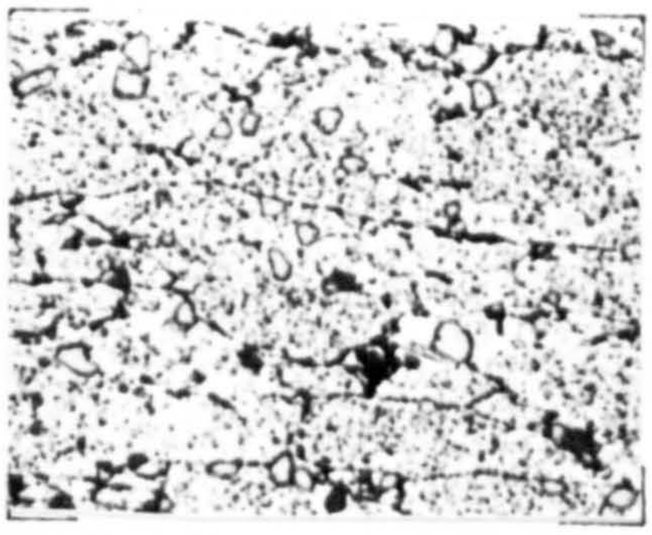

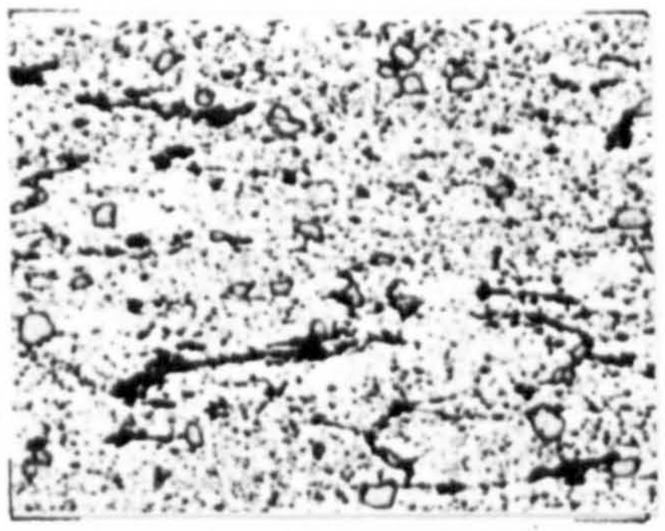

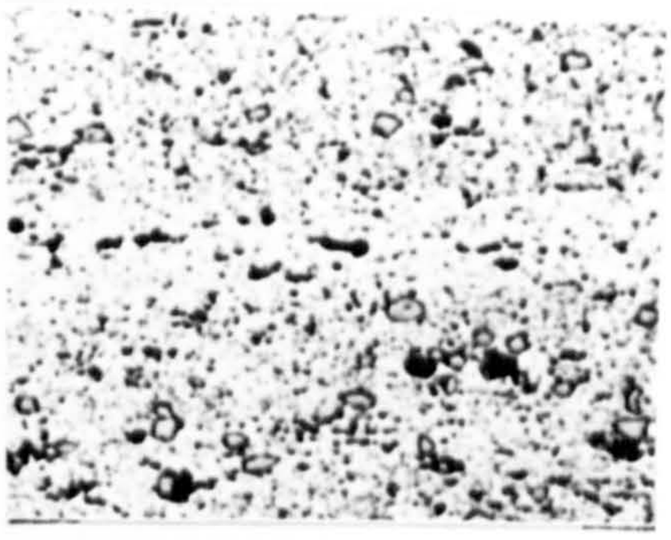

400°C

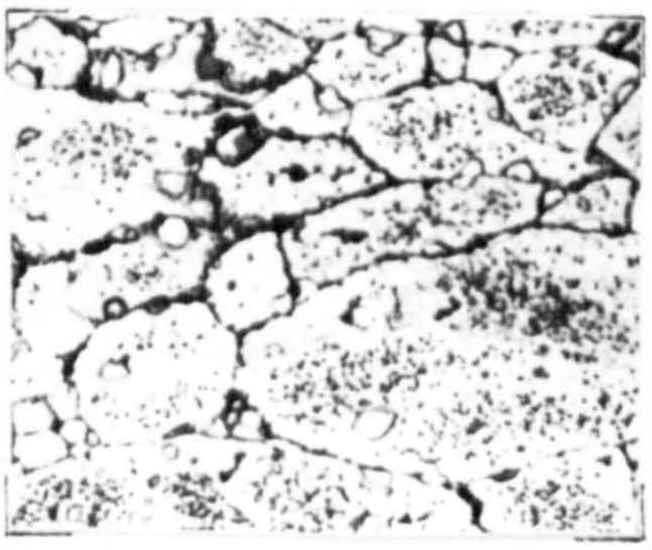

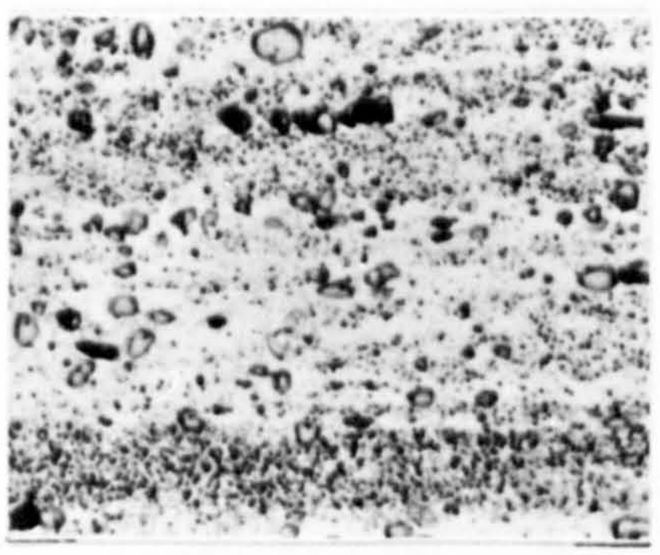

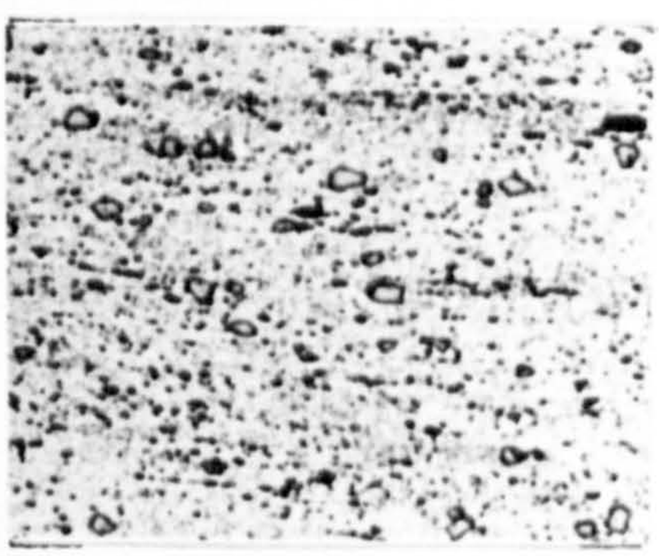

500°C

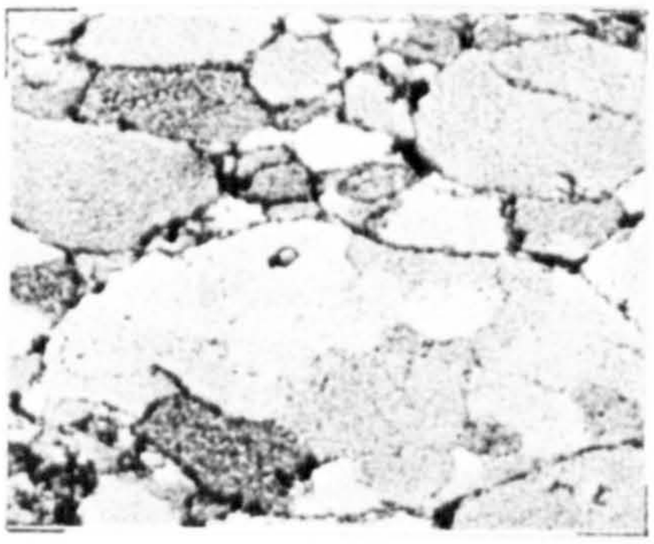

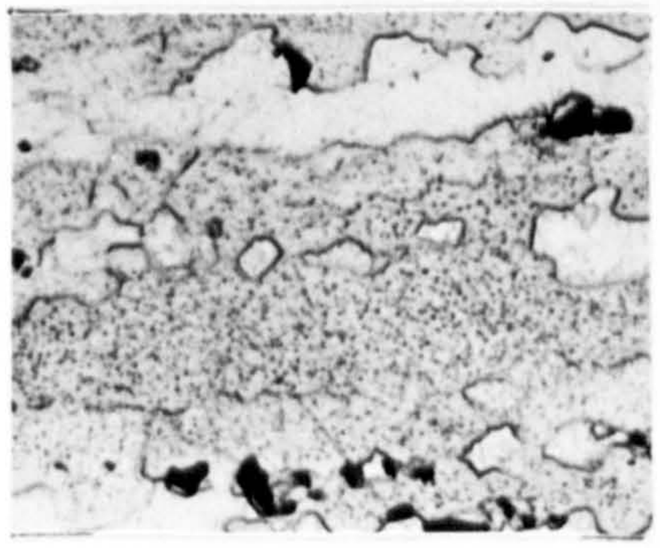

550°C

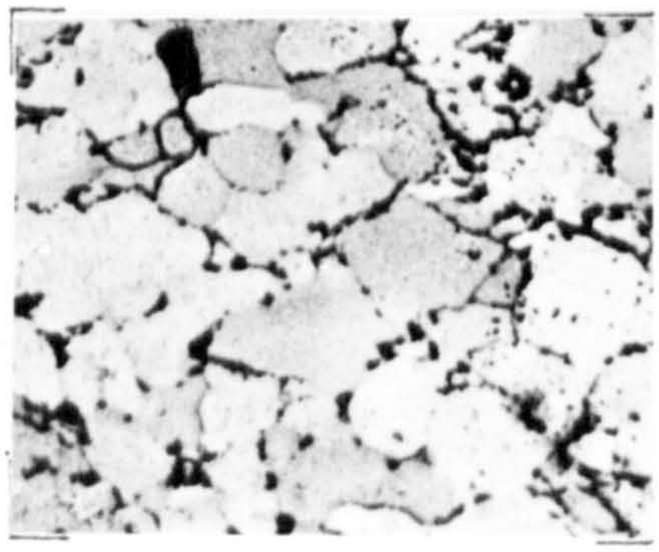

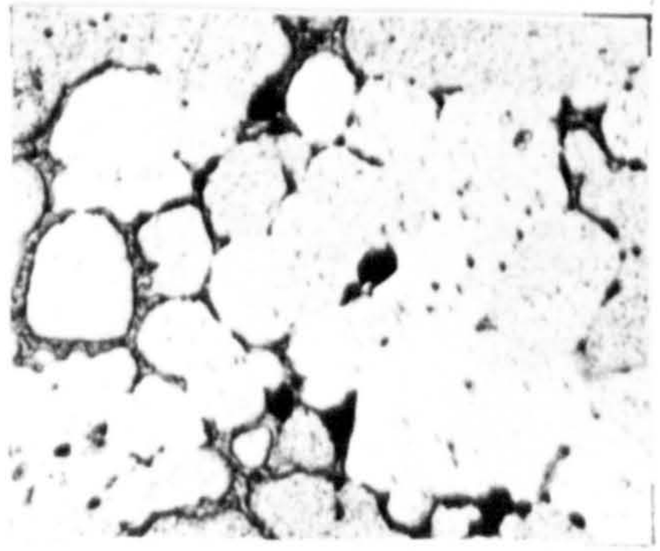

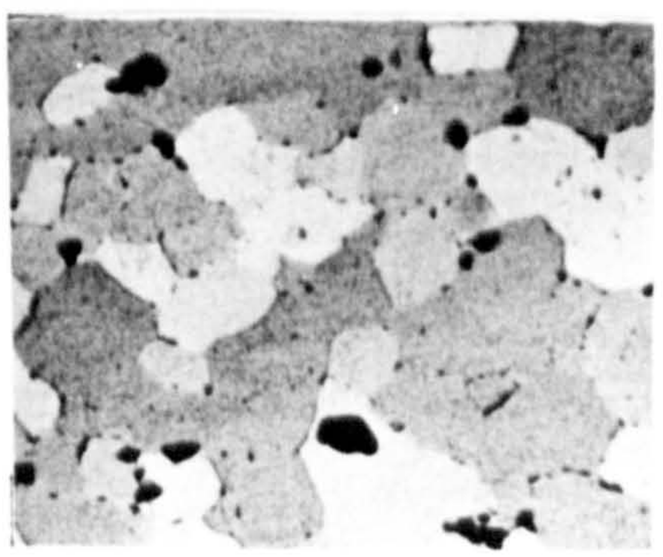

$\epsilon = 0.8, \dot{\epsilon} = 0.8$

$\epsilon = 1.6, \dot{\epsilon} = 3.4$

$\epsilon = 2.4, \dot{\epsilon} = 6.9$

Plate 20

X675

250°C

300°C

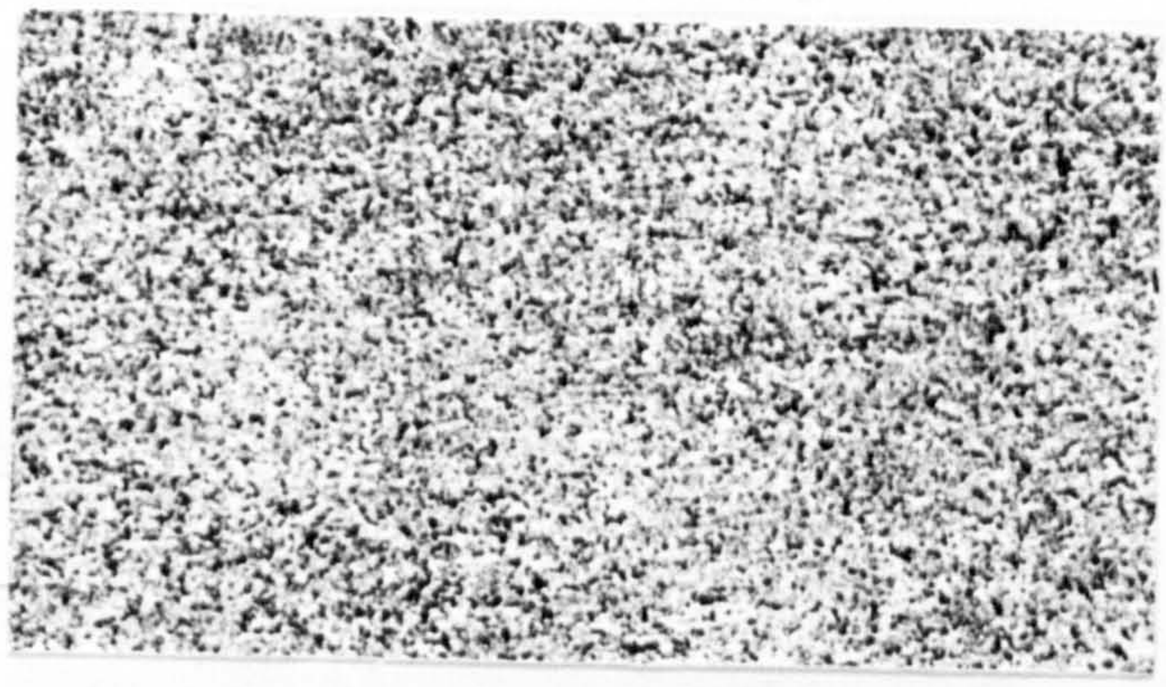

400°C

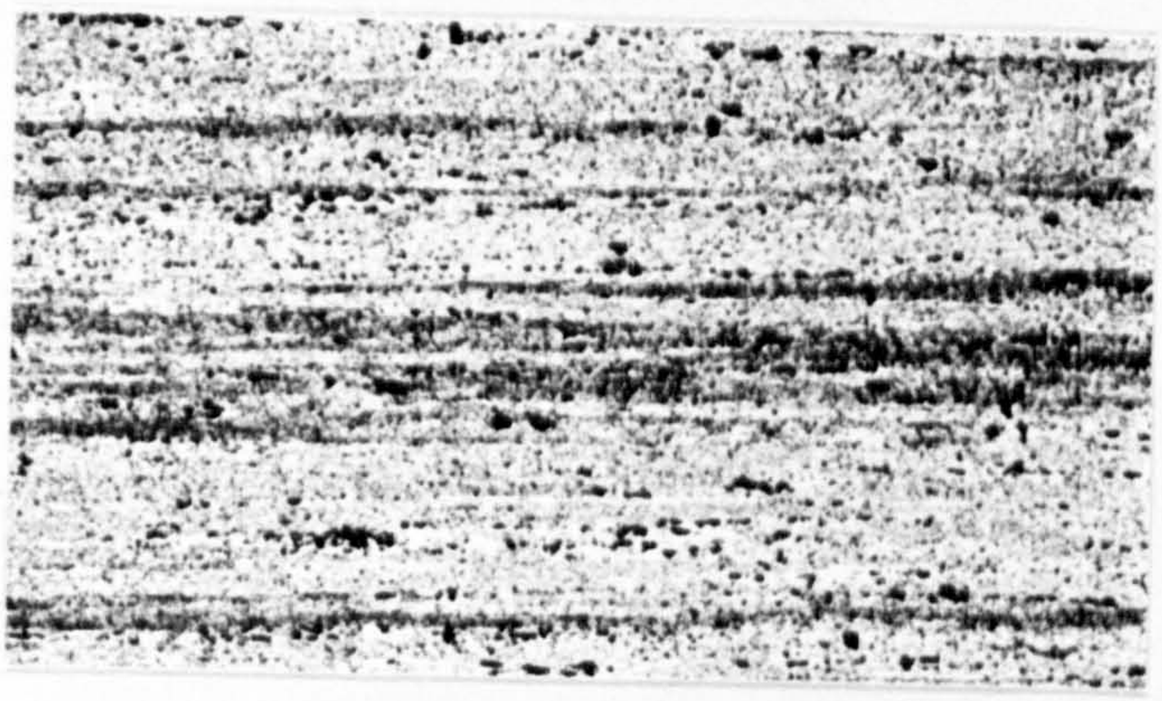

500°C

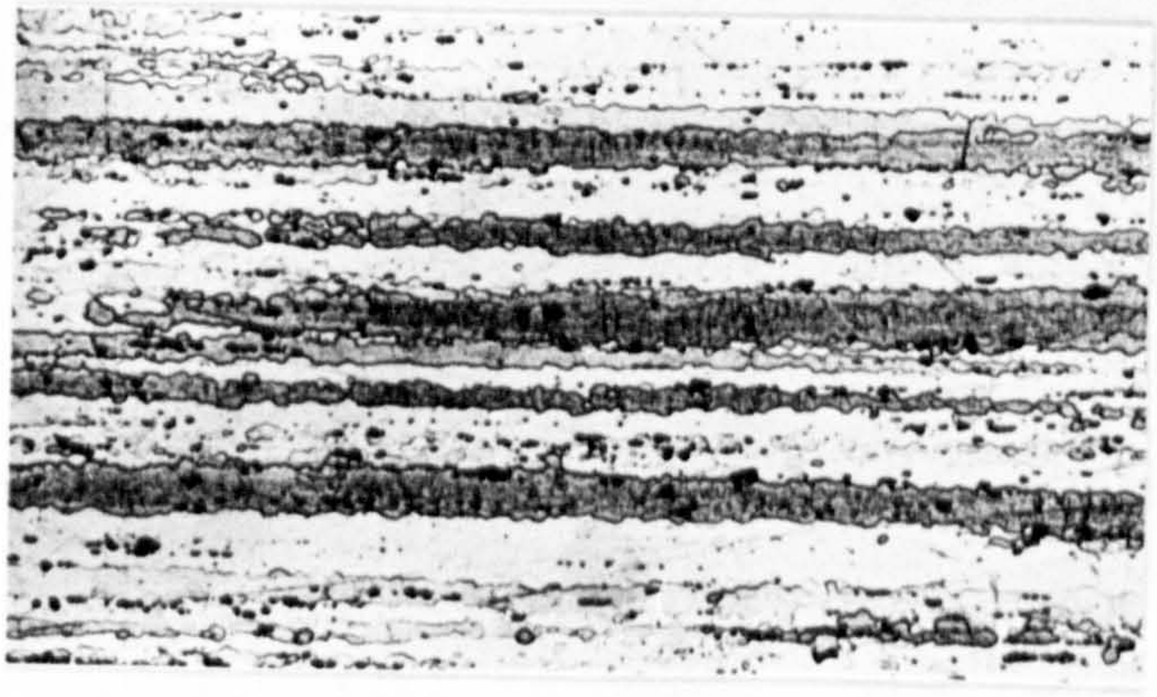

550°C

$\epsilon = 1.6, \dot{\epsilon} = 3.4$ X135

Plate 21

250°C

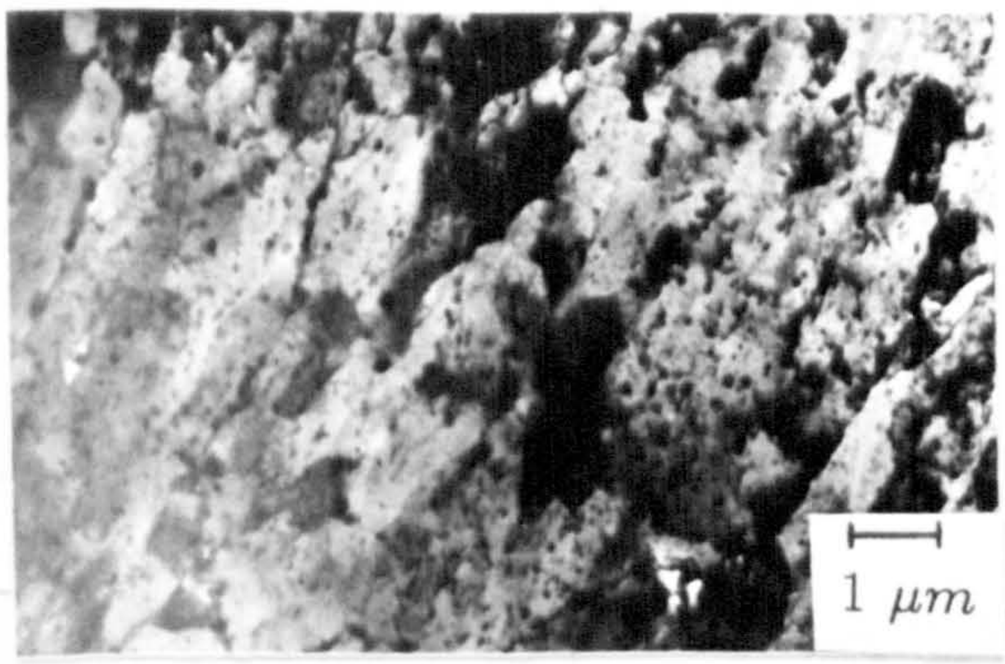

300°C

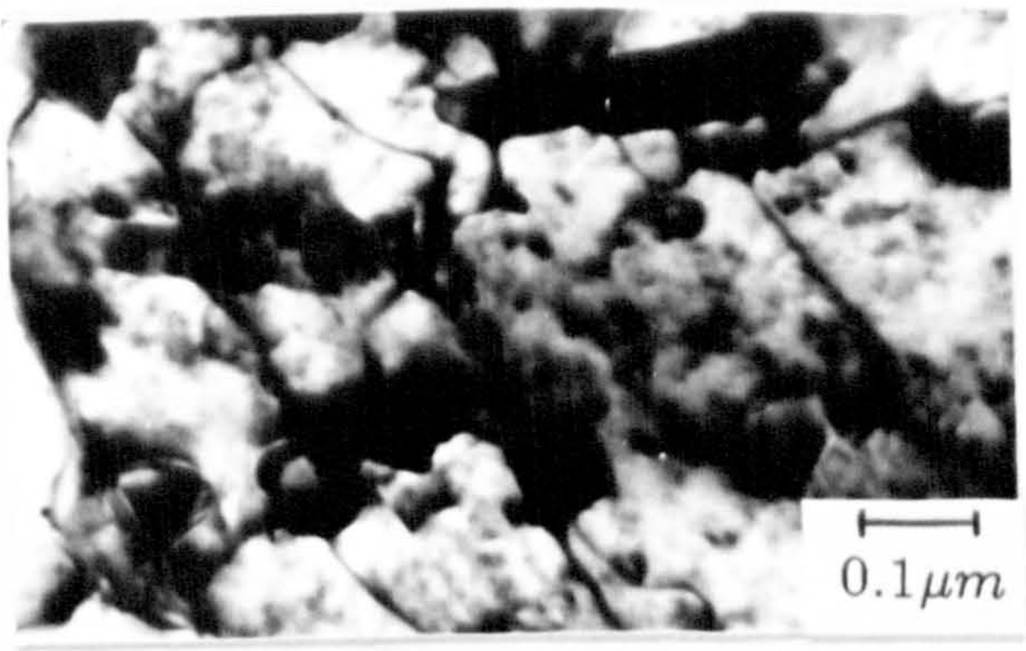

400°C

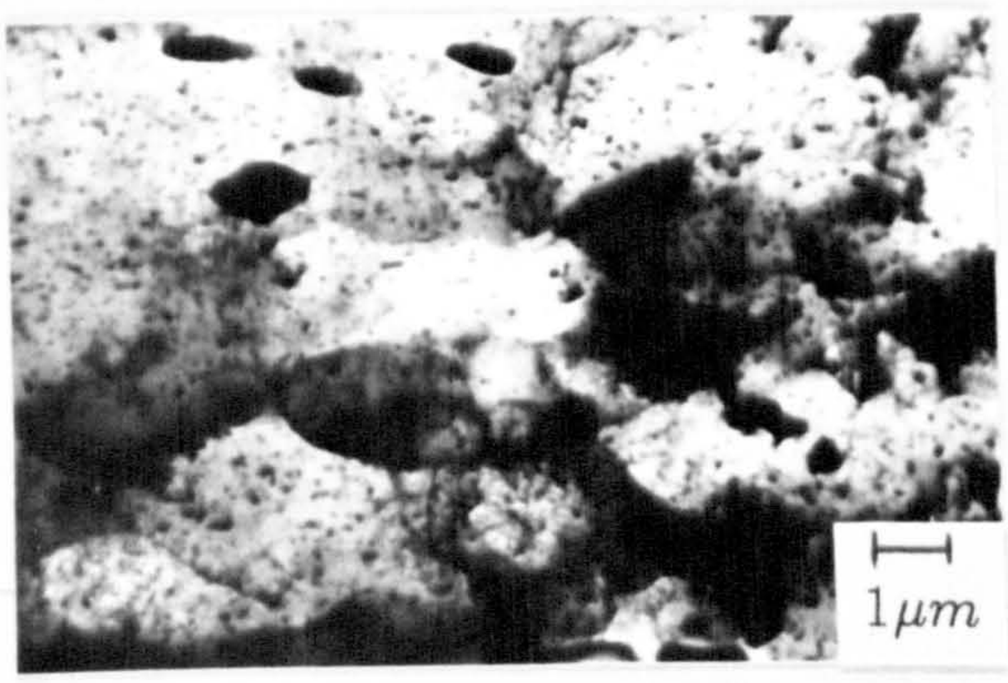

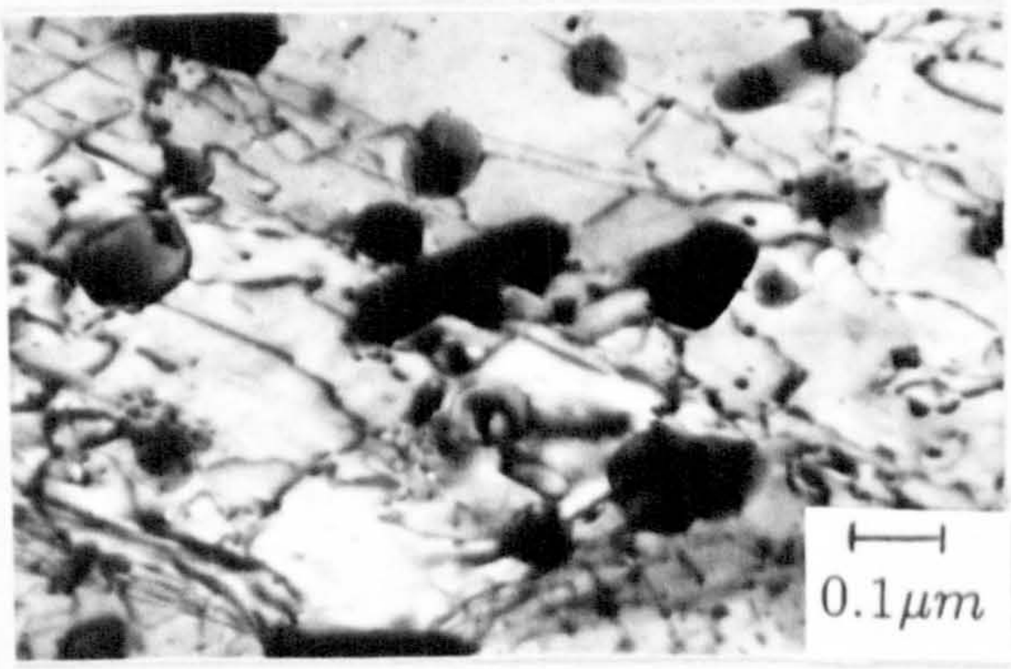

500°C

550°C

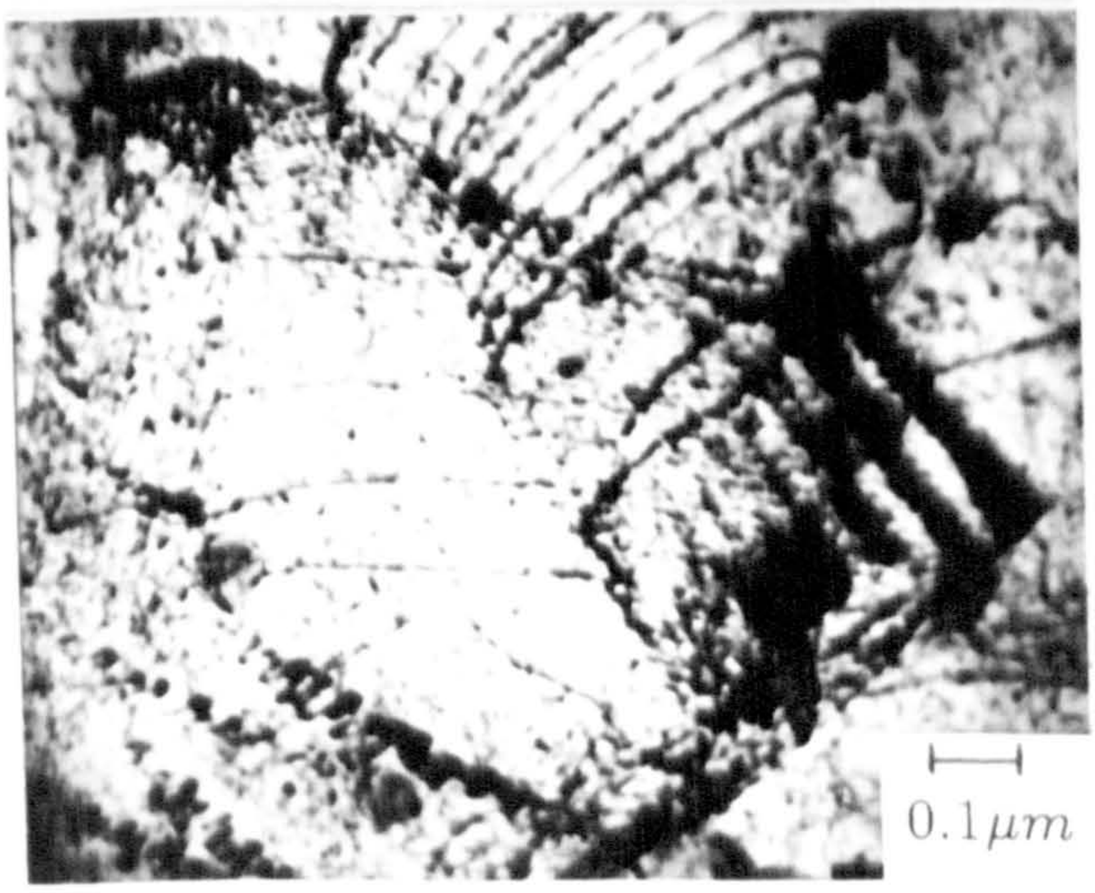

$\epsilon = 1.6, \dot{\epsilon} = 3.4$

Plate 22

Ti=400°C

Tx=416°C

Ti=450°C

Tx=432°C

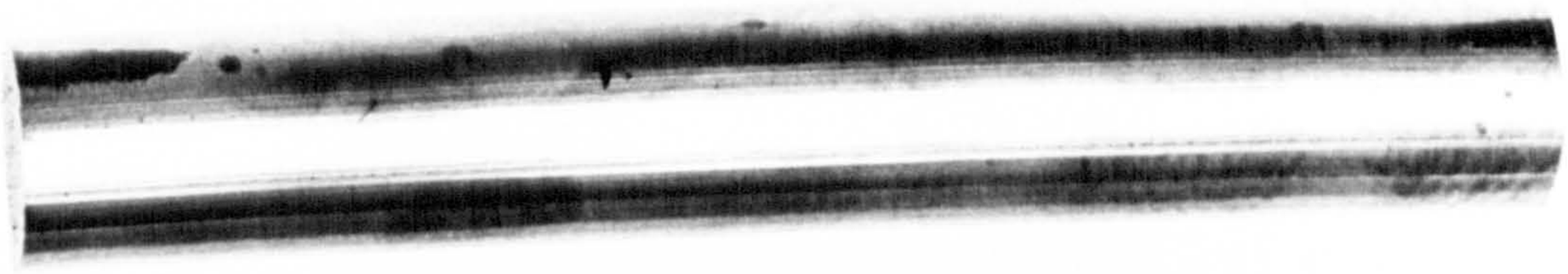

Ti=500°C

Tx=477°C

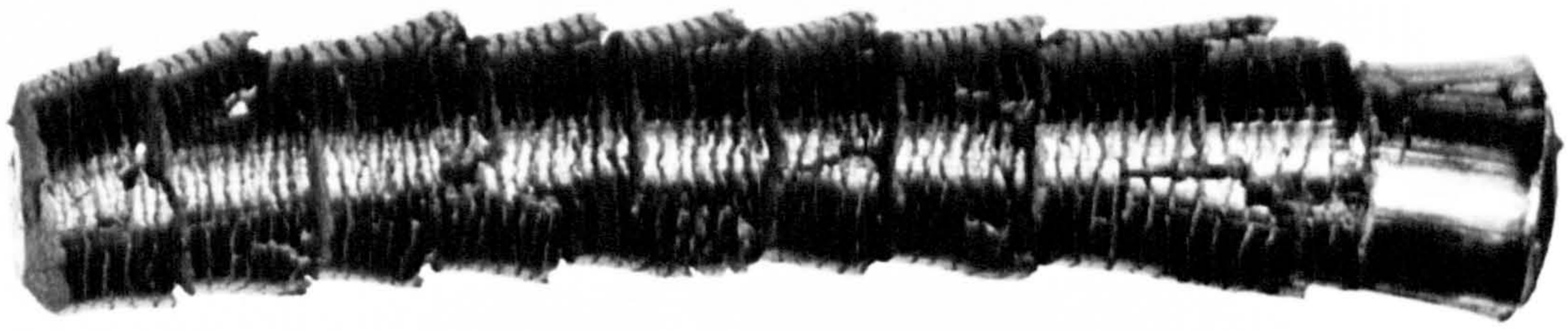

Ti=553°C

Tx=498°C

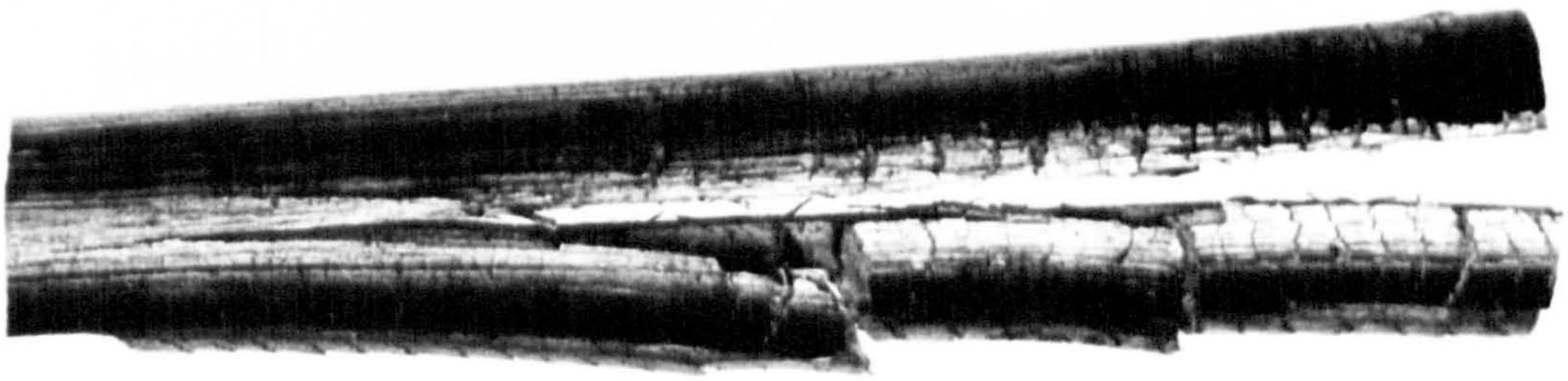

Plate 23

Ti=250°C
Tx=356°C

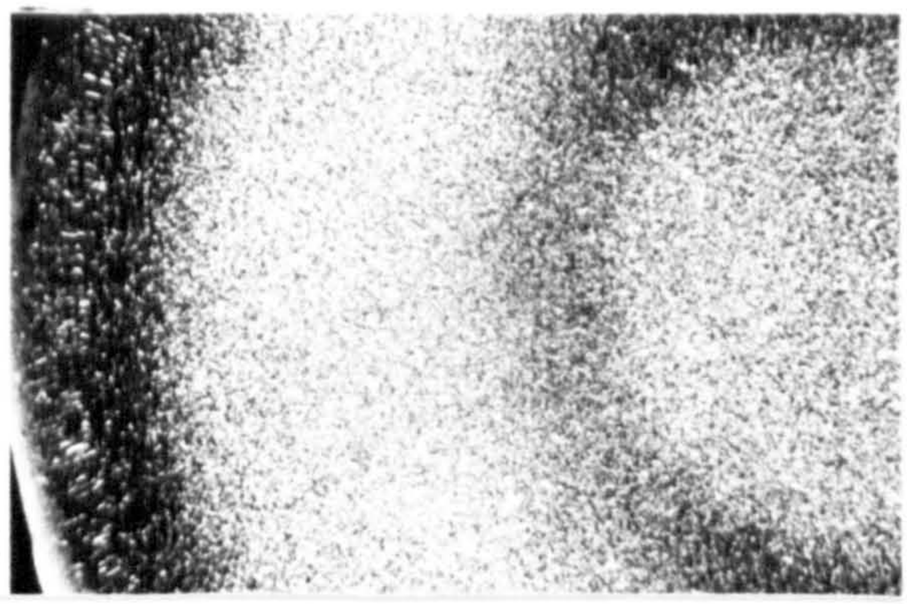

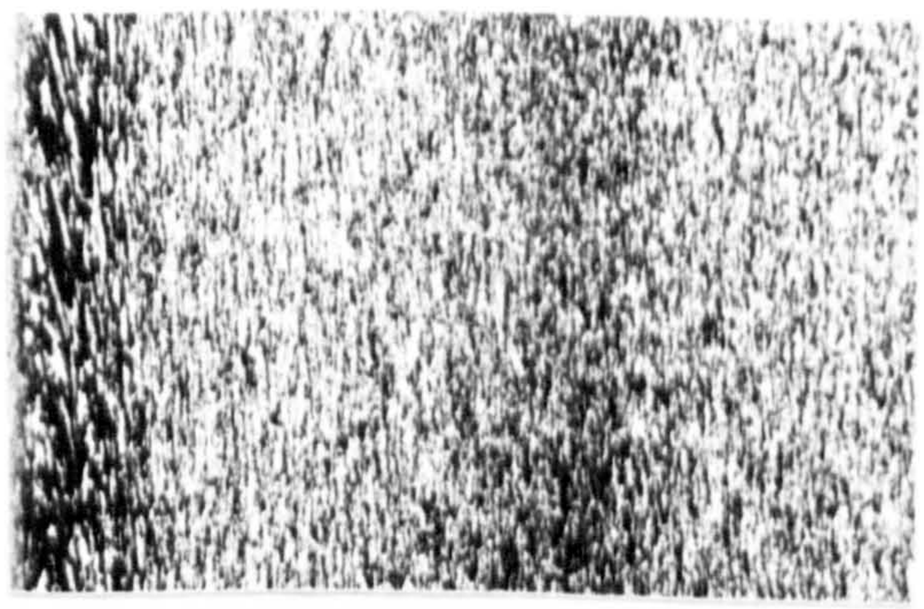

Ti=400°C
Tx=416°C

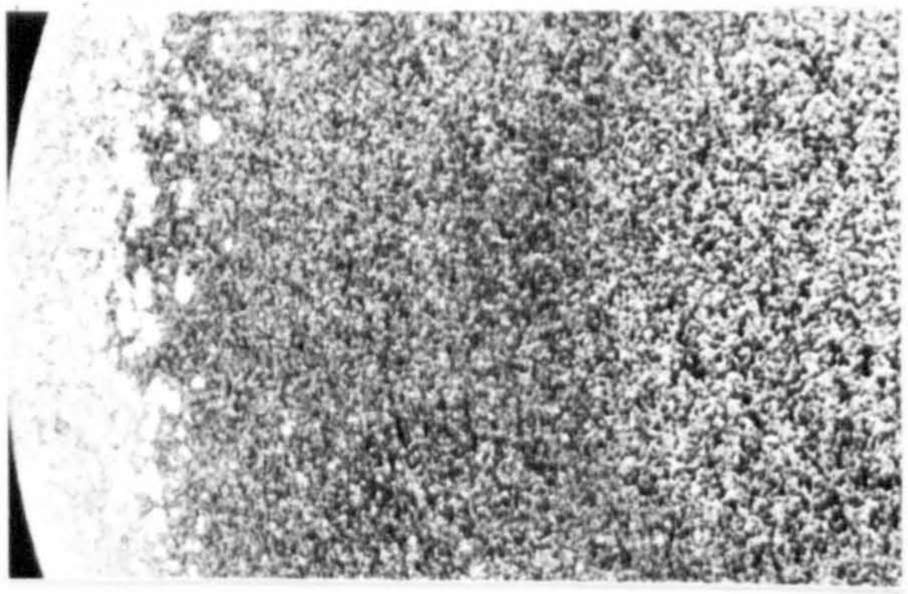

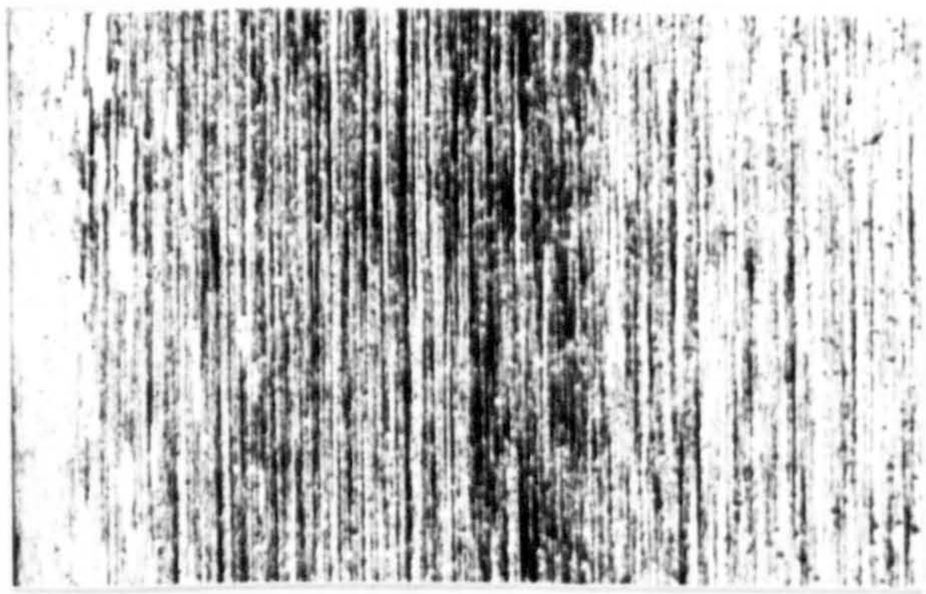

Ti=450°C
Tx=432°C

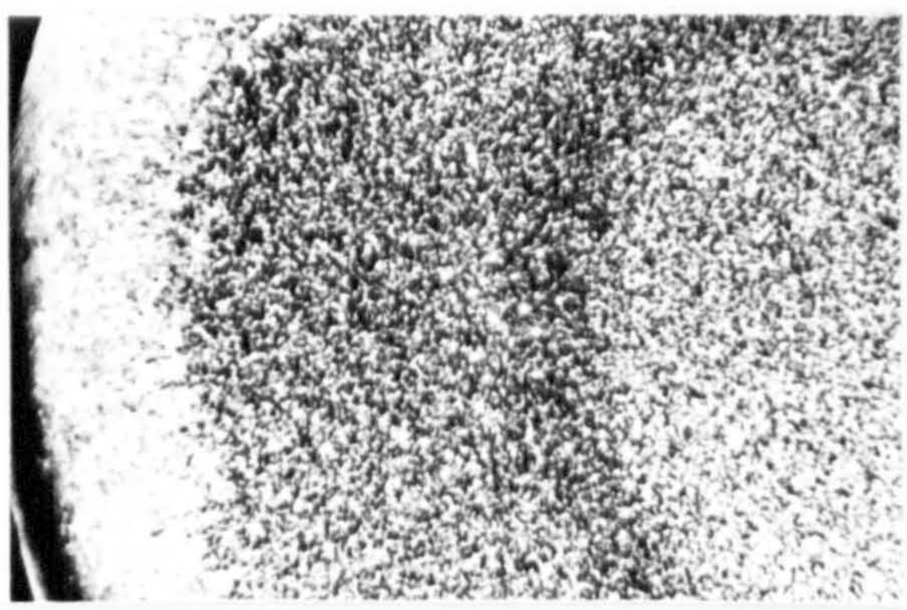

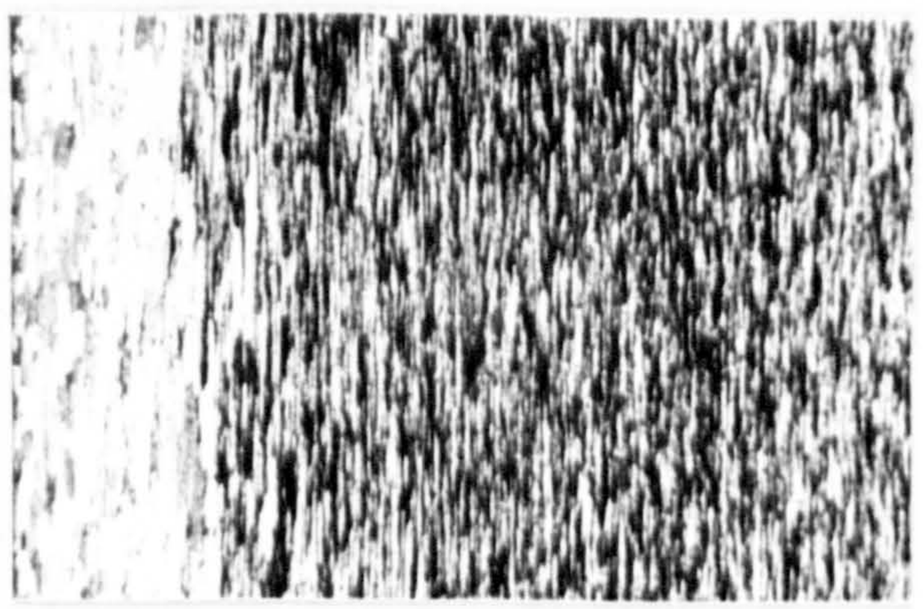

Ti=500°C
Tx=477°C

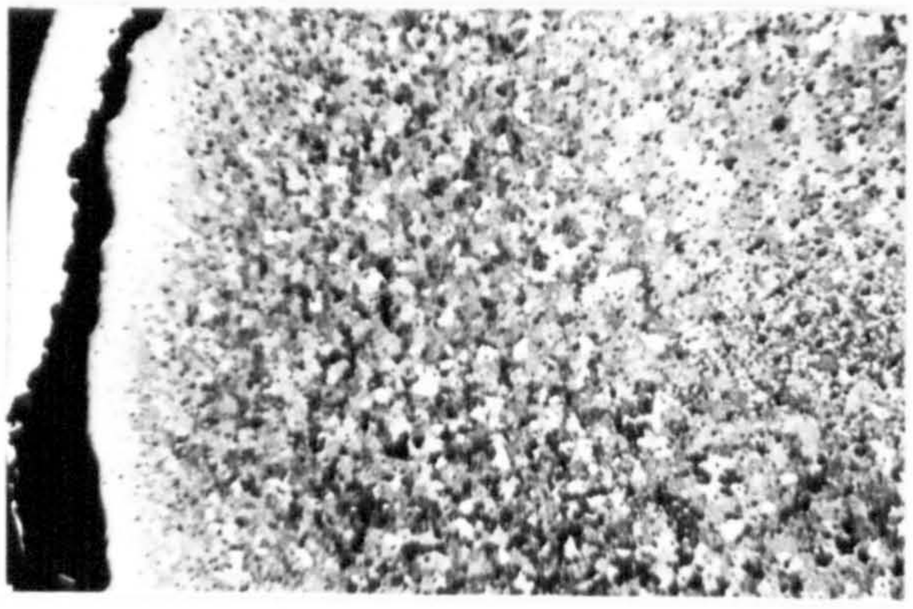

Ti=553°C
Tx=498°C

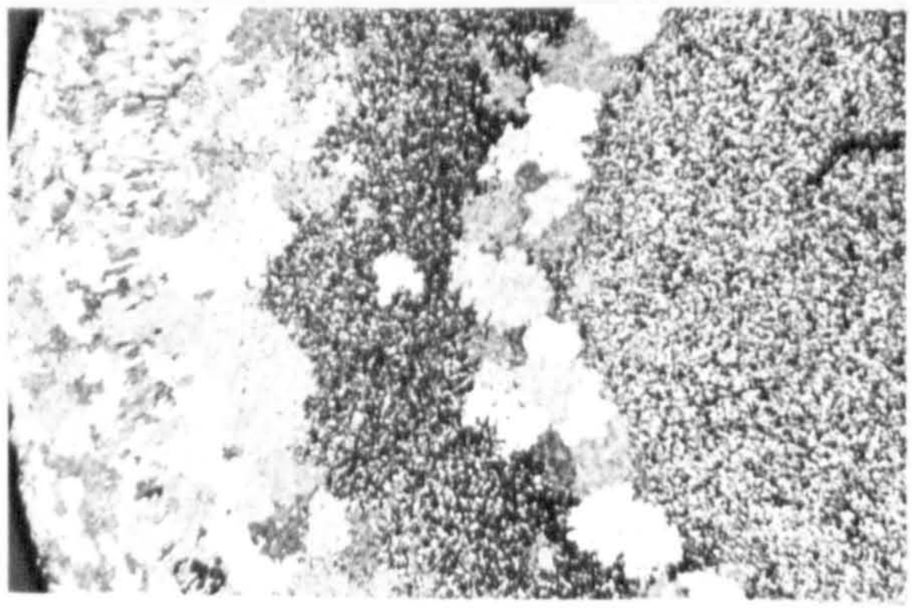

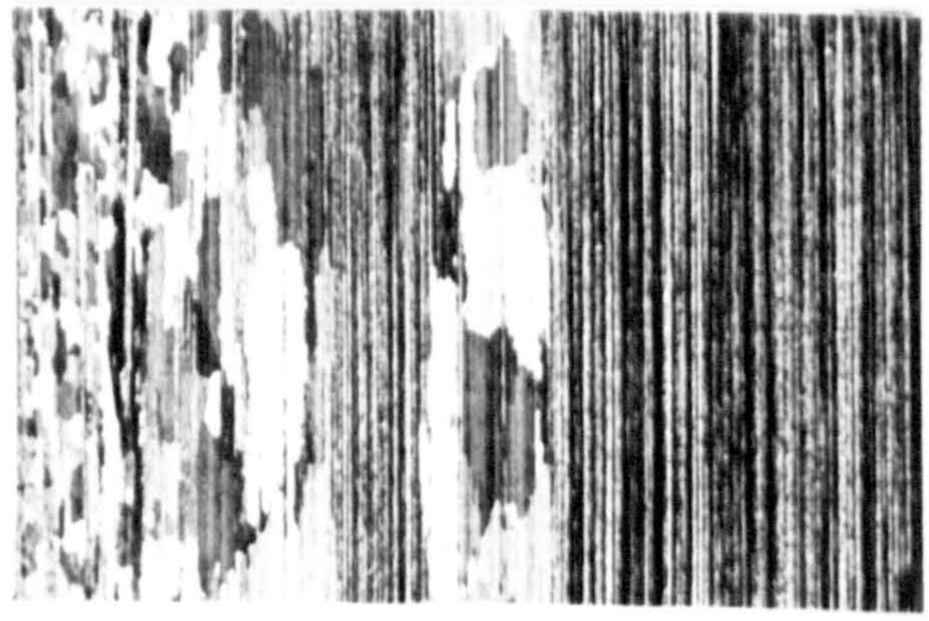

Trans.

Long.

X7.2

Plate 24

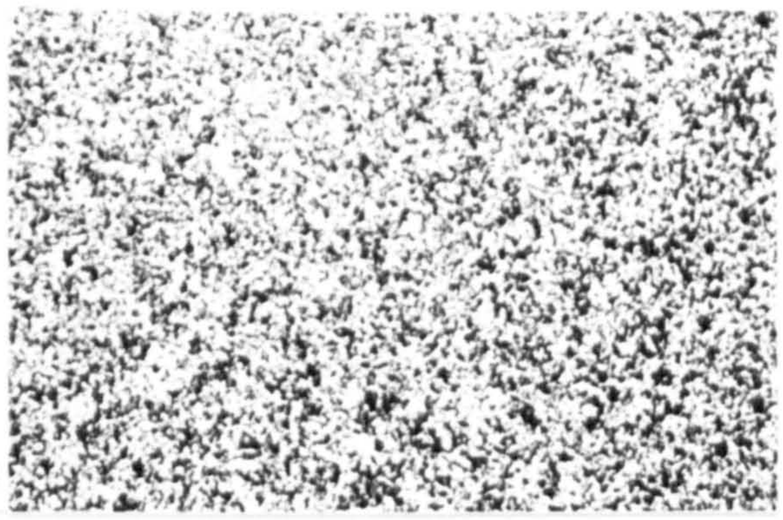

Ti=250°C

Tx=356°C

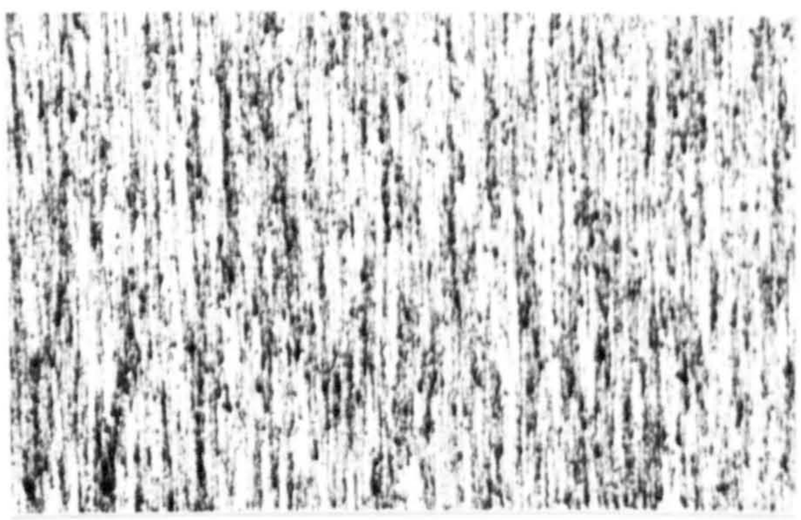

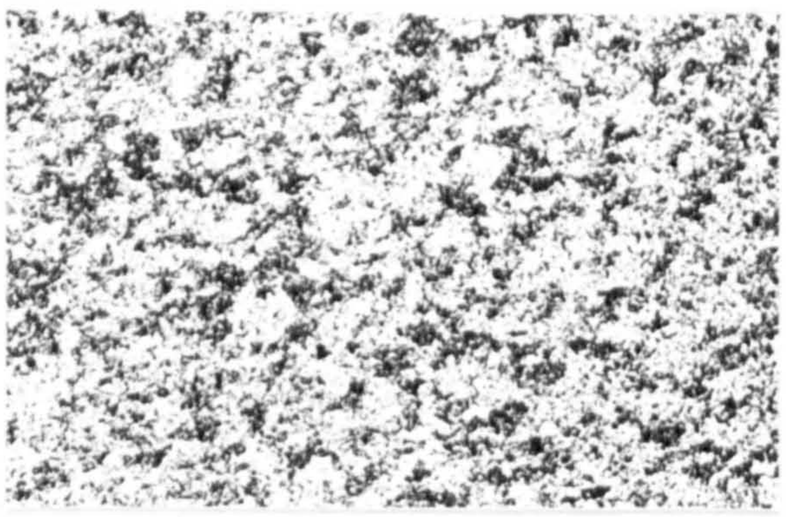

Ti=400°C

Tx=416°C

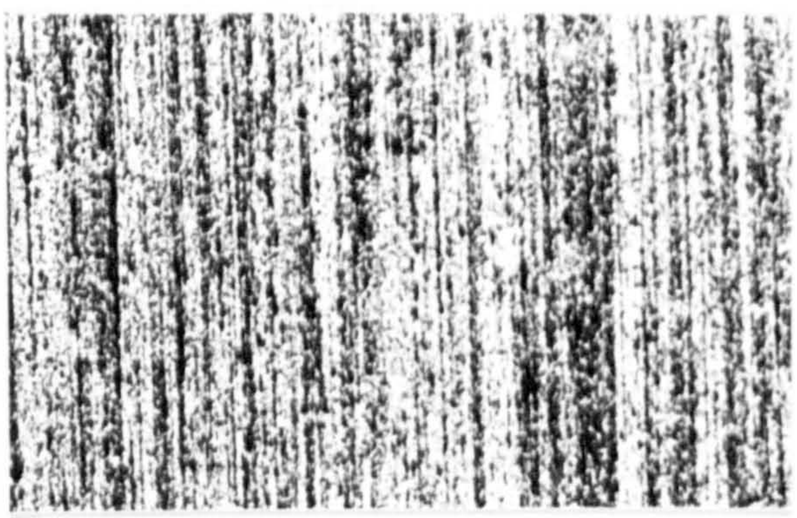

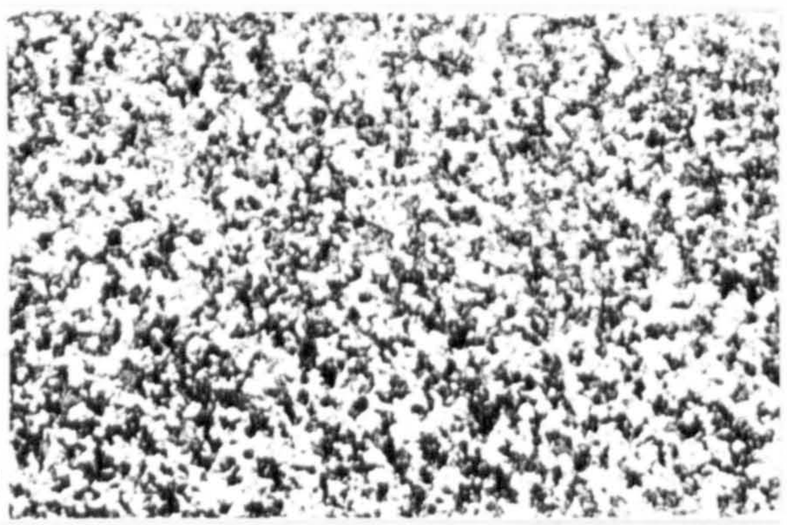

Ti=450°C

Tx=432°C

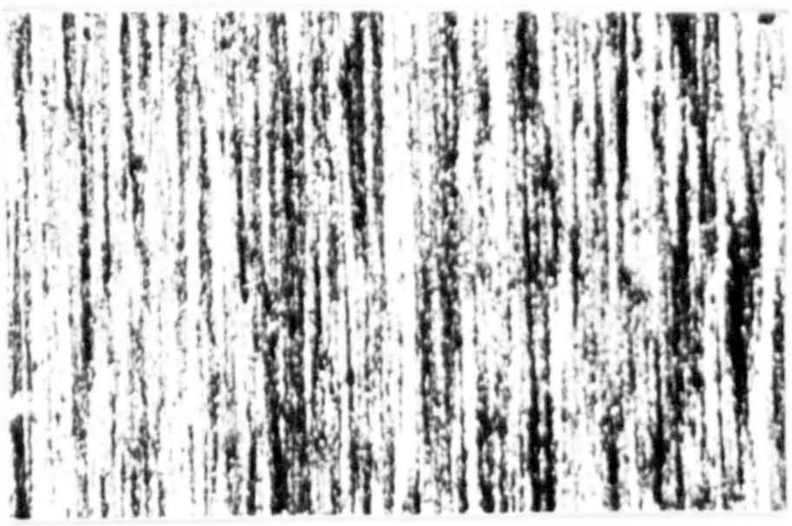

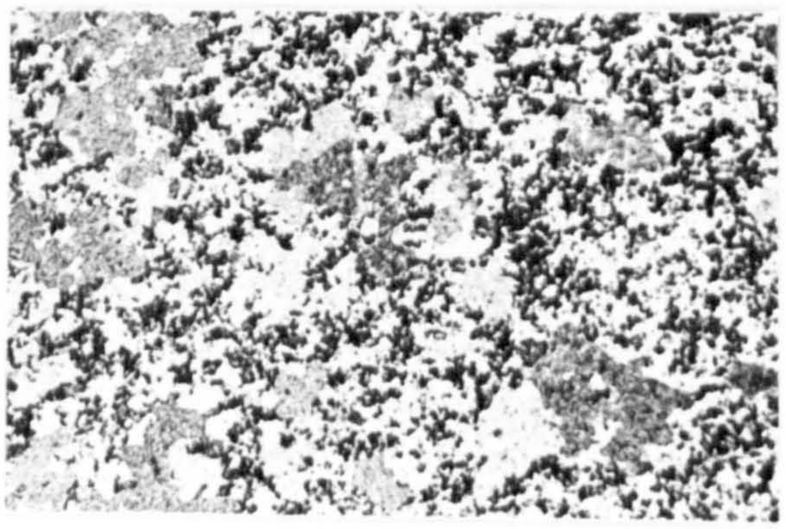

Ti=500°C

Tx=477°C

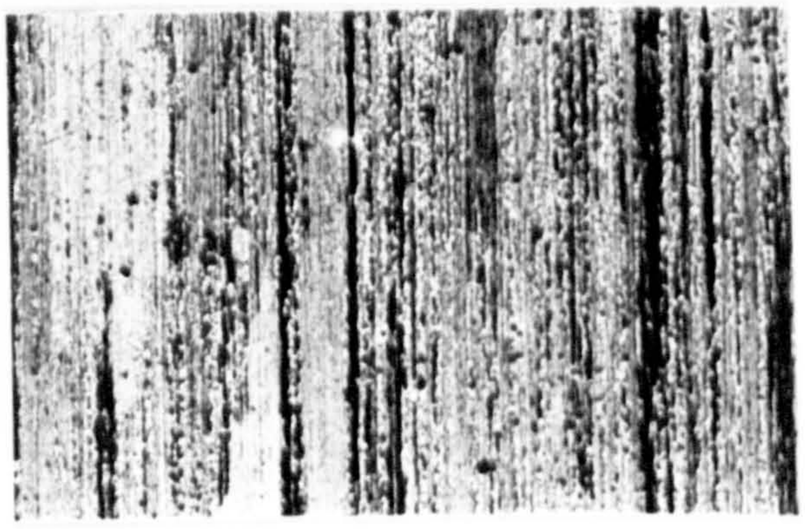

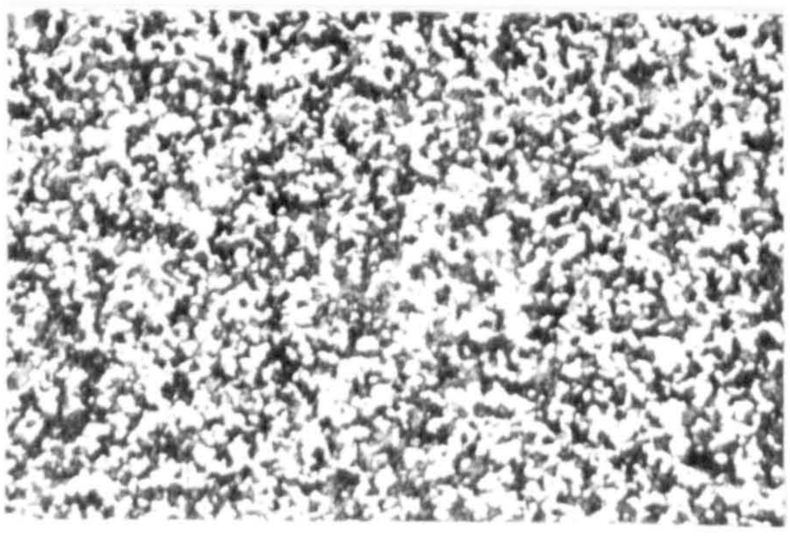

Ti=553°C

Tx=498°C

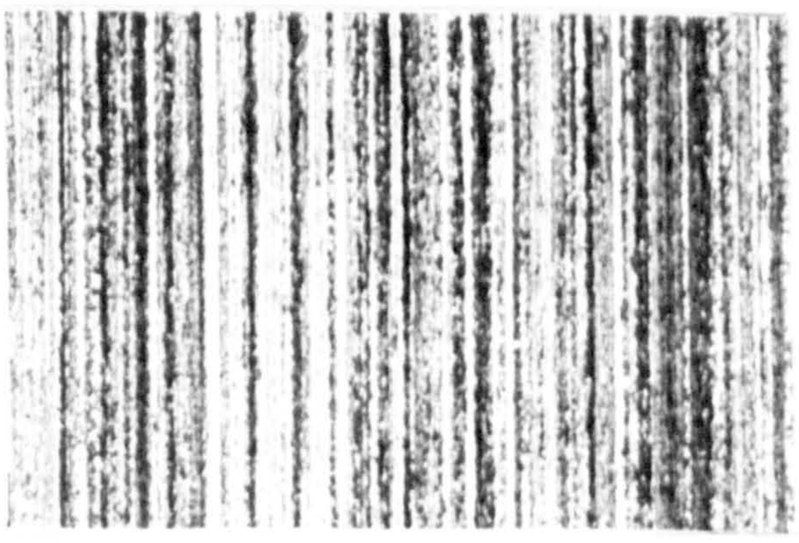

Trans.

Long.

X54

Plate 25

Ti=250°C

Tx=356°C

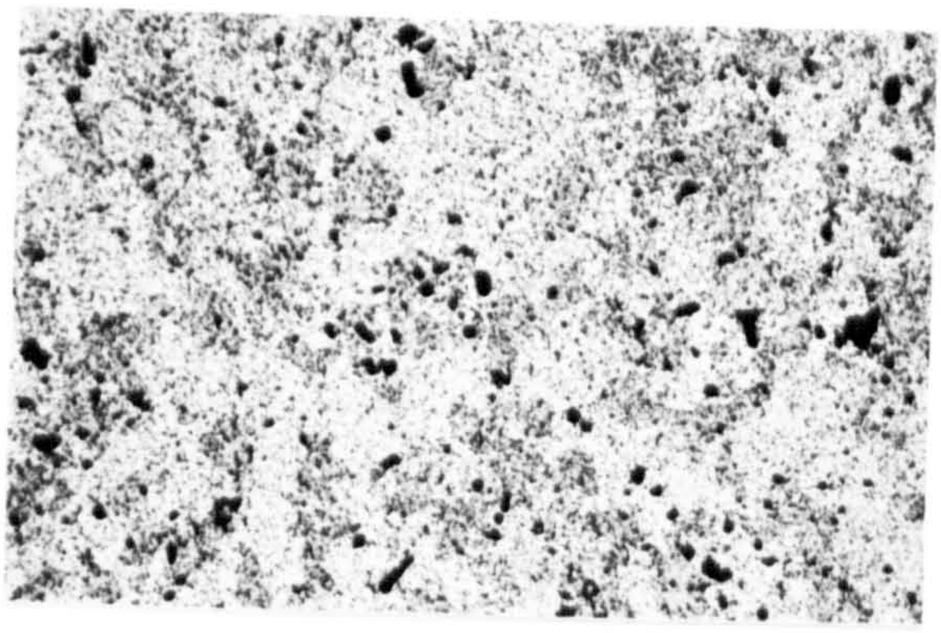

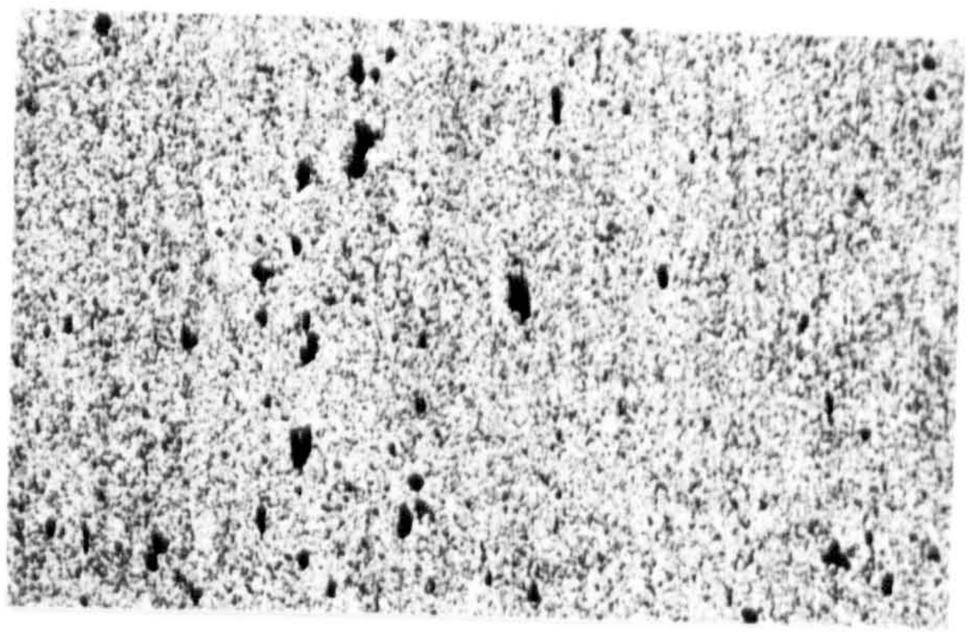

Ti=400°C

Tx=416°C

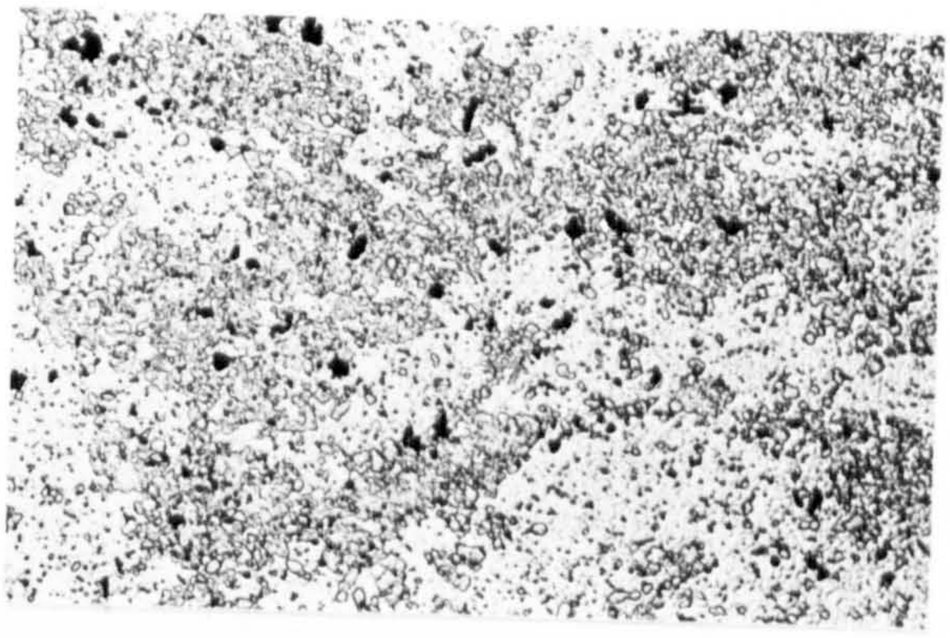

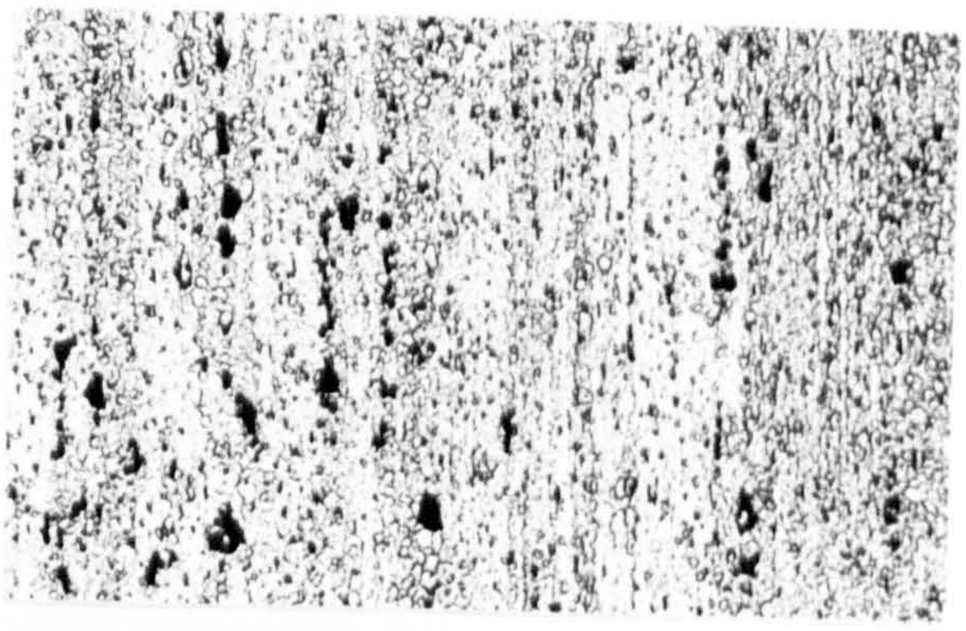

Ti=450°C

Tx=432°C

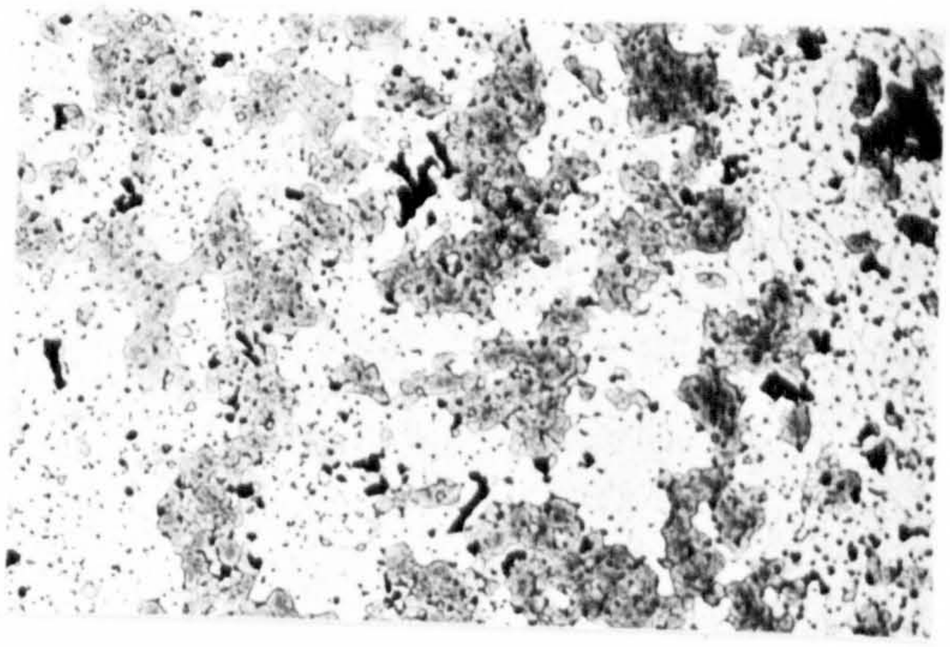

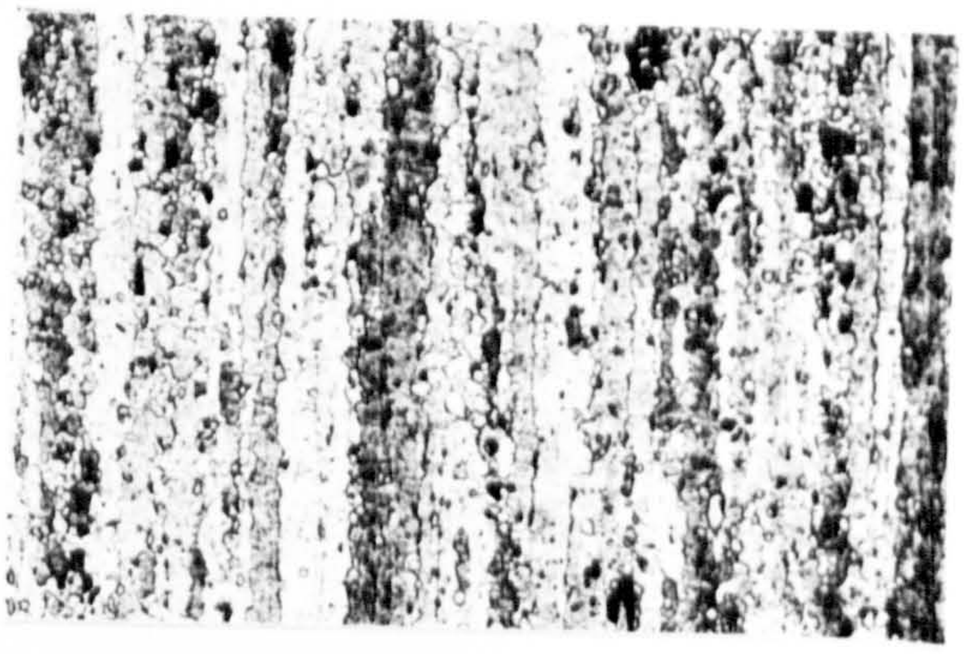

Ti=500°C

Tx=477°C

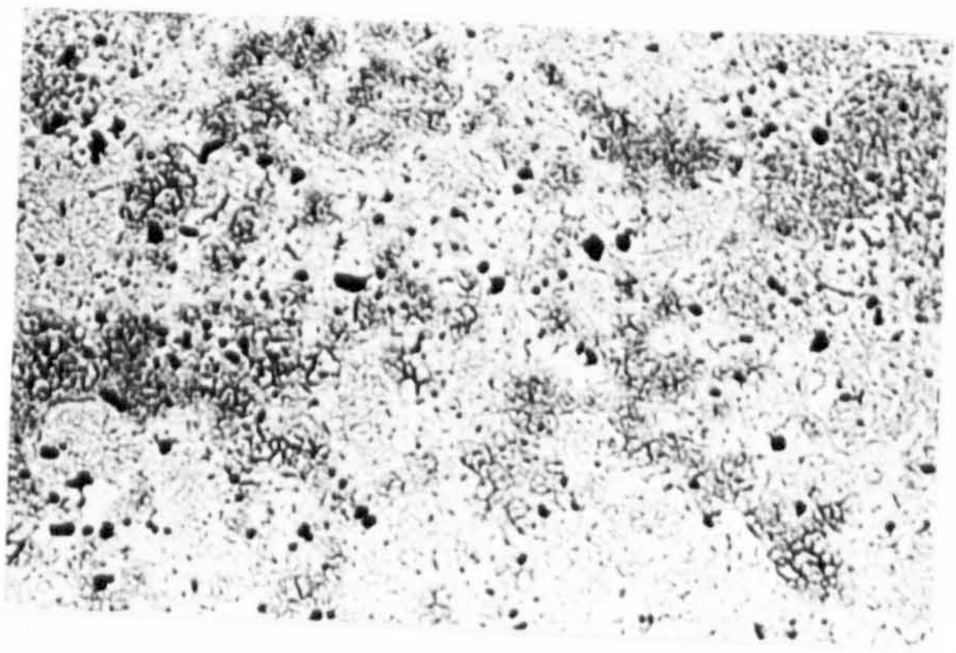

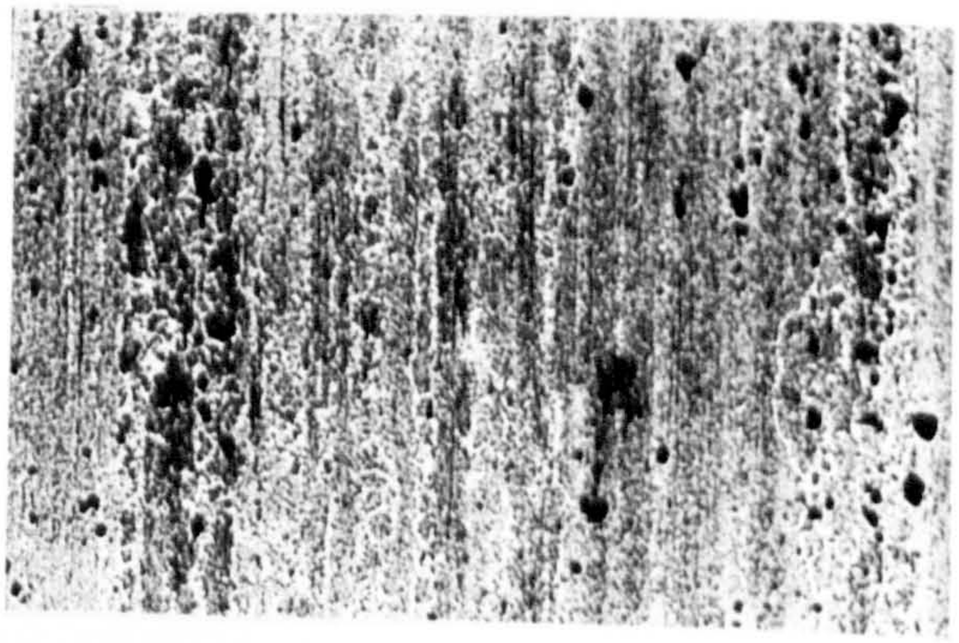

Ti=553°C

Tx=498°C

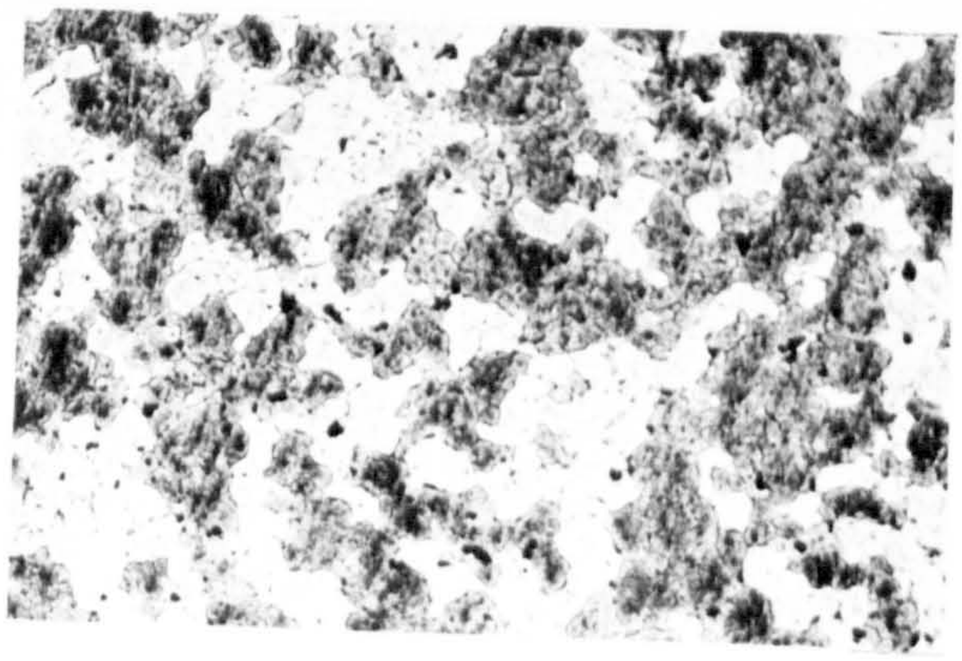

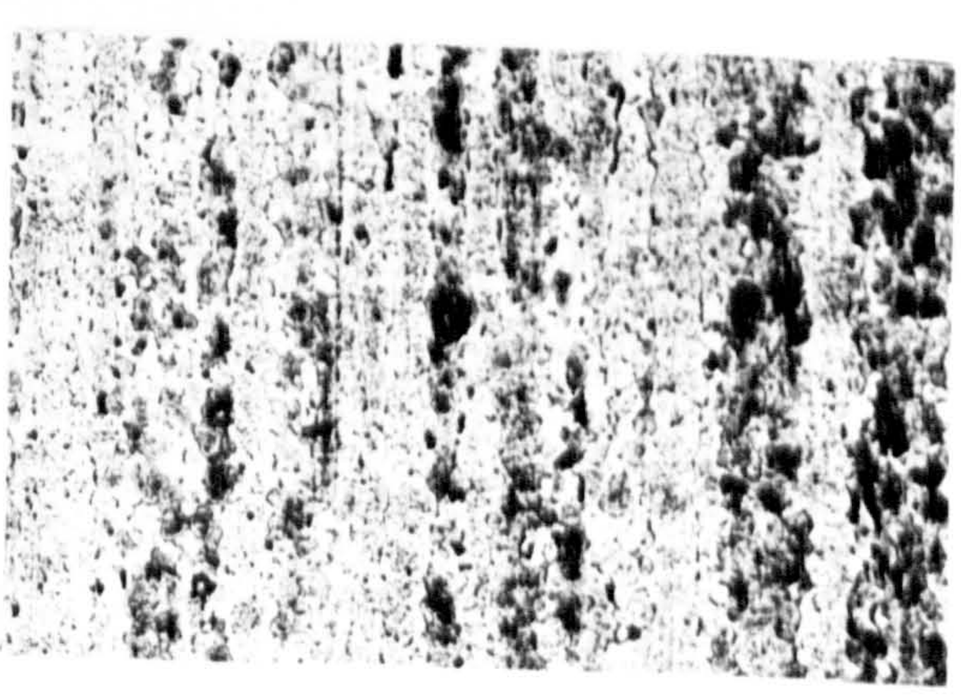

Trans.

Long.

X270

Plate 26

Ti=250°C

Tx=356°C

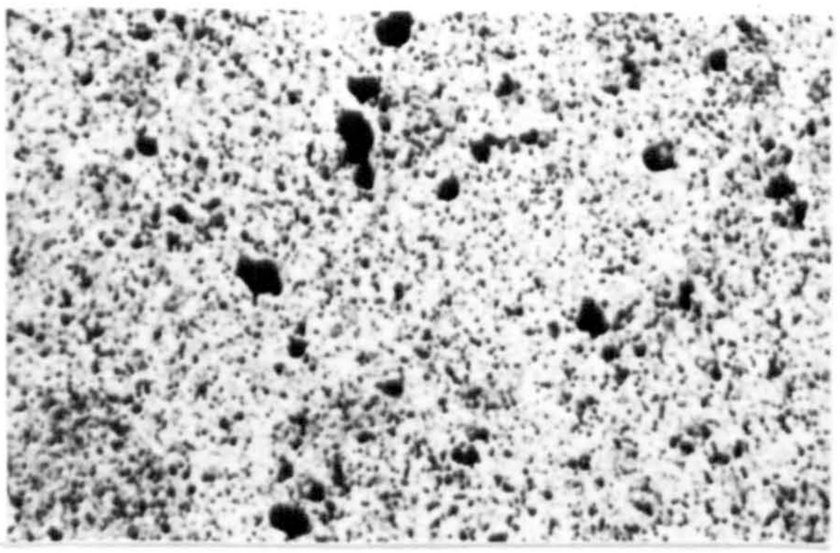

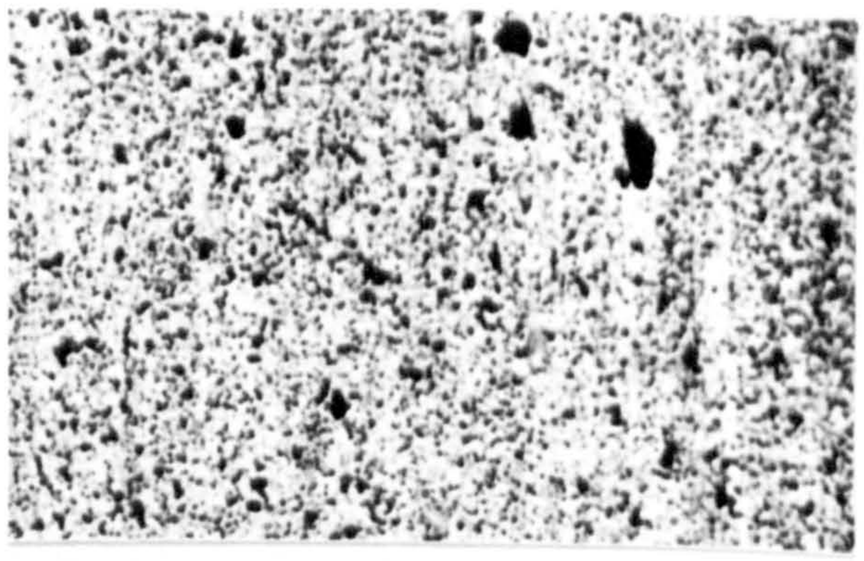

Ti=400°C

Tx=416°C

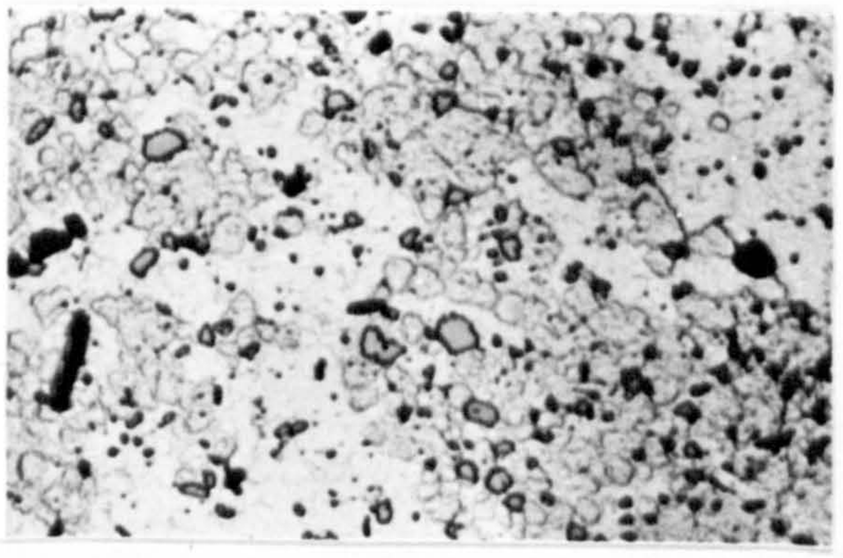

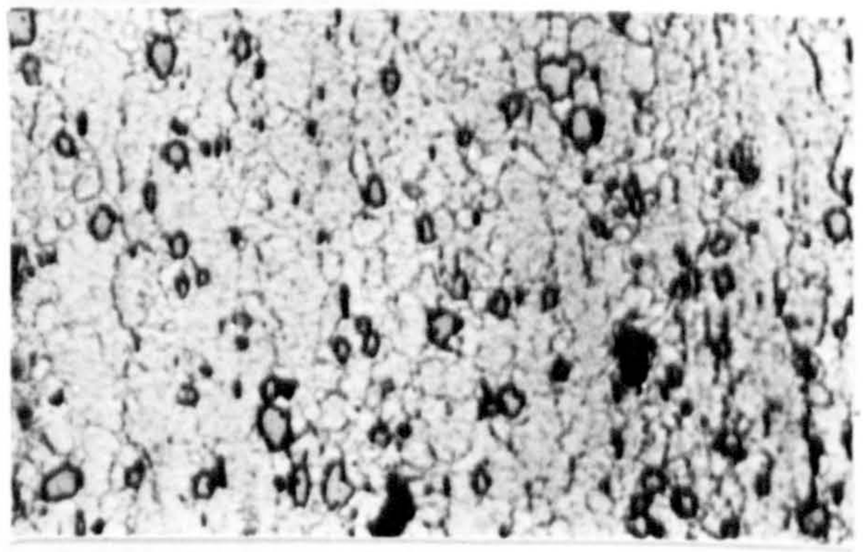

Ti=450°C

Tx=432°C

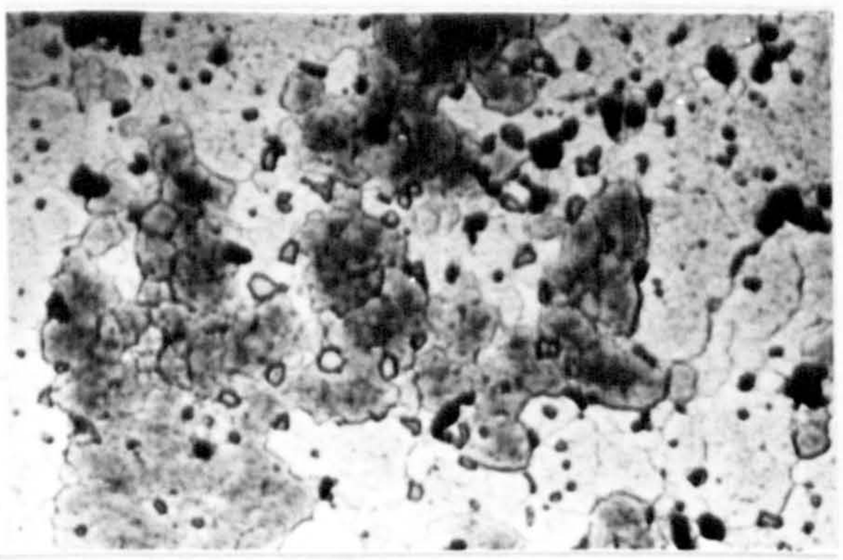

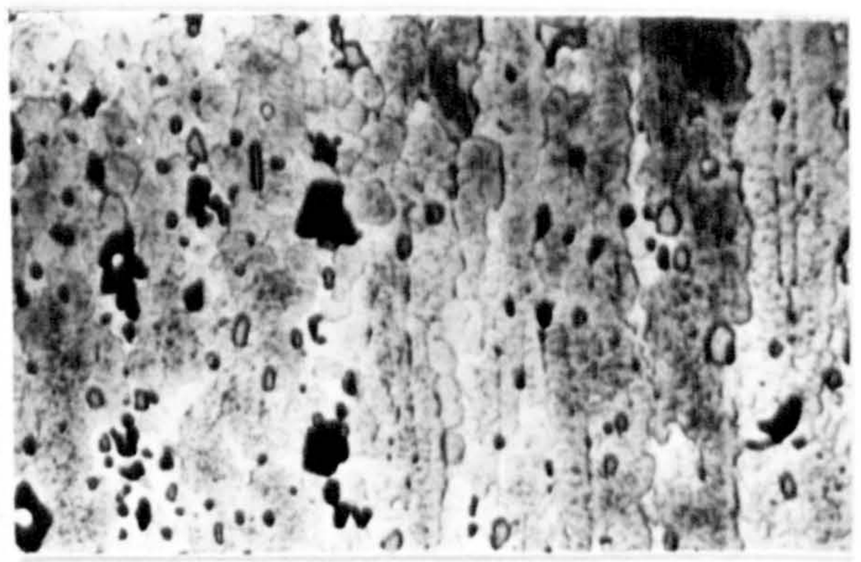

Ti=500°C

Tx=477°C

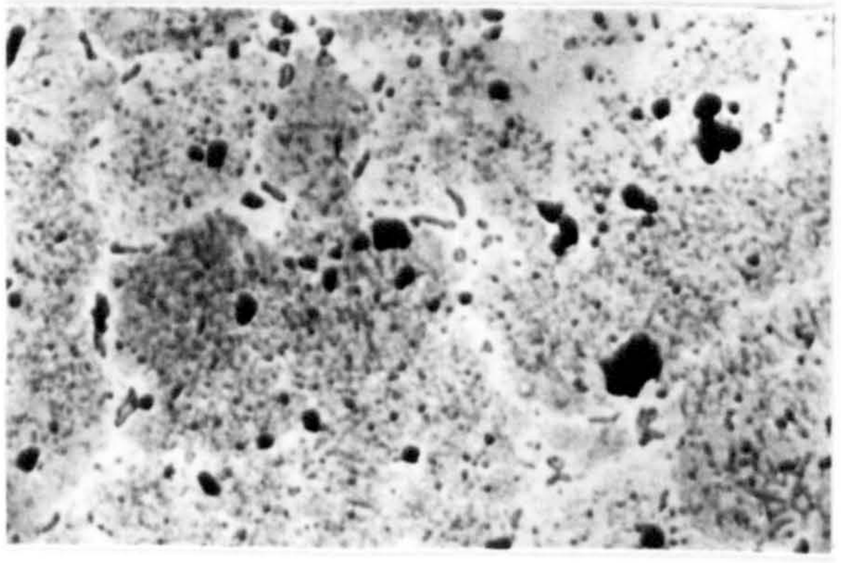

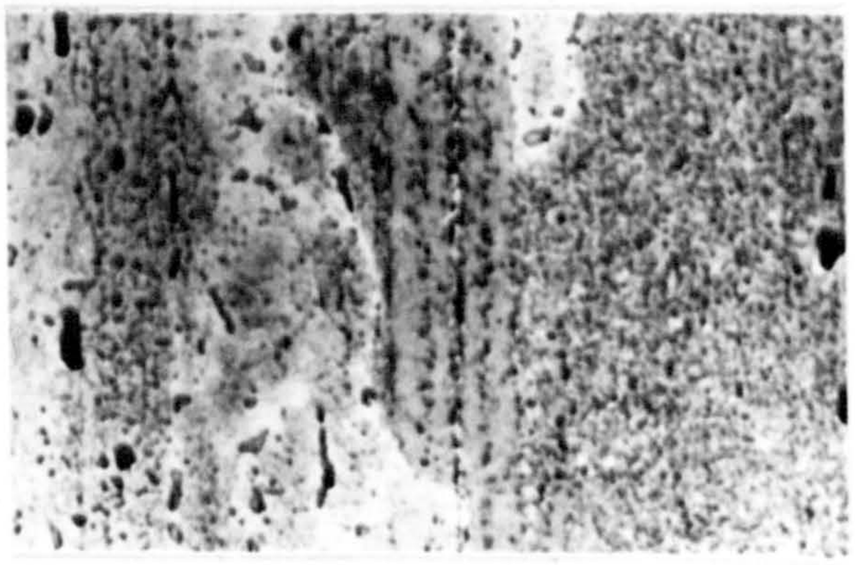

Ti=553°C

Tx=498°C

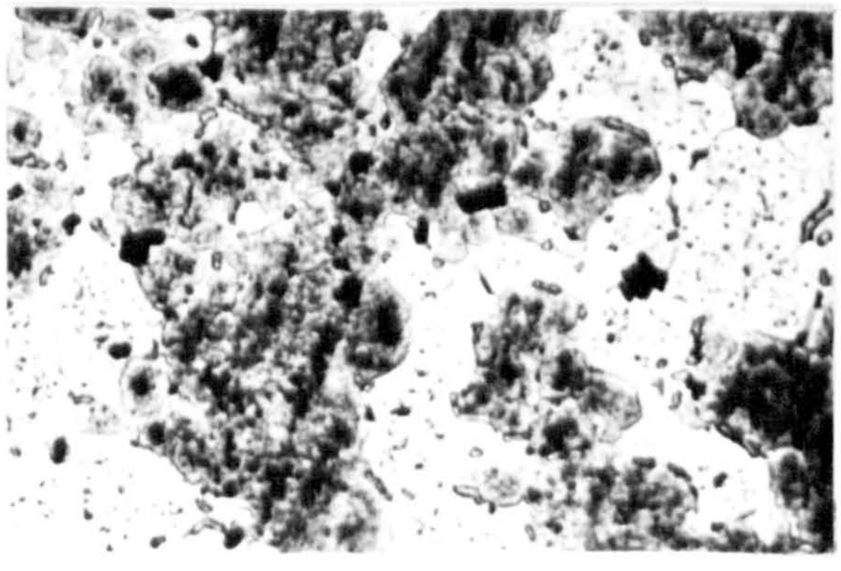

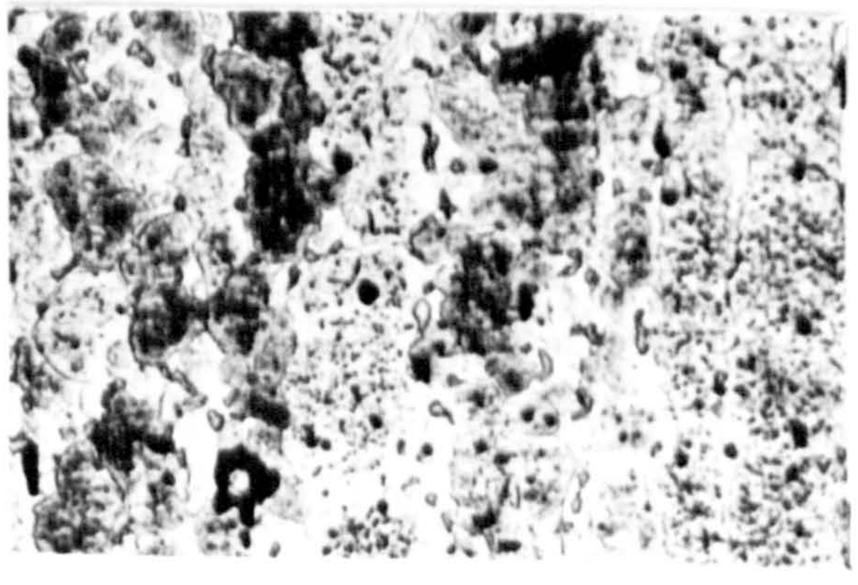

Trans.

Long.

X810

Plate 27

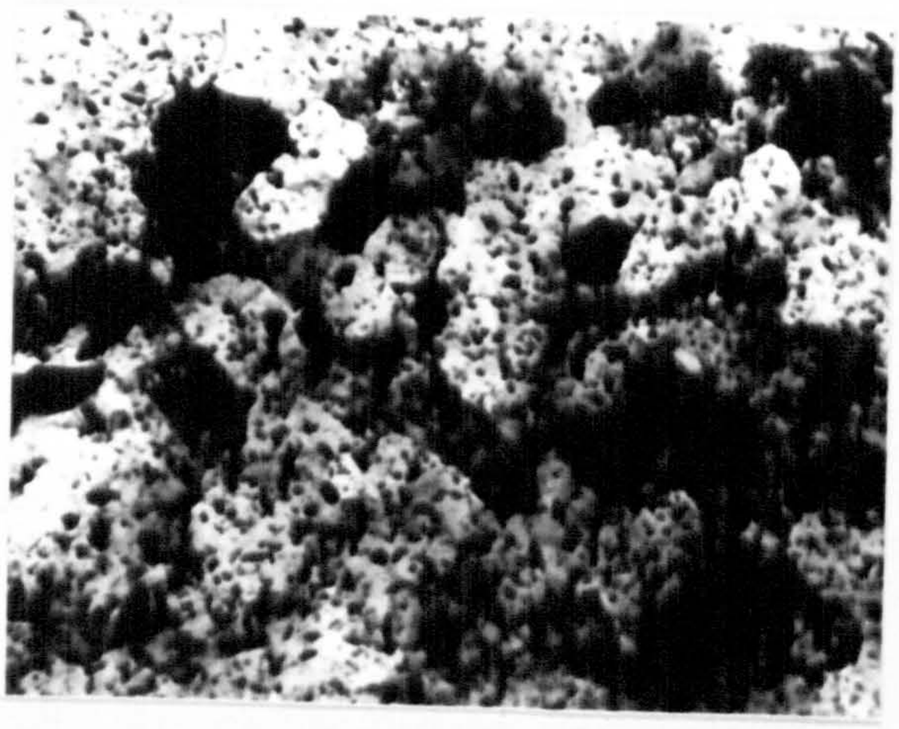

Ti=250°C

Tx=356°C

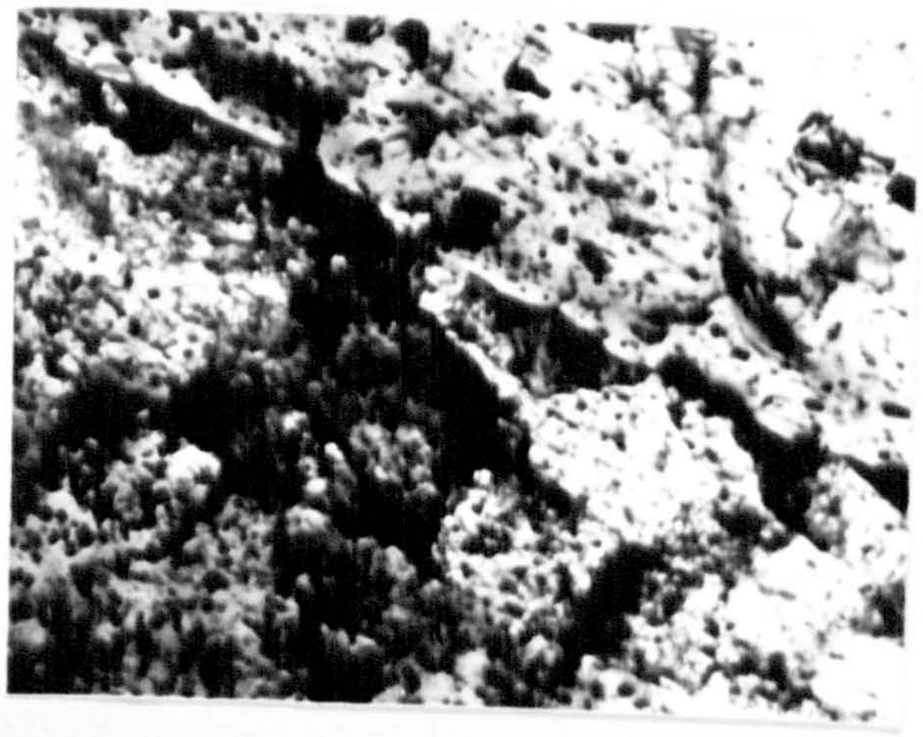

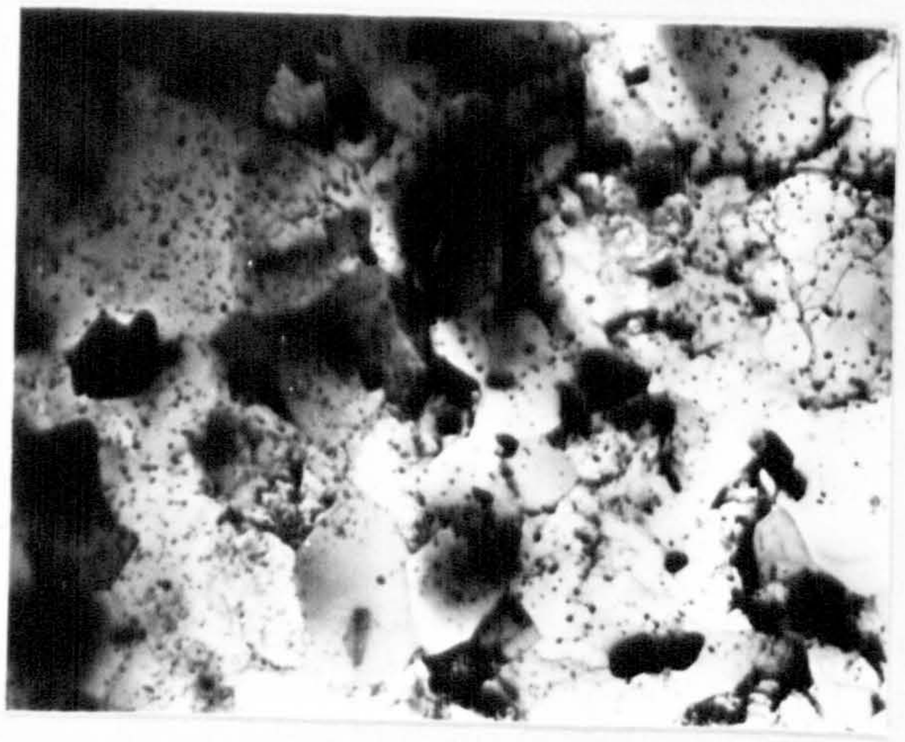

Ti=400°C

Tx=416°C

Ti=450°C

Tx=432°C

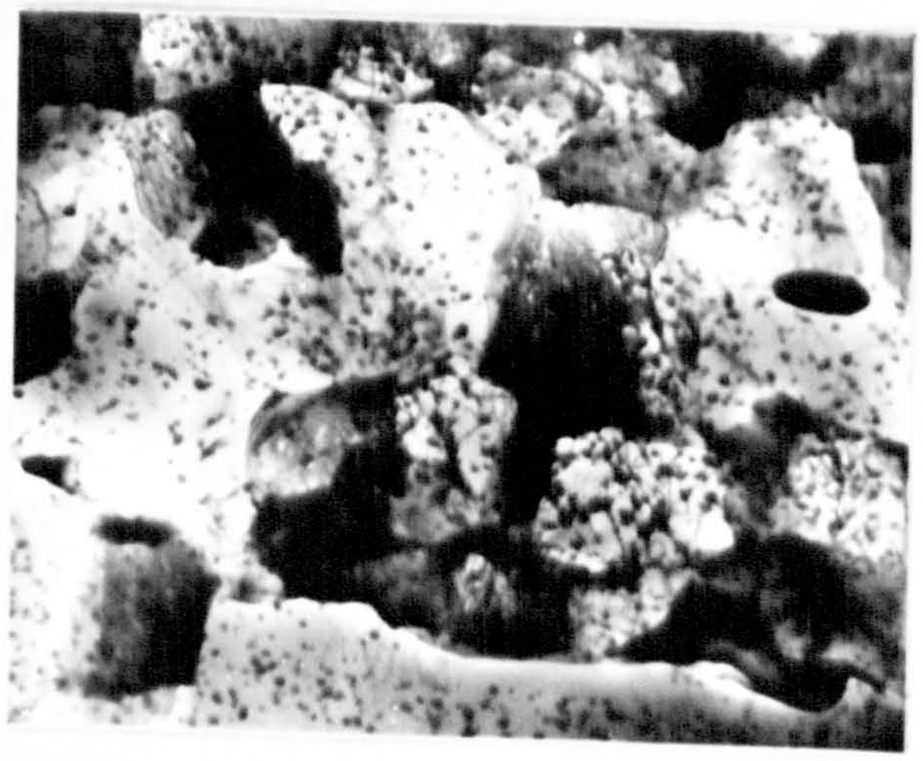

Trans.

Long.

$1\mu m$

Plate 28

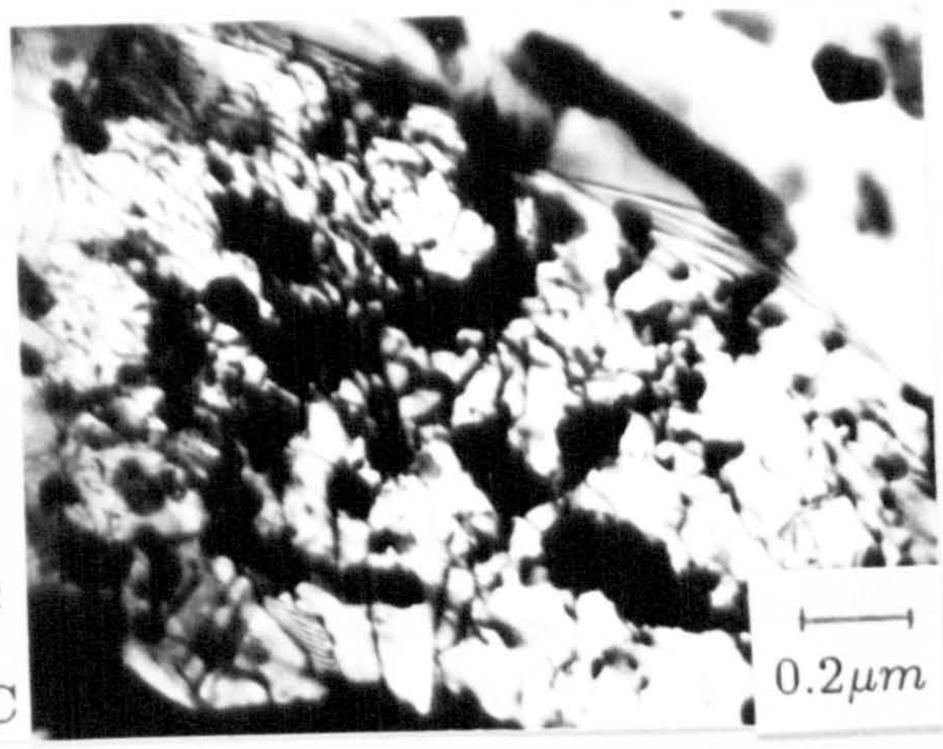

Ti=250°C

Tx=356°C

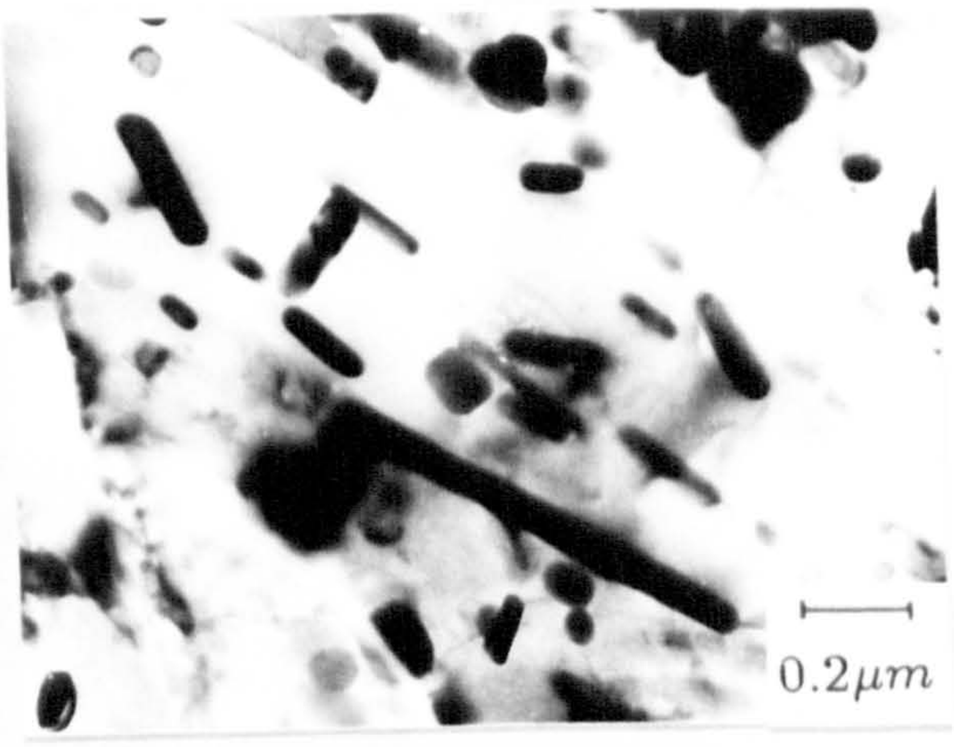

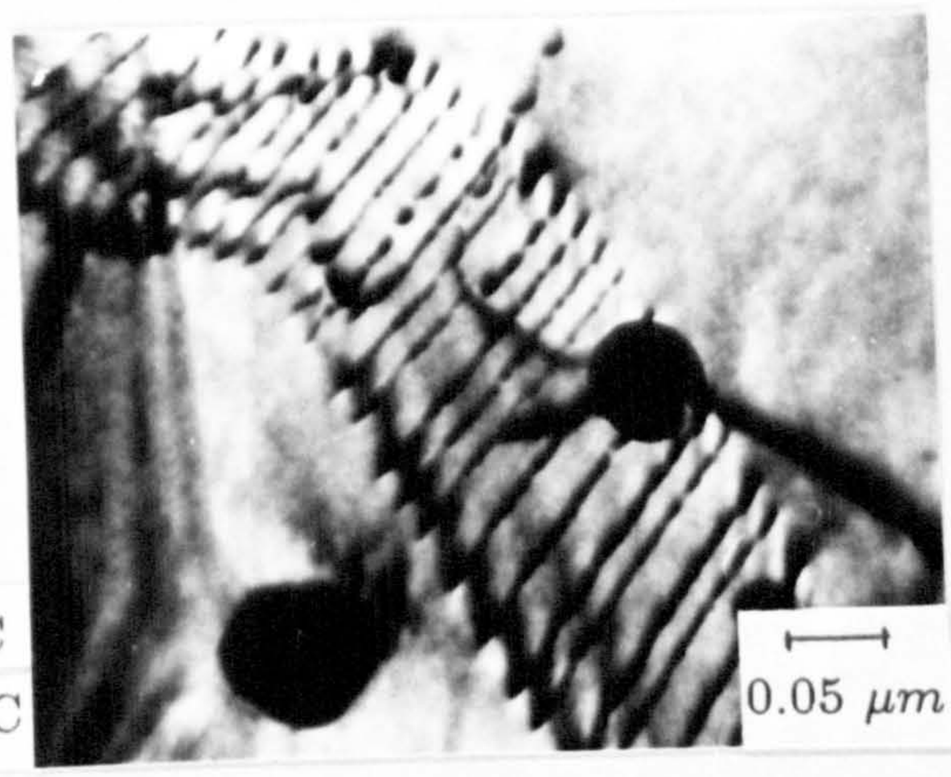

Ti=400°C

Tx=416°C

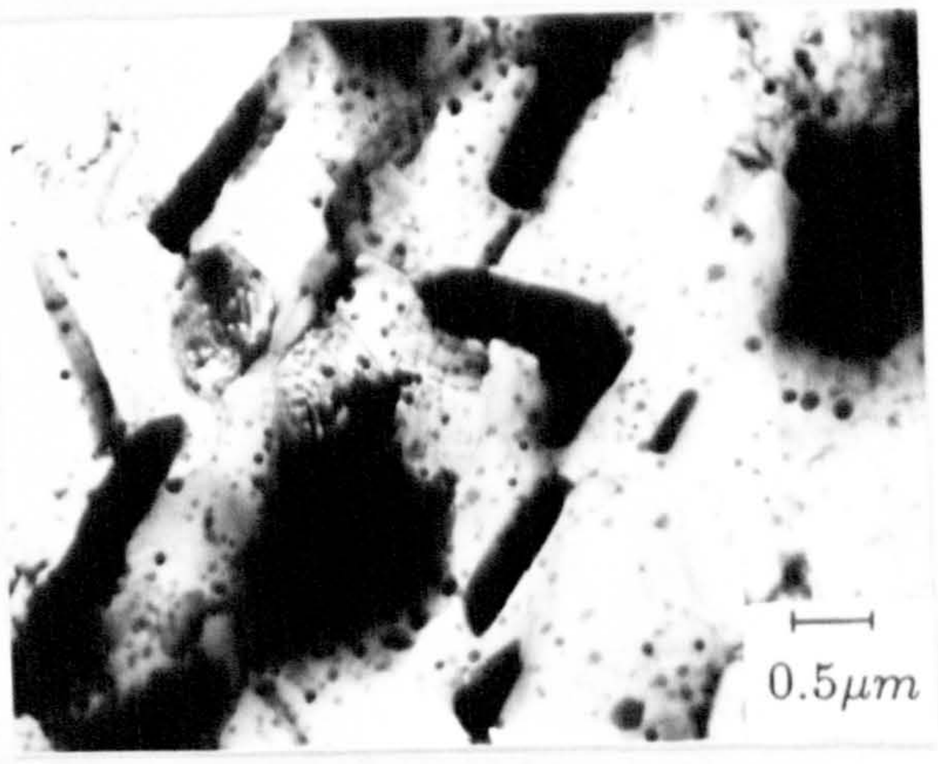

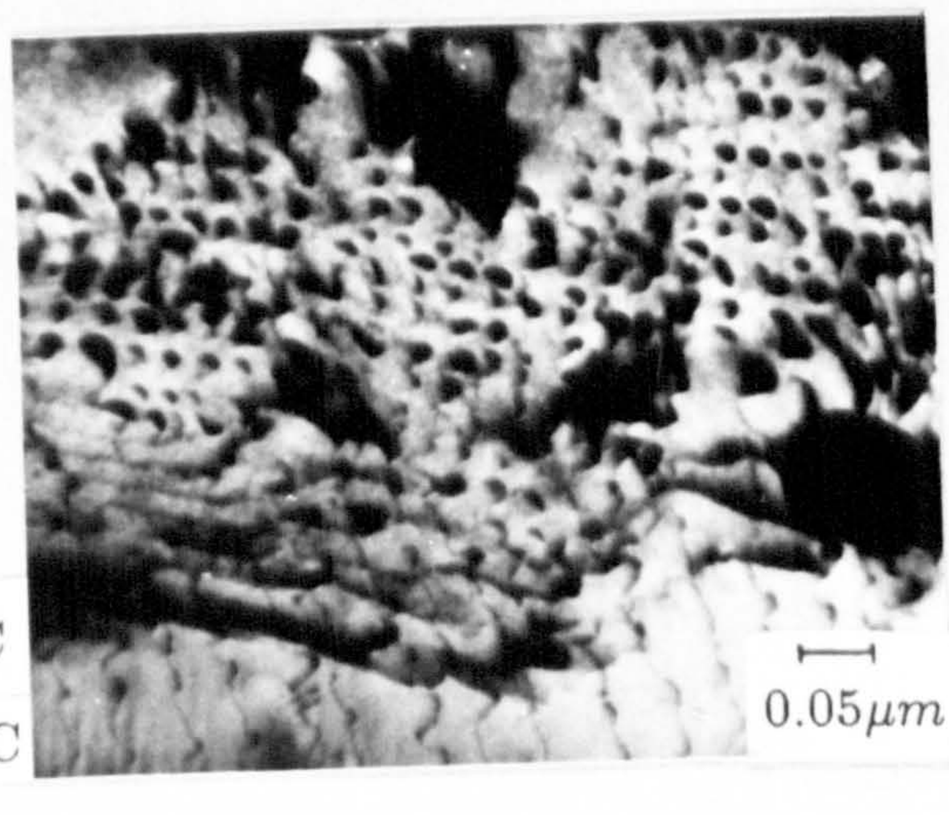

Ti=450°C

Tx=432°C

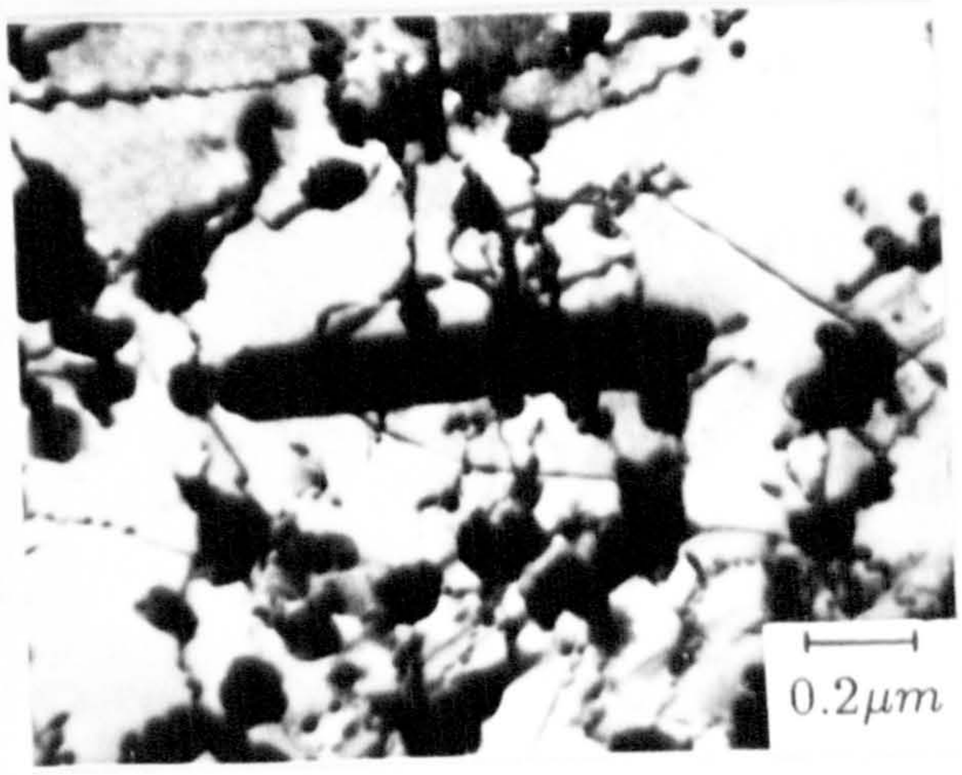

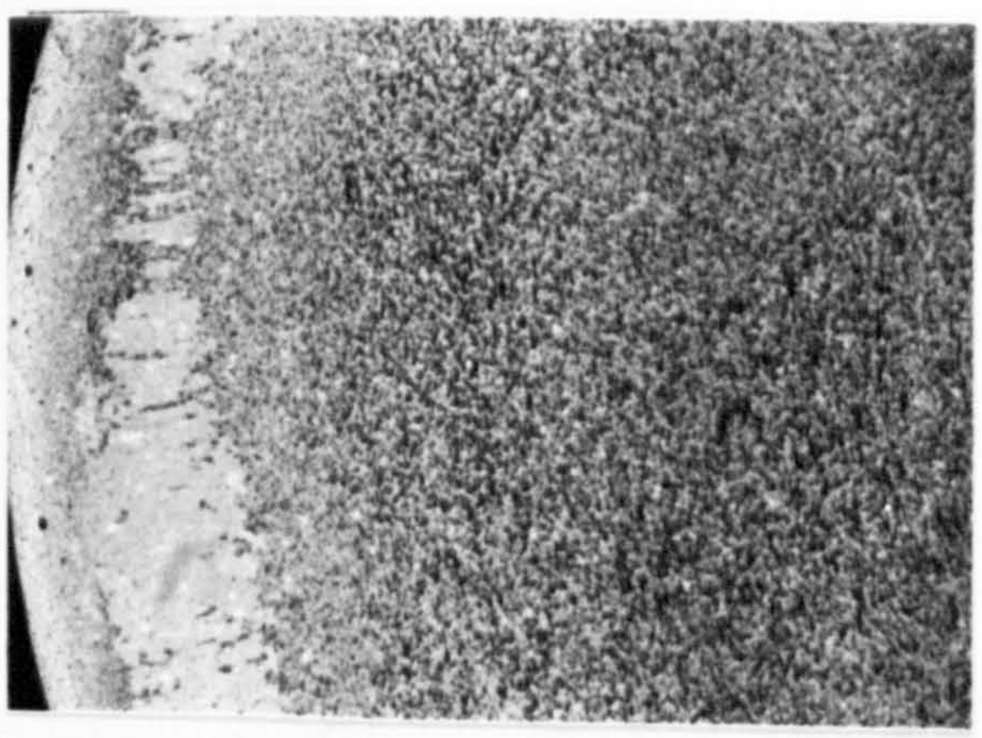

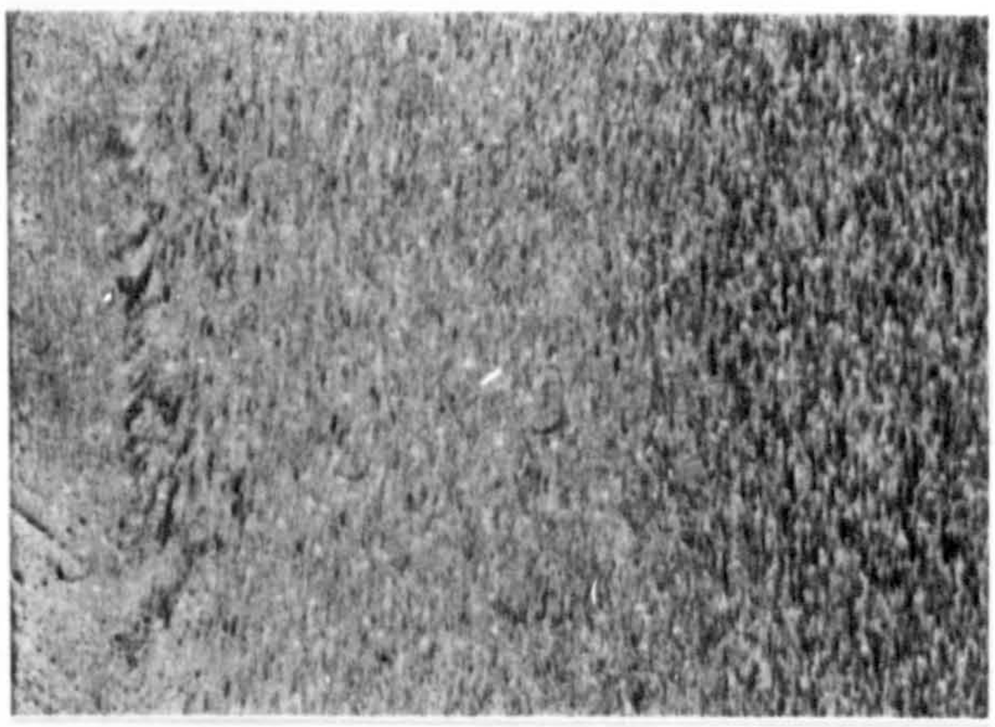

R=10
Ti=375°C
Tx= 382°C

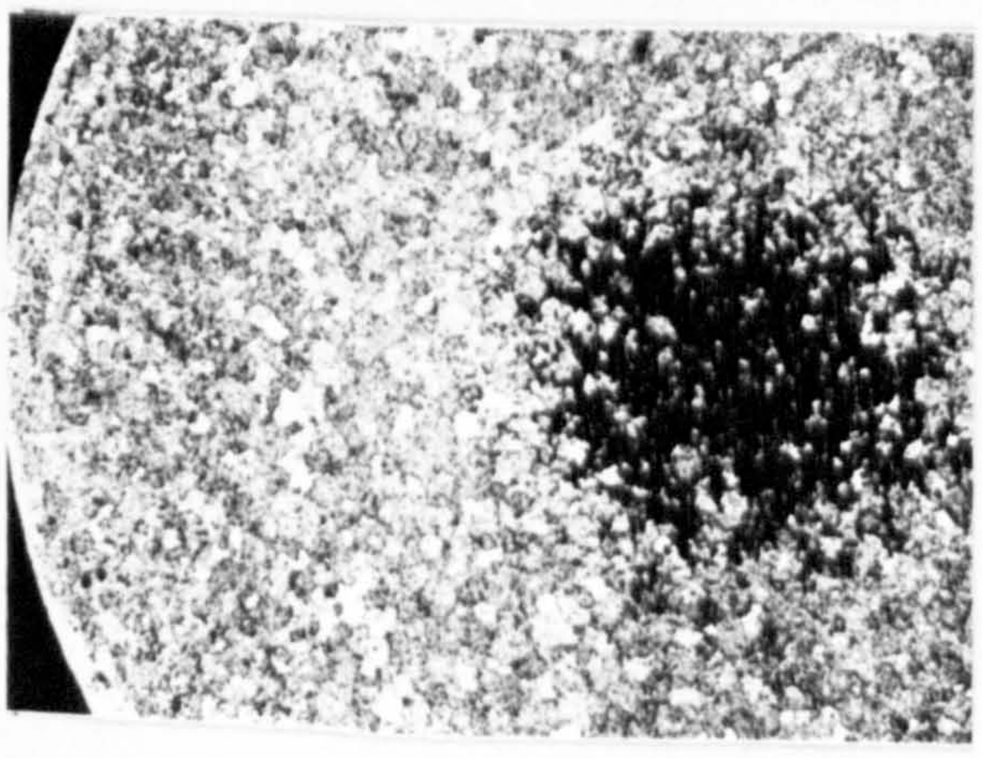

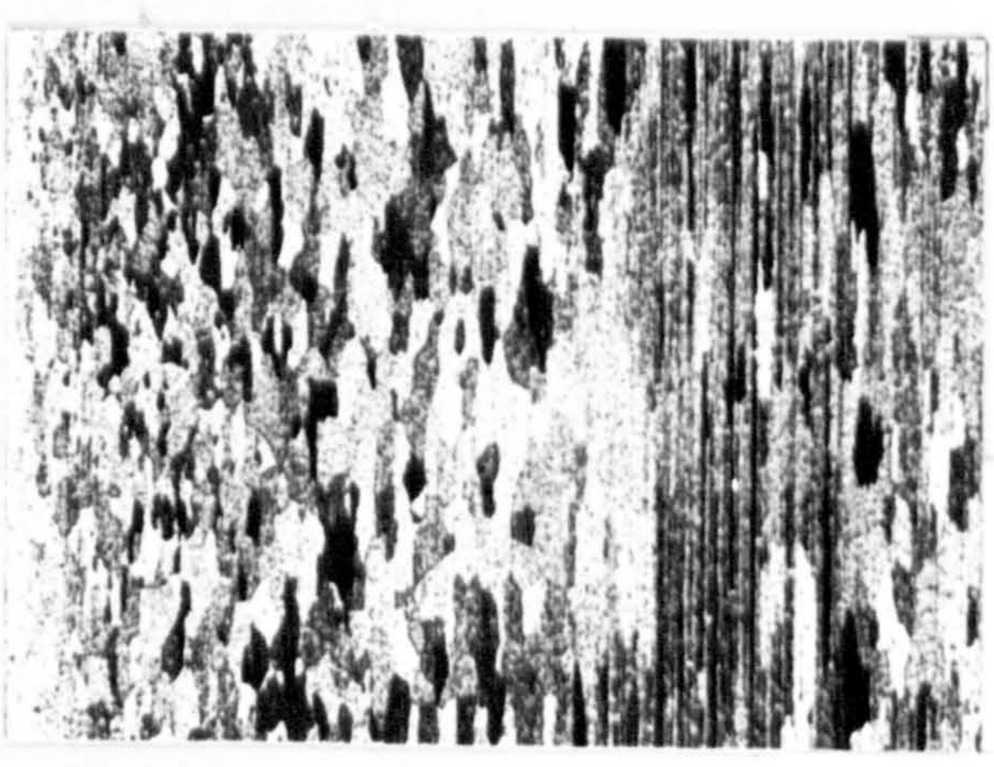

R=30
Ti=375°C
Tx= 41

X7.2

Trans.

Long.

Plate 30

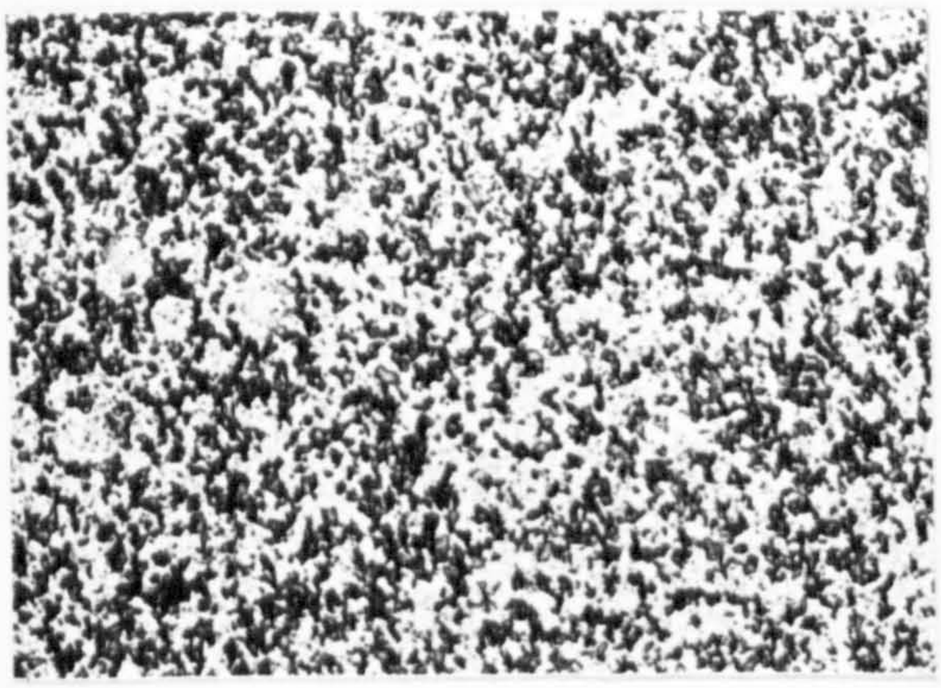

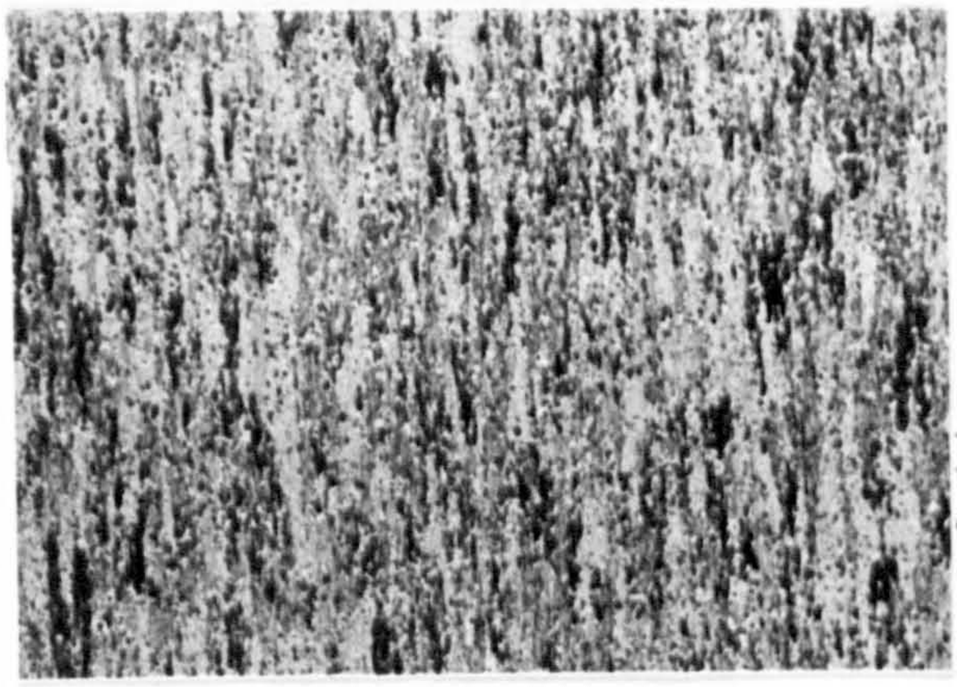

R=10
Ti=375°C
Tx= 382°C

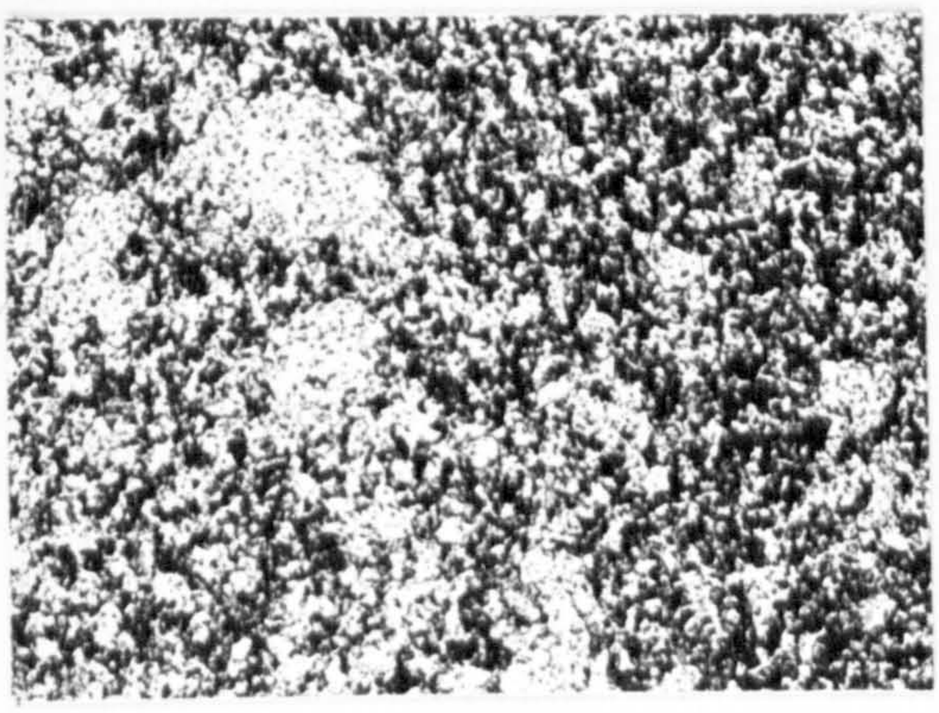

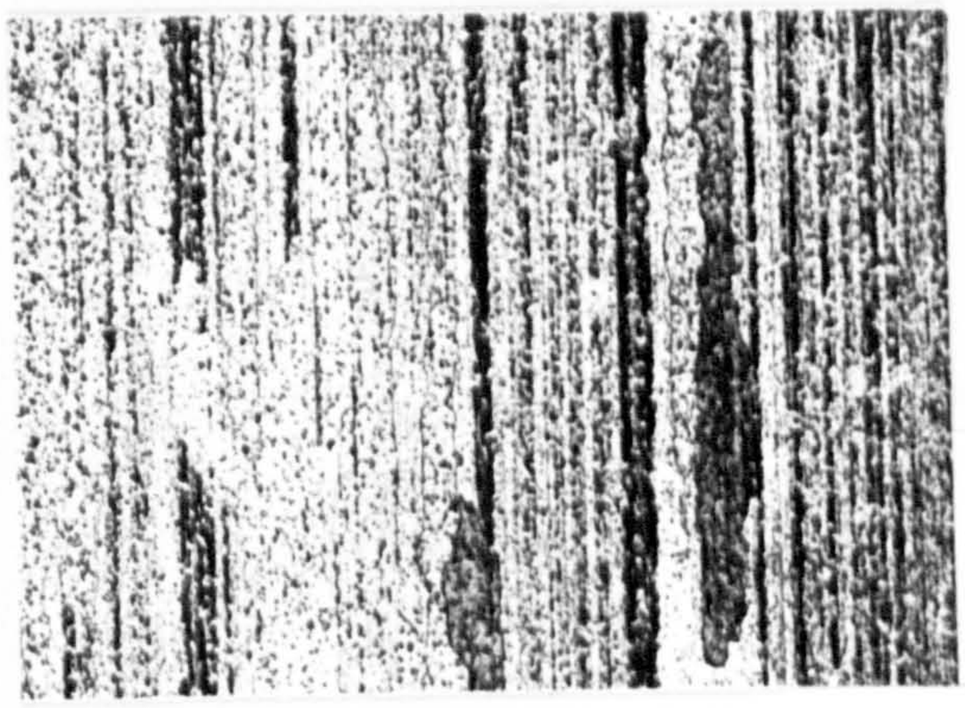

R=30
Ti=375°C
Tx= 411°C

X54

Trans.

Long.

Plate 31

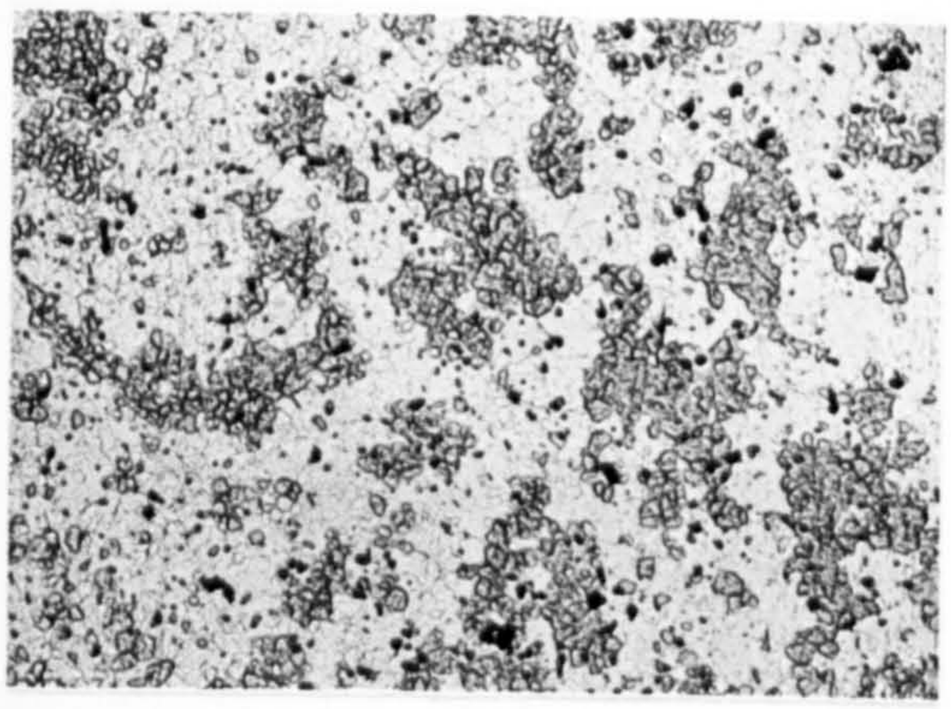

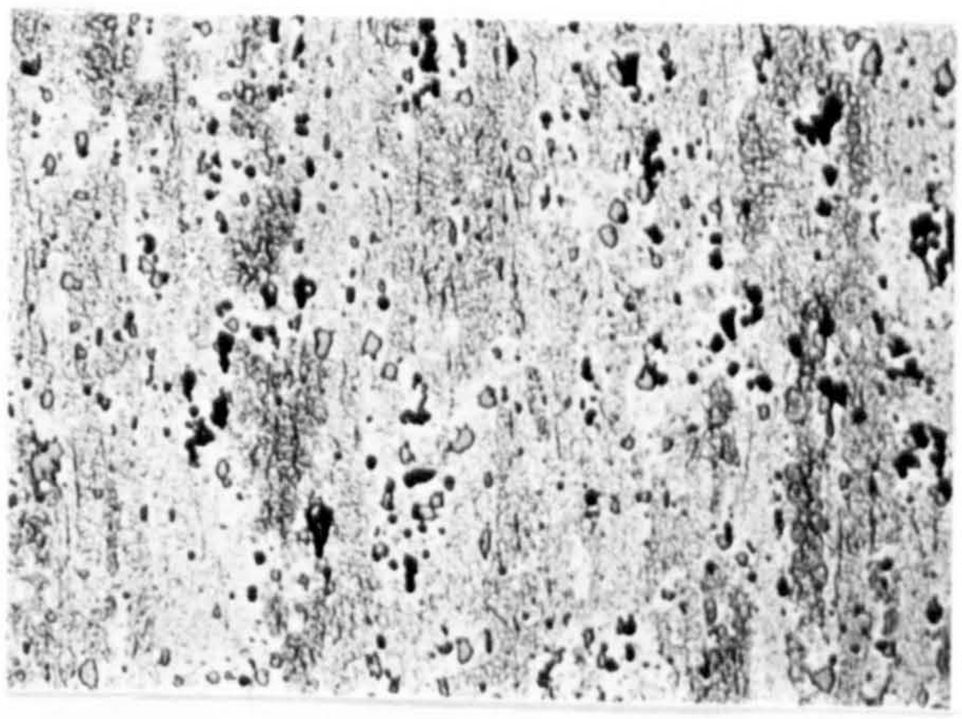

R=10
Ti=375°C
Tx=382°C

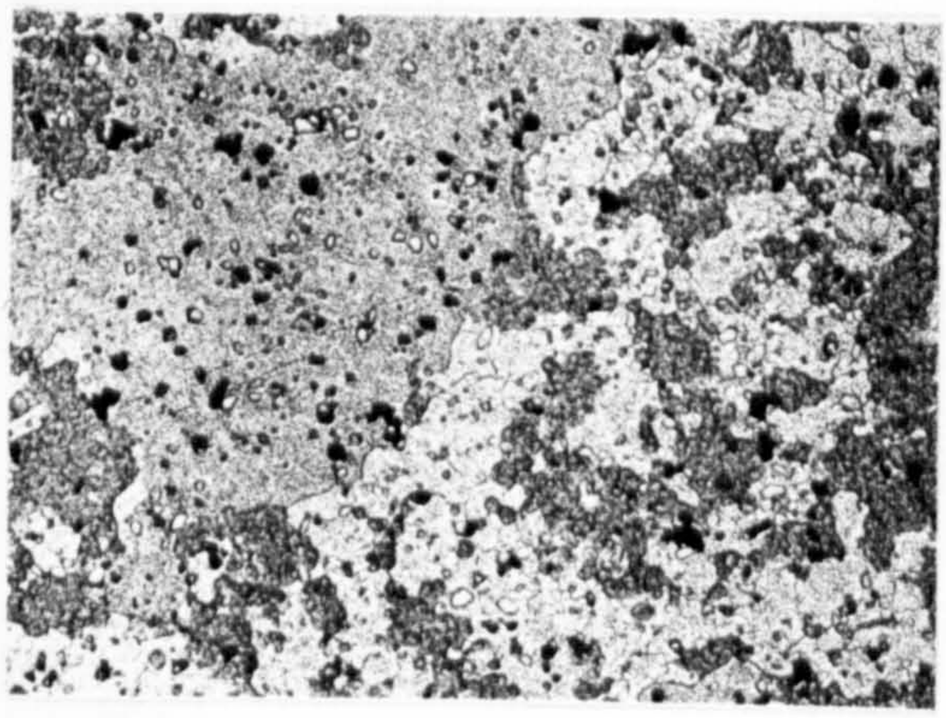

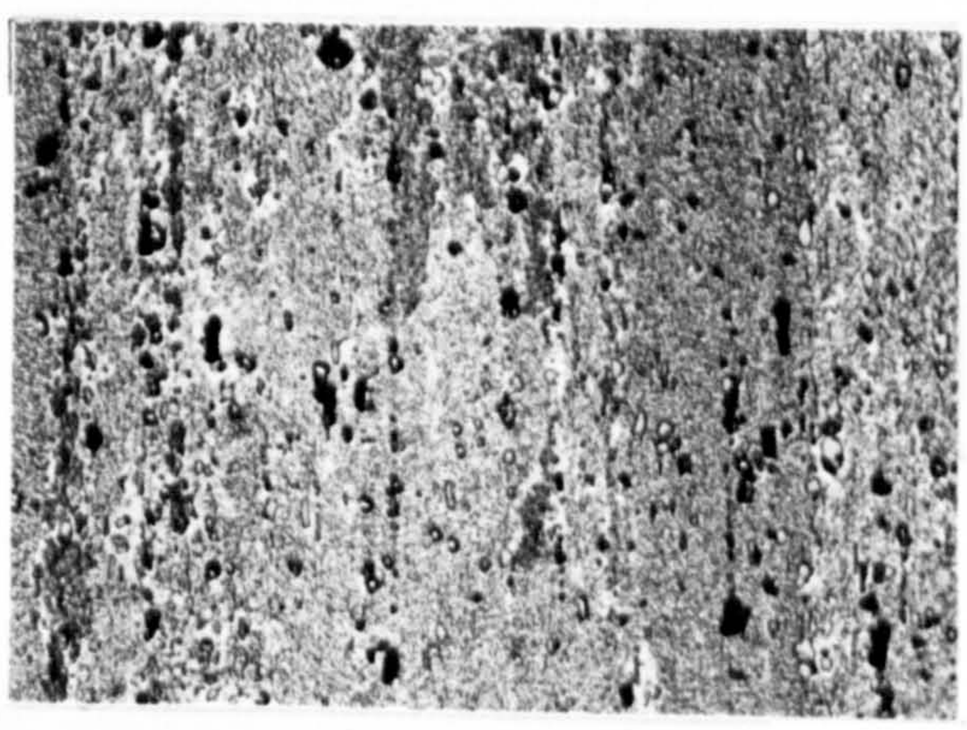

R=30
Ti=375°C
Tx=411°C

X270

Trans.

Long.

Plate 32

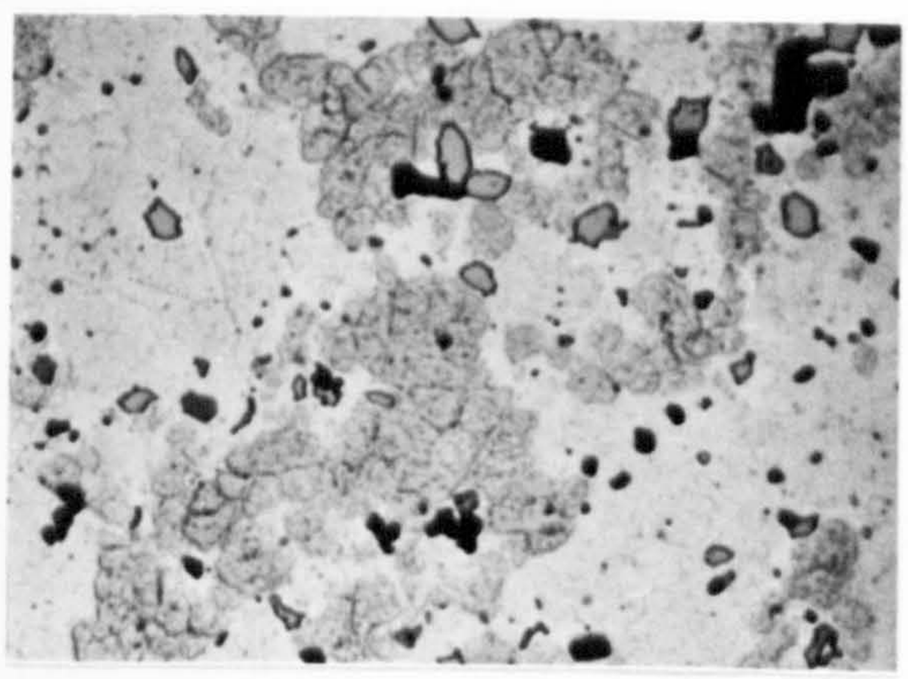

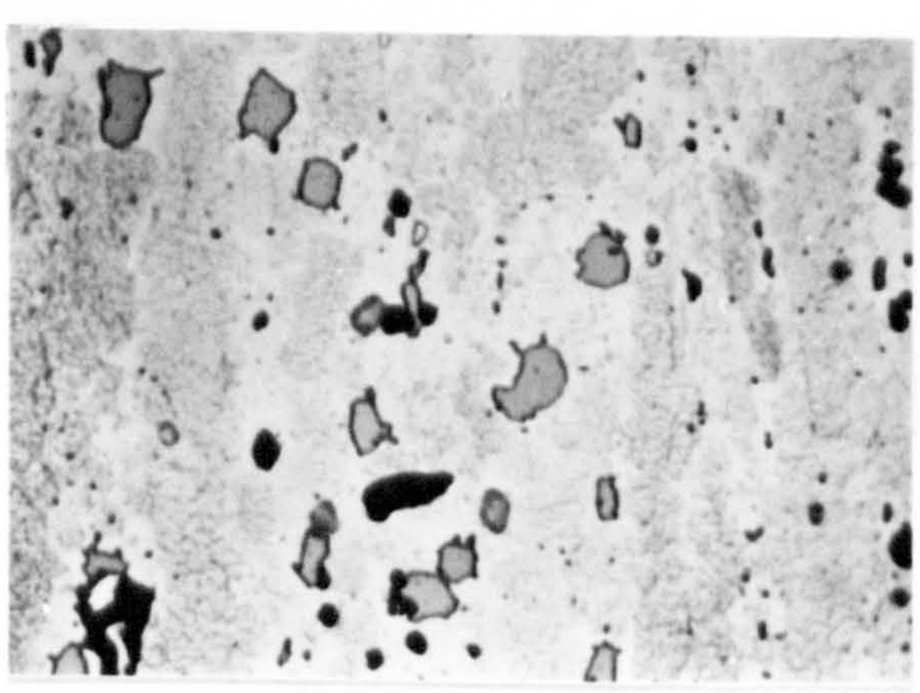

R=10
Ti=375°C
Tx=382°C

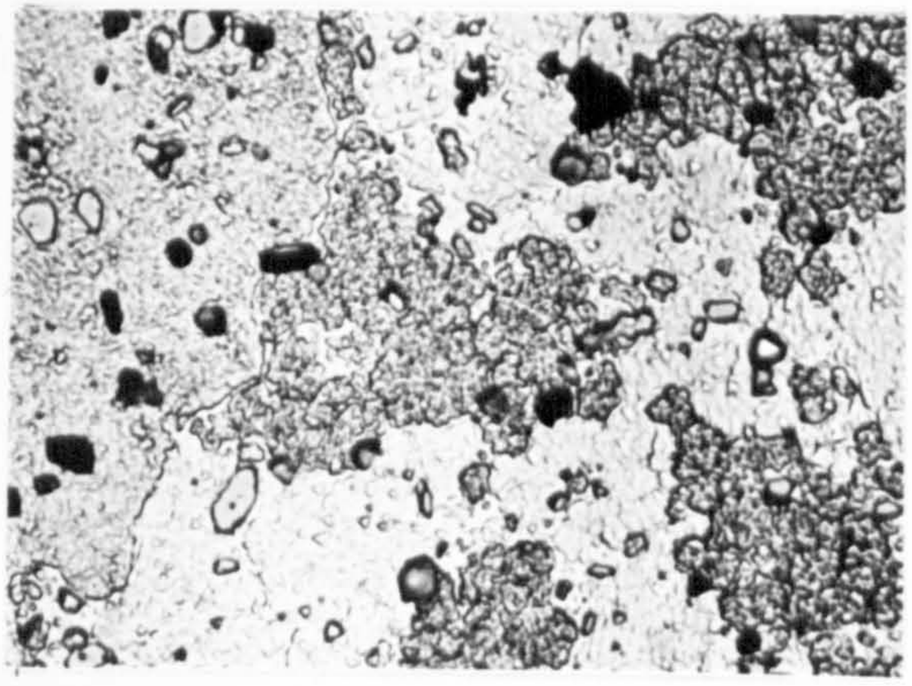

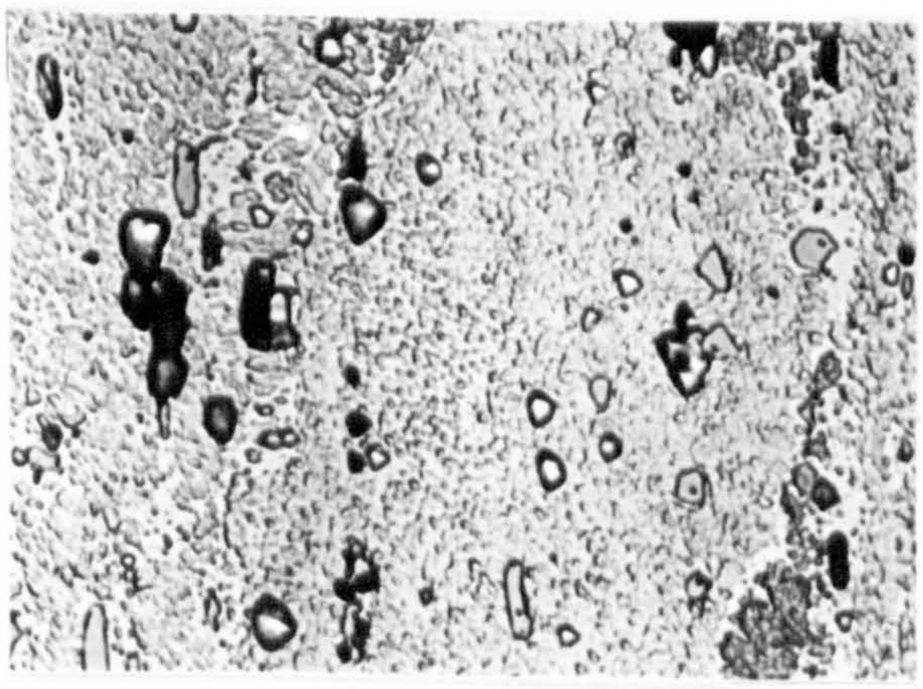

R=30
Ti=375°C
Tx=411°C

X810

Trans.

Long.

Plate 33

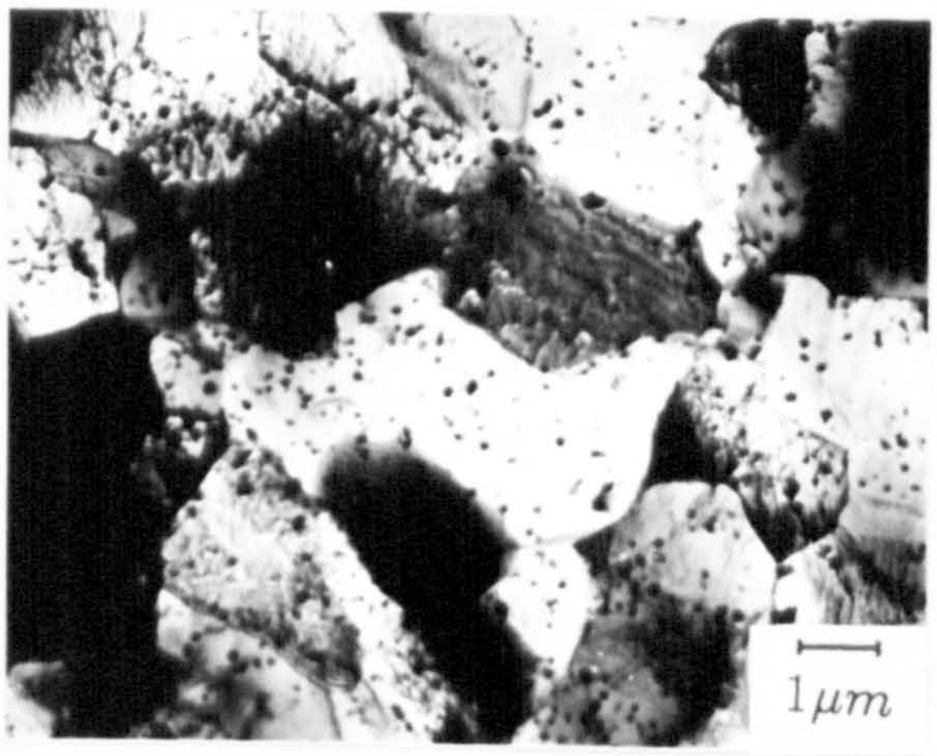

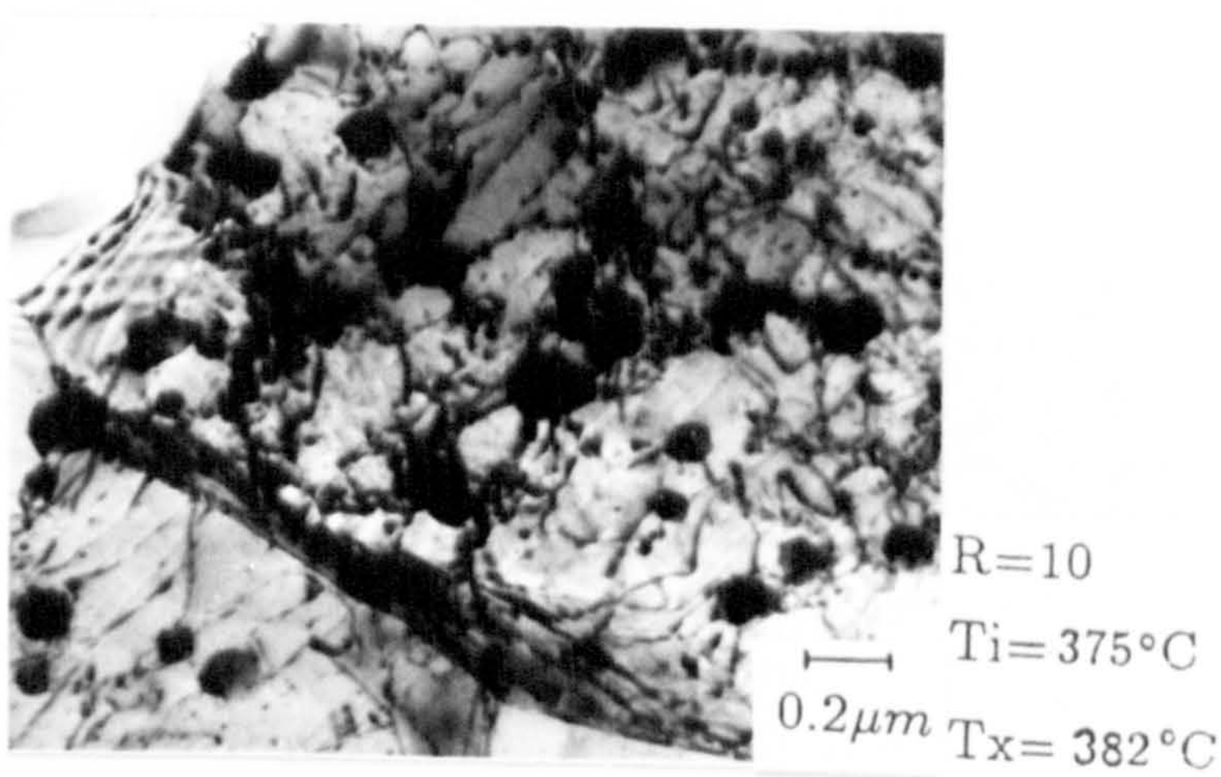

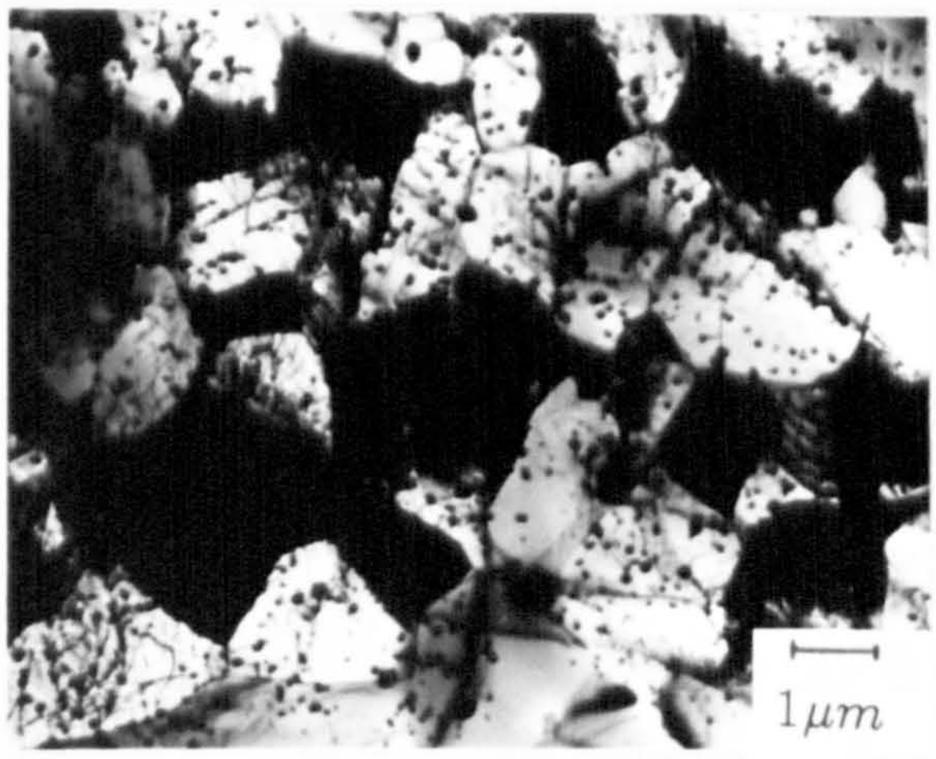

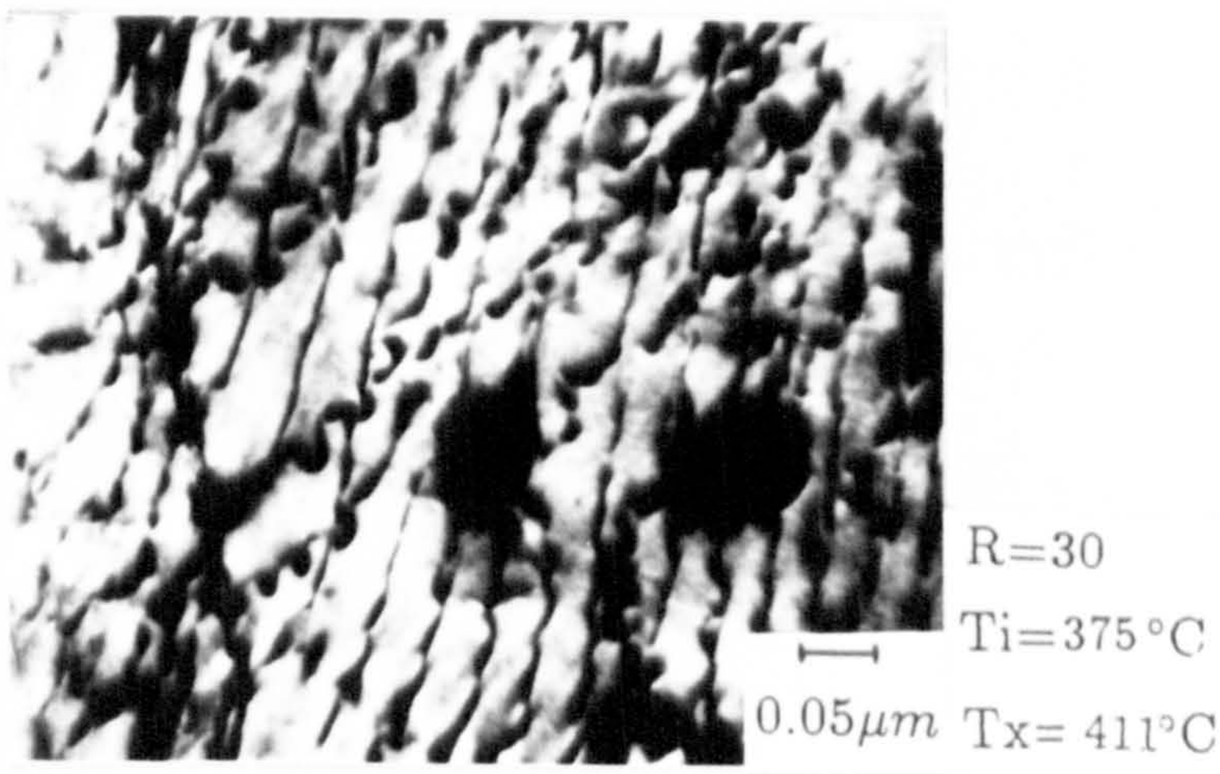

Plate 34

Ti=250°C
Tx=347°C

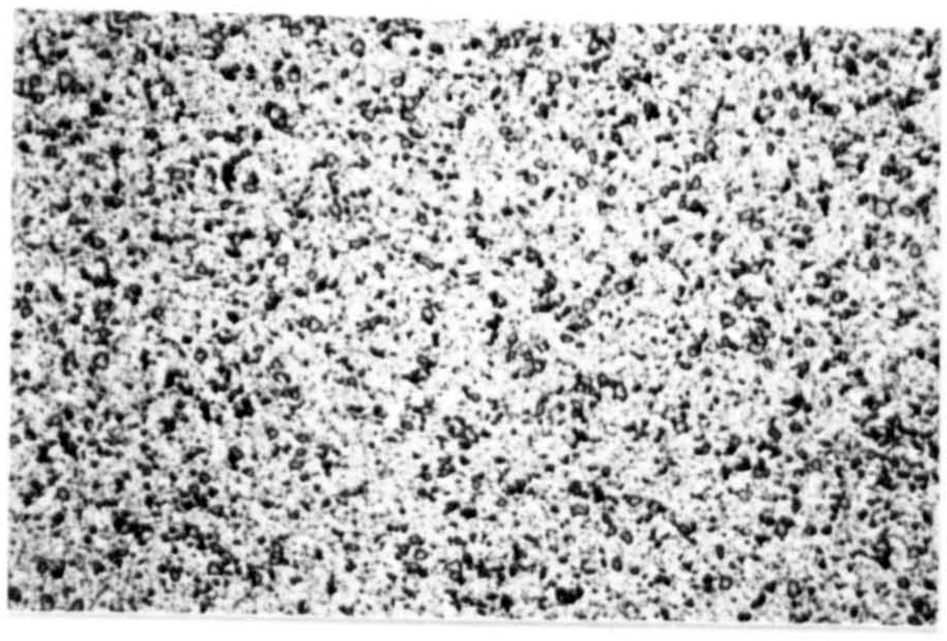

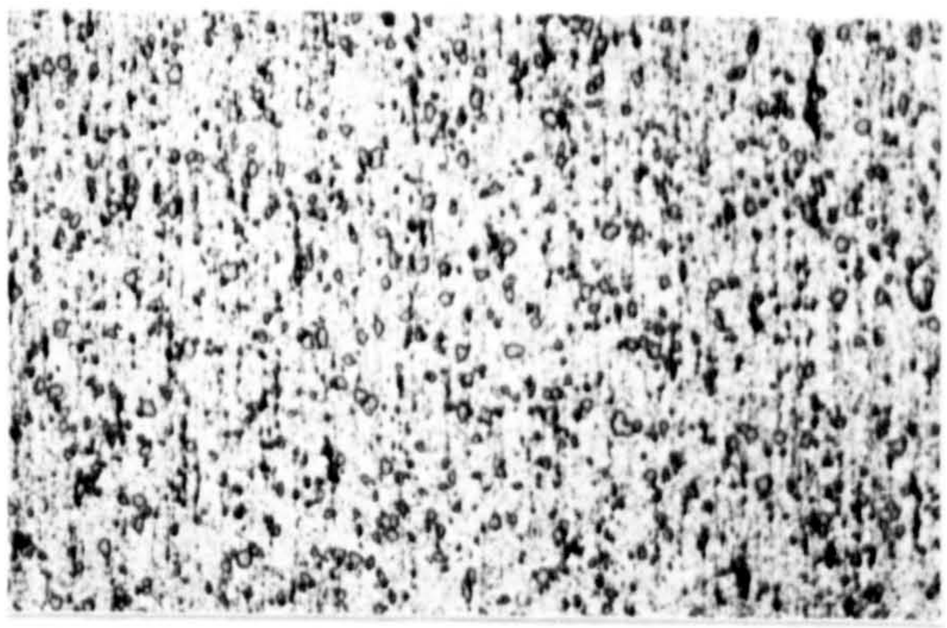

Ti=400°C
Tx=360°C

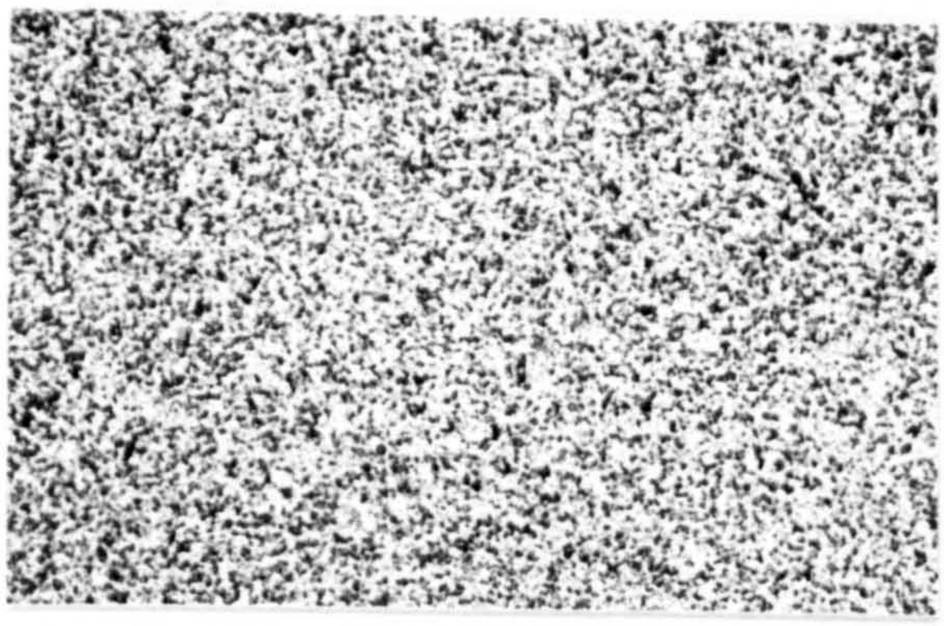

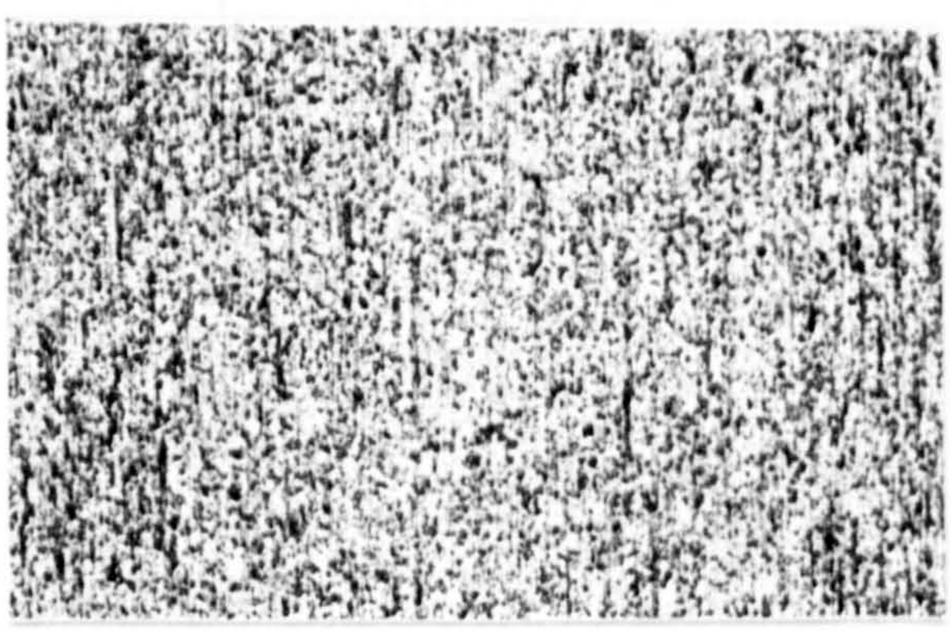

Ti=450°C
Tx=377°C

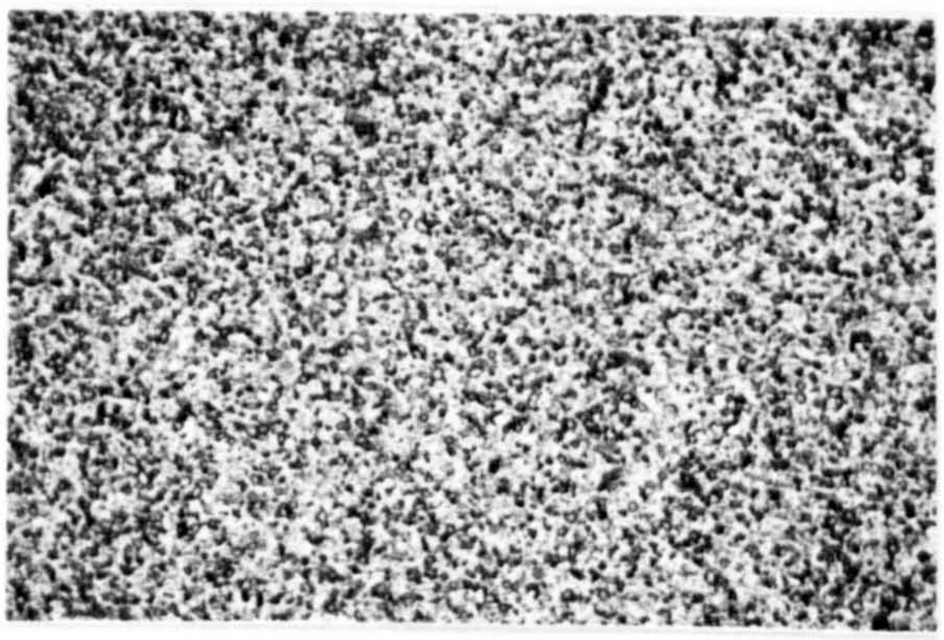

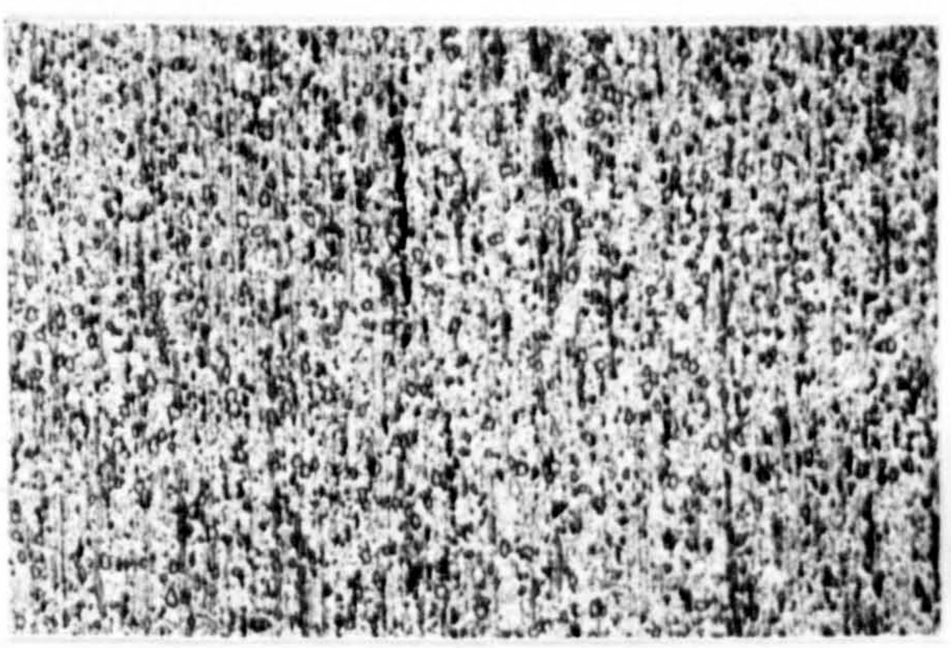

Ti=500°C
Tx=397°C

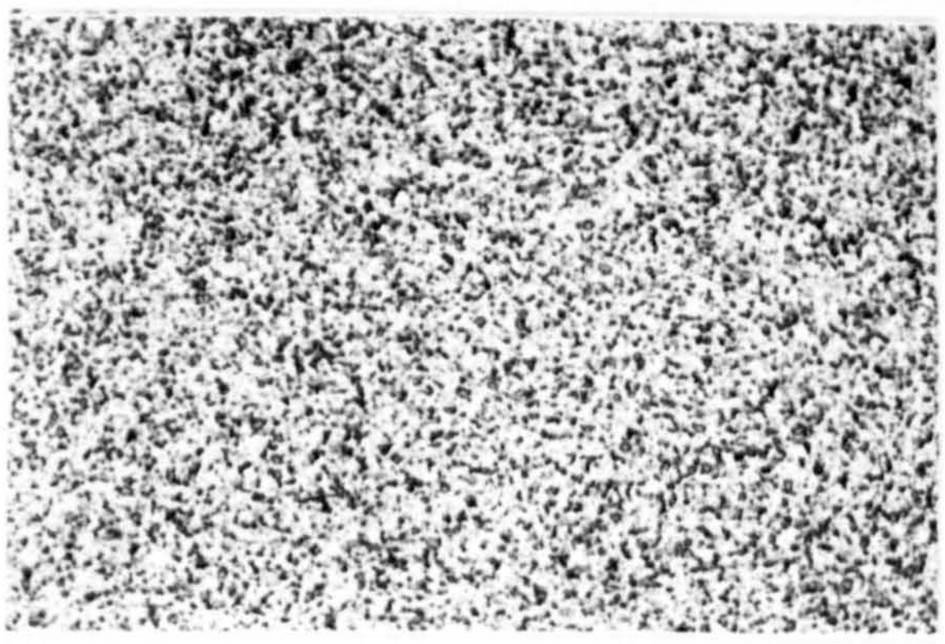

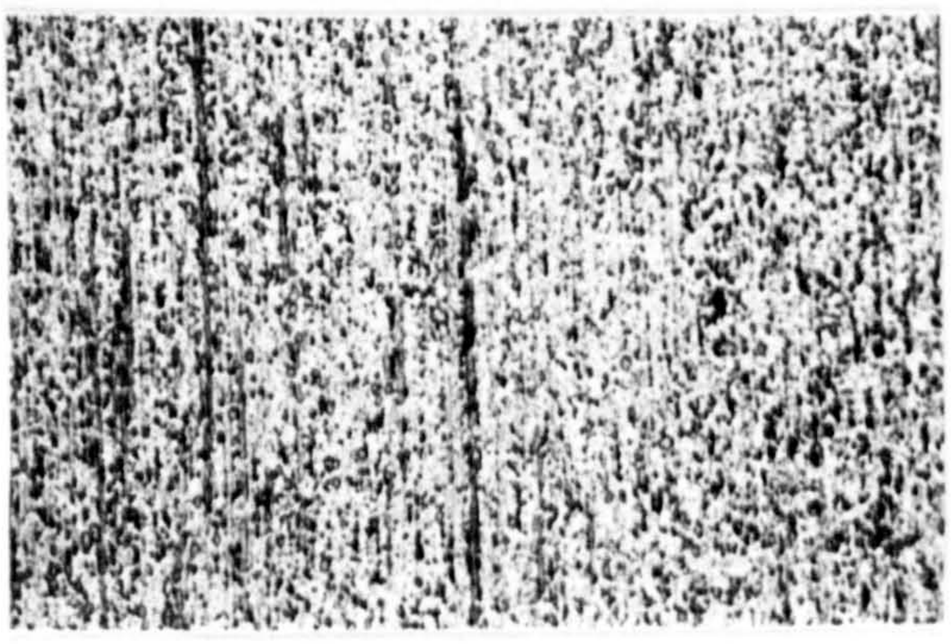

Ti=550°C
Tx=421°C

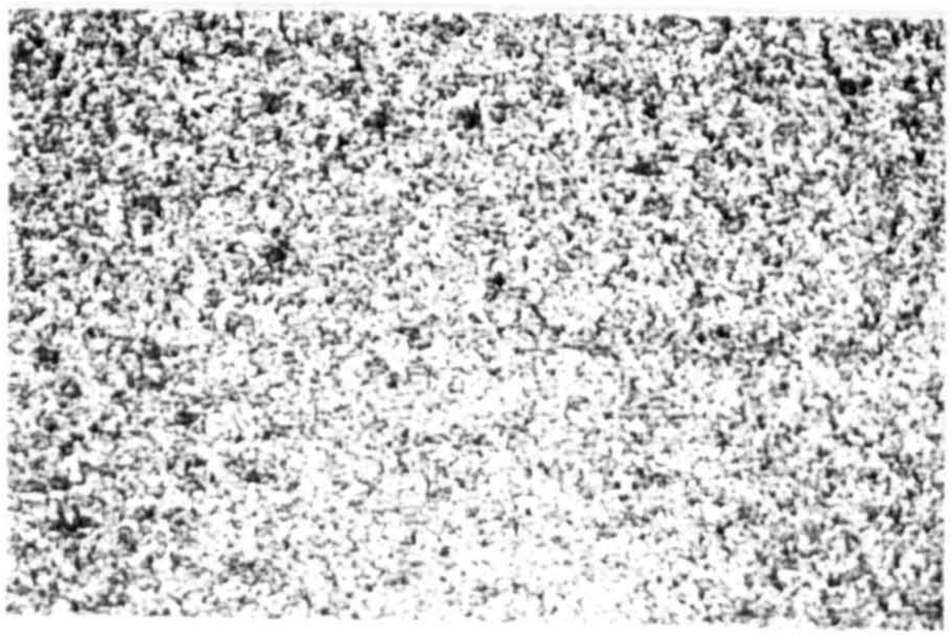

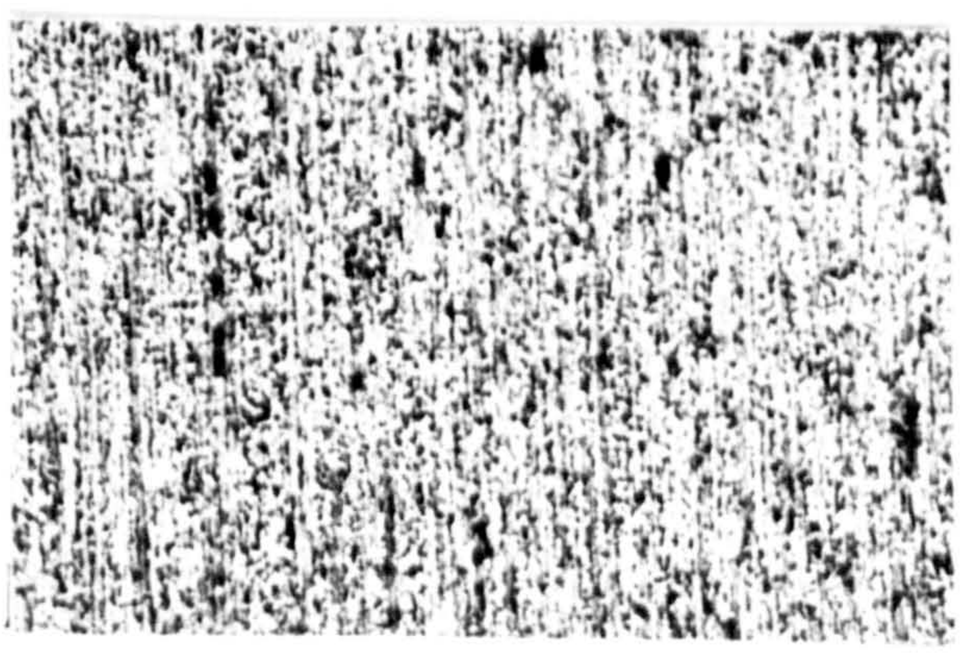

Trans.

Long.

X270

Plate 35

Ti=250°C
Tx=347°C

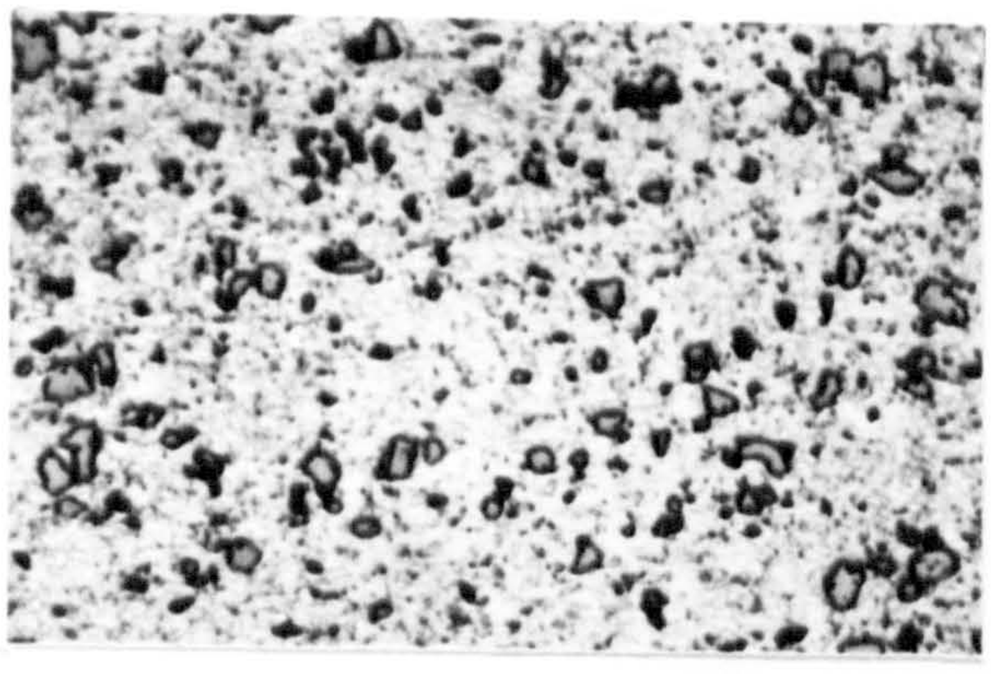

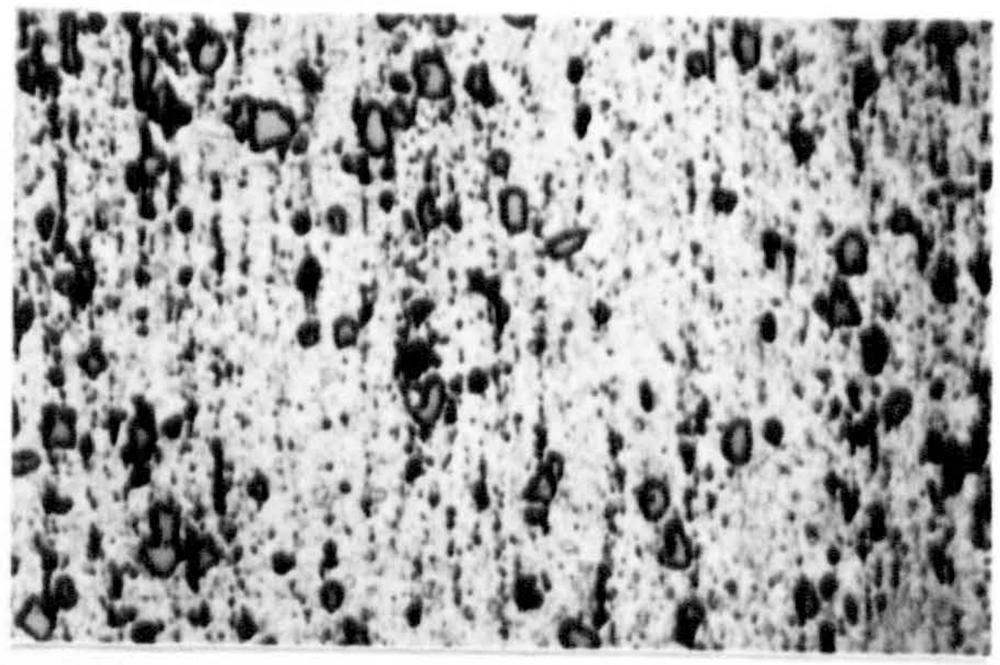

Ti=400°C
Tx=360°C

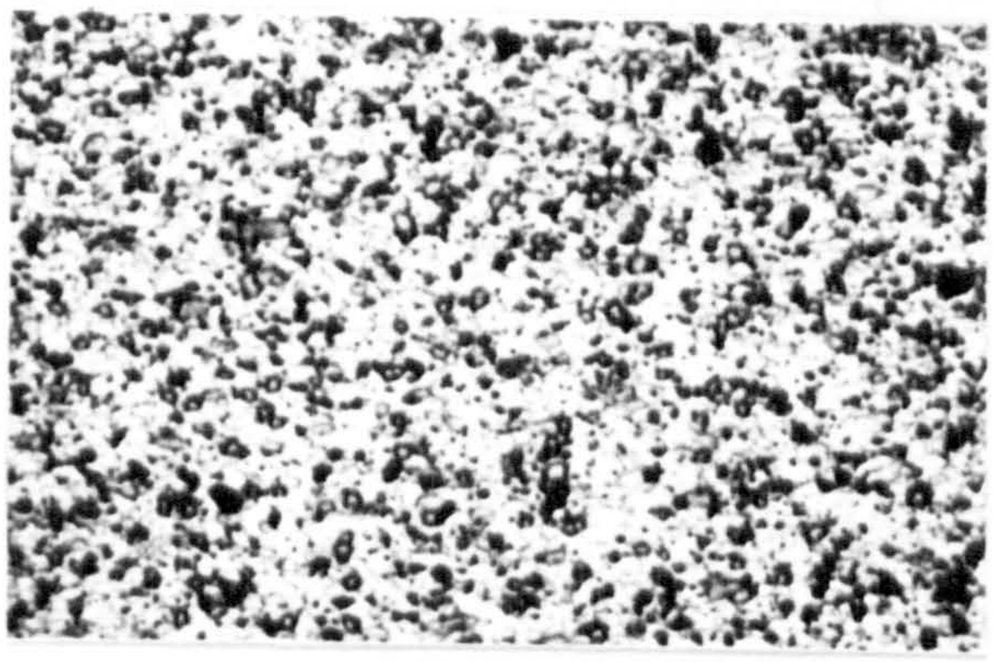

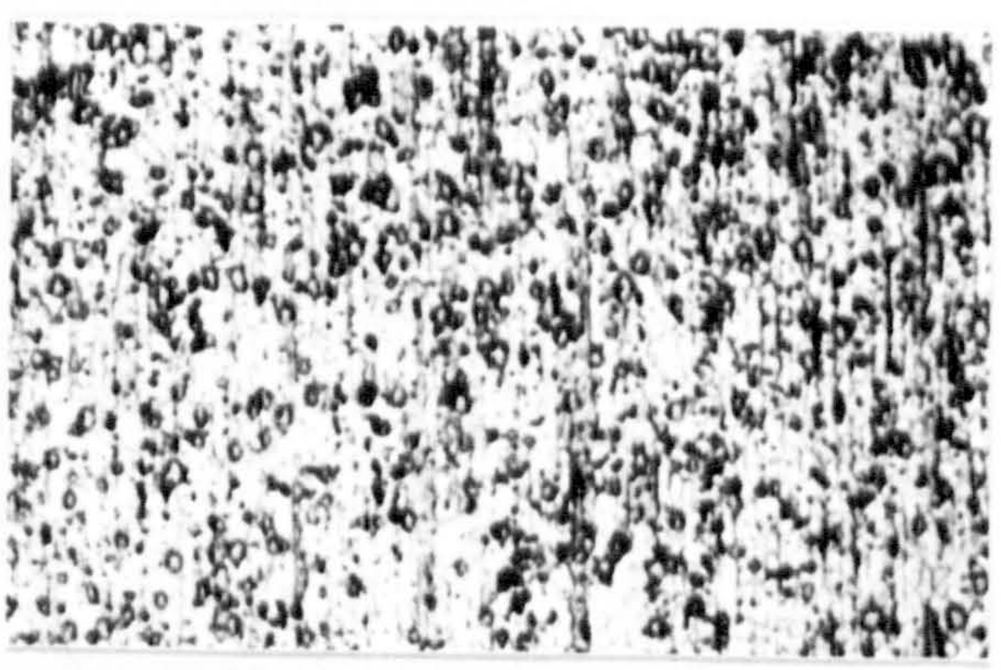

Ti=450°C
Tx=377°C

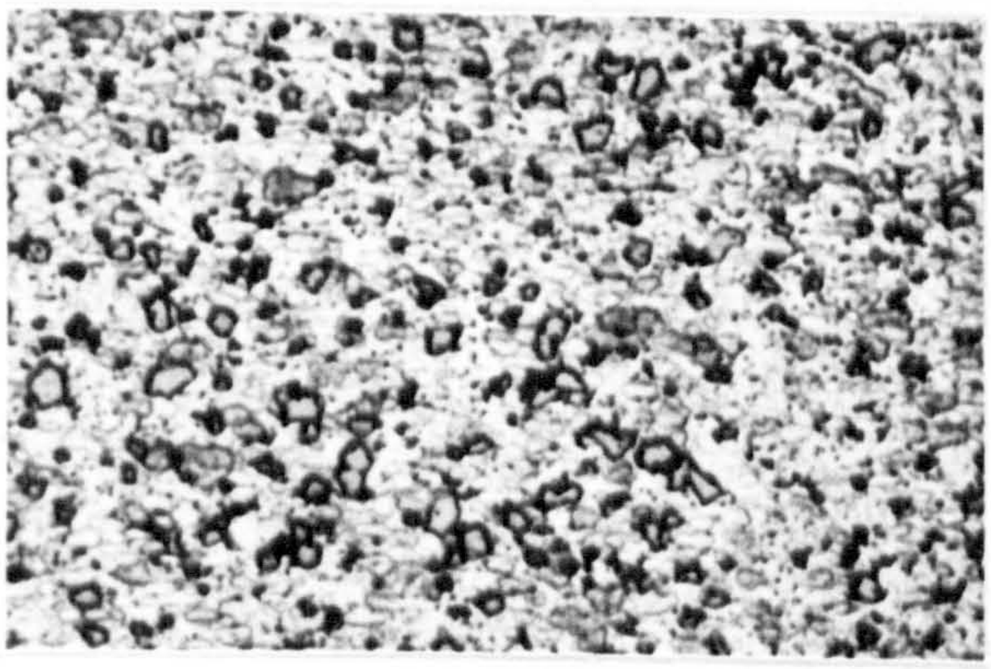

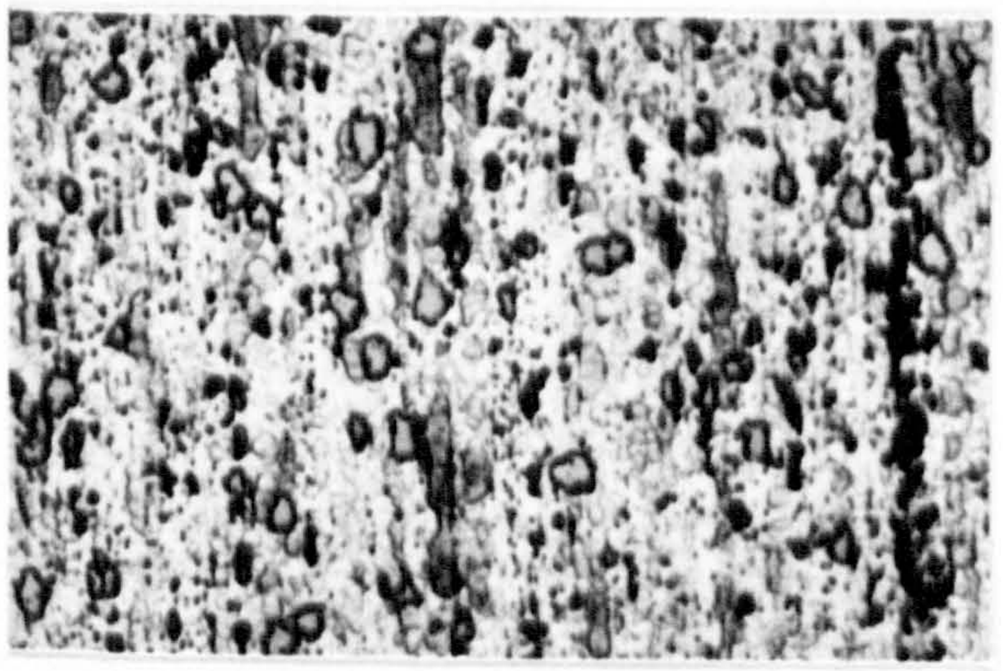

Ti=500°C
Tx=397°C

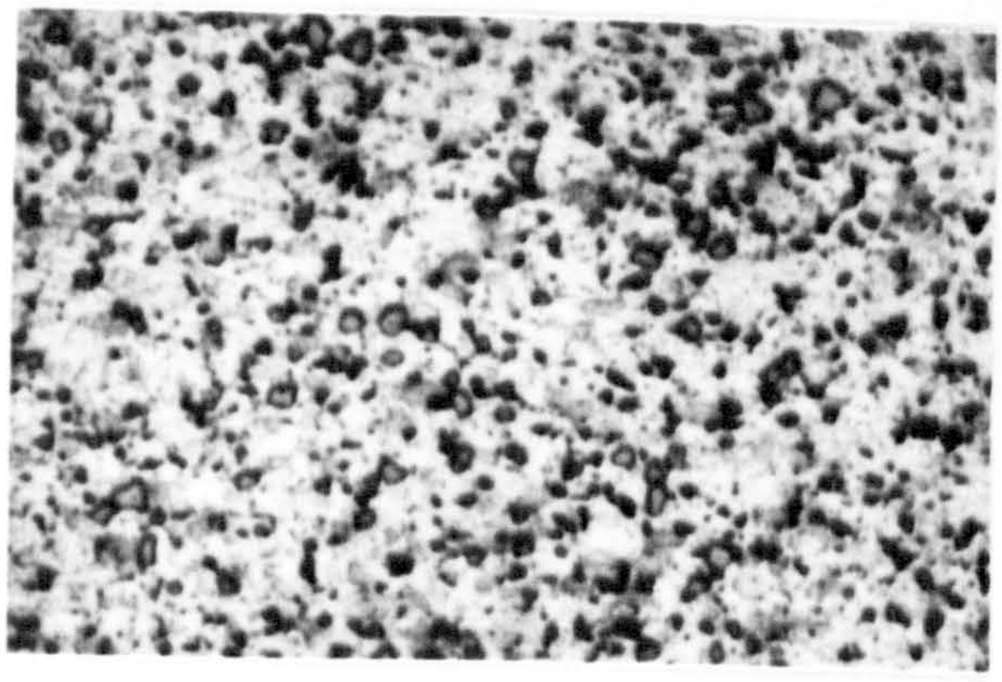

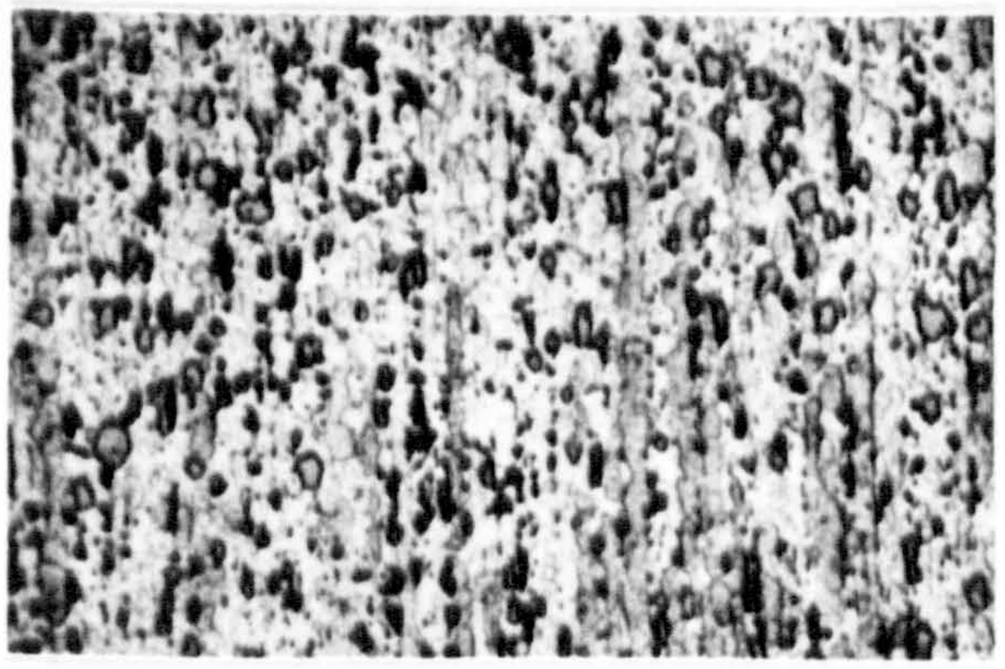

Ti=550°C
Tx=421°C

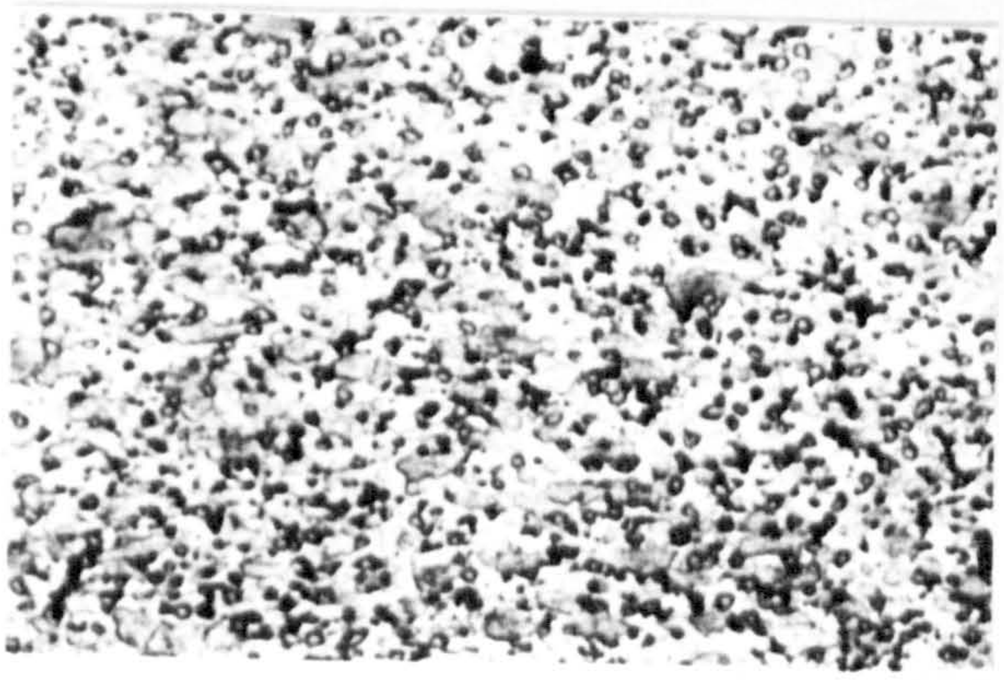

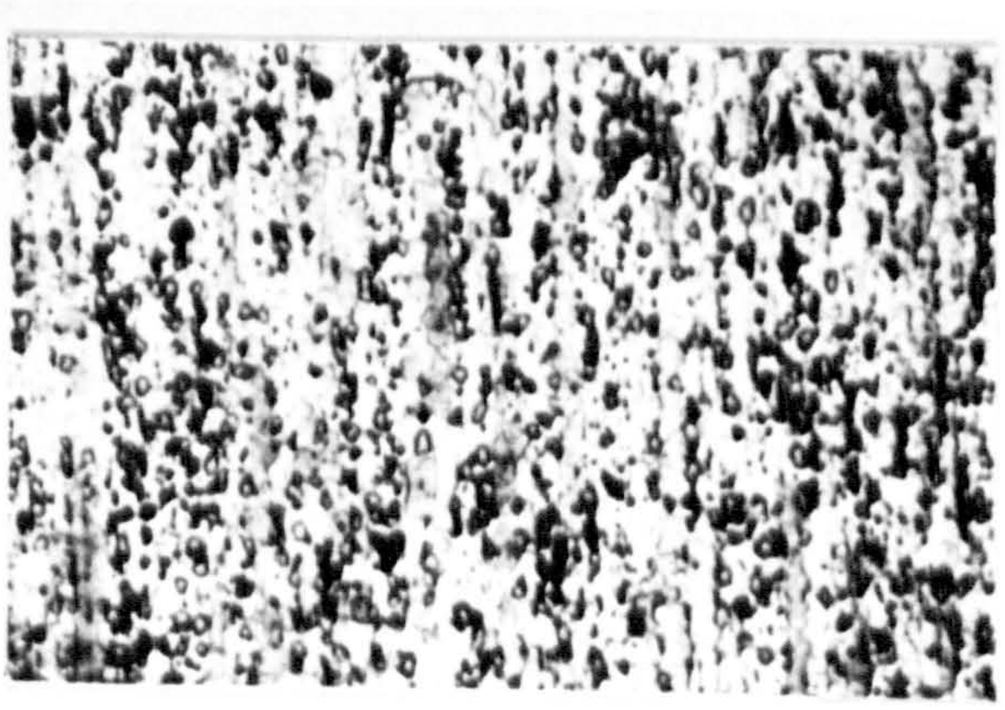

Trans.

Long.

X810

Plate 36

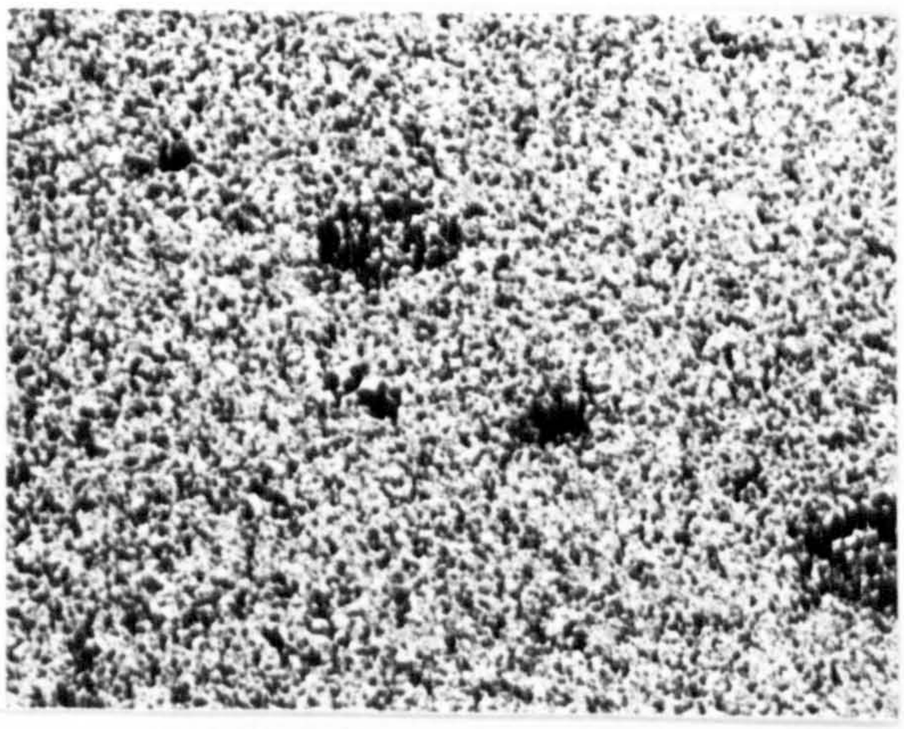

Ti=411°C

Tx=372°C

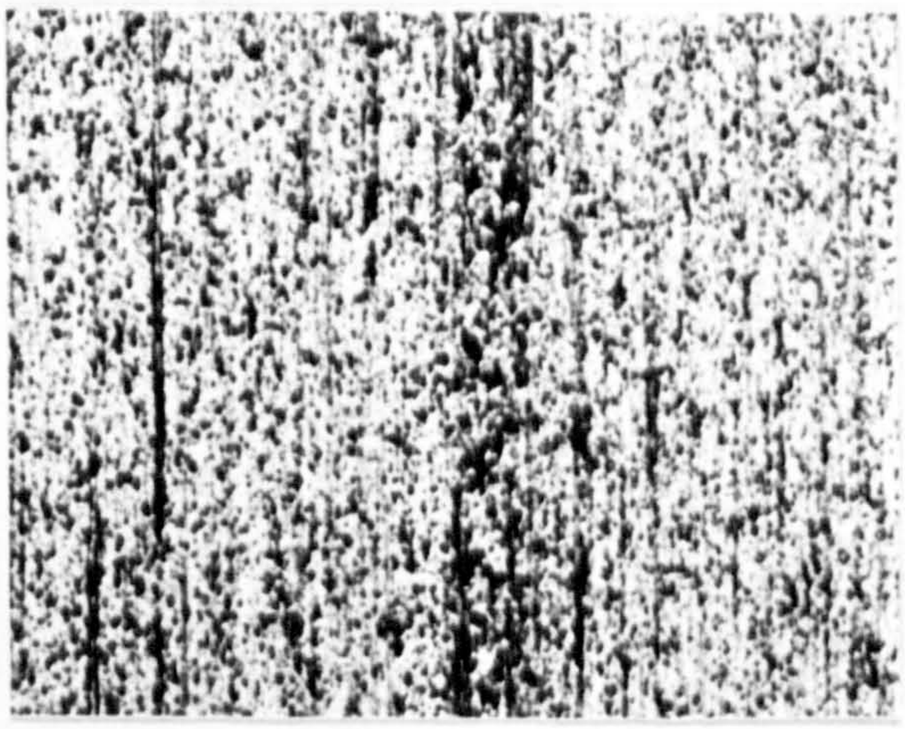

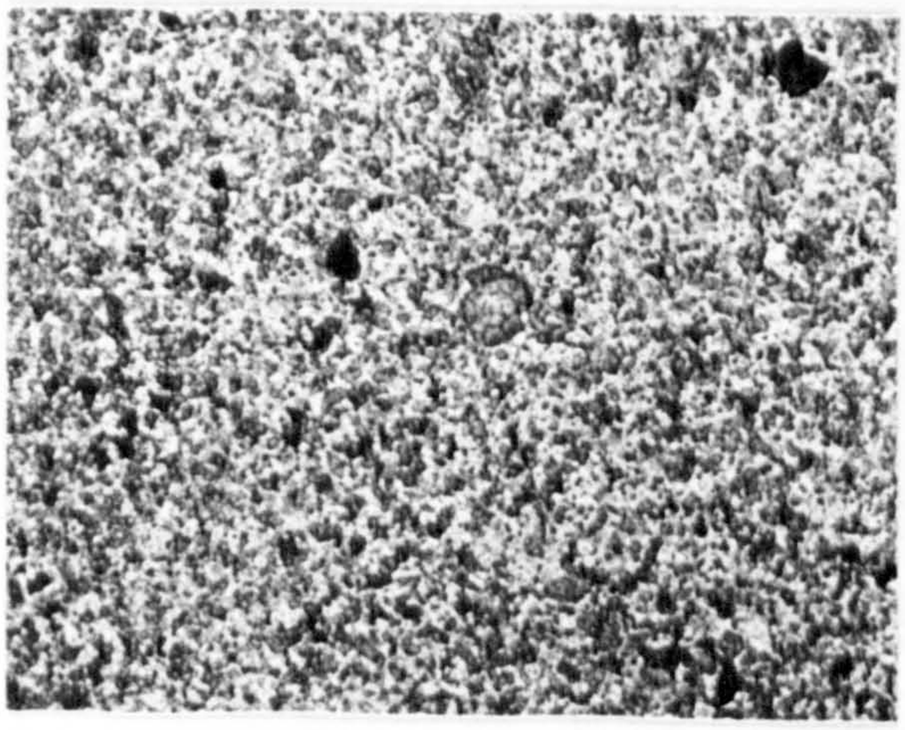

Ti=552°C

Tx=463°C

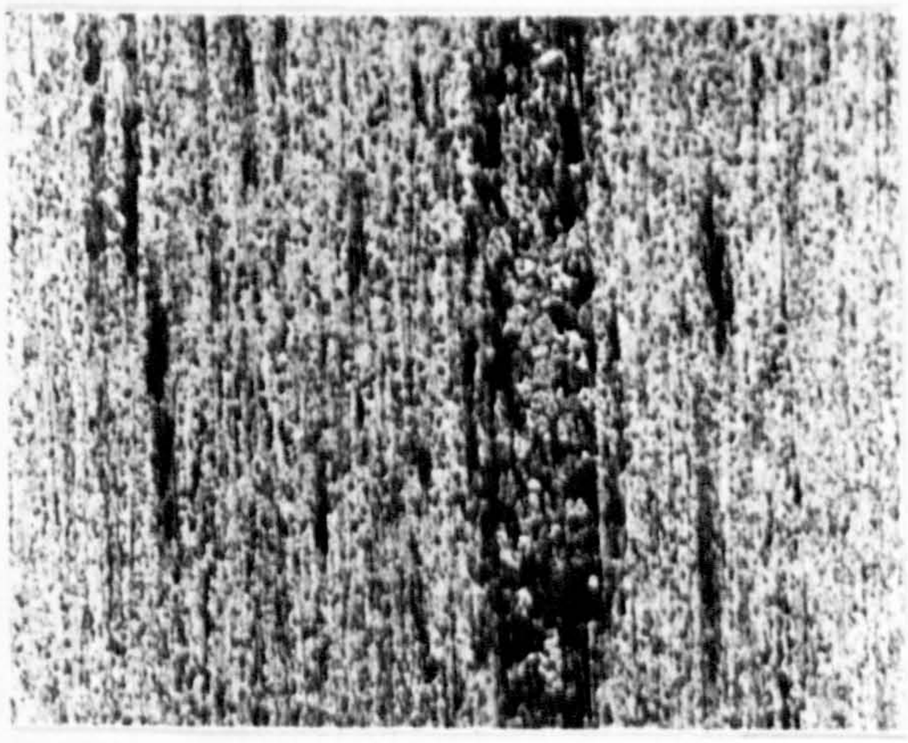

X270

Trans.

Long.

Plate 37

Ti=411°C

Tx=372°C

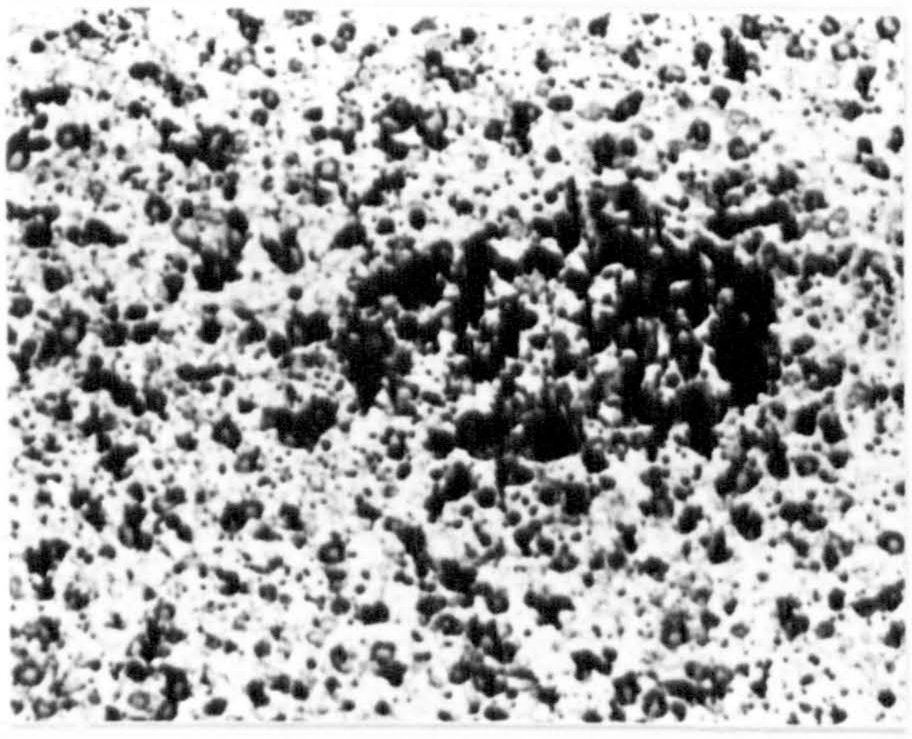

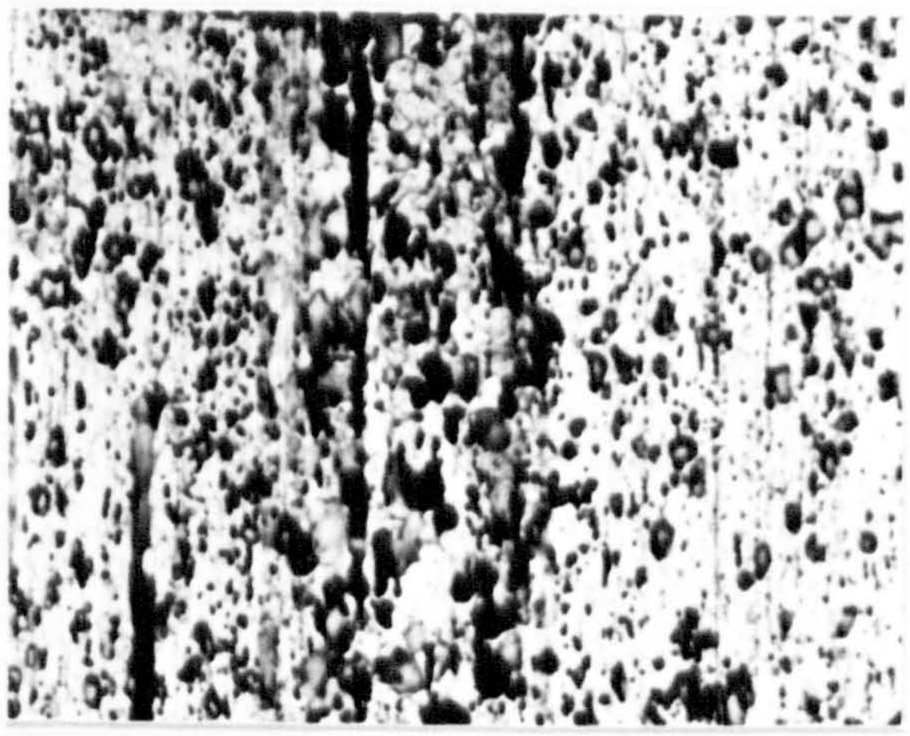

Ti=552°C

Tx=463°C

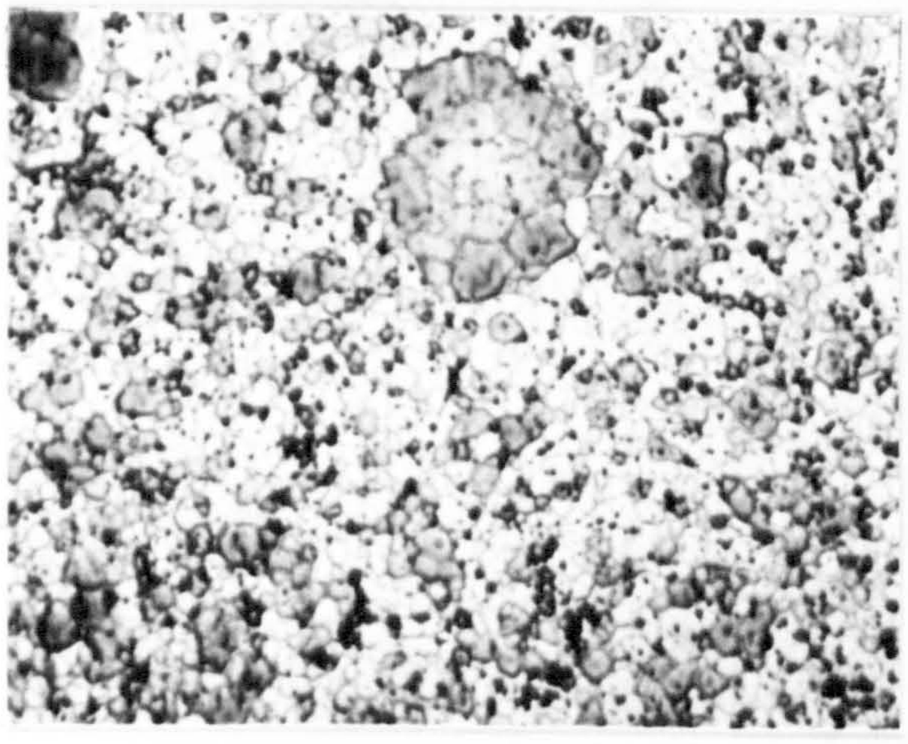

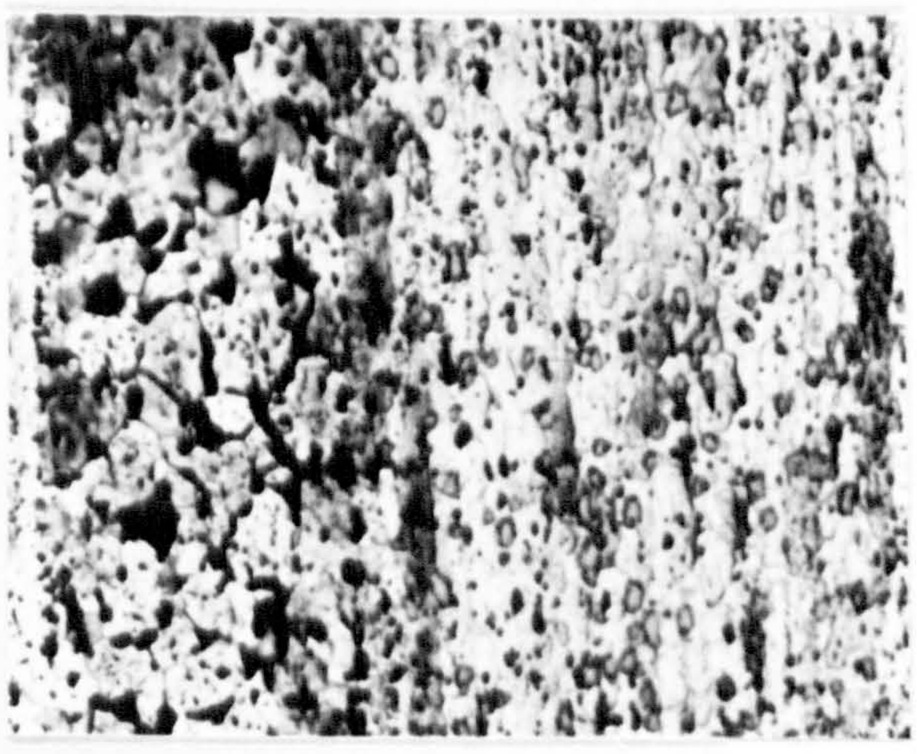

X810

Trans.

Long.

Plate 38

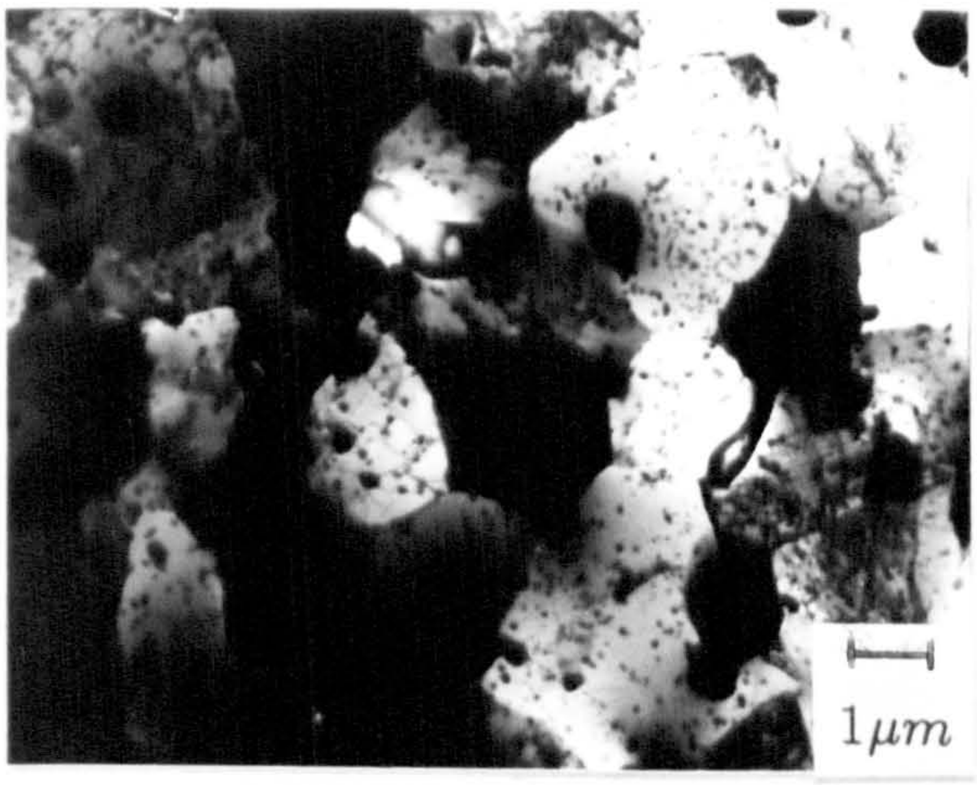

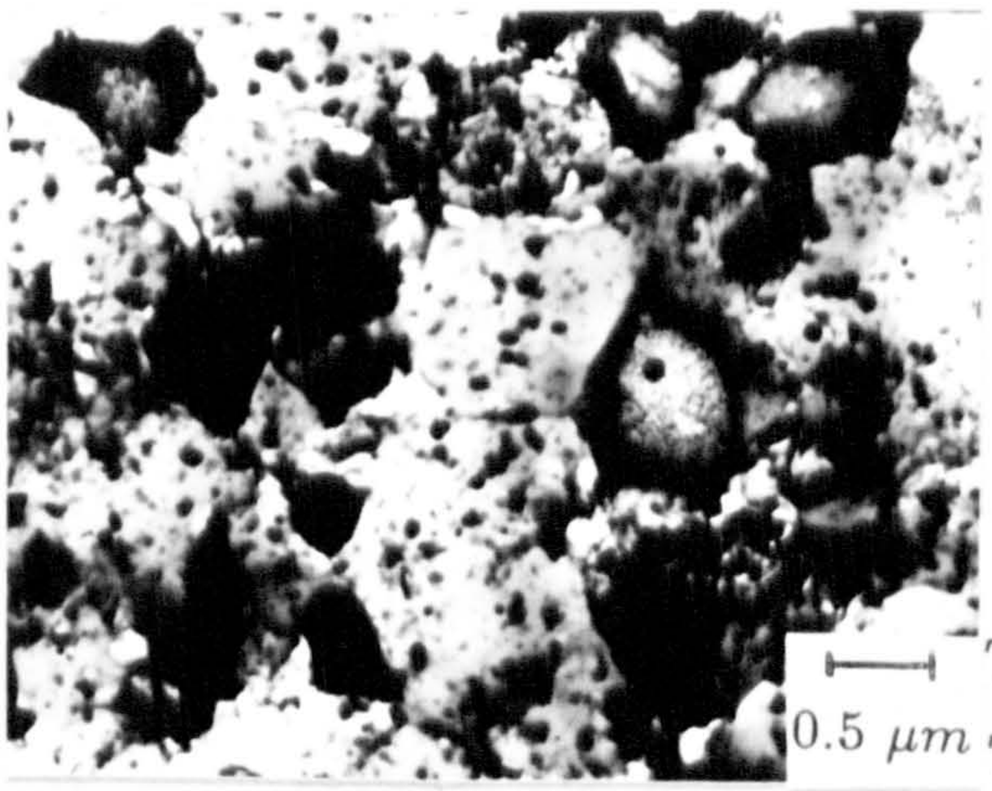

Fine
Ti=400°C
Tx=360°C

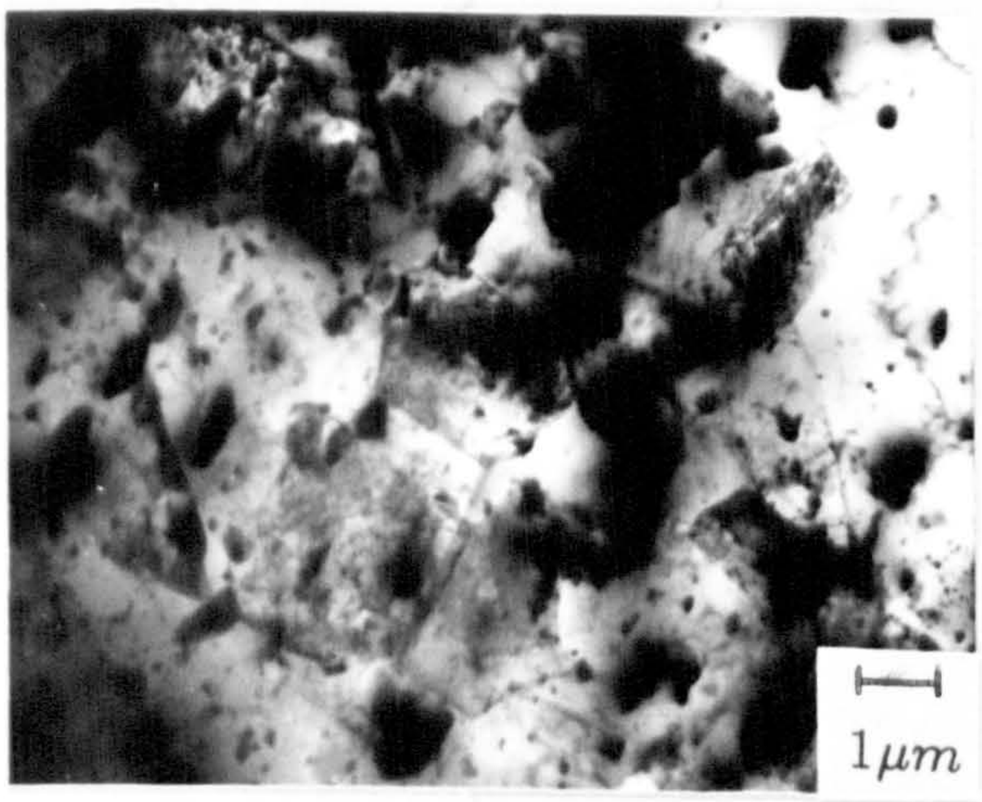

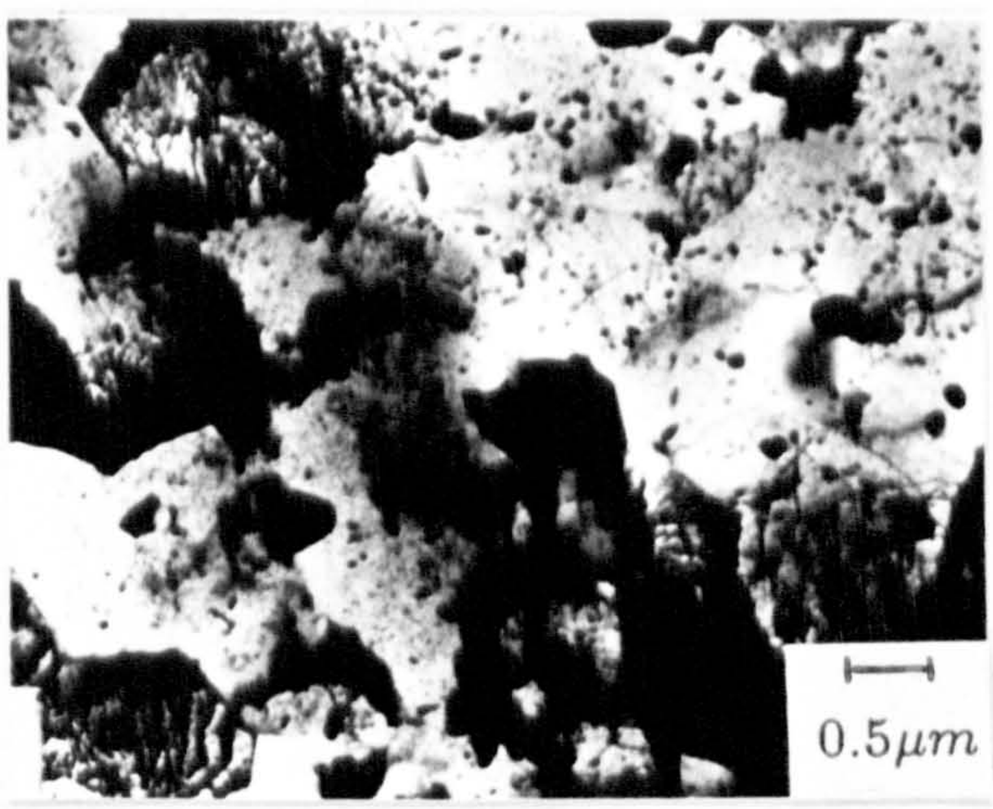

Coarse Ti=552°C
Tx=463°C

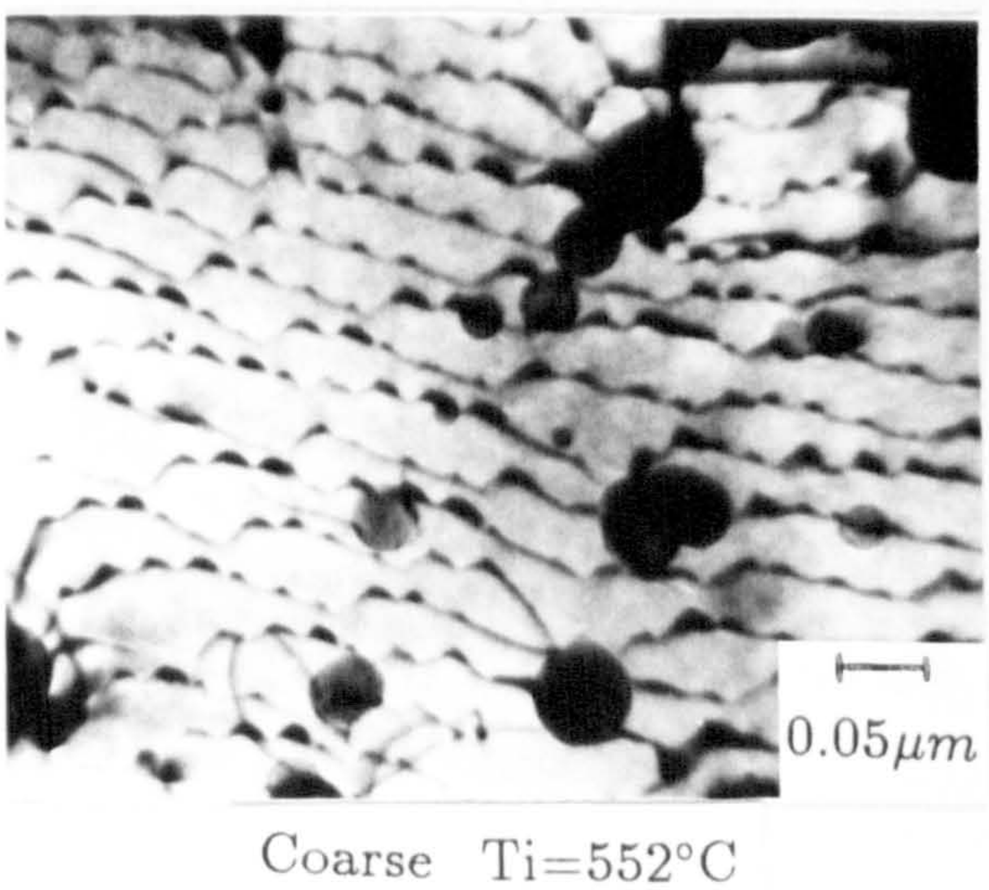

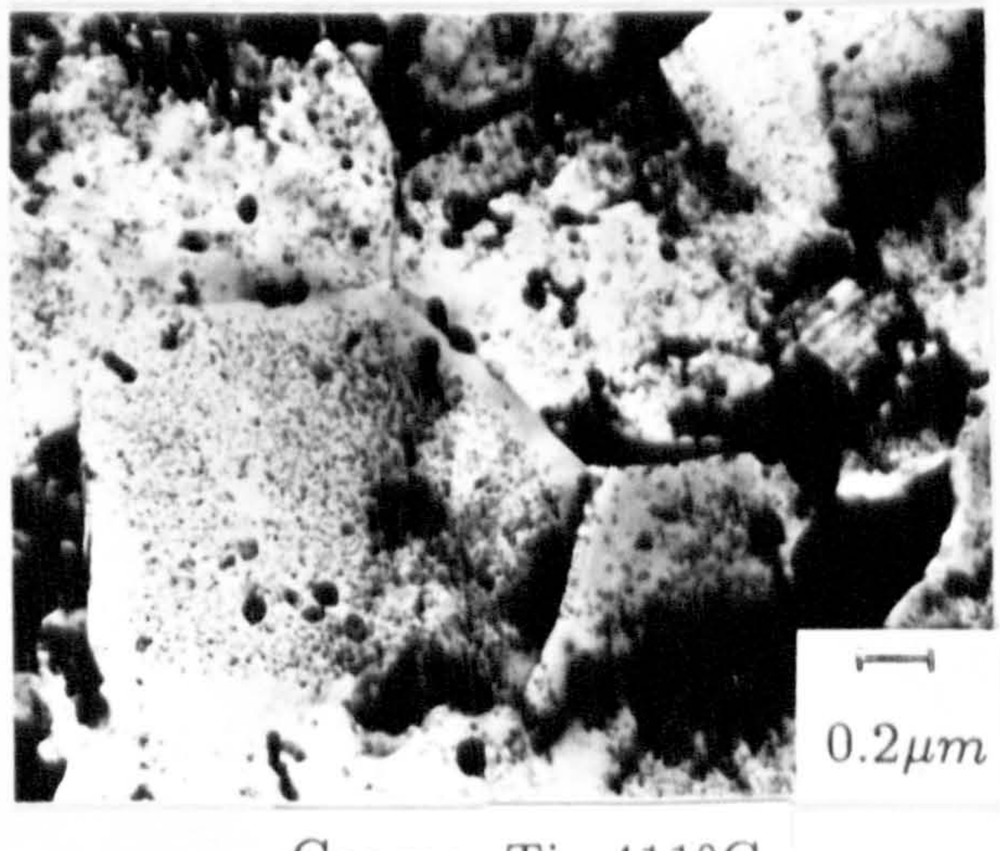

Coarse Ti=411°C
Tx=372°C

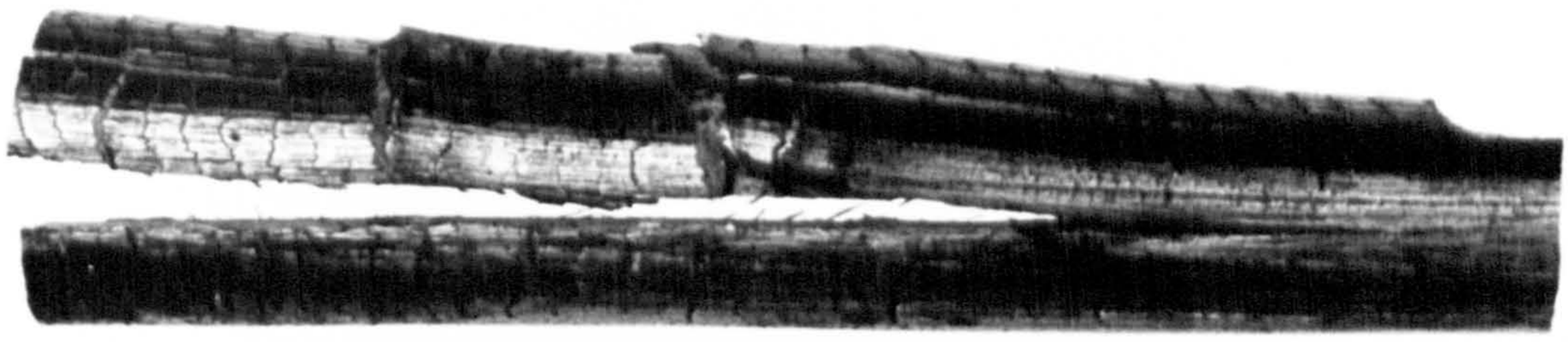

Solid

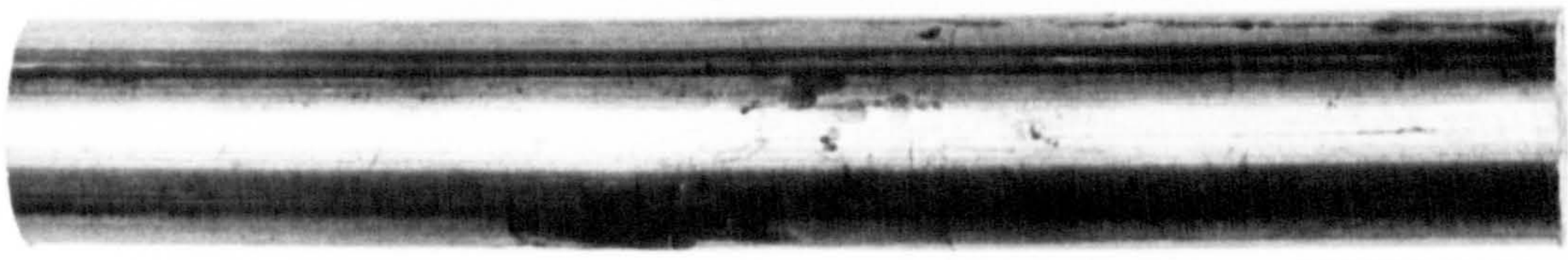

Powder

Plate 40

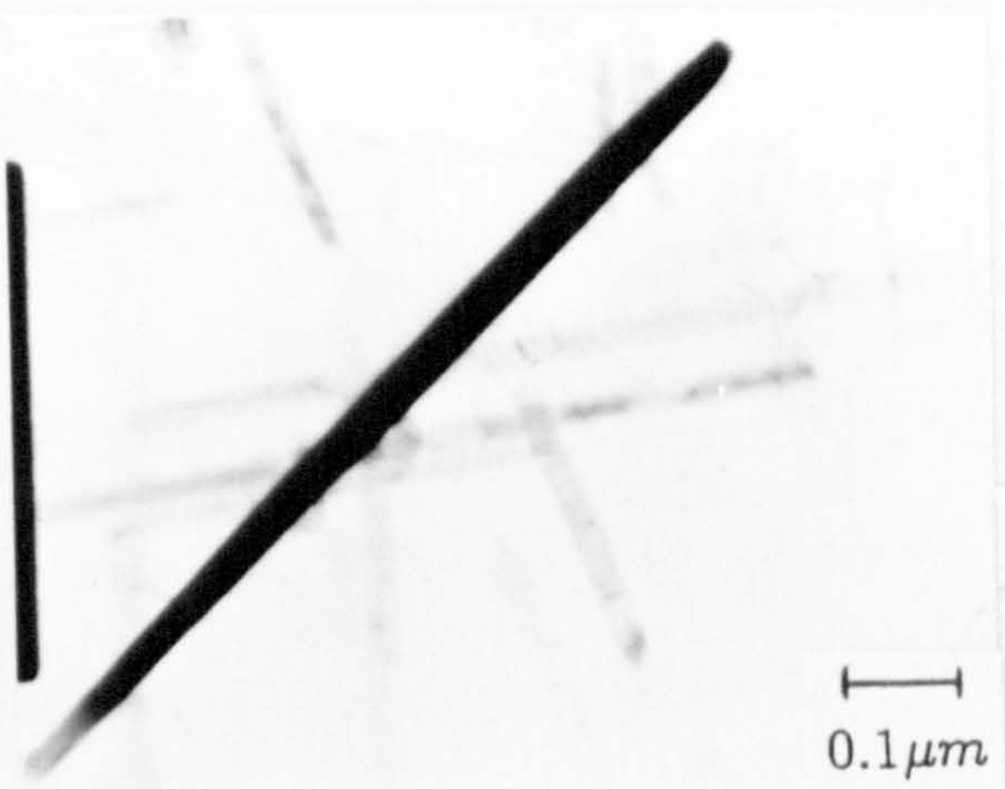

Solid billet heated at 400°C and quenced

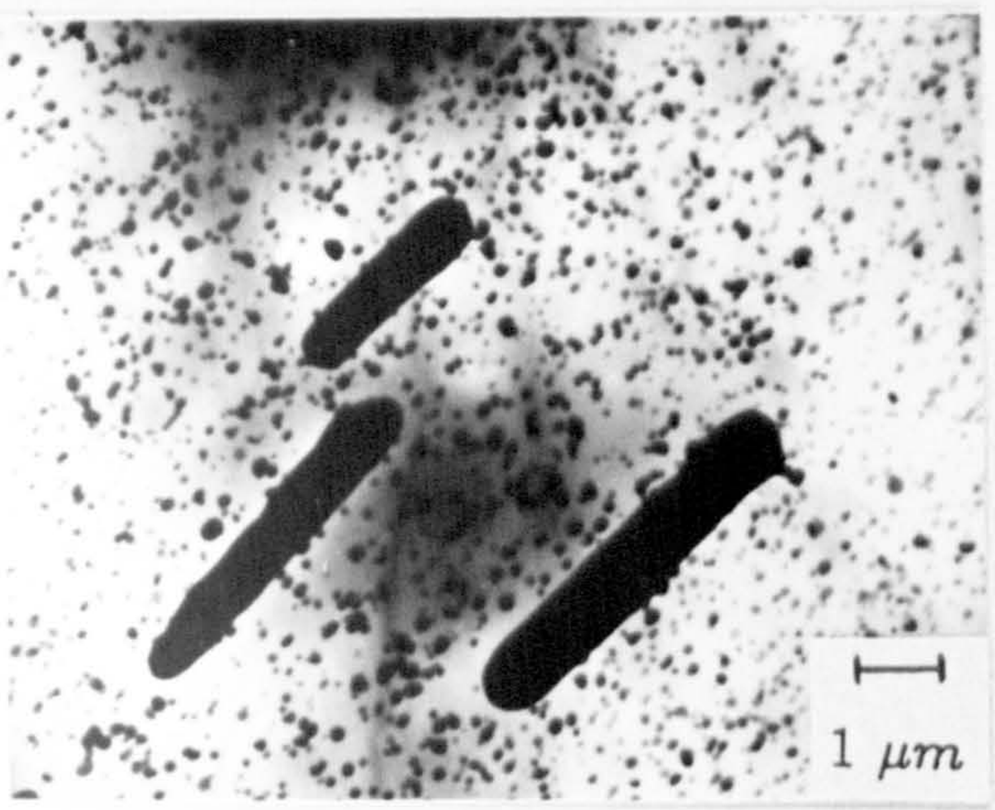

Solid extruded at Tx=411°C

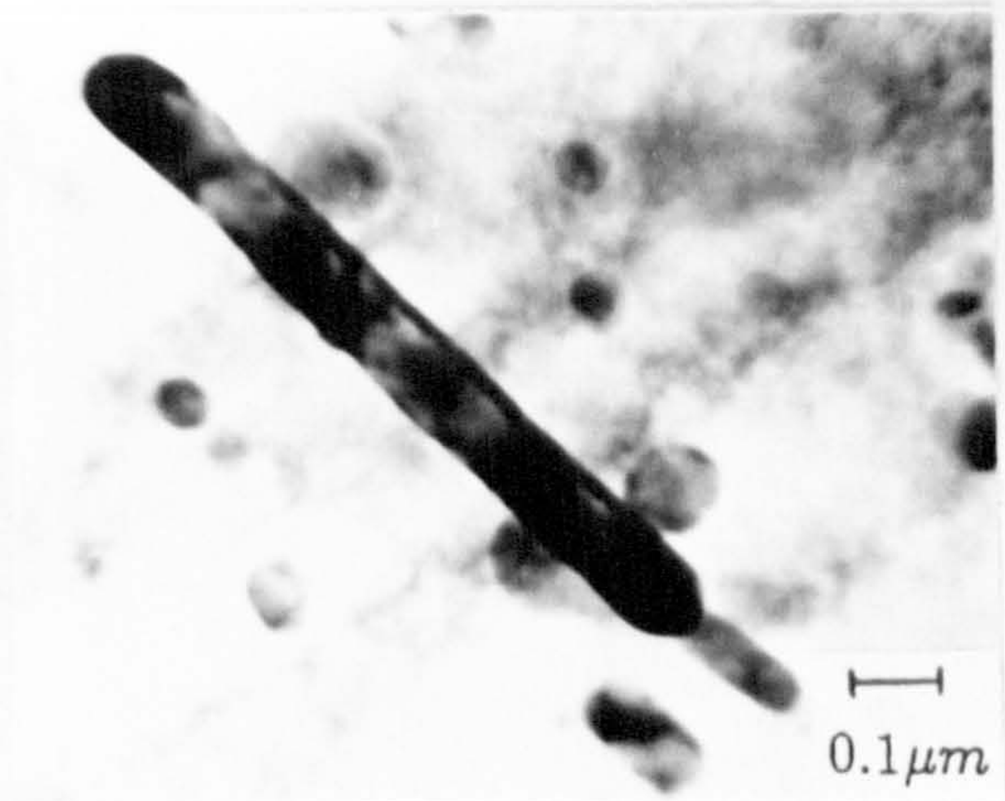

Powder compression tested at 400°C

Plate 41

THESIS CONTAINS MICROFICHE